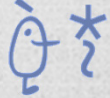


Computations on electroactive molecular materials:
from donor-acceptor architectures
to supramolecular polymers

Joaquín Calbo Roig

 { Doctorado en Química Teórica
y Modelización Computacional }



VNIVERSITAT
ID VALÈNCIA

Supervisors:

Enrique Ortí Guillén
Juan Aragó March

February, 2017

Joaquín Calbo Roig | PhD Thesis



2017

Joaquín Calbo Roig

**Computations on electroactive molecular materials:
from donor–acceptor architectures
to supramolecular polymers**

PhD Thesis

Supervised by

Prof. Enrique Ortí Guillén and Dr. Juan Aragó March

MolMatTC Group

Theoretical Chemistry Research Unit

Institute of Molecular Science



VNIVERSITAT
DE VALÈNCIA

Valencia, February 2017



VNIVERSITAT
E VALÈNCIA

Departament de Química Física

D. Enrique Ortí Guillén y **D. Juan Aragón March**, Catedrático del Departamento de Química Física y Doctor-Investigador en el Instituto de Ciencia Molecular (ICMol), respectivamente, CERTIFICAN que la memoria presentada por el licenciado Joaquín Calbo Roig con el título "*Computations on electroactive molecular materials: from donor-acceptor architectures to supramolecular polymers*" corresponde a su Tesis Doctoral y ha sido realizada bajo su dirección, autorizando mediante este escrito la presentación de la misma.

En Valencia, a 1 de febrero de 2017.

Prof. Enrique Ortí Guillén

Dr. Juan Aragón March

*Al papa, a la mama,
i als germans Javi i Migue.*

Acknowledgements

Si bien ésta es una de las secciones más cortas de la Tesis, sin duda es la más importante. Nada de este trabajo habría sido posible sin las personas que me han acompañado durante todo este viaje. Disculpas de antemano a todas aquellas personas que no he podido nombrar y que también han participado de alguna manera en el desarrollo de esta Tesis.

En primer lugar, quiero agradecer a Enrique Ortí la oportunidad que me brindó para hacer ciencia. «Gracias Enrique por acogerme en tu grupo de investigación, el que ha sido como una segunda familia para mí.» A la par, quiero agradecer a Juan Aragón, quien en Valencia o en Warwick siempre ha estado guiando mis pasos durante esta Tesis. «Gracias a ambos por ser mis supervisores a lo largo de este camino que ha sido una gran experiencia tanto a nivel profesional como personal, y que nunca olvidaré. Vosotros me habéis enseñado no sólo ciencia, sino valores como el esfuerzo, la entrega y la ilusión por el trabajo.»

Vull agrair, en segon lloc però tal vegada el més important, a la meua família. «Moltes gràcies al papa, a la mama, als germans Javi i Migue, i al gosset Betoven, per haver estat sempre al meu costat, recolzant-me en tot moment i en totes les decisions que he tingut que prendre. Mai podré expressar en paraules tot el què vos vull, així que considereu esta Tesi com un xicotet regal per a vosaltres. Espere que poc a poc pugua tornar-vos tot l'esforç i sacrifici que m'heu dedicat, i que estigueu orgullosos de mi. Vosaltres sou la raó per la qual he aplegat fins aquí.»

Me gustaría reconocer a todas las personas que me han rodeado en el trabajo del día a día en el ICMol. En especial quiero agradecer a todo el

grupo de MatMolTC por tener siempre la puerta abierta a mis incansables dudas y cavilaciones. Gracias Pedro, Rafa, J.M., Paula, Toni “el experimental”, Dani “el tostao”, y al pequeño padawan Jesús. «Jesús, no te preocupes, heredarás mi monitor.» Tampoco me olvido de Pepe “el sabio”, que siempre nos ha deleitado con su gran conocimiento, además de haber sido un fuerte apoyo en el periodo de máster.

A la par, quiero agradecer a todas las personas que han ido poblando el “otro” despacho. A pesar de pertenecer a otros grupos de investigación, su labor no ha sido menos importante, formando parte de las mejores amistades que he sembrado en este periodo; «gracias Toni, Angelo, Javi, Dani, Juanjo, Jelle, Vicente, Pedro, Vicenta...». Asimismo, nunca me olvidaré de todos los compañeros *Erasmus Mundus* que han pasado fugazmente por el ICMol pero cuya huella será perpetua: Benji, Pablito, María, Tirso, Gustavo, Vijay, José Manuel, Bin, Meilani, Ahmad, Jake, Sebastian... Y, también, al recién llegado Michael (o Maikol, “bien” pronunciado).

A pesar de no contribuir directamente, también quisiera agradecer al grupo de amigos de mi pueblo que me han ayudado a desconectar de vez en cuando durante la Tesis; para ir a tomar unas birras, charlar de algo que no fuera trabajo, o viciarnos al *League of Legends*.

Last but not least, I would like to acknowledge all the fruitful collaborations I have been involved along the PhD period. I am especially grateful to the groups of Nazario Martín, Emilio M. Pérez, Luis Sánchez, Concepció Rovira, Julia Contreras and Filippo de Angelis, just to mention a few of them. The nice piece of work I will present in the next pages would have not become reality without the intense cooperation of these research groups we have collaborated with side by side.

*“The important thing is
to not stop questioning.”*

Albert Einstein

Index

Acknowledgements.....	I
Index.....	V
Chapter 1. Introduction.....	1
Chapter 2. Objectives.....	9
Chapter 3. Methodology: computational chemistry.....	11
3.1. Density functional theory.....	12
3.2. Hierarchy rungs of functionals.....	16
3.3. Dispersion-corrected DFT.....	20
3.4. Time-dependent density functional theory.....	24
3.5. Basis sets.....	26
3.6. Semiempirical methods.....	28
3.7. Molecular mechanics.....	29
3.8. Molecular dynamics.....	31
3.9. Solvation models.....	33
3.10. Periodic boundary conditions.....	34
3.11. Symmetry-adapted perturbation theory.....	35
3.12. Noncovalent index.....	36
Chapter 4. Covalent donor–acceptor architectures.....	39
4.1. Introduction.....	41
4.2. Results and discussion.....	45
4.2.1. Mono-branched exTTF-based chromophores.....	45
4.2.2. Di-branched hemiexTTF derivatives.....	50
4.2.3. Single- vs. double-anchoring adsorption modes.....	54
4.3. Summary.....	60
4.4. Publications.....	63
Chapter 5. Supramolecular donor–acceptor complexes.....	91

5.1. Introduction	93
5.2. Results and discussion.....	97
5.2.1. Metal-atom effect: monotopic porphyrin•C ₆₀ assemblies	97
5.2.2. Cooperativity in ditopic porphyrin•C ₆₀ complexes.....	102
5.2.3. The truxTTF•hemifullerene supramolecular complex.....	109
5.2.4. Buckybowls for donor–acceptor assemblies	115
5.3. Summary	121
5.4. Publications.....	123
Chapter 6. Supramolecular polymers.....	157
6.1. Introduction	159
6.2. Results and discussion.....	163
6.2.1. Tricarboxamide supramolecular polymers.....	163
6.2.2. Pyreneimidazole-based oligomers.....	169
6.3. Summary	175
6.4 Publications.....	177
Chapter 7. Conclusions	189
Capítulo 8. Resumen	193
8.1. Introducción.....	193
8.2. Objetivos.....	196
8.3. Metodología.....	197
8.4. Arquitecturas dador–aceptor covalentes.....	201
8.5. Complejos dador–aceptor supramoleculares	207
8.6. Polímeros supramoleculares	216
8.7. Conclusiones	224
Bibliography.....	229
List of publications	243
Collaborations	249

*“Education is the key to unlock
the golden door of freedom.”*

George Washington Carver

Chapter 1. Introduction

An electroactive compound is, by definition, any chemical entity that undergoes a change of oxidation state, or the breaking/formation of chemical bonds, in a charge-transfer step.^[1] In the context of organic electronics, electroactive compounds can be classified attending to their electronic nature into electron-rich (donor) systems and electron-deficient (acceptor) compounds.^[2] Whereas electron-donor systems are easily oxidized showing a low ionization potential, electron-acceptor compounds readily accept electron density providing highly favourable electron affinities. Due to the enormous possibilities that brings synthetic chemistry, electroactive carbon-based compounds have been subjected to uncountable modifications, and their bulk properties have been widely tuned by small variations in the molecular, usually π -conjugated, structure.^[3] This has led to interesting systems with semiconducting and optical characteristics that can be applied in commercial products. For example, electroactive π -conjugated organic systems have burgeoned applications across various branches of modern research such as organic electronics and optoelectronics,^[4] electronic conductors,^[5] photovoltaics^[6] and solar photon conversion.^[7]

The junction of an electron-donor and an electron-acceptor entity leads to one of the most important processes studied in nature: the electron transfer.^[8] When these two entities are placed in the same molecular system, the electron transfer can occur intramolecularly upon external stimuli, either through light, electrical or thermal activation. These composite entities are named as push-pull systems, in which the donor

and acceptor moieties are usually separated by means of a π -conjugated bridging structure (see Figure 1 for the scheme of a push-pull system).

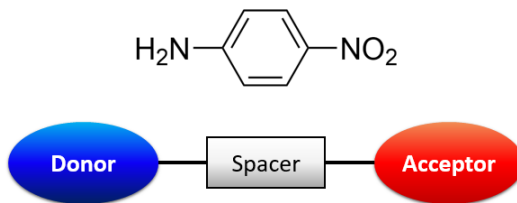


Figure 1. Prototypical donor- π -acceptor (push-pull) organic molecule: the so-called *p*-nitroaniline.^[9]

Push-pull molecules have found predominant applications as chromophores with appealing nonlinear optical (NLO) properties,^[10] as electro-optic^[11] and piezochromic^[12] materials, NLO switches,^[13] photochromic^[14] and solvochromic^[15] probes, as well as in photovoltaics.^[16] Although vastly utilized in the fabrication of small-molecule bulk heterojunction solar cells,^[17] the most prominent photovoltaic application of push-pull chromophores has focused on the so-called Grätzel's dye-sensitized solar cells.^[18] A dye-sensitized solar cell (DSC) is a low-cost photovoltaic cell that belongs to the group of thin film devices, and is based on a semiconductor between a photosensitized anode and an electrolyte.^[19] The modern version of a DSC was originally co-invented in 1988 by Brian O'Regan and Michael Grätzel at UC Berkeley,^[20] and thenceforth a maddening race for achieving conversion efficiencies near conventional silicon-based technologies has taken place.^[19b, 21] In these devices, a dye-sensitizer absorbs the solar radiation and the photoexcited electron is transferred to the conduction band of the semiconductor, typically constituted by nanoparticles of TiO₂. Then, a

redox mediator, commonly based on the iodide/triiodide couple, regenerates the oxidized dye, thus completing the circuit (Figure 2).

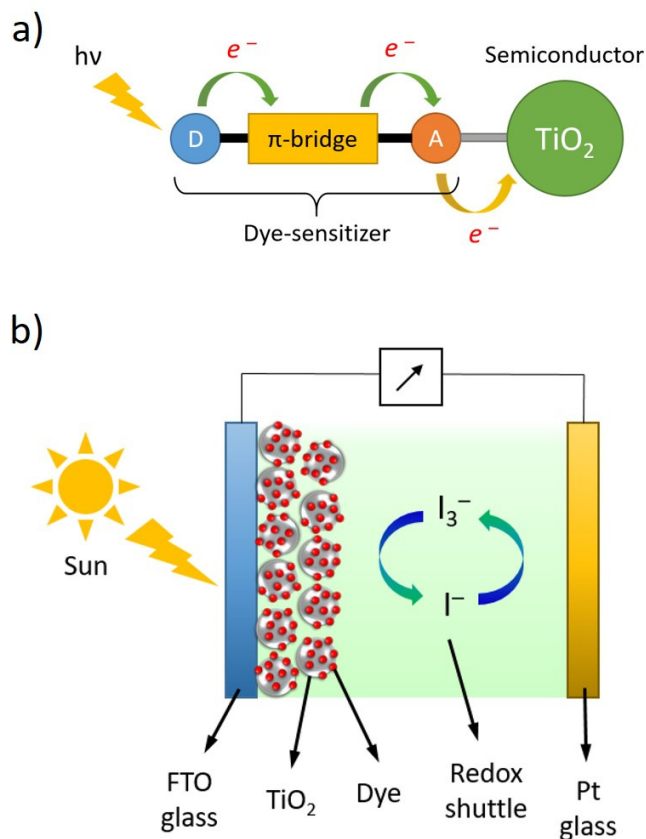


Figure 2. Schematic representation of the different parts of a DSC. a) Components of a donor–acceptor chromophore linked to the TiO₂ semiconductor showing the electron-transfer process from the dye to the semiconductor. b) Scheme of a dye-sensitized solar cell device.

Since the discovery of the efficient ruthenium(II)-based complexes, such as N3 and N719,^[22] much effort has been done to synthesize high performing push–pull organic dyes as sensitizers for DSCs, especially metal-free derivatives. The low-cost, tuneability and environmental

friendliness constitute the main advantages of purely organic dyes in contrast to metal-based analogues. However, only very few organic dyes have recorded efficiencies that can compete directly with the most prominent Ru-based complexes.^[23] Not only the nature of the chromophore but also the characteristics of the electrolyte couple, the solvent environment and the topology of the semiconducting material have demonstrated to play an important role for achieving high efficiencies.^[19b] Understanding each of the components of a DSC that directly impact on the final photoconversion performance has therefore attracted much attention of the scientific community.

Whereas electron transfer can occur intramolecularly upon photoexcitation in a donor–acceptor compound, the analogous intermolecular process is present in the context of supramolecular chemistry.^[24] Supramolecular chemistry bears any kind of chemical system constituted by two or more entities linked by means of noncovalent forces, i.e., through electrostatic or dispersion forces, H-bonding, etc.

From the second half of the past century, the outbreak of donor–acceptor complexes was originated owing to the discovery of two of the most-ever-studied electroactive organic molecules: the electron-acceptor tetracyanoquinodimethane (TCNQ)^[25] and the electron-donor tetrathiafulvalene (TTF)^[26] compounds. The combination of both led in 1973 to the formation of a strong charge-transfer complex, referred to as TTF–TCNQ (Figure 3).^[27] This molecular material showed metal electrical conductance and constitutes the first purely donor–acceptor organic conductor. In a TTF–TCNQ crystal, TTF and TCNQ molecules are arranged in separate parallel-aligned stacks; however, the charge-

transfer phenomena are usually analysed in terms of a supramolecular donor–acceptor TTF•TCNQ dimer model as shown in Figure 3b.^[28]

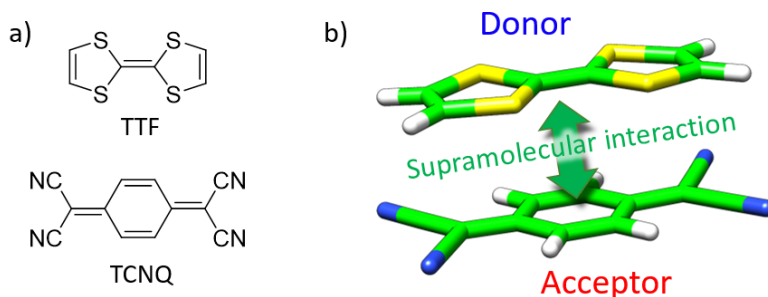


Figure 3. a) Chemical structure of the prototypical electron-donor TTF and electron-acceptor TCNQ molecules. b) Schematic representation of the supramolecular association of TTF and TCNQ in the TTF•TCNQ complex model.

Ever since the discovery of the TTF–TCNQ complex, the supramolecular chemistry of donor–acceptor complexes has been exploited in a fruitful new interdisciplinary avenue of research.^[29] Original and creative host–guest complexes have risen by combining the understanding of individual electron-donor and electron-acceptor chemical entities with the many opportunities brought by the supramolecular chemistry. Host–guest complexes have received special attention for the supramolecular recognition of carbon-based nanoforms (such as fullerenes, nanotubes and fullerene fragments) and other target chemical entities of interest.^[30] In such self-assembled complexes, the donor and acceptor moieties remain close to each other through different noncovalent interactions, and may undergo energy-transfer and electron-transfer processes upon light induction.^[31] Artificial small-scale supramolecular complexes designed *in situ* have already helped to better understand the physical

origin of the forces involved in the self-assembly process, and to shed light on the complex electron-transfer phenomena.^[32] However, scientific community is still far away from fully comprehending the entrails of the self-assembling operation, which has recently demonstrated to go beyond the traditional thermodynamic regime.^[33] As long as the supramolecular chemistry of donor–acceptor assemblies progresses, society will gain insight into the fundamentals of electron transfer while building up novel host–guest chemical constructs with potential applications in materials science.

Self-assembly has become a widely applied approach in chemistry and material science to direct individual electroactive molecules into larger functional structures.^[34] In contrast to the conventional covalent polymerization, in which chemical units are covalently linked to their neighbours, supramolecular polymerization is based on the directional growth of self-assembled discrete molecular entities by means of noncovalent interactions (Figure 4). With the introduction of supramolecular polymers, the playground for polymer scientists broadened and is no longer limited to macromolecular species only. Although the area of self-assembly of molecules into one-dimensional multicomponent structures has been known for decades, it is only of recent date that these supramolecular polymers deserve a steadily increasing interest due to their unprecedented and highly useful functional opportunities.^[35] The high expectations for self-assembled supramolecular polymers have mainly focused on their appealing electronic properties, such as tuneable emission, energy transfer, charge transport, and electrical conductivity.^[36] Such properties are amenable to modulation through size and shape control of the molecular assemblies.^[37] Supramolecular polymers have therefore found

applications in recyclable, degradable, stimulus-responsive, and self-healing materials.^[37b, 38]

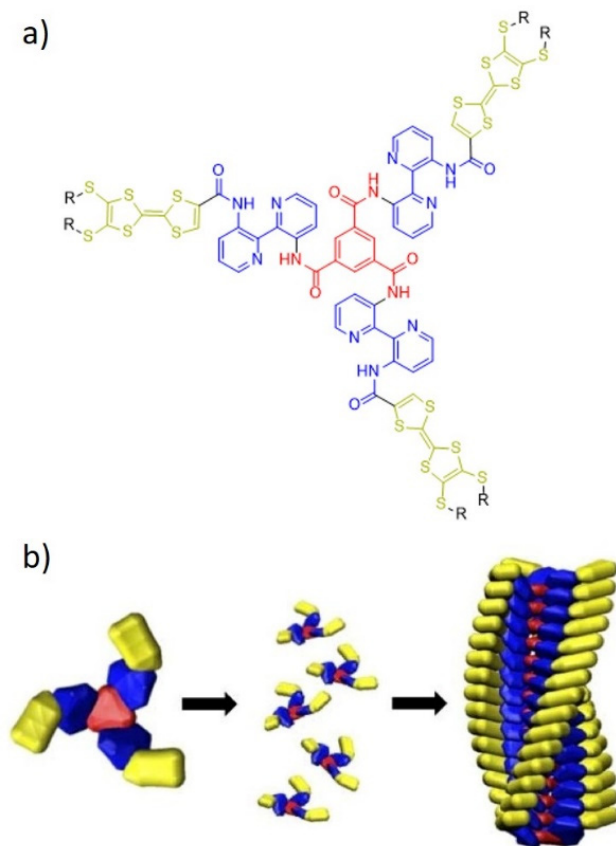


Figure 4. Supramolecular polymerization of a discotic benzene trisamide derivative (a) featuring chirality upon self-assembly (b).^[38c]

Supramolecular assemblies are commonly found to exhibit a basic characteristic of living matter and nature: chirality.^[38a, 39] There are many biological macromolecules or supramolecular systems with chirality, from microorganisms with helix-shaped viruses to macroscopic living systems such as snails. On a larger scale, one finds that many plants express chiral sense, such as mountain climbing vines. Even on a light-

year scale, our galaxy system is also chiral. Among these various levels (Figure 5), chirality at a molecular and supramolecular level is of vital importance since it is strongly related to chemistry, physics, biology, materials, and nanoscience, which treat the matter in scales from atomic to molecular and supramolecular. In the specific field of supramolecular chemistry, self-assembly occurs upon autonomous organization of individual molecular components into patterns or superstructures without human intervention.^[40] For instance, molecular self-assembly plays an important role in biological systems, the transfer and storage of genetic information in nucleic acids, and the folding of proteins into efficient molecular machines.^[41] Although supramolecular chirality is strongly related to the chirality of the molecular components, it is not necessary that all components be chiral. To this end, achiral molecules can also produce supramolecular chirality in a self-assembled system.^[38a] A deep exploration of stereogenic supramolecular aggregates will provide a more complete understanding of the origin of chirality in biological systems and self-assembling processes, as well as assistance in developing drugs and materials with new functional opportunities.

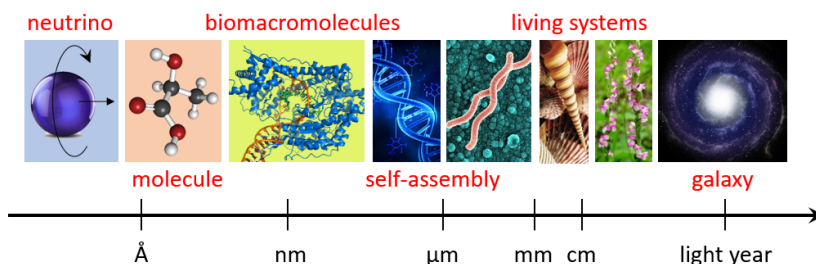


Figure 5. Chiral architectures at different scales, from neutrinos to enantiomeric molecules, nanosized biomacromolecules with chiral structures (DNA), microorganisms (helix-shaped bacteria), macroscopic living systems (seashells and plants), and galaxies.

Chapter 2. Objectives

The aim of the present Thesis is to unravel and disentangle the chemical origins of the appealing optical, electronic and self-assembling properties exhibited by novel electroactive molecular systems of interest in organic electronics and materials science.

1. Theoretical calculations will be performed on novel donor-acceptor chromophores absorbing in the whole visible spectrum to provide important structure-property relationships towards the discovery of efficient light-harvesters for dye-sensitized solar cells. The linkage of the chromophores to the semiconductor surface will be studied in depth by means of first-principles calculations to better understand the implications of a multi-anchoring adsorption mode in the solar cell performance.
2. In the search of model candidates for deepening in the comprehension of the ubiquitous photoinduced charge-transfer phenomena, donor-acceptor supramolecular complexes based on carbon nanoforms were theoretically characterised. The nature and strength of the supramolecular interactions that govern the self-assembly of porphyrin-based hosts with a fullerene guest will be analysed by means of quantum chemistry calculations. The theoretical inspection of supramolecular donor-acceptor assemblies of carbon-based buckybowls will provide insight into the forces governing the self-assembly of these novel donor-acceptor complexes that undergo charge-transfer processes upon photoexcitation.

3. The cooperative supramolecular polymerization of discotic-like benzene-trisamide derivatives will be theoretically investigated to understand the role of H-bond interactions in the generation of helical superstructures. Molecular dynamics simulations will be carried out to help rationalize the effect on the preferred helical orientation by (i) the connectivity of the amide groups, and (ii) the presence of stereogenic peripheral alkyl chains. Finally, a thorough theoretical characterization of the supramolecular assembly of pyreneimidazole derivatives will be performed to explain the unexpected blue-emission properties of the gels formed upon aggregation. The rationalization of the noncovalent forces guiding the supramolecular organization will ultimately aim the design of self-assembled materials *a la carte*.

Chapter 3. Methodology: computational chemistry

During the last decades, the discovery of theoretical and computational principles and algorithms, together with the development of increasingly faster computers, has resulted in an enormous leap on the accuracy and speed of computational methods.^[42] The predictive power of the current numerical simulation approaches, based on both quantum mechanics and molecular mechanics descriptions, underpins the emerging field of computational materials design.^[43] The scientific community has now access to theoretically characterise systems inconceivable to compute several years ago (Figure 6).

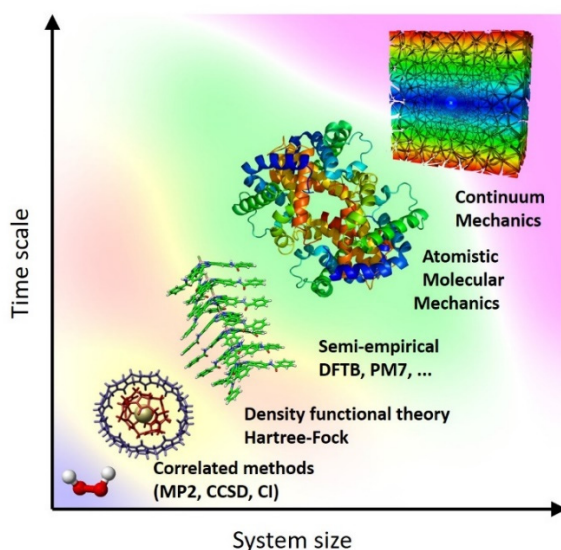


Figure 6. Schematic representation of the available computational approaches most used in the calculation of chemical systems of increasing size.

The development of quantum mechanical techniques, and density functional theory (DFT) in particular, have proceeded an ever accelerating pace.^[44] Whilst first-principles methodologies were once limited to simple structures and compositions with tenths of atoms, modern computer architectures enable the direct simulation of hundreds of atoms. By making a judicious choice of the methodology to be used, from small covalent structures to large supramolecular complexes can be computed at almost any desired accuracy, as long as sufficient computer resources are available.

In this chapter, the different methodologies and computational tools used to carry out the studies included in this Thesis are presented and briefly summarised. Most calculations included in this work have been done under the density functional theory framework. Otherwise, in order to reduce the computational cost required to explore molecular systems of increasing size, semiempirical as well as molecular mechanics methodologies have also been employed. All the computational techniques together with the theoretical specifications are fully detailed in the corresponding publications.

The following program packages have been used to perform the different calculations presented in this Thesis: Gaussian 09,^[45] ORCA,^[46] Quantum Espresso,^[47] MOPAC,^[48] Tinker,^[49] Psi4,^[50] and NCIPLLOT.^[51]

3.1. Density functional theory

Density functional theory (DFT) is arguably the computational quantum mechanical method most used in physics, chemistry and materials

science to investigate the electronic structure of many-body systems, in particular atoms, molecules, and condensed matter.

The density functional theory is based on the Hohenberg and Kohn theorem, which states that the ground-state electronic energy of a system is determined by its electron density ρ .^[52] The complicated and hard-to-compute many-electron wavefunction, which contains $3N$ variables for an N -electron system, is therefore substituted by a functional of the one-electron density, which contains only 3 coordinates independently of the number of electrons. Henceforth, whereas the complexity of a wavefunction increases with the number of electrons, the electron density has always the same number of variables and, in principle, does not depend on the system size. Unfortunately, the exact mathematical expression for the functional that connects the electron density of a system and its energy is unknown. Thereby, the main developments in the DFT field have been focused on the design of density functionals that properly connect these two terms.^[53]

A functional is a mathematical recipe for producing a number from a function, which in turn is a recipe for producing a number from a set of variables, in this case coordinates. In DFT, the energy depends on the electron density and is, therefore, a functional of it. The energy functional may be divided into three components: kinetic energy $T[\rho]$, attraction between the electrons and nuclei $E_{ne}[\rho]$, and electron–electron repulsion $E_{ee}[\rho]$. The nuclear–nuclear repulsion is considered constant since the most common DFT implementations are based on the Born–Oppenheimer approximation.^[54] Moreover, the E_{ee} term may be divided into the Coulomb and exchange parts, $J[\rho]$ and $K[\rho]$, respectively. The $E_{ne}[\rho]$ and $J[\rho]$ functionals are given by their classical expression,^[42]

$$E_{ne}[\rho] = \sum \int \frac{Z_a \rho(r)}{|R_a - r|} dr \quad (1)$$

$$J[\rho] = \frac{1}{2} \int \int \frac{\rho(r)\rho(r')}{|r - r'|} dr dr' \quad (2)$$

where Z_a and R_a are the atomic number and the position of atom a , respectively, and the factor of $\frac{1}{2}$ in $J[\rho]$ is needed to avoid double-counting in integrating over all space for both electronic coordinates r and r' . The application of DFT methods in computational chemistry was possible due to the introduction of the Kohn and Sham equations.^[55] Since the exact density matrix is not known, the approximate density $\rho(r)$ is written in terms of a set of auxiliary one-electron functions, the Kohn-Sham (KS) orbitals $\phi_i(r)$, by means of the following expression:

$$\rho(r) = \sum_{i=1}^N |\phi_i(r)|^2 \quad (3)$$

The basic idea in the KS formalism is splitting the kinetic energy functional into two parts, one of which can be calculated exactly by applying the classical kinetic operator on the KS molecular orbitals, and the other corresponding to the kinetic correlation energy part, which is always a positive energy. Thus, the exact part of the kinetic energy functional is given by

$$T_S = \sum_{i=1}^N \langle \phi_i | -\frac{1}{2} \nabla^2 | \phi_i \rangle \quad (4)$$

where the subscript S denotes that the kinetic energy is calculated from a Slater determinant. The remaining kinetic energy is absorbed into the exchange–correlation term ($E_{xc}[\rho]$), and a general DFT energy expression can be written as

$$E_{DFT}[\rho] = T_S[\rho] + E_{ne}[\rho] + J[\rho] + E_{xc}[\rho] \quad (5)$$

Additionally, it is customary to separate $E_{xc}[\rho]$ into two parts, a pure exchange E_x and a correlation E_c term, according to

$$E_{xc}[\rho] = E_x[\rho] + E_c[\rho] \quad (6)$$

The major problem in DFT is to derive accurate formulas to describe the exchange–correlation term. Assuming that such a functional is available, the problem is then similar to that found in wavefunction-based Hartree–Fock (HF) theory: determine a set of orthogonal orbitals which minimize the energy. Since $J[\rho]$ and $E_{xc}[\rho]$ functionals depend on the total density, the determination of the orbitals involves an iterative process (Figure 7). The first step is to give a trial electron density usually computed as a superposition of atomic densities. Then, the exchange–correlation potential (V_{xc}) is calculated on the basis of an appropriate expression for E_{xc} and the initial density. With this information, the Kohn–Sham equations are solved in order to obtain an initial set of orbitals, which is used to compute the density. The process is repeated until the electron density and the ground state energy converge.



Figure 7. Scheme of the iterative procedure used to solve the Kohn-Sham equations.

It is possible to prove that the exchange–correlation potential is unique and valid for all systems; however, an explicit functional form of this potential has been elusive to date. The difference between the plethora of DFT methods available is therefore the form of the exchange–correlation energy functional.

3.2. Hierarchy rungs of functionals

The local density approximation (LDA) was first introduced by P. Dirac within the Thomas–Fermi model, and it is based on the homogeneous electron gas density.^[56] LDA functionals depend locally on the density:

$$E_{xc}^{LDA}[\rho] = \int \varepsilon_{LDA}(\rho) dr \quad (7)$$

The LDA approximation can be improved by considering α and β densities separately, leading to the local spin density approximation (LSDA).

In the generalized gradient approximation (GGA), the exchange–correlation energy not only depends on the density but also on its gradients:

$$E_{xc}^{GGA}[\rho] = \int \varepsilon_{GGA}(\rho, \nabla\rho) dr \quad (8)$$

Using the GGA approximation, very good results for molecular geometries and ground-state energies have been achieved, e.g. with the popular Perdew–Burke–Ernzerhof PBE functional.^[57]

Another level of improvement was achieved by adding to the GGA formalism a dependence on the noninteracting kinetic energy density (τ) in the meta-GGA functionals:^[58]

$$E_{xc}^{meta-GGA}[\rho] = \int \varepsilon_{meta-GGA}(\rho, \nabla\rho, \tau) dr \quad (9)$$

A representative example of this type of functional is the TPSS.^[58]

Considering the exact wavefunction as a single Slater determinant composed of KS orbitals, the exchange energy is in this case exactly that given by the Hartree–Fock theory. If the KS orbitals are identical to the HF orbitals, then the “exact” exchange is precisely the exchange energy calculated by the HF wavefunction method. Models that include a portion of exact exchange are called hybrid methods, and the B3LYP functional is probably the most popular functional of this type,^[59] whose exchange–correlation energy is given by

$$E_{xc}^{B3LYP} = (1 - a)E_x^{VWN} + aE_x^{HF} + b\Delta E_x^{B88} + (1 - c)E_c^{VWN} + c\Delta E_c^{LYP} \quad (10)$$

where the a , b and c values are determined by fitting the experimental data to be 0.20, 0.72 and 0.81, respectively, B88, LYP and VWN refer to the Becke 88,^[60] Lee–Yang–Parr^[61] and Vosko–Wilk–Nusair^[62] functionals, respectively, $\Delta E_x^{B88} = E_x^{B88} - E_x^{VWN}$ and $\Delta E_c^{LYP} = E_c^{LYP} - E_c^{VWN}$.

Another popular hybrid functional is that designed by Perdew–Burke–Ernzerhof, so-called PBE0,^[63] which mixes the PBE exchange energy and Hartree–Fock exchange energy in a set 3-to-1 ratio, along with the full PBE correlation energy:

$$E_{xc}^{PBEO} = \frac{1}{4}E_x^{HF} + \frac{3}{4}E_x^{PBE} + E_c^{PBE} \quad (11)$$

Meta-GGA functionals can be modified to account for a certain amount of exact HF exchange, leading to the family of hybrid-meta-GGA functionals. Functionals of this type are the Minnesota M06,^[64] M06-2X^[65] and M06-HF^[66] with 27, 54 and 100 % of HF exchange, respectively, and the MPWB1K with 44 %.^[67]

An alternative and perhaps more sophisticated approach to the exact functional are the range-separated hybrid (RSH) functionals, where the exchange part is separated into a short-range and long-range regime by means of the standard error function $\text{erf}(x)$ such that:

$$\frac{1}{r_{12}} = \frac{1 - \text{erf}(\omega r_{12})}{r_{12}} + \frac{\text{erf}(\omega r_{12})}{r_{12}} \quad (12)$$

where ω is a parameter that determines the ratio of both parts. The short-range is treated as any of the exchange schemes shown before, while the

long-range part is computed by the HF exchange functional. CAM-B3LYP^[68] and ω B97X^[69] are representative functionals of this family.

Finally, double-hybrid (DH) functionals have also been developed,^[70] which include a certain amount of HF exchange and second-order perturbation PT2 correlation energy according to

$$E_{xc}^{DH} = (1 - a_x)E_x^{DFT} + a_x E_x^{HF} + (1 - a_c)E_c^{DFT} + a_c E_c^{PT2} \quad (13)$$

The amount of exact exchange is usually much bigger in these methods compared to the simple hybrids, since the perturbational correlation can correct for HF deficiencies while improving the self-interaction error.^[70] One of the most popular double-hybrid functionals is the Grimme's B2-PLYP,^[71] relative of the hybrid B3LYP functional, with parameters $a_x = 0.31$ and $a_c = 0.27$.

A schematic representation of the different rungs of functionals available to date sorted by increasing sophistication and accuracy is shown in Figure 8.

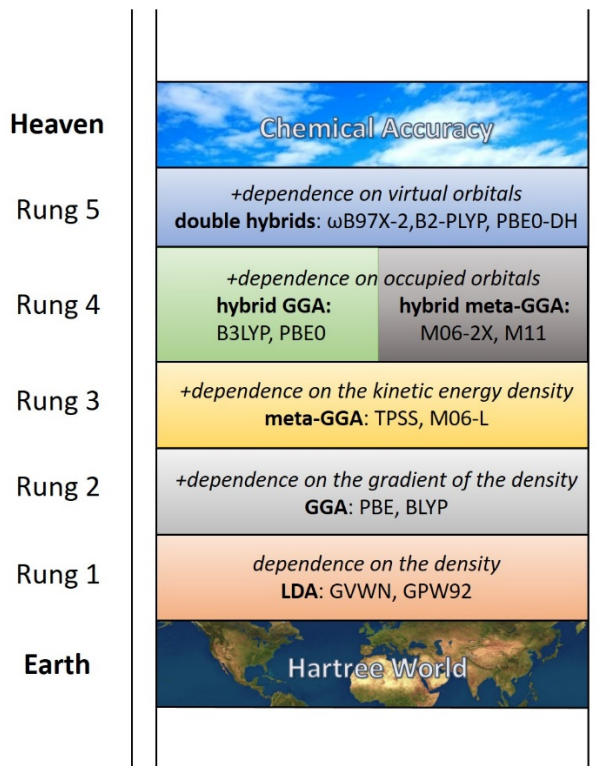


Figure 8. Perdew Jacob's ladder of density functional approximations.^[72]

3.3. Dispersion-corrected DFT

Dispersion forces arise from long-range instantaneous and correlated fluctuations of the electron density and, thus, nonlocal electron correlation terms are required for an appropriate description of these interactions. Dispersion forces are not exclusively intermolecular but take place also between large-separated regions of the same molecule.

The most common density functionals available in the literature are based on local or semilocal density correlation functionals and, therefore, the long-range electron correlation phenomenon responsible for these

elusive dispersion interactions is not fully captured. Only some highly-parameterised meta-GGA functionals can properly describe dispersion forces at the short range, such as the M06 and later Minnesota functionals.^[64-65]

The most popular low-cost approach to deal with dispersion interactions within the DFT framework is the Grimme's correction.^[73] This protocol consists in an atom-pairwise correction to the standard Kohn-Sham density functional to describe the total energy as:

$$E_{DFT-D} = E_{KS-DFT} + E_{disp} \quad (14)$$

where E_{KS-DFT} is the self-consistent Kohn-Sham energy as obtained from the chosen density functional, and E_{disp} is the dispersion correction term.

There are several ways to define the dispersion correction term, but the one proposed by Grimme and coworkers is based on the classical definition of long distance forces.^[73] The Grimme's dispersion correction term is directly proportional to the $C_{n,AB}/(r_{AB})^n$ relationship, where $C_{n,AB}$ is a parameterised n th-order dispersion coefficient for atom pair AB , and $(r_{AB})^n$ is the intermolecular AB distance (n can take the values 6, 8, 10, etc.)

In the original and latest version of Grimme's dispersion correction,^[73] known as D3, the dispersion interaction is computed according to the following pairwise energy expression:

$$E_{disp} = - \sum_{n=6,8} s_n \sum_i^{Nat-1} \sum_{j=i+1}^{Nat} \frac{C_{n,AB}}{(r_{AB})^n} f_{damp}(r_{ij}) \quad (15)$$

where s_n are customary parameters fitted for individual density functionals. Unlike the former D2 version of Grimme's correction, the dispersion $C_{n,AB}$ coefficients are geometry dependent as they are adjusted on the basis of local geometry (coordination number) around atoms A and B . f_{damp} is a damping function that depends on the distance r_{AB} , and may adopt several forms to attenuate the dispersion correction term in the short range.^[74] The D3 scheme can be further corrected by accounting for the influence of three-body terms (i.e., the energy contributions for all triple atom combinations A , B , and C) by means of the following expression:^[75]

$$E^{ABC} = \sum_{A<B<C}^N C_{9,ABC} \frac{(3 \cos \theta_a \cos \theta_b \cos \theta_c + 1)}{(R_{AB}R_{BC}R_{AC})^3} \times f_n(R_{AB}, R_{BC}, R_{AC}) \quad (16)$$

where θ_i are the internal angles of the triangle formed by the interatomic distances $(R_{AB}R_{BC}R_{AC})$, f_n is a damping function, and $C_{9,ABC}$ is the corresponding coefficient approximated by

$$C_{9,ABC} \approx -\sqrt{C_{6,AB}C_{6,BC}C_{6,AC}} \quad (17)$$

A more general, elegant and seamless approximation introduced by Dion and coworkers,^[76] widely known as the van der Waals density functional (vdW-DF), has recently received a great deal of attention to treat dispersion interactions owing to its low degree of empiricism. The vdW-DF approach accounts for the long-range electron correlation effects by means of an explicit nonlocal DF correlation kernel Φ , which depends on the electron density ρ at two different sampling points in space r and r' :

$$E_c^{vdW-DF}[\rho] = \frac{\hbar}{2} \int \int dr dr' \rho(r) \Phi(r, r') \rho(r') \quad (18)$$

In its most modern version (VV10),^[77] also known as the nonlocal (NL) approximation in quantum chemistry contexts, Vydrov and Voorhis employed a particularly simple expression for the nonlocal DF correlation kernel and introduced a new parameter to avoid the possible double counting of the dispersion or vdW energy at short-range distances. The incorporation of an adjustable short-range parameter allowed one to easily merge the VV10-type nonlocal correlation functional with a wide variety of standard exchange–correlation DFs giving impressive results close to the “chemical accuracy” in small- and medium-size molecular complexes.^[77]

Although the VV10 approximation is not used in the work discussed herein, our research group, and in particular the PhD student, has extensively worked in testing and validating the accuracy of the nonlocal approach in dealing with large supramolecular complexes governed by noncovalent interactions (see article 24 and book chapter in the List of publications).

Other approaches worth to mention that account for the weak dispersion interactions are the symmetry-adapted intermolecular perturbation theory (SAPT, see below for a brief description),^[78] the Tkatchenko–Scheffler (TS) approximation,^[79] the Corminboeuf density dependent dispersion correction (dDsC),^[80] and the Becke–Johnson exchange–hole dipole model (XDM).^[81] The reader is referred to the original literature for further details.

3.4. Time-dependent density functional theory

Time-dependent density functional theory (TDDFT) is an extension of DFT to deal with excitations or more general time-dependent phenomena. The TDDFT approach, in analogy to the ground-state DFT treatment, replaces the complex many-body time-dependent Schrödinger equation by a set of time-dependent single-particle equations. Whenever one wants to move beyond static ground-state properties (for instance, to evaluate the optical properties) within the DFT framework, the description of the molecular response to time-dependent fields has to be somehow introduced. E. Runge and E. K. U. Gross published a theorem in 1984 that permitted a generalization of the first HK theorem for a time-dependent density treatment.^[82] Very briefly, the approach of Runge and Gross considers a single-component system in the presence of a time-dependent scalar field, for which the Hamiltonian takes the form

$$\hat{H}(t) = \hat{T} + \hat{V}_{ext}(t) + \hat{W} \quad (19)$$

where \hat{T} is the kinetic energy operator, \hat{W} the electron–electron interaction, and $\hat{V}_{ext}(t)$ the time-dependent external potential.^[83] Nominally, the external potential contains the electrons’ interaction with the nuclei of the system. For non-trivial time-dependence, an additional explicitly time-dependent potential is present, which can arise, for example, from a time-dependent electric or magnetic field. The many-body wavefunction evolves according to the time-dependent Schrödinger equation under a single initial condition:

$$\hat{H}(t)|\Psi(t)\rangle = i\hbar \frac{\partial}{\partial t} |\Psi(t)\rangle, \quad |\Psi(0)\rangle = |\Psi\rangle \quad (20)$$

Employing the Schrödinger equation as its starting point, the Runge–Gross theorem shows that at any time, the density uniquely determines the external potential.

As ground-state DFT, TDDFT also requires a suitable approximation for time-dependent exchange–correlation potential to be applied in practice. This approach is known as the adiabatic exchange–correlation approximation (AXCA), and relates the time-dependent exchange–correlation potential to a ground-state exchange–correlation potential. Although AXCA is a crude approximation, its great advantage is that common ground-state DFT functionals (LDA, GGA, hybrids, etc.) can be easily used for the time-dependent problem.

Within TDDFT, linear-response TDDFT can be used if the external perturbation is small enough.^[84] This is a great advantage as, to first order, the variation of the system will depend only on the ground-state density so that all the properties of DFT can be used. In its most general form, the TDDFT linear response problem can be expressed in terms of a

Dyson-like equation.^[85] This equation allows computing a generalized susceptibility, whose poles are the excitation energies of the system under investigation. Casida transformed the Dyson-like equation for susceptibility into an eigenvalue problem, whose eigenvalues and eigenvectors are used to build up the optical absorption spectra.^[86] Nowadays, Casida's approach is the implementation set up in the majority of quantum chemistry codes.

3.5. Basis sets

The computed KS orbitals are usually expanded in a set of known basis functions. The one-electron atomic orbital ϕ_i can be linearly expanded by:

$$\phi_i = \sum_{j=1}^{\infty} C_{ij} \varphi_j \quad (21)$$

where φ_j correspond to the atomic basis functions. The expansion of the atomic basis functions can be done in terms of Slater-type orbitals (STOs) or in Gaussian-type orbitals (GTOs):

$$\varphi_{nlm_l}^{STO} = N \xi r^{n-1} e^{-\xi r} Y_{lm_l} \quad (22)$$

$$\varphi_{nlm_l}^{GTO} = N \xi r^{n-1} e^{-\xi r^2} Y_{lm_l} \quad (23)$$

where N is the normalization constant, Y_{lm_l} is the spherical harmonics, and ξ is a variational parameter related to the radial function that indicates the orbital compression.

STOs reproduce accurately the electronic behaviour round the nuclei. However, the two-electron integrals cannot be solved analytically using Slater functions, so a numerical procedure is required. The only difference of the GTOs with respect to STOs is a quadratic dependence on r in the exponential part. However, this difference is crucial since the form of the two-electron integrals written in terms of GTOs can be analytically solved saving a huge amount of computational time. GTOs do not have a cusp at the nucleus and decay to zero too rapidly; thus, a linear combination of several GTO functions are needed to represent accurately the electronic behaviour close to the nucleus and in the tail.

Valence electrons are usually described with several GTO combinations. Further improvement of basis sets can be achieved by the addition of extra functions (polarization and/or diffuse functions). It is common to represent valence orbitals by more than one basis function (each of which can in turn be composed of a fixed linear combination of primitive Gaussian functions). Additionally, basis sets can be designed with multiple basis functions corresponding to each valence atomic orbital (e.g., the so-called split-valence basis sets). Some of the most widely used basis sets are the Pople's split-valence basis sets,^[87] the correlation-consistent basis sets developed by Dunning and coworkers,^[88] and the basis sets of Ahlrichs and coworkers.^[89]

In addition to localized basis sets, plane-wave basis sets can also be used in quantum-chemical simulations. Typically, a finite number of plane-wave functions are used, below a specific energy cutoff which is chosen

for a certain calculation. Several integrals and operations are much easier to code and carry out with plane-wave basis functions than with their localized counterparts and, therefore, they have become popular in solid-state electronic structure calculations involving periodic boundary conditions.

In practice, plane-wave basis sets, and in general any basis set used to treat elements with high atomic number, are used in combination with a pseudopotential. The pseudopotential is an effective core potential constructed to replace the atomic all-electron potential such that core states are eliminated and the valence electrons are described by current basis set. In this approach, only the chemically active valence electrons are treated explicitly, while the core electrons are 'frozen', being considered together with the nuclei as rigid non-polarizable ion cores.

3.6. Semiempirical methods

The high cost of *ab initio* molecular orbital calculations is largely due to the many integrals that need to be calculated, especially the two-electron integrals. Semiempirical quantum chemistry methods are based on the Hartree–Fock formalism, but approximate various integrals with functions of some empirical parameters. These parameters are adjusted to improve the agreement with experimental data (or *ab initio* calculations). The semiempirical methods are widely used in computational chemistry for treating large molecules where the conventional Hartree–Fock, post-Hartree–Fock or DFT methods become prohibitive.

The most frequently-used semiempirical methods are based on the Neglect of Differential Diatomic Overlap (NDDO) integral approximation (MNDO,^[90] AM1,^[91] PM3,^[92] etc.), while older methods use simpler integral schemes such as CNDO and INDO. All three approaches (NDDO, CNDO and INDO) belong to the class of Zero Differential Overlap (ZDO) methods,^[93] in which all two-electron integrals involving two-centre charge distributions are neglected. The recently developed PM7,^[94] a modified version of PM3 in its latest parameterization —so called PM6—^[95] not only removes some errors of the NDDO approximation that affect large systems, but also average errors in organic compounds are reduced by $\sim 10\%$, and errors in large organic and solid systems are significantly diminished. More importantly, PM7 implicitly accounts for weak noncovalent interactions, which allows its use in supramolecular complexes of increasing size.

3.7. Molecular mechanics

Molecular mechanics is based on classical mechanics to model molecular systems.^[96] Molecular mechanics can be used to study molecular entities of large size and complexity (e.g., biological systems or material assemblies with many thousands of atoms). The potential energy of any system in molecular mechanics is calculated using a force field. This potential function or force field calculates the molecular system's potential energy (E) in a given conformation as a sum of individual energy terms:

$$E = E_{covalent} + E_{noncovalent} \quad (24)$$

where the components of the covalent and noncovalent contributions are given by:

$$E_{covalent} = E_{bond} + E_{angle} + E_{dihedral} \quad (25)$$

$$E_{noncovalent} = E_{electrostatic} + E_{van\ der\ Waals} \quad (26)$$

The bond and angle terms are usually modelled by quadratic energy functions that do not allow bond breaking:

$$E_{bond} = \sum K_r (r - r_{eq})^2 \quad (27)$$

$$E_{angle} = \sum K_\varphi (\varphi - \varphi_{eq})^2 \quad (28)$$

where K_r and K_φ are the bond and angle force constants, respectively, and $r - r_{eq}$ and $\varphi - \varphi_{eq}$ are the distance and angle from equilibrium, respectively.

The functional form for the dihedral energy is however highly variable; the most employed expression being:

$$E_{dihedral} = \sum K_\phi [1 + \cos(n\phi - \delta)] \quad (29)$$

where K_ϕ is the dihedral force constant, n is the multiplicity of the function, ϕ is the dihedral angle, and δ is the phase shift. Improper torsional terms may be added to enforce the planarity of aromatic rings

and other conjugated systems, as well as ‘cross-terms’ to describe coupling of different internal variables, such as angles and bond lengths.

The nonbonded terms are more computationally intensive. A popular choice is to limit interactions to atomic pairwise energies, which are calculated for those atom pairs belonging to different molecules, or separated by at least 3 bonds. The van der Waals term is usually computed with a Lennard–Jones potential,^[97] and the electrostatic term with Coulomb’s law:

$$E_{noncovalent} = \sum \left\{ \underbrace{\epsilon \left[\left(\frac{r_0}{r} \right)^{12} - 2 \left(\frac{r_0}{r} \right)^6 \right]}_{E_{van\ der\ Waals}} + \underbrace{\frac{q_i q_j}{\epsilon r}}_{E_{electrostatic}} \right\} \quad (30)$$

where r_0 is the distance at which the potential reaches its minimum, ϵ is the potential depth, ϵ is the dielectric constant and q is the atomic charge. Both nonbonded terms can be buffered or scaled by a constant factor to account for electronic polarizability and provide better agreement with experimental observations.

3.8. Molecular dynamics

Molecular dynamics (MD) is a computer simulation method that allows studying the time-dependent motion of atoms and molecules.^[98] The trajectories of atoms and molecules are usually determined by numerical resolution of Newton’s equations of motion for a system of interacting particles, where the forces and potential energies between particles are calculated using the previously described force fields. Because of its

simplicity and stability, the Verlet algorithm is commonly used in MD simulations.^[99] The basic formula for this algorithm can be derived from the Taylor expansions for the positions

$$\mathbf{r}_i(t + \Delta t) \cong 2\mathbf{r}_i(t) - \mathbf{r}_i(t - \Delta t) + \frac{\mathbf{F}_i(t)}{m_i} \Delta t^2 \quad (31)$$

where $\mathbf{r}_i(t) = (x_i(t), y_i(t), z_i(t))$ is the position vector of i th particle at time t , \mathbf{F}_i is the force acting upon i th particle at time t , and m_i is the mass of the particle.

Ab initio molecular dynamics, in contrast to classical MD where the potential surface is represented by a force field, describes the electronic behaviour during the simulation by using first-principles quantum mechanical methods.^[100] The Car–Parrinello (CP) method is a popular *ab initio* molecular dynamics method proposed by Roberto Car and Michele Parrinello in 1985.^[101] In contrast to Born–Oppenheimer molecular dynamics, where the nuclear (ions) degree of freedom are propagated using ionic forces calculated at each iteration by approximately solving the electronic problem, the Car–Parrinello method explicitly introduces the electronic degrees of freedom as (fictitious) dynamical variables, writing an extended Lagrangian for the system. This leads to a system of coupled equations of motion for both ions and electrons, in which explicit electronic minimization at each time step is not required. In order to maintain the adiabaticity condition, it is necessary that the fictitious mass of the electrons is chosen small enough to avoid a significant energy transfer from the ionic to the electronic degrees of freedom.

The equations of motion of the CP molecular dynamics method are obtained by finding the stationary point of the Lagrangian under variations of the Kohn–Sham orbitals ϕ_i and nuclear positions \mathbf{R}_j :

$$M_I \ddot{\mathbf{R}}_I = -\nabla_I E[\{\phi_i\}, \{\mathbf{R}_j\}] \quad (32)$$

$$\mu \ddot{\phi}_i(\mathbf{r}, t) = -\frac{\delta E}{\delta \phi_i^*(\mathbf{r}, t)} + \sum_j \Lambda_{ij} \phi_j(\mathbf{r}, t) \quad (33)$$

where Λ_{ij} is a Lagrangian multiplier matrix to comply with the orthonormality constraint.

3.9. Solvation models

Within the field of computational chemistry, solvent models are a variety of methods to account for the behaviour of solvated condensed phases. Solvent models enable simulations and thermodynamic calculations applicable to reactions and processes which take place in solution, either in molecular biology, chemistry or environmental science.

Many protocols exist to model solution environments within computational chemistry.^[42, 102] Explicit models consist in adding n solvent molecules around the solute, and therefore provide a physical spatially resolved description of the solvent. However, many of these explicit models are computationally very demanding and can fail to reproduce some experimental results, often due to certain fitting methods and parametrization.

Implicit models are, on the other hand, generally more efficient computationally, and can provide a reasonable description of the solvent behaviour.^[103] In implicit solvent models, the solvent is described as a homogeneous dielectric around the solute, which is placed in a cavity dug out of the solvent. The main idea is that the charge distribution of the solute polarises the dielectric continuum, which in turn polarises the solute charge distribution. The solute–solvent interactions are described in terms of a solvent reaction field, which is introduced into the Hamiltonian as a perturbation. Among the reaction field methods, the polarizable continuum model (PCM)^[104] and the solvation model based on density (SMD)^[105] are the most common approaches to include solvent effects.

3.10. Periodic boundary conditions

Periodic boundary conditions (PBC) are a set of boundary conditions used in computational modelling for approximating a large (infinite) system by using a small part called unit cell.^[98] In this approximation, an infinite system is constructed as a periodically repeated array of the finite system through the replication of the box simulation (Figure 9). Along the simulation, when a molecule moves in the main box, its periodic images move with exactly the same orientation in all the other boxes. Thus, as a molecule leaves the main box, one of its images will enter through the opposite site. PBCs are widely used in molecular dynamics simulations to avoid problems with boundary effects caused by the finite nature of the simulated system, and create a representation similar to infinite.

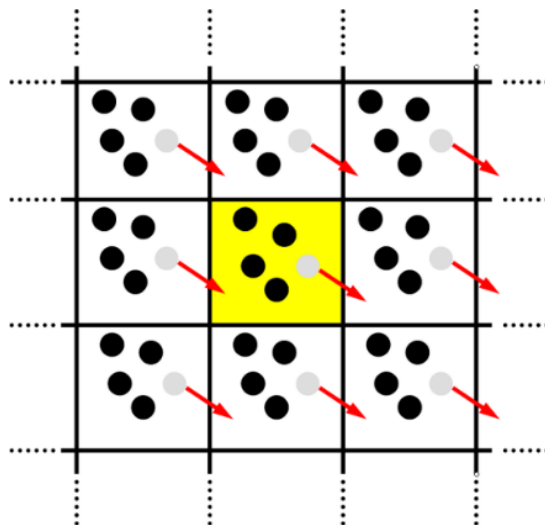


Figure 9. Schematic representation of periodic boundary conditions in two dimensions. The shaded box is replicated in both dimensions. A particle moving out of a box will be replaced by one moving in from the opposite side.

3.11. Symmetry-adapted perturbation theory

Symmetry-adapted perturbation theory (SAPT) provides a means of directly computing the noncovalent interaction between two molecules, that is, the interaction energy is determined without computing the total energy of the monomers or dimer.^[78] Besides, SAPT provides a decomposition of the interaction energy into physically meaningful components: electrostatic (elst), exchange (exch), induction (ind), and dispersion (disp) terms. In SAPT, the Hamiltonian of the dimer is partitioned into contributions from each monomer and the interaction between them according to:

$$H = F_A + W_A + F_B + W_B + V \quad (34)$$

where the Hamiltonian (H) is written as a sum of the monomer Fock operators, F ; the fluctuation potential of each monomer, W , and the interaction potential, V . The monomer Fock operators, $F_A + F_B$, are treated as the zeroth-order Hamiltonian, and the interaction energy is evaluated through a perturbative expansion of V , W_A , and W_B .

Several truncations of the closed-shell SAPT expansion are available. The simplest truncation of SAPT is denoted SAPT0^[78, 106] and defined by

$$E_{SAPT0} = E_{elst}^{(10)} + E_{exch}^{(10)} + E_{ind,resp}^{(20)} + E_{exch-ind,resp}^{(20)} + E_{disp}^{(20)} + E_{exch-disp}^{(20)} + \delta_{HF}^{(2)} \quad (35)$$

where v and w in $E^{(vw)}$ defines the order in V and $W_A + W_B$, respectively, the subscript *resp* indicates that orbital relaxation effects are included, and the $\delta_{HF}^{(2)}$ term takes into account higher-order induction effects.

3.12. Noncovalent index

The noncovalent index (NCI) analysis provides a magnitude, based on the electron density and its derivatives, that enables the identification of the spatial regions where the noncovalent interactions are acting.^[51] The NCI index is based on a 2D plot of the reduced density gradient s and the electron density ρ according to

$$s = \frac{1}{2(3\pi^2)^{1/3}} \frac{|\nabla\rho|}{\rho^{4/3}} \quad (36)$$

When a weak inter- or intramolecular interaction is present, there is a crucial change in the reduced gradient between the interacting atoms, producing density critical points between interacting fragments; troughs appear in $s(\rho)$ associated with each critical point. Since the behaviour of s at low densities is dominated by ρ , s tends to diverge except in the regions around a density critical point, where $\nabla\rho$ dominates, and s approaches zero.

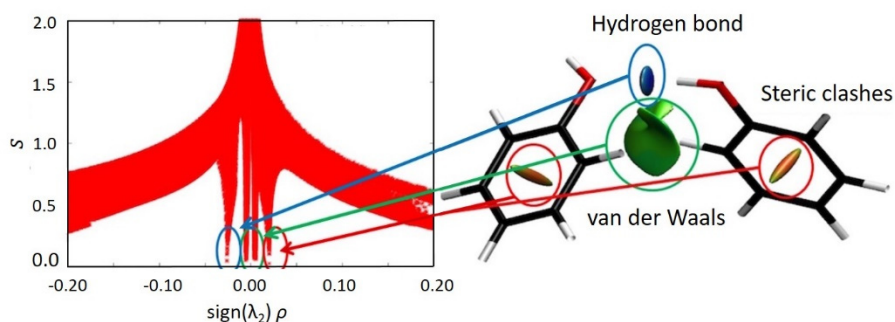
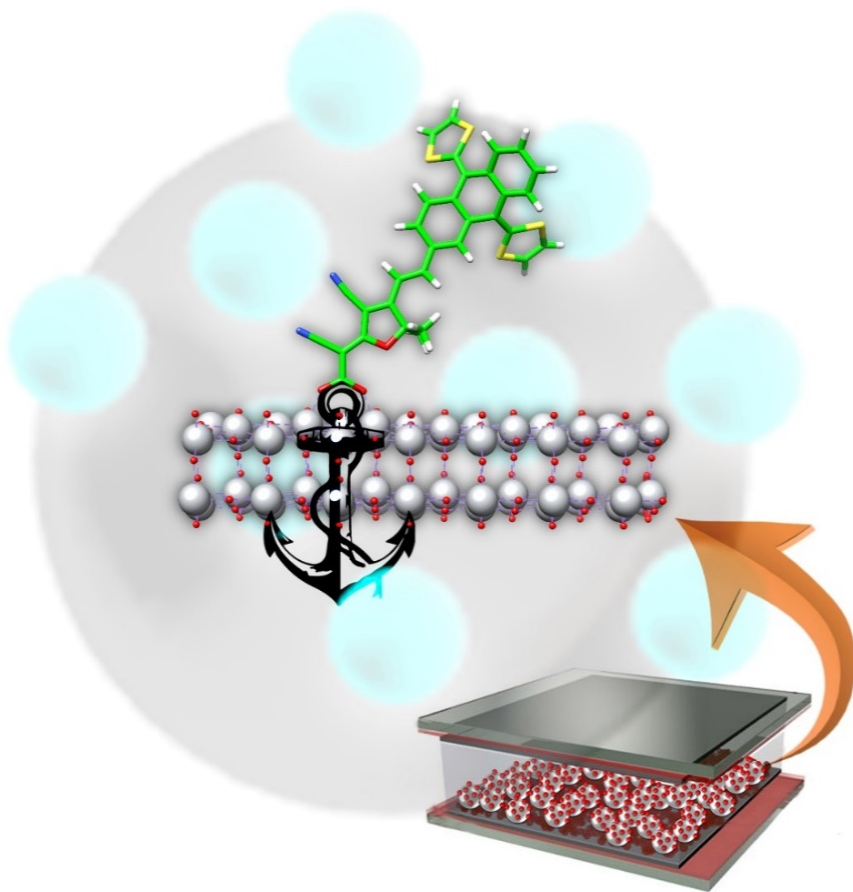


Figure 10. Representation of the NCI index s vs. the density coupled to the sign of λ_2 (left), and the 3D plot of the troughs colored by the strength of the interaction: blue (strong, attractive) – green (weak) – red (strong, repulsive).

The electron density values within the troughs are an indicator of the interaction strength. However, both attractive and repulsive interactions (i.e., hydrogen-bonding and steric repulsion) appear in the same region of density/reduced gradient space. On the basis of the divergence theorem, the sign of the Laplacian of the density $\nabla^2\rho$ indicates whether the net gradient flux of density is entering ($\nabla^2\rho < 0$) or leaving ($\nabla^2\rho > 0$) an infinitesimal volume around a reference point. To distinguish

between different types of weak interactions, contributions to the Laplacian along the axes of its maximal variation must be analysed ($\nabla^2\rho = \lambda_1 + \lambda_2 + \lambda_3$, where $\lambda_1 < \lambda_2 < \lambda_3$). On the one hand, bonding interactions, such as hydrogen bonds, are characterised by an accumulation of density perpendicular to the bond, and $\lambda_2 < 0$ (Figure 10). On the other hand, nonbonded interactions such as steric repulsion produce density depletion so that $\lambda_2 > 0$. Finally, weak van der Waals interactions are characterised by a negligible density overlap that gives $\lambda_2 \lesssim 0$.



Chapter 4. Covalent donor-acceptor architectures

4.1. Introduction

A donor–acceptor compound is a chemical system formed by at least one electron-donor (D) and one electron-acceptor (A) fragment. These two D and A units are commonly linked by covalent bonding, usually through a π -conjugated bridge that favours the electronic communication between the two parts (see Figure 1 in the Introduction Chapter).

Among the wide variety of electroactive chemical entities, tetrathiafulvalene (TTF) is one of the most exploited electron-rich systems due to its strong electron-donor behaviour (Figure 11).^[107] The high interest in TTFs has spawned the development of many synthetic pathways of TTF and its analogues and, therefore, a large variety of molecular and supramolecular TTF-based donor–acceptor compounds has been reported.^[108] Besides the traditional use for the development of organic conducting materials, the tetrathiafulvalene unit and its derivatives have appeared as key constituents for new applications such as in molecular machines, organic magnets, organic field-effect transistors, and solar cells.^[107, 109]

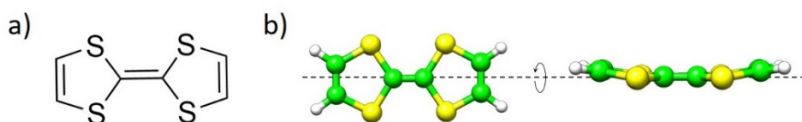


Figure 11. a) Chemical structure of TTF. b) Top and side views of the minimum-energy structure of TTF in the ground state.

Similar in nature but in contrast to the quasi-planar shape of its parent TTF, π -extended TTF (exTTF) has become an efficient electron-rich alternative with promising electronic and geometrical properties.^[110] The

exTTF system incorporates two 1,3-dithiole rings in a π -conjugated quinoid spacer of the type of anthracene, conferring a strong electron-donor character and an uncommon butterfly-like shape (Figure 12). Contrarily to the TTF analogues, which show two well-separated one-electron oxidation processes at relatively low oxidation potential values, exTTF exhibits a unique two-electron oxidation process to form directly the dication species. Interestingly, the oxidation process to form the aromatic dication is accompanied by a dramatic geometrical change from a butterfly shaped (neutral state) to a planar anthracene structure (dication, Figure 12).^[111]

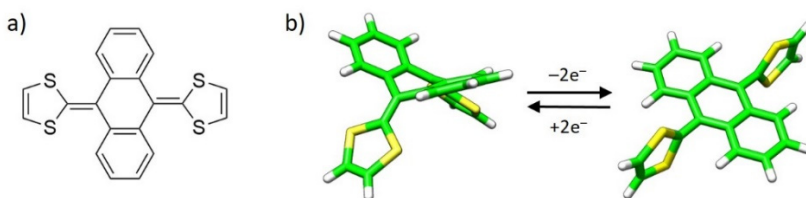


Figure 12. a) exTTF chemical structure. b) Geometry evolution of the exTTF minimum-energy structure upon two-electron oxidation.

Since its discovery, exTTF and its derivatives have been extensively combined with a vast array of electron-acceptor moieties in the design of efficient push–pull systems with interesting nonlinear and absorption properties.^[112] For instance, exTTF–fullerene molecular wires connected through an oligo(*p*-phenylenevinylene) (oPPV) bridge (Figure 13a),^[113] exTTF and perfluoroalkylfullerene dyads and triads (Figure 13b),^[114] and donor–acceptor exTTF-based endohedralfullerene derivatives have been synthesized and characterised by Nazario Martín and coworkers.^[115] Other applications of exTTF-based derivatives comprise the supramolecular recognition of fullerene and carbon-based nanoforms

(Figure 13c);^[116] some examples of these will be briefly discussed in Chapter 5.

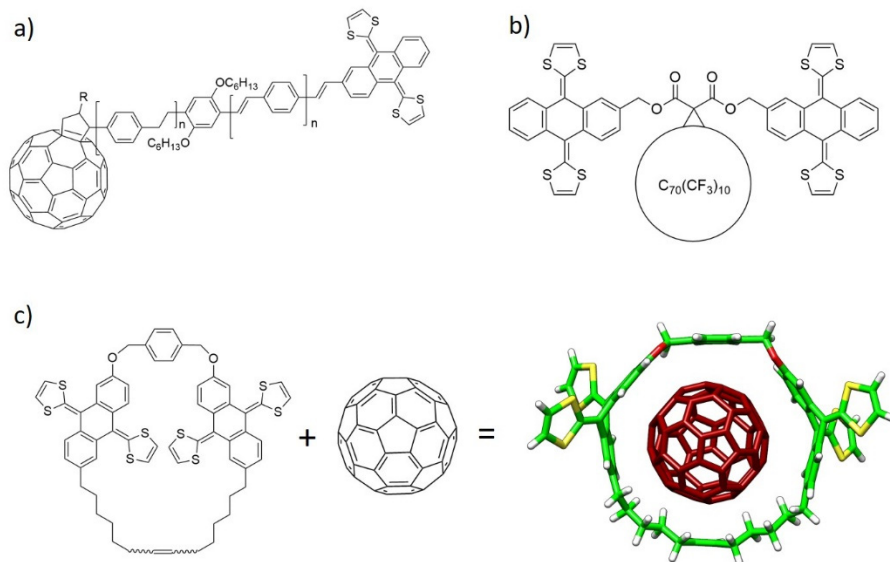


Figure 13. Examples of the exTTF-based derivatives in the generation of: (a) donor–acceptor dyads (exTTF–fullerene connected through an oPPV bridge), (b) triads (two π -exTTF fragments and a perfluoroalkylfullerene), and (c) supramolecular donor–acceptor assemblies (exTTF–macrocycle and fullerene).

Despite the great success of organic chemistry in providing a large variety of donor–acceptor exTTF dyads, only few examples have shown promising absorption features to be exploited in molecular electronics and photovoltaics.^[112] The recently synthesized donor–acceptor exTTF-based compound containing the electron-acceptor tricyanofuran (TCF) moiety (known as exTTF-TCF, Figure 14a) has demonstrated to absorb light in the whole visible spectrum.^[117] Its use in dye-sensitized solar cells would further benefit from the butterfly shape of the exTTF unit, preventing the undesirable self-aggregation usually found in planar chromophores upon the attachment to the semiconductor surface.^[118]

However, the electron-acceptor TCF moiety must present efficient anchoring groups to strongly bind the semiconductor, usually constituted by titanium dioxide (TiO_2) nanoparticles.^[119] Substitution of weak anchoring cyano groups by carboxylic acid moieties in the prototypical exTTF-TCF compound might open doors to a new generation of efficient purely-organic light harvesters for dye-sensitized solar cells.

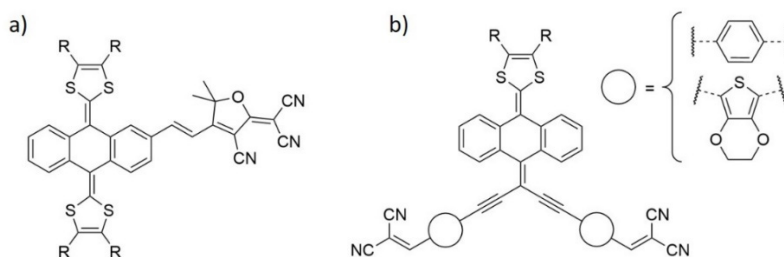


Figure 14. a) exTTF-TCF dye absorbing in the whole visible spectrum. b) hemiexTTF-based donor–acceptor derivatives.

A recent work of Nazeeruddin and coworkers demonstrated, in the most efficient ruthenium-based complexes, that the increasing number of anchoring groups of the dye (two in N719, three in black dye, and four in N3) is a determining factor explaining the high photoconversion of these devices.^[120] Inspired by the great success of these multi-anchoring dyes, Nazario Martín and coworkers developed purely organic di-branched, donor–acceptor chromophores. Substitution of the exTTF donor moiety by the analogous hemiexTTF unit has permitted the generation of di-branched chromophores decorated with two electron-acceptor moieties absorbing in the whole visible range (Figure 14b). In order to improve the anchoring strength of the novel absorbing hemiexTTF-based dyes, analogous donor–acceptor molecular tweezers incorporating the hemiexTTF unit as donor and two cyanoacrylic units as

accepting/anchoring groups have been recently reported as metal-free sensitizers for dye-sensitized solar cells.^[121] The adsorption mode of each anchoring group to the semiconductor surface remained however unclear so far. A theoretical exploration of the anchoring mechanism in these di-branched light-harvesters would shed light into the unknowns determining the performance of multi-branched dyes in Grätzel-type DSCs. Additionally, this theoretical insight might provide guidelines for the design of improved purely-organic chromophores exceeding the current state of the art.

In this Chapter, we report on the theoretical characterization of the electronic and optical properties of efficient light-harvesters that absorb light in the entire visible spectrum. The chromophores under study are based on the electron-donor exTTF and its analogue hemiexTTF combined with electron-acceptor moieties containing the carboxylic acid group through a π -conjugated bridge. The structural and electronic implications of a double- vs. single-anchoring mode of the dye to bind the semiconductor surface in dye-sensitized solar cells are theoretically analysed.

4.2. Results and discussion

4.2.1. Mono-branched exTTF-based chromophores

Theoretical calculations based on the density functional theory framework were carried out to disentangle the structural and electronic properties of the whole-visible-absorbing exTTF-TCF compound upon substitution of one cyano group by a carboxylic acid moiety (DCF). Geometry optimizations of the three possible exTTF-DCF carboxyl-

substituted isomers (exTTF-DCF-A/B/C, Figure 15a) provide structures in which the exTTF moiety is strongly distorted out of planarity (see Figure 15b for exTTF-DCF-A). As previously reported,^[111a, b, 117, 122] the donor exTTF unit adopts a butterfly- or saddle-like folded structure that obstructs the negative dye-aggregation process.^[123] Otherwise, the acceptor DCF moiety remains planar through the ethylene bridge that joins the anthracene moiety of exTTF with the furan ring of DCF. For further details in the geometry structure, the reader is referred to **Publication 1** included at the end of the Chapter.

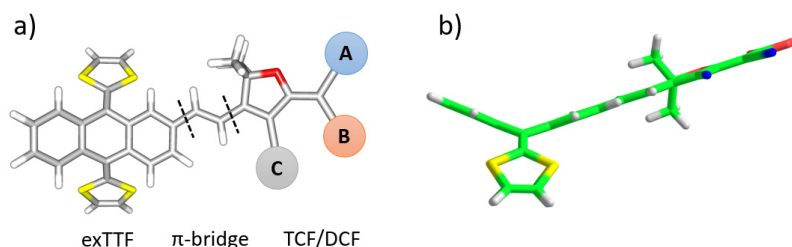


Figure 15. a) Schematic representation of the three possible regioisomers studied by substitution of one cyano group in the TCF unit of exTTF-TCF by a carboxylic acid (A, B or C). b) Side view of the minimum-energy geometry of the exTTF-DCF-A regioisomer.

Mulliken atomic charges accumulated by the different molecular fragments constituting the exTTF-TCF system and its carboxyl-substituted derivatives were calculated at the B3LYP/6-31G** level. For all the dyes, a similar charge transfer of around 0.17e takes place from the electron-donor exTTF moiety to the electron withdrawing TCF/DCF unit. However, whereas the cyano groups bear a charge around $-0.20e$ in all cases, the carboxyl group holds a significantly larger negative charge of approximately $-0.40e$. This result suggests that, compared to the nitrile group, the carboxyl group, already in its neutral form, is not only

more appropriate to anchor the dye to the semiconductor but also to favour the electron injection to the semiconductor in a DSC device.

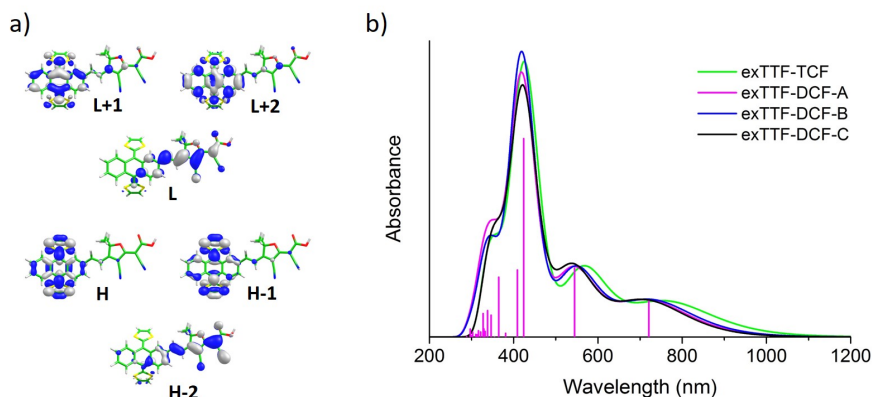


Figure 16. a) Topology of the frontier molecular orbitals of exTTF-DCF-A. b) Simulated absorption spectra calculated at the TD-B3LYP/6-31G** level of theory.

The electronic structure of the exTTF-based chromophores, calculated at the same level of theory, was found to be similar in all TCF/DCF derivatives. As shown in Figure 16a for exTTF-DCF-A, the highest-occupied molecular orbital (HOMO) and the HOMO–1 are fully localized on the donor exTTF moiety, whereas the HOMO–2 spreads over the ethylene bridge and the acceptor TCF/DCF fragment with some contribution from the anthracene unit. The lowest-unoccupied molecular orbital (LUMO) is also located on the TCF/DCF unit and the ethylene bridge, whereas the LUMO+1 and LUMO+2 are mainly confined on the exTTF moiety. The energy gap between HOMO and LUMO was calculated at ~ 2.0 eV at the B3LYP/6-31G** level, suggesting that low-lying charge-transfer transitions are expected upon photoexcitation.

The optical properties of the exTTF-DCF regioisomers and the exTTF-TCF compound were thoroughly analysed using time-dependent DFT (TDDFT) calculations, namely at the TD-B3LYP/6-31G** level. Interestingly, the optical absorption properties of exTTF-TCF are preserved in the exTTF-DCF derivatives, and the three carboxylic regioisomers provide quasi-identical absorption features in terms of position and intensity of the electronic transitions (Figure 16b). The major contributing monoexcitations to the two lowest-lying transitions located theoretically at 550 and 700–800 nm, respectively, is the promotion of one electron from the HOMO and HOMO–1, which are completely localized on the exTTF moiety, to the LUMO, which spreads over the DCF moiety (Figure 16). These electronic excitations are therefore of charge-transfer nature. Moreover, a very intense band at around 410 nm is predicted in all chromophores (Figure 16b). This band originates mainly from a π - π^* transition centred in the bridge+acceptor moiety (HOMO–2 \rightarrow LUMO) plus the typical π - π^* exTTF transition (HOMO \rightarrow LUMO+1).

Finally, periodic boundary conditions (PBC) calculations were performed to disentangle the conformational implications of the adsorption of the dyes onto titanium dioxide (or titania). The two carboxyl-substituted regioisomers exTTF-DCF-A and exTTF-DCF-B were placed onto a periodic slab of TiO₂ exposing the (101) surface of the anatase polymorph, and their geometries were fully optimized using the PBE functional and the Car–Parrinello algorithm. The most common bridging bidentate mode was used for the adsorption.^[118, 124] exTTF-DCF-C was not computed due to evident steric hindrance between the exTTF moiety and the semiconductor surface. As depicted in Figure 17, the exTTF-DCF-A and exTTF-DCF-B dyes are strongly adsorbed onto titania by their

carboxylate groups, which are attached to the semiconductor surface through two O–Ti bonds. Importantly, the main molecular axis of the dye forms an angle with the titania surface of 54° in exTTF-DCF-A, whereas this angle is computed at 39° in exTTF-DCF-B. As a consequence, the separation between the donor moiety and the titania surface is predicted significantly larger in the exTTF-DCF-A regioisomer compared to exTTF-DCF-B (Figure 17). The donor–surface distance is of paramount importance to reduce the charge recombination phenomena that limits the power conversion efficiency in a DSC.^[125] Besides the slightly stronger anchoring predicted theoretically for exTTF-DCF-A through the analysis of the characteristic C–O and O–Ti bonds, its more perpendicular disposition to the semiconductor surface would generate a more significant sensitizer’s dipole component normal to TiO_2 , which has been directly related with a shift to higher energies of the conduction band (CB).^[126] Assuming that the charge transfer to the semiconductor is practically the same in both regioisomers, the more perpendicular disposition of exTTF-DCF-A should lead to an increased open-circuit voltage with beneficial implications for dye-sensitized solar cells.^[127]

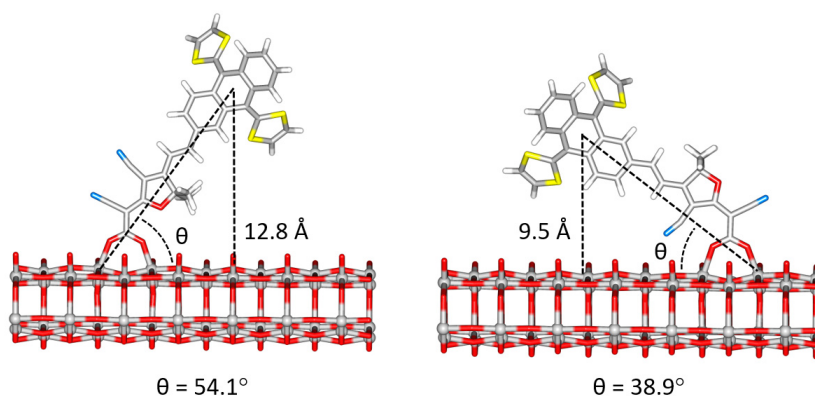


Figure 17. Minimum-energy structures calculated for exTTF-DCF-A (left) and exTTF-DCF-B (right) adsorbed onto a periodic slab of anatase (101).

4.2.2. Di-branched hemiexTTF derivatives

Inspired by the recent evidences pointing towards the number of anchoring branches as a great enhancer of the performance of the dye in a DSC,^[120] a series of novel donor–acceptor dyads were studied in collaboration with Prof. Nazario Martín’s group based on the exTTF donor molecule with two electron-acceptor branches. We first explored the electronic and optical properties of the donor- π -acceptor chromophores shown in Figure 18, in which the 10-(1,3-dithiol-2-ylidene)-anthracene core (hemiexTTF) was combined with the electron-acceptor dicyanovinylene (DCV) moiety through two different π -conjugated bridges —either a benzene (Ph) or a 3,4-ethylenedioxythiophene (EDOT)—. The EDOT spacer was shown in a previous work to yield a red-shift in the spectroscopic response and an enhancement of the molar extinction coefficient in triphenylamine- and exTTF-based sensitizers.^[128]

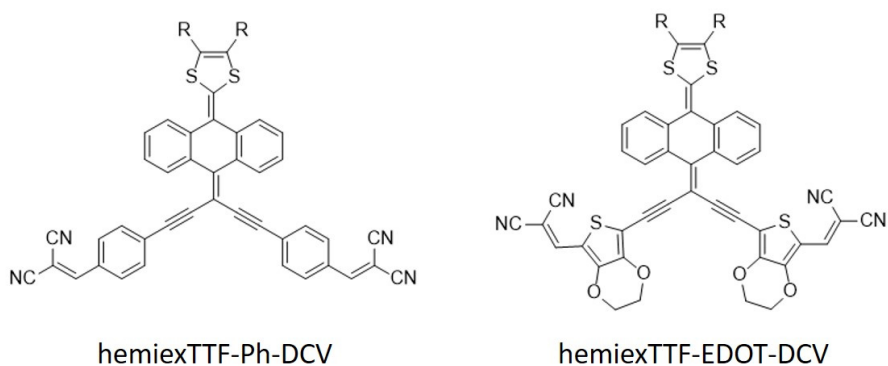


Figure 18. Chemical structure of the hemiexTTF-based push–pull chromophores including two types of π -conjugated spacers: a phenyl (hemiexTTF-Ph-DCV, left) and an EDOT (hemiexTTF-EDOT-DCV, right) bridge.

Theoretical calculations at the B3LYP/6-31G** level predict concave saddle-like structures, in which the central ring of the anthracene unit folds up in a boat conformation, and the dithiole ring and the acceptor arms are tilted down (Figure 19a), similarly to that obtained for the above-mentioned exTTF-DCF derivatives. Otherwise, the acceptor arms remain mostly planar in both dyes. The reader is referred to the original **Publication 2** below for further details.

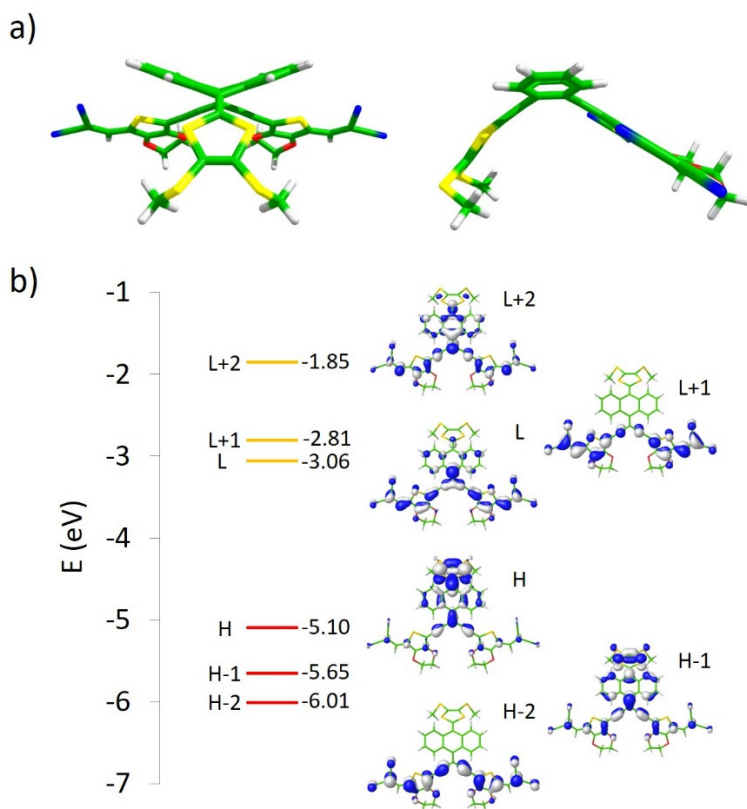


Figure 19. a) Front (left) and side (right) views of hemiexTTF-EDOT-DCV. b) Energy diagram of the frontier molecular orbitals calculated for the dye.

The HOMO and HOMO–1 in both dyes are mainly localized on the electron-donor hemiexTTF, whereas the HOMO–2 spreads over the electron-acceptor moiety with no hemiexTTF participation. The presence of the electron-rich EDOT fragments in hemiexTTF-EDOT-DCV slightly increases the energy of the HOMO (–5.10 eV) compared to hemiexTTF-Ph-DCV (–5.17 eV), thus reducing the HOMO–LUMO gap from 2.16 eV in hemiexTTF-Ph-DCV to 2.04 eV in hemiexTTF-EDOT-DCV.

The absorption properties of the light-harvesters under study were measured in dichloromethane solution by the group of Prof. Nazario Martín (Figure 20a). Experimentally, hemiexTTF-Ph-DCV displays two main absorption bands in the UV and visible range ($\lambda_1 = 366$ nm; $\lambda_2 = 536$ nm). Both transitions are red-shifted upon inclusion of the EDOT spacer ($\lambda_1 = 443$ nm; $\lambda_2 = 590$ nm). TDDFT calculations predict that the lowest-energy absorption band observed for both chromophores above 500 nm is due to electronic transitions to the first two excited singlets S_1 and S_2 (Figure 20b). These states originate from the HOMO \rightarrow LUMO and HOMO \rightarrow LUMO+1 monoexcitations, respectively, and imply an electron density transfer from the hemiexTTF moiety, where the HOMO resides, to the acceptor moiety, where the LUMO and LUMO+1 are mainly located (Figure 19b). The moderately high intensities observed for this charge-transfer (CT) band are in agreement with the oscillator strengths (f) around 0.4–0.5 calculated for S_1 and S_2 , and are due to the significant overlap between the HOMO and the LUMO/LUMO+1. The intense absorption band observed at higher energies mainly results from the HOMO–2 \rightarrow LUMO excitation (state S_6 for hemiexTTF-Ph-DCV and S_5 for hemiexTTF-EDOT-DCV, Figure 20b), which involves the electron-acceptor part of the molecule (Figure 19b). Theoretical calculations therefore confirm for these novel di-branched light-harvesters the

presence of low-lying, moderately-intense, charge-transfer transitions, which results in a wide range absorbance over the whole visible spectrum.

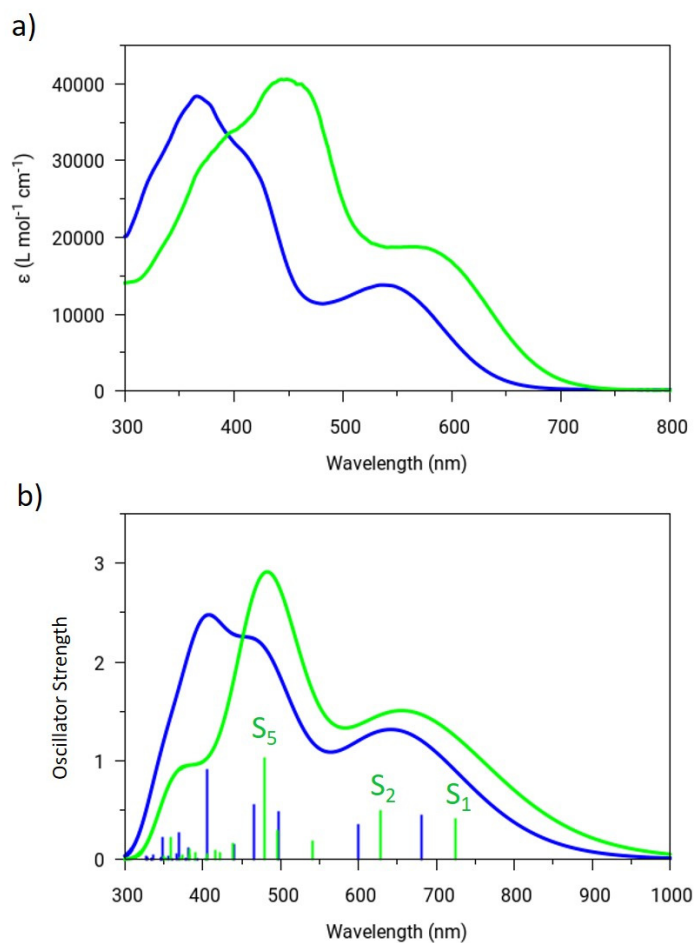


Figure 20. a) Absorption spectra of hemiexTTF-Ph-DCV (blue) and hemiexTTF-EDOT-DCV (green) recorded in dichloromethane at room temperature. b) Theoretical simulation of the UV-Vis absorption spectra. Vertical lines indicate the vertical excitation energies with the corresponding oscillator strength.

4.2.3. Single- vs. double-anchoring adsorption modes

Due to the great absorbing properties showed by the novel di-branched hemiexTTF-based dye derivatives, subsequent studies were focused on analogous compounds but with substitution of two cyano groups by efficient anchoring carboxylic moieties (see dye **A** in Figure 21).^[121] These systems presented intramolecular charge-transfer bands in the low-energy range and exhibited a broad and intense absorption band in the whole UV–Vis spectrum, in analogy to the chromophores hemiexTTF-Ph-DCV and hemiexTTF-EDOT-DCV. Whereas Fourier transform infrared spectroscopy (FTIR) experiments indicated a di-anchoring adsorption mode to the TiO_2 , the unambiguous elucidation of the carboxylic coordination mode to the semiconductor remained unclear. The reader is referred to the original work for further details.^[121]

In order to disentangle the adsorption coordination of the two carboxylic groups of the hemiexTTF-based di-branched dyes with the TiO_2 surface and the implications of the di-anchoring adsorption mode on the DSC performance, a comprehensive theoretical investigation combining first-principles DFT and *ab initio* molecular dynamics calculations was carried out on model di-branched dyes (Figure 21).

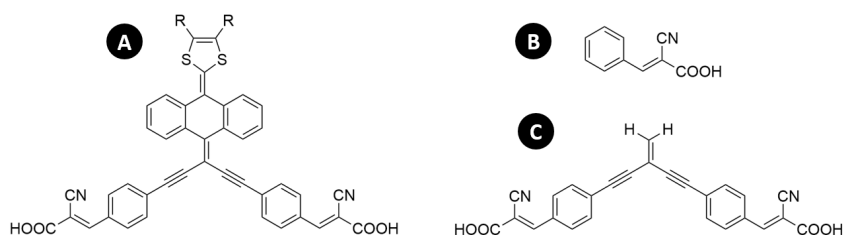


Figure 21. Chemical structure of the prototypical di-branched hemiexTTF-based dye with two cyanoacrylic anchoring units (**A**), and the two simplified molecular models used in the study (**B** and **C**).

It is possible to differentiate three anchoring modes between the carboxylic acid group and the anatase (101) surface of TiO₂: monodentate (M), chelated (CB) and bridged bidentate (BB). Among them, the monodentate and especially the bridged bidentate modes displayed in Figure 22 are the most common modes found in the field of organic sensitizers attached to the TiO₂ anatase (101) surface.^[118, 124b, 126a, 129] In the case of the monodentate, two binding modes, M1 and M2, are distinguishable due to the oxygen atom (O₄ or O₃, respectively) to which the carboxylic hydrogen is linked (Figure 22).

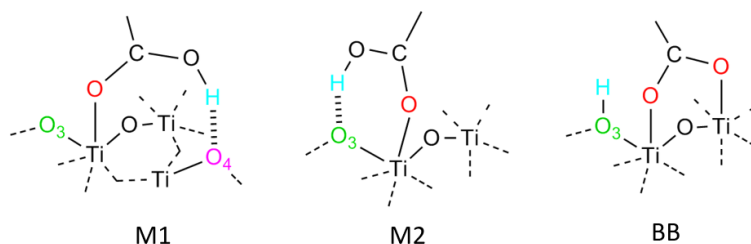


Figure 22. Graphical representation of the three main carboxylic/carboxylate binding modes in DSCs: two different monodentate (M1 and M2) and one bridged bidentate (BB) adsorptions.

By means of computing the frequency of the symmetric and antisymmetric vibration of the carboxylic acid group in a simplified anchoring system (**B** in Figure 21), we were able to correlate their stretching wavenumber difference ($\Delta\nu_{as}$) with the characteristic adsorption mode. Whereas the di-branched cyanoacrylic-acid dyes are arranged in a dimeric fashion in powder samples, $\Delta\nu_{as}$ values of the dyes attached to the TiO₂ semiconductor are explained in terms of a monodentate linkage; for full details on the theoretical analysis see the original **Publication 3** below.

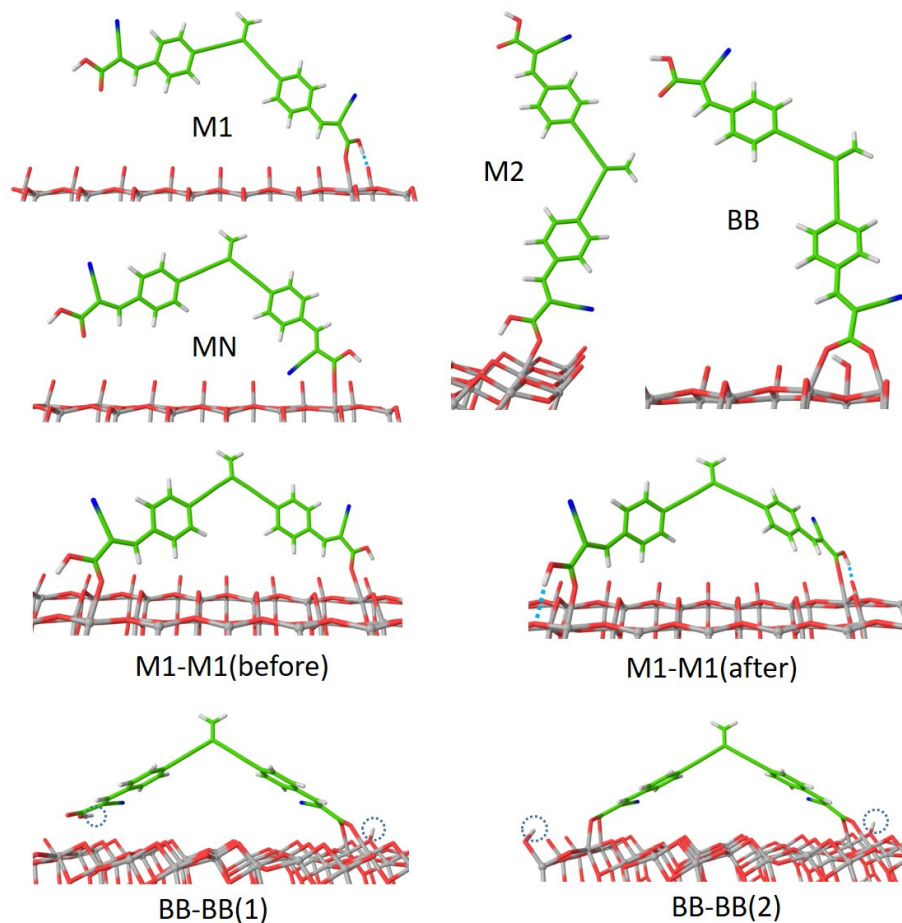


Figure 23. Adsorption conformations calculated for model system **C**. M1-M1(before) and M1-M1(after) correspond to minimum-energy conformers optimized before and after the *ab initio* molecular dynamics simulation, respectively.

To shed light onto the energetics of the different possible structures for the combined dye•TiO₂ system, we modelled the simplified di-branched system **C** (Figure 21) anchored to the anatase (101) surface using periodic boundary conditions. Four single-anchored adsorption configurations, i.e. three monodentate (M1, M2 and MN) and one

bidentate (BB) structures, and two di-anchored conformations, i.e. one monodentate (M1-M1) and one bidentate (BB-BB) structures, were optimized using the Car–Parrinello algorithm. The M1-M1 conformation was optimized before and after running a long *ab initio* molecular dynamics simulation (termed M1-M1(before) and M1-M1(after), respectively, in Figure 23). The relative energies of the different anchoring modes are summarised in Table 1.

Table 1. Relative stabilities of the adsorption conformations modelled for $\mathbf{C}\cdot\text{TiO}_2$.

Structure	E_{rel} (kcal mol ⁻¹)
M1	4.98
M2	3.70
MN	9.70
BB	14.16
M1-M1(before)	0.00
M1-M1(after)	-9.39
BB-BB(1)	30.27
BB-BB(2)	38.55

Among the four single-anchored conformations, M2 is calculated to be the most stable adsorption mode, with the M1 structure being quite close in energy (1.28 kcal mol⁻¹). However, taking into account the spatial arrangement of the COOH groups (Figure 23), a di-anchored M2-M2 conformation is not feasible due to the geometric rigidity of the dye, and it was therefore ruled out. The MN adsorption mode also gives a relatively small energy and is found to be 6.00 kcal mol⁻¹ less stable than M2. The bridging bidentate (BB) mode is computed to be more than 10 kcal mol⁻¹ higher in energy than M2, in good agreement with previous theoretical studies employing Car–Parrinello calculations and periodic boundary conditions.^[129-130]

Moving to the di-anchoring conformations, M1-M1(before) stands much more stable than BB-BB (30 kcal mol^{-1}). After a long *ab initio* molecular dynamics simulation of 3 ps and the corresponding reoptimization procedure, M1-M1(after) gains an extra stabilization of more than 9 kcal mol^{-1} compared to M1-M1(before). This additional stability is a consequence of the efficient formation of two H-bonds upon deformation of the dye structure from planarity. BB-BB(1) and BB-BB(2), where one H is bonded to the anchoring group or linked to a further $\text{O}_{3/4}$ atom, respectively (Figure 23), both lie much higher in energy than M1-M1. In fact, the di-anchored BB structures are less stable than the single anchored BB conformation by more than 15 kcal mol^{-1} . This huge destabilization is due to the inefficient bond interactions caused by the rigid structure of the dye, the fixed topology of the TiO_2 surface and the additional π -conjugation breaking experienced by the dye to adopt the di-anchored BB structures. In passing from M1 to M1-M1(after), a stabilization of around 14 kcal mol^{-1} is obtained for the di-anchored conformation, which mostly corresponds to the energy gain associated with the anchorage of one carboxylic acid group to the anatase (101) surface (around $18.5 \text{ kcal mol}^{-1}$).^[130]

Figure 24 displays the time evolution of the $\text{O}_2\text{-H}$ and $\text{H-O}_{3/4}$ distances during the CP molecular dynamics simulation. Theoretical calculations indicate that the room temperature (298 K) energy is high enough to break and form again the bonds involving the carboxylic hydrogen, thus giving flexibility to the system to explore a huge zone of the potential energy surface. At around 1.25–1.50 ps, the $\text{H-O}_{3/4}$ distance presents large values indicating a breaking of the H-bond (Figure 24), whereas at 0.75 and 2.30 ps the distance predicted for $\text{H-O}_{3/4}$ is shorter than that for

O₂-H suggesting a proton transfer from the carboxylic acid to the oxygen of the semiconductor.

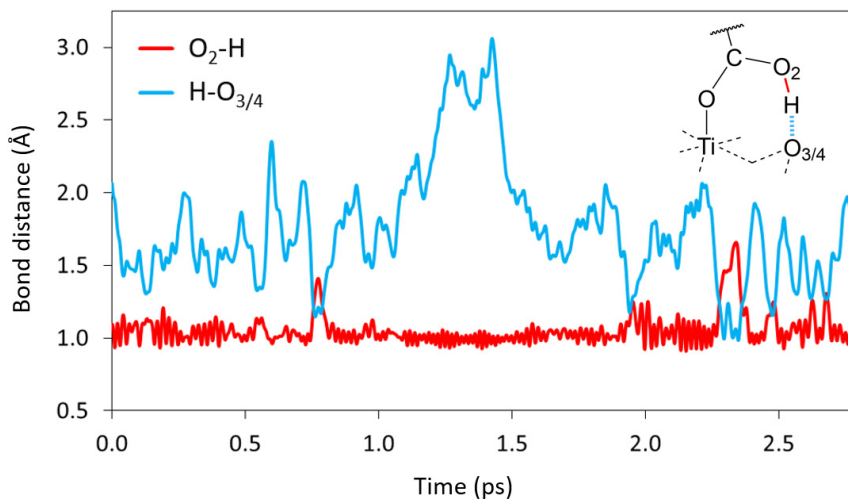


Figure 24. Time evolution of the characteristic O₂-H and H-O_{3/4} bond distances during the Car-Parrinello molecular dynamics simulation.

Finally, the projected density of states (PDOS) was analysed for M1, BB, M1-M1 and BB-BB adsorption modes. Calculations predict that the doubly anchored systems shift the conduction band of TiO₂ to slightly higher energies compared to the singly anchored analogues. This shift allows for an increase in the open-circuit voltage permitting higher conversion efficiencies for DSC purposes. Moreover, an extensive analysis of the PDOS show differences in the characteristics of the LUMO bands corresponding to the C•TiO₂ system depending on the coordination mode. Overall, the energetically favoured M1-M1 structure provides appropriate LUMO-CB energy differences with two broad and intense LUMO bands located in the anchoring branches, which favour the electron injection into the semiconductor and would explain the good

performance experimentally achieved in the device (power-conversion efficiency of 3.7 %).^[121]

Other systems not discussed in the Thesis but directly related with this Chapter have also been studied theoretically and in collaboration with the experimental groups of Profs. Michael Grätzel, Concepció Rovira, Nazario Martín and Fernando Langa. In particular, donor–acceptor exTTF-based dyes including electron-acceptor tetracyanobutadiene moieties,^[122] porphyrin–fullerene-based push–pull systems,^[131] fluorene and bi-fluorenylidenes for application in DSCs,^[132] and prototypical donor–acceptor–donor TTF-based mixed-valence triads for deeper understanding of the charge-transfer processes^[133] have been investigated. Likewise, other electroactive compounds such as electron-acceptor derivatives based on polycyclic aromatic hydrocarbons (PAHs) have been studied,^[134] as well as novel azoheteroarene photoswitches in collaboration with the groups of Profs. Julia Contreras and Matthew Fuchter.^[135] The reader is referred to the original literature for further details: articles 10–15, 23 and 25 in the List of publications.

4.3. Summary

In this chapter, a quantum–chemical investigation has been performed on both mono-branched and di-branched donor- π -acceptor chromophores based on the electron-rich π -extended TTF molecule in the context of dye-sensitized solar cells. First, the donor exTTF moiety was coupled to a tricyanofuran unit in which one cyano group is substituted by a carboxylic anchoring group in the design of a push–pull system with absorption in the whole range of the UV–Vis solar spectrum. Theoretical

calculations gave insight into the preferential regioisomers of interest to be synthesized for a maximum performance in the DSC device. Di-branched chromophores based on an analogous donor hemiexTTF moiety were theoretically characterised, and the nature of the bridge connecting the donor and acceptor fragments was analysed by comparing phenyl and EDOT π -conjugated spacers. The implications of a di-anchoring mode in the di-branched chromophores for DSC purposes were assessed by means of first-principles solid-state calculations. We showed that the most plausible adsorption mode was a monodentate coordination of the cyanoacrylic acid group in both anchoring branches. This coordination displayed the most stable anchorage of the target dye to the semiconductor surface, as well as two broad and intense LUMO bands that would enhance the electron injection into the semiconductor with the consequent benefits in the DSC performance.

4.4. Publications

Publication 1 J. Calbo, P. M. Viruela, E. Ortí, “Theoretical insight on novel donor-acceptor exTTF-based dyes for dye-sensitized solar cells”, *J. Mol. Model.* **2014**, *20*, 1-10.

Publication 2 P.-A. Bouit, L. Infantes, J. Calbo, R. Viruela, E. Ortí, J. L. Delgado, N. Martín, “Efficient Light Harvesters Based on the 10-(1,3-Dithiol-2-ylidene)anthracene Core”, *Org. Lett.* **2013**, *15*, 4166-4169.

Publication 3 J. Calbo, M. Pastore, E. Mosconi, E. Ortí, F. De Angelis, “Computational modelling of single- versus double-anchoring modes in di-branched organic sensitizers on TiO₂ surfaces: structural and electronic properties”, *Phys. Chem. Chem. Phys.* **2014**, *16*, 4709-4719.

Reproduced with permission of Springer, American Chemical Society and Royal Society of Chemistry.

Theoretical insight on novel donor-acceptor exTTF-based dyes for dye-sensitized solar cells

Joaquín Calbo · Pedro M. Viruela · Enrique Ortí

Received: 24 December 2013 / Accepted: 24 February 2014 / Published online: 19 March 2014
© Springer-Verlag Berlin Heidelberg 2014

Abstract A thorough density functional theory study is performed for the three carboxyl-based derivatives of the exTTF-TCF chromophore, where the π -extended tetrathiafulvalene (exTTF) electron-donor is linked to the tricyanofuran (TCF) electron-acceptor through an ethylene bridge, as dyes for dye-sensitized solar cells. Calculations predict that the carboxyl group in the acceptor moiety adopts an adequate orientation for an efficient anchoring on the semiconductor TiO₂ surface. The carboxylic acid group holds a negative charge twice larger than the cyano moiety that favors the electron injection to the semiconductor. Time-dependent calculations allow for the assignment of the absorption bands in the UV–vis spectrum of exTTF-TCF and confirm the presence of two low-lying charge-transfer electronic transitions that account for the moderately-intense absorption in the 450–800 nm range. The striking optical absorption properties of exTTF-TCF are preserved for the carboxylic analogues. Finally, periodic calculations show relevant topological differences between the carboxylic derivatives anchored on the TiO₂ surface, which would notably influence in the power conversion efficiency of a dye-sensitized solar cell.

Keywords DFT calculations · Donor-acceptor dyes · Dye-sensitized solar cells · exTTF-based dyes · Periodic calculations

Introduction

Solar power generation has emerged as one of the most rapidly growing renewable sources of electricity to replace

fossil fuels. Among the different types of next-generation solar cells, dye-sensitized solar cells (DSCs) have attracted a great deal of attention due to their low-cost and high-flexibility [1–3]. However, DSCs have not evolved as much as other emerging photovoltaic solar cells and, for their commercial application, it is necessary to achieve higher photoelectric conversion efficiencies (especially in terms of the photocurrent). In DSCs, a dye-sensitizer absorbs the solar radiation and the photoexcited electron is transferred to the conduction band (CB) of a semiconductor, typically TiO₂ nanoparticles. Then, a redox mediator, commonly based on the iodide/triiodide couple, regenerates the oxidized dye completing the circuit. It is thus of paramount importance that the dye absorbs in the visible spectrum as much as possible. Moreover, since a charge separation phenomenon occurs during the electron injection to the semiconductor, the photocurrent is thought to be dependent on the dye adsorption structure, and therefore elucidation and control of the adsorption structure on real devices are indispensable for increasing the conversion efficiency.

Even though organometallic ruthenium-based dyes have demonstrated to provide the most efficient DSC devices up to now [2–4], increasing effort has been made to synthesize purely organic dyes due to their low-cost, environmental friendliness and tunable properties [5, 6]. All the organic dyes used for DSCs possess a donor– π –acceptor (D– π –A) scheme, which favors the efficient charge separation and the rapid electron injection to the semiconductor. Metal-free donor architectures such as diphenylamine [7], fluoreneamine [8], and indoline [9] have been shown to provide high efficiencies in the device standing close to the most efficient Ru-based complexes. The π -extended tetrathiafulvalene (exTTF) fragment, which offers an extraordinary donor ability as well as unusual electrochemical properties, has been recently introduced in D– π –A chromophores for the preparation of DSCs which exhibit efficient photovoltaic conversion [10]. An

This paper belongs to Topical Collection QUITEL 2013

J. Calbo · P. M. Viruela · E. Ortí (✉)
Instituto de Ciencia Molecular, Universidad de Valencia,
46980 Paterna, Spain
e-mail: enrique.orti@uv.es

example of these D- π -A exTTF-based dyes is the push-pull molecule shown in Fig. 1a, where the exTTF fragment, as electron donor, is connected to the tricyanofuran (TCF) moiety, as electron acceptor, through a conjugated ethylene bridge that allows for the electronic communication between the donor and the acceptor [11]. This molecule will be hereafter called exTTF-TCF and has been demonstrated to absorb light over the whole visible spectrum, which makes it very appealing for dye-sensitized solar cells. However, the cyano groups do not strongly bind to the titania surface so chemical engineering is required to substitute at least one cyano moiety with strong-anchoring groups such as carboxylic or phosphonic acids.

Computational modeling has demonstrated to provide very useful information to understand the processes occurring in DSCs and has served as a guide to fabricate more efficient devices [12–15]. De Angelis et al. have recently showed the influence of the chemical structure of the dye on the TiO₂ conduction band in terms of charge transfer and electrostatic effects by means of first-principle calculations [16]. Furthermore, theoretical predictions have allowed the rationalization of the anchoring adsorption topology [15, 17], dye aggregation [18], Stark [19] and solvent effects [20], and electrolyte-dye interactions in several dyes for DSCs purposes [21, 22]. Troisi et al. have recently investigated the effect of the dye and the anchoring group on electron injection [23, 24], and have computed the charge recombination rates at the semiconductor-adsorbate interface in the presence of defects [25, 26] and at the semiconductor-electrolyte interface.

Herein, we report a thorough theoretical study of the three carboxylic derivatives of exTTF-TCF: exTTF-DCF-A, exTTF-DCF-B, and exTTF-DCF-C, where DCF denotes the carboxyl-substituted dicyanofuran moiety and A, B, and C distinguish the position of the carboxylic acid group (Fig. 1). Our goal is to provide, by means of density functional theory (DFT) calculations, useful geometrical and electronic information for the guidance in the design of novel and improved chromophores for DSCs. Special attention is paid to the understanding of the interactions of the carboxyl group with the furan moiety to elucidate the relative disposition of the acid in the acceptor moiety. A comparative analysis of the absorption electronic spectra computed for the three

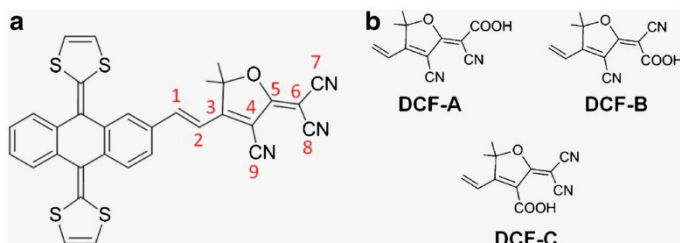
derivatives with respect to exTTF-TCF is performed to predict the optical behavior of the carboxylic analogues. The electronic nature of the different excitations is carefully analyzed allowing the assignment of the most important bands in the UV-vis spectrum. Finally, preliminary models of the dyes adsorbed onto titanium dioxide have permitted to reveal remarkable dispositional differences between the regioisomers that directly affect the DSC efficiency.

Computational details

First-principle DFT calculations were performed for the carboxyl-substituted homologues of the exTTF-TCF system using the Gaussian09 (rev. B01) suite of programs [27]. The very popular hybrid exchange-correlation B3LYP functional was employed in combination with the 6-31G** Pople's basis set [28–33]. The three possible carboxylic analogues of exTTF-TCF were modeled by substituting one of the cyano groups by a carboxylic acid group (Fig. 1b). The minimum-energy conformation of the carboxyl group in the exTTF-DCF-A, exTTF-DCF-B, and exTTF-DCF-C regioisomers was determined by geometry optimization calculations and was analyzed in terms of relative energy and spatial disposition of the carboxylic acid group. Mulliken analysis was carried out by computing the accumulated charges of different atomic groups. Electron density contours (0.03 e bohr⁻³) of the frontier molecular orbitals were plotted by means of the Chemcraft 1.6 software [34].

Vertical electronic excitation energies were computed at the B3LYP/6-31G** level using the time-dependent DFT (TDDFT) approach [35–37] and the optimized ground-state molecular geometries. The 20 lowest-lying singlet excited states were computed for both exTTF-TCF and its carboxylic analogues. It is well known that the most popular hybrid functionals such as B3LYP and PBE0 usually provide an accurate description for local π - π^* excitations whereas they underestimate the energy of the charge-transfer (CT) excited states, especially for long-range CT excitations [38–40]. This shortcoming of standard global hybrid functionals has been reported for donor-acceptor compounds for which there is a negligible overlap between the molecular orbitals involved in

Fig. 1 **a** Chemical structure of exTTF-TCF and atom numbering used in the text. **b** Chemical structure of the three exTTF-DCF regioisomers (only the acceptor part is drawn) resulting from substitution of one cyano group in the electron-acceptor TCF unit by a carboxyl group



the excitation [41, 42]. In our case, the overlap between orbitals involved in the main charge-transfer excitations is large enough to consider that B3LYP will provide reliable energies for those electronic transitions. This assumption is corroborated by the excellent agreement obtained between the theoretical PBE0 excitation energies and the position of the experimental bands reported for the exTTF-TCF compound [11]. The theoretical simulation of the electronic spectra were obtained by using the values calculated for the vertical excitation energies and the oscillator strengths convoluted by Gaussian functions with full width at half maximum (FWHM) of 0.47 eV ($\sigma=0.20$ eV).

To model the adsorption of the different exTTF-DCF regioisomers onto titania, a periodic slab of anatase (101) containing $(\text{TiO}_2)_n$ with $n=56$ was employed. The thickness of the considered slab is large enough to nicely reproduce the electronic structure of thicker films [43]. Periodic calculations were performed using the density functional theory within the generalized gradient approximation (GGA) by means of the PBE exchange-correlation functional [44]. The Car-Parrinello (CP) algorithm [45] as implemented in the Quantum-Espresso 5.0 program package [46] was employed for the periodic boundary conditions (PBC) geometry optimizations. Electron-ion interactions were described using ultrasoft pseudopotentials with electrons for O, N, and C 2s, 2p, H 1s, Ti 3s, 3p, 3d, 4s, and S 3s and 3p explicitly included in the calculations. Plane-wave basis set cutoffs for the smooth part of the wave functions and the augmented density were 25 and 200 Ry, respectively. The dye molecules were adsorbed on only one side of the slab and the distance between the top of the molecule and the adjacent upper slab was larger than 6 Å. The size of the unit cell was $10.244 \times 26.495 \times 29.000$ Å. Identical periodic TiO_2 slabs were considered to model the exTTF-DCF-A and exTTF-DCF-B regioisomers. The exTTF-DCF-C regioisomer was not computed due to the steric hindrance in the adsorbed structure because of the dithiole rings of the exTTF moiety. Preliminary modeling of the adsorption disposition in this regioisomer did anticipate a completely parallel orientation of the dye with respect to the surface.

Results and discussion

Conformational analysis

The electron-acceptor TCF fragment is commonly used in push-pull chromophores and has been successfully applied in efficient bulk heterojunction organic solar cells [47]. It has also been used in dyes for DSCs, but it is well known that nitrile functional groups do not attach well to the semiconductor surface, commonly titania nanoparticles. In contrast, the carboxyl group binds very strongly to TiO_2 and is by far the most frequently used functional group to anchor a dye onto

the semiconductor surface. Substitution of one nitrile in TCF by a carboxyl group is therefore highly desired because it preserves the electron-acceptor ability of the TCF moiety and allows for an effective anchoring on the TiO_2 surface. Although position 9 in the TCF unit of exTTF-TCF (see Fig. 1a) is synthetically deactivated from substitution [48], we have modeled the three regioisomers exTTF-DCF-A, exTTF-DCF-B, and exTTF-DCF-C resulting from the substitution of the nitrile groups in positions 7, 8, and 9, respectively, by a carboxyl group (Fig. 1b).

The conformation depicted in Fig. 1a, in which the central ethylene bridge is in *s-trans* with respect to the adjacent double bonds in exTTF and TCF units, has been adopted for the exTTF-TCF skeleton. The *s-cis* rotamer resulting from the rotation around the C2–C3 single bond is computed to be $0.6 \text{ kcal mol}^{-1}$ higher in energy because of the short H1–C9 and H1–N9 distances. Although both rotamers are easily interconvertible at room temperature, we have selected the more stable *s-trans* rotamer from now on. The relative orientation of the carboxyl group in the three exTTF-DCF regioisomers was modeled by calculating the different conformers resulting from the internal rotation around the C–COOH single bond for DCF units. Internal rotation around the C–OH bond was also studied for DCF-A and DCF-B to generate intramolecular H-bonds with the oxygen of the furan ring and N7, respectively (Fig. 1). The formation of an intramolecular H-bond would hinder the adequate binding with the semiconductor surface in DSCs.

For DCF-A, the most stable rotamer corresponds to a conformation in which the carboxyl group is completely planar, thus preserving the π -conjugation with the DCF unit, and is pointing outward from the furan ring (Fig. 2a). The hydroxylic hydrogen and the carbonylic oxygen are in a *cis*-like orientation at 2.24 Å due to the stabilizing electrostatic interaction that takes place (charges of $+0.33e$ and $-0.47e$, respectively). An identical orientation is adopted in the other carboxylic derivatives. Interestingly, the rotamer that forms a H-bond (1.81 Å) with the oxygen of the furan ring is calculated $3.7 \text{ kcal mol}^{-1}$ higher in energy as the least stable conformer.

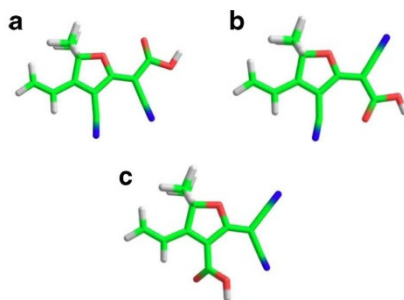


Fig. 2 Most stable conformers calculated for exTTF-DCF-A (a), exTTF-DCF-B (b), and exTTF-DCF-C (c)

The increase in the C5–C6–C7 angle (see Fig. 1a for atom numbering) from 121° to 127° demonstrates that the carboxylic acid is too close to the oxygen of the furan ring and thus unfavorable angle distortions are required for H-bond formation. The most stable conformation shown in Fig. 2a is favorable for an adequate binding with the semiconductor surface.

In analogy to DCF-A, the most stable rotamer for DCF-B is completely planar and places the OH group pointing outward of the molecule (Fig. 2b), which is beneficial for a correct anchorage on the semiconductor surface in DSCs. The repulsive electrostatic interaction between the carbonyl oxygen and the vicinal cyano group distorts the linearity of this group and the C4–C9=N9 angle changes from 174° in DCF-A to 168° in DCF-B. The rotamer in which the OH group points toward this cyano group is 3.5 kcal mol⁻¹ less stable and is therefore ruled out.

Regioisomer DCF-C is computed 2 kcal mol⁻¹ less stable than DCF-A and DCF-B, which are mostly isoenergetic, and is not expected to be formed in the synthetic process reported by Bartholomew et al. [48]. In all rotamers studied for DCF-C, the carboxylic acid group is out of the plane defined by the furan ring owing to the steric hindrance with the neighboring nitrile and ethylene moieties. For the most stable conformer (Fig. 2c), the OH group is closer than the C=O group to the vicinal nitrile unit. In conclusion, although the three regioisomers provide an adequate directionality of the carboxylic acid for the anchorage to the semiconductor, only the DCF-A and DCF-B regioisomers retain the planarity of the carboxyl group and therefore maintain the π -electron conjugation required for an efficient electron injection.

Ground state properties

Geometry optimizations of the three exTTF-DCF carboxyl-substituted derivatives provide structures in which the exTTF moiety is strongly distorted from planarity (see Fig. 3 for exTTF-DCF-A). As previously reported [11, 49–53], the donor exTTF unit adopts a butterfly- or saddle-shape folded structure, which can be taken advantage of to generate dyes for DSCs because it prevents the well-known shortcoming of dye-aggregation [54–56]. Otherwise, the acceptor DCF moiety remains planar through the ethylene bridge that joins the anthracene moiety of exTTF with the furan ring of DCF. The carboxyl group in exTTF-DCF-A, -B, and -C displays the spatial dispositions shown in Fig. 2a–c, respectively. Compared to exTTF-TCF, the substitution of one cyano by a

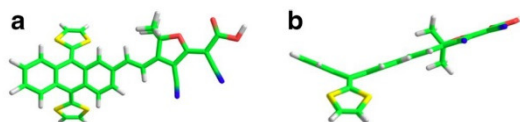


Fig. 3 Top (a) and side (b) view of the minimum-energy structure calculated for exTTF-DCF-A

carboxyl group has a negligible effect on the exTTF unit and the ethylene bridge, and only minor changes (< 0.01 Å) are obtained for the acceptor unit.

Table 1 collects the Mulliken charges accumulated by the different molecular fragments constituting the exTTF-TCF system and its carboxyl-substituted derivatives. For all the dyes, a similar charge transfer of around 0.17e takes place from the electron-donor exTTF moiety to the electron-withdrawing TCF/DCF unit. The main difference between exTTF-TCF and its carboxyl derivatives resides in the charge accumulated by the substituent groups. Whereas the cyano groups bear a charge around -0.20e in all cases, the carboxyl groups hold a significantly higher negative charge of approximately -0.40e. This result suggests that compared to the nitrile group the carboxyl group is not only more appropriate to anchor the dye to the semiconductor but also to favor the electron injection.

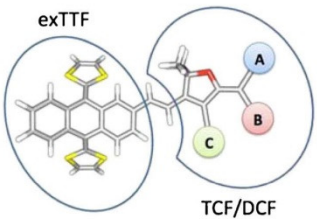
Calculations predict the same atomic orbital composition for the frontier molecular orbitals of exTTF-TCF and its carboxylic derivatives. As shown in Fig. 4 for exTTF-DCF-A, the highest-occupied molecular orbital (HOMO) and the HOMO-1 are fully localized on the donor exTTF moiety, whereas the HOMO-2 spreads over the ethylene bridge and the acceptor TCF/DCF fragment with some contribution from the anthracene unit. The lowest-unoccupied molecular orbital (LUMO) is also located on the TCF/DCF unit and the ethylene bridge, whereas the LUMO+1 and LUMO+2 are mainly confined on the exTTF moiety. A general destabilization of approximately 0.10 eV is predicted in passing from exTTF-TCF to the carboxylic derivatives (Table 2). The LUMO energy is an exception, as it is destabilized by 0.20 eV thus causing a small increase in the HOMO-LUMO energy gap for the carboxylic derivatives. The higher energy predicted for the LUMO of the exTTF-DCF derivatives is due to the lower electron-withdrawing character of the carboxyl group compared to the cyano group. The increase in the HOMO-LUMO energy gap determines a shift to higher energies of the lowest-energy charge transfer excitations (*vide infra*).

Excited state properties

The exTTF-TCF molecule absorbs over the whole visible spectrum [11]. Its push-pull design with the electron-donor exTTF moiety and the electron-withdrawing TCF fragment allows for low-lying charge-transfer excited states that can be harnessed for rapid electron injection to the semiconductor in a DSC device. In addition, the exTTF and TCF fragments absorb light around 450 nm giving rise to an intense and broad band in the blue region. As discussed above, nitrile groups have to be replaced by other anchoring groups like carboxylic acid for a strong and stable binding of the dye to the semiconductor. Therefore, for DSC purposes, it is essential that the

Table 1 Mulliken charges accumulated by the different molecular fragments of exTTF-TCF and its carboxylic exTTF-DCF derivatives^a

^a A, B, and C refer to the position of the carboxyl group in exTTF-DCF-A, exTTF-DCF-B, and exTTF-DCF-C, respectively; the other positions are occupied by cyano groups



Compound	exTTF	Bridge	TCF/DCF	A	B	C	A+B+C
exTTF-TCF	+0.19	-0.02	-0.17	-0.17	-0.21	-0.23	-0.61
exTTF-DCF-A	+0.17	-0.02	-0.15	-0.38	-0.25	-0.23	-0.86
exTTF-DCF-B	+0.17	-0.01	-0.16	-0.20	-0.40	-0.21	-0.81
exTTF-DCF-C	+0.17	0.00	-0.17	-0.20	-0.22	-0.41	-0.83

excellent optical properties of exTTF-TCF are maintained in the carboxylic derivatives.

The exTTF-DCF regioisomers were thoroughly analyzed using time-dependent DFT (TDDFT) calculations to compare their optical properties with those obtained for exTTF-TCF. The vertical excitation energies, oscillator strengths (f), and electronic nature calculated for the lowest-energy excited states are given in Table 3. Figure 5 displays the theoretical simulation of the electronic spectra obtained by using Gaussian-type convolution functions of width=0.20 eV. As

shown in Table 3 and Fig. 5, the optical absorption properties of exTTF-TCF are preserved in the exTTF-DCF derivatives and the three carboxylic regioisomers provide quasi-identical absorption features in terms of position and intensity of the electronic transitions.

In the low-energy part of the spectra, two low-lying electronic transitions ($S_0 \rightarrow S_1$ and $S_0 \rightarrow S_2$) are computed around 1.7 eV (720 nm) and 2.3 eV (540 nm) for exTTF-DCF derivatives. The major contributing monoexcitation to these transitions is the promotion of one electron from the HOMO and HOMO-1, which are completely localized on the exTTF moiety, to the LUMO, which spreads over the DCF moiety (see Fig. 4). The $S_0 \rightarrow S_1$ and $S_0 \rightarrow S_2$ transitions therefore imply an intramolecular charge transfer (CT) from the donor to the acceptor. They show moderate oscillator strengths ($f=0.15-0.30$), and undergo a shift to higher energies of 0.1 eV in passing from exTTF-TCF to its carboxyl-derivatives. The displacement of the CT bands results from the larger HOMO-LUMO gap computed for the exTTF-DCF derivatives, which is ascribed to the lower electron-withdrawing character of the carboxyl group. The 0.1 eV shift is not large enough to change the absorption properties of the dye, and similar CT features are predicted for exTTF-TCF and its carboxyl-substituted derivatives (Table 3).

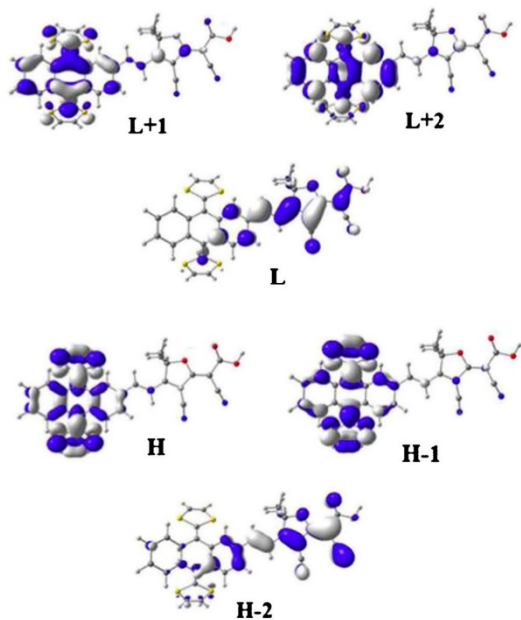


Fig. 4 Electron density contours (0.03 e bohr^{-3}) calculated at the B3LYP/6-31G** level for the frontier molecular orbitals of exTTF-DCF-A

Table 2 Molecular orbital energies in eV

Orbital	exTTF-TCF	exTTF-DCF-A	exTTF-DCF-B	exTTF-DCF-C
HOMO-2	-6.27	-6.15	-6.15	-6.12
HOMO-1	-5.76	-5.66	-5.65	-5.66
HOMO	-5.16	-5.07	-5.06	-5.08
LUMO	-3.22	-3.02	-3.04	-3.01
LUMO+1	-1.77	-1.66	-1.66	-1.66
LUMO+2	-1.30	-1.20	-1.19	-1.19

Table 3 Lowest singlet excited states calculated at the TDDFT level (B3LYP/6-31G** in vacuum) for exTTF-TCF and its carboxylic derivatives. Vertical excitation energies (E), oscillator strengths (f), dominant monoexcitations with contributions (within parentheses) greater than 15 %, and description of the excited states are given

Compound	State	E (eV / nm)	f	Monoexcitations (%) ^a	Description ^b
exTTF-TCF	S ₁	1.62 / 766	0.141	H→L (97)	CT
	S ₂	2.18 / 568	0.284	H-1→L (96)	CT
	S ₃	2.88 / 431	0.873	H-2→L (95)	TCF
	S ₄	3.02 / 411	0.271	H→L+1 (95)	exTTF
	S ₅	3.24 / 383	0.010	H→L+2 (74)	exTTF
	S ₆	3.35 / 371	0.182	H-3→L (93)	Anthr.+TCF
exTTF-DCF-A	S ₁	1.72 / 721	0.145	H→L (97)	CT
	S ₂	2.28 / 545	0.279	H-1→L (97)	CT
	S ₃	2.93 / 424	0.804	H-2→L (94)	DCF
	S ₄	3.03 / 409	0.271	H→L+1 (95)	exTTF
	S ₅	3.26 / 381	0.015	H→L+2 (74)	exTTF
	S ₆	3.40 / 365	0.242	H-3→L (91)	Anthr.+DCF
exTTF-DCF-B	S ₁	1.70 / 730	0.146	H→L (97)	CT
	S ₂	2.26 / 549	0.282	H-1→L (97)	CT
	S ₃	2.93 / 423	0.891	H-2→L (95)	DCF
	S ₄	3.03 / 409	0.270	H→L+1 (95)	exTTF
	S ₅	3.25 / 381	0.011	H→L+2 (73)	exTTF
	S ₆	3.40 / 365	0.168	H-3→L (92)	Anthr.+DCF
exTTF-DCF-C	S ₁	1.73 / 715	0.145	H→L (97)	CT
	S ₂	2.29 / 541	0.287	H-1→L (97)	CT
	S ₃	2.90 / 427	0.770	H-2→L (95)	DCF
	S ₄	3.04 / 408	0.269	H→L+1 (95)	exTTF
	S ₅	3.26 / 380	0.014	H→L+2 (74)	exTTF
	S ₆	3.40 / 364	0.275	H-3→L (91)	Anthr.+DCF

^aH and L denote HOMO and LUMO, respectively. ^bCT, TCF, DCF, exTTF, and Anthr. denote charge-transfer and TCF-, DCF-, exTTF-, and anthracene-centered electronic transitions, respectively

In the blue part of the spectrum, a very intense electronic transition ($S_0 \rightarrow S_3$) is calculated for both exTTF-TCF

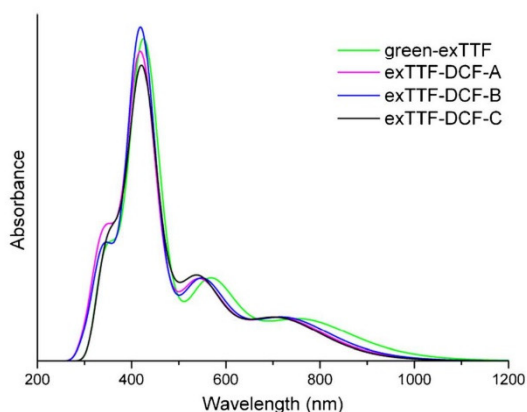


Fig. 5 TDDFT simulations of the UV-vis absorption spectra of exTTF-TCF and its carboxylic derivatives

(2.88 eV, 431 nm) and its exTTF-DCF derivatives (2.90–2.93 eV) (Table 3 and Fig. 5). The $S_0 \rightarrow S_3$ transition implies an electron promotion from the HOMO-2 to the LUMO and is therefore associated to the $\pi \rightarrow \pi^*$ excitation of the acceptor unit and the ethylene bridge (Fig. 4). It is the main responsible for the very intense absorption band observed in the experimental spectrum of exTTF-TCF at 418 nm [11]. A moderately- to highly-intense exTTF-centered $\pi\text{-}\pi^*$ electronic transition ($S_0 \rightarrow S_4$ associated with the HOMO→LUMO+1 excitation) is also predicted around 3.0 eV (400 nm), but this transition is hidden under the more intense $S_0 \rightarrow S_3$ transition. The integration of the theoretical simulated spectra (Fig. 5) shows that all the systems absorb practically the same amount of light under the considered region. The carboxyl-substituted derivatives exTTF-DCF-A and exTTF-DCF-B present a slightly higher absorption (integration of 1.11 and 1.10 eV, respectively) than exTTF-TCF and exTTF-DCF-C (1.05 and 1.01 eV, respectively).

TDDFT calculations therefore predict exactly the same characteristics (electronic nature, energy, and intensity) for

the electronic transitions that shape the absorption spectra of exTTF-TCF and its exTTF-DCF derivatives. The optical absorption spectrum remains mainly unaffected upon the introduction of the carboxyl group (Fig. 5) and the carboxyl-substituted exTTF-DCF derivatives are thus predicted to intensely absorb from 300 to 800 nm being good candidates as dyes for DSCs.

Adsorption onto titania

To investigate the adsorption of the dyes onto titania, periodic boundary conditions (PBC) calculations were performed. The two carboxyl-substituted regioisomers exTTF-DCF-A and exTTF-DCF-B were placed onto a periodic slab of TiO₂ exposing the (101) surface of the anatase polymorph. PBC geometry optimizations were performed and the final structures for the two isomers are shown in Fig. 6. The regioisomer exTTF-DCF-C was not computed due to evident steric hindrance between the exTTF moiety and the semiconductor surface. Although both monodentate and bidentate adsorption modes are present in dyes adsorbed onto titania, only the bridged bidentate coordination was modeled because it is the most commonly found [14, 18, 19, 57–59].

The (101) surface of anatase presents active, five-coordinated Ti atoms on which the carboxylic/carboxylate groups of the dye are bound. As depicted in Fig. 6, the exTTF-DCF-A and exTTF-DCF-B dyes are strongly adsorbed onto titania by their carboxylate groups which are attached to the semiconductor surface by two O–Ti bonds. exTTF-DCF-A binds to the semiconductor surface in a more perpendicular way than exTTF-DCF-B. The main molecular axes of the dye forms an angle with the titania surface of 54° in exTTF-DCF-A and of 39° in exTTF-DCF-B. As a consequence, the distance between the center of the donor exTTF moiety and the semiconductor surface is notably different: values of 12.8 and 9.5 Å are computed for exTTF-DCF-A and exTTF-DCF-B, respectively. For dye-sensitized solar cells, the separation between the donor moiety and the titania surface is of paramount importance since the larger the

Table 4 Interatomic distances (in Å) for the bonds defining the anchorage of exTTF-DCB-A and exTTF-DCB-B onto titania

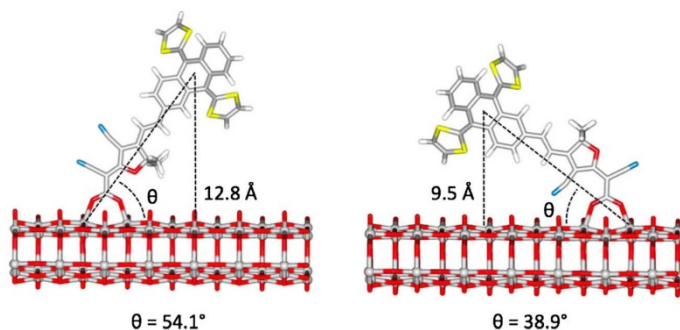
	exTTF-DCF-A	exTTF-DCF-B
C–O	1.286	1.284
	1.287	1.286
O–Ti	2.071	2.105
	2.133	2.136

distance, the less probable the electron–hole recombination processes that reduce the power conversion efficiency. On the other hand, in a DSC device the electrolyte interacts favorably with the donor part of the absorber. Therefore, by keeping away the donor moiety from the semiconductor surface the redox couple will stay far from titania, thus also reducing the electron–hole recombination with the electrolyte. In terms of stability, both dyes have almost identical energies adsorbed on the TiO₂ slab, yet exTTF-DCF-A is computed 1.7 kcal mol^{−1} lower in energy than exTTF-DCF-B. In the latter, the steric repulsion between the C9≡N9 cyano group and the closely located semiconductor surface may be the cause of this energy difference. An angle distortion of the cyano from 171.6° in exTTF-DCF-A to 164.9° in exTTF-DCF-B supports this assumption.

Table 4 compares the bond distances defining the anchorage of the carboxylate group to the titania surface in exTTF-DCF-A and exTTF-DCF-B. The carboxylate C–O bonds are marginally longer in exTTF-DCF-A by 0.001–0.002 Å, and the O–Ti bonds are significantly shorter especially for the better-linked carboxylate oxygen atom (0.034 Å). Both signatures reflect that the exTTF-DCF-A regioisomer is more strongly bound to the semiconductor surface thus favoring the stability of the adsorbed dye@TiO₂ species and, as a consequence, of the device.

By taking into account the dipole moment generated by the dye when linked onto titania, it is possible to estimate the differences expected in the open-circuit voltage (V_{OC}) in the DSC device between the two regioisomers since the sensitizer's dipole component normal to the surface of TiO₂

Fig. 6 Minimum-energy structures calculated for exTTF-DCF-A (left) and exTTF-DCF-B (right) adsorbed onto a periodic slab of anatase (101)



induces a shift in the energy of the CB [57, 60]. As observed in Fig. 6, the exTTF-DCF-A regioisomer lies more perpendicular to the semiconductor surface than exTTF-DCF-B. It is thus expected that the exTTF-DCF-A dye causes a larger shift to higher energies of the CB of the semiconductor, which will give rise to an increase of the V_{OC} in the device. However, the situation is more entangled than that, and a recent work has shown that the CB shift is the result of the combined effect of i) the amount of electron density transferred in the ground state from the dye to the semiconductor and ii) the electric field generated by the dye on the TiO_2 surface [16]. Assuming that the charge transfer to the semiconductor is practically the same in both regioisomers, the more perpendicular disposition of the exTTF-DCF-A absorber should lead to an increased V_{OC} , which is beneficial for dye-sensitized solar cells.

Conclusions

A first-principles investigation on the carboxyl-substituted exTTF-DCF derivatives of the donor- π -acceptor exTTF-TCF chromophore as dyes for DSCs has been performed by means of density functional theory calculations. The spatial arrangement and conformational isomerism of the electron-withdrawing tricyanofuran moiety and its three carboxylic DCF analogues have been first analyzed. The three carboxylic regioisomers show in their most stable conformation a disposition in which the carboxyl group points outward from the system thus acquiring an adequate orientation for an efficient anchorage to the semiconductor TiO_2 surface in DSCs. Whereas the carboxyl group remains coplanar to the acceptor moiety in DCF-A and DCF-B and the electron π -conjugation is maintained, it is displaced out from planarity in DCF-C due to steric hindrance effects. The latter, besides being unfavorable from a synthetic point of view, presents a rupture of the π -conjugation in the carboxylic acid that would hinder fast electron injection to the semiconductor.

The net charges accumulated by the different molecular fragments constituting the dyes show that, in the ground state, a charge transfer of around 0.17e takes place from the donor exTTF moiety to the acceptor carboxyl-substituted DCF unit. The anchoring carboxyl group holds a negative charge twice larger than the cyano moiety, which is beneficial for an efficient electron injection to the semiconductor in a DSC. In the excited state, the photoinduced charge transfer reinforces the negative charge accumulated by the acceptor unit. Time-dependent calculations confirmed the charge-transfer nature of the two moderately intense, low-lying bands predicted for exTTF-DCF derivatives and observed experimentally in the 500–800 nm range in the UV–vis spectrum of exTTF-TCF. The three carboxylic regioisomers preserve the absorption features of the parent exTTF-TCF system absorbing over the

whole UV–vis spectrum. This supports the interest in synthesizing them for dye-sensitized solar cell purposes.

Finally, periodic calculations have been carried out for the more probable exTTF-DCF-A and exTTF-DCF-B regioisomers anchored onto a periodic slab of TiO_2 (101). The absorbers were fully optimized, showing relevant differences in terms of the relative orientation with respect to the semiconductor surface. The exTTF donor moiety lies closer to the semiconductor surface in exTTF-DCF-B than in exTTF-DCF-A. The distance between the exTTF fragment and the surface is more than 3 Å larger in exTTF-DCF-A thus reducing the possible electron–hole recombination processes both with the donor moiety and with the electrolyte that might happen in the device. exTTF-DCF-A is calculated to be slightly more stable than exTTF-DCF-B when anchored on TiO_2 and is predicted as the better performing candidate for application in DSCs.

Acknowledgments This work has been supported by the Spanish Ministry of Economy and Competitiveness MINECO (CTQ2012-31914), the Generalitat Valenciana (PROMETEO/2012/053) and European Feder funds (CTQ2012-31914). JC acknowledges the Ministry of Education, Culture and Sport (MECS) of Spain for a Formación de Profesorado Universitario (FPU) grant.

References

- Hagfeldt A, Boschloo G, Sun L, Kloo L, Pettersson H (2010) Dye-Sensitized Solar Cells. *Chem Rev* 110:6595–6663. doi:10.1021/cr900356p
- O'Regan B, Grätzel M (1991) A low-cost, high-efficiency solar cell based on dye-sensitized colloidal TiO_2 films. *Nature* 353:737–740. doi:10.1038/353737a0
- Nazeeruddin MK, De Angelis F, Fantacci S, Selloni A, Viscardi G, Liska P, Ito S, Takeru B, Grätzel M (2005) Combined experimental and DFT-TDDFT computational study of photoelectrochemical cell ruthenium sensitizers. *J Am Chem Soc* 127:16835–16847. doi:10.1021/ja0524671
- Nazeeruddin MK, Kay A, Rodicio I, Humphry-Baker R, Mueller E, Liska P, Vlachopoulos N, Grätzel M (1993) Conversion of light to electricity by cis-X2bis(2,2'-bipyridyl)-4,4'-dicarboxylate/ruthenium(II) charge-transfer sensitizers (X = Cl-, Br-, I-, CN-, and SCN-) on nanocrystalline titanium dioxide electrodes. *J Am Chem Soc* 115: 6382–6390. doi:10.1021/ja00067a063
- Mishra A, Fischer MKR, Bäuerle P (2009) Metal-free organic dyes for dye-sensitized solar cells: from structure: property relationships to design rules. *Angew Chem Int Ed* 48:2474–2499. doi:10.1002/anie.200804709
- Pastore M, Mosconi E, Fantacci S, De Angelis F (2012) Computational investigations on organic sensitizers for dye-sensitized solar cells. *Curr Org Chem* 9:215–232
- Hagberg DP, Edvinsson T, Marinado T, Boschloo G, Hagfeldt A, Sun L (2006) A novel organic chromophore for dye-sensitized nanostructured solar cells. *Chem Commun*:2245–2247. doi:10.1039/b603002e
- Kim S, Lee JK, Kang SO, Ko J, Yum JH, Fantacci S, De Angelis F, Di Censo D, Nazeeruddin MK, Grätzel M (2006) Molecular engineering of organic sensitizers for solar cell applications. *J Am Chem Soc* 128:16701–16707. doi:10.1021/ja066376f

9. Horiuchi T, Miura H, Sumioka K, Uchida S (2004) High efficiency of dye-sensitized solar cells based on metal-free indoline dyes. *J Am Chem Soc* 126:12218–12219. doi:10.1021/ja0488277
10. Wenger S, Bouit P-A, Chen Q, Teuscher J, Censo DD, Humphry-Baker R, Moser J-E, Delgado JL, Martin N, Zakeeruddin SM, Grätzel M (2010) Efficient electron transfer and sensitizer regeneration in stable π -extended tetrathiafulvalene-sensitized solar cells. *J Am Chem Soc* 132:5164–5169. doi:10.1021/ja909291h
11. Bouit P-A, Villegas C, Delgado JL, Vinuela PM, Pou-Amérigo R, Ortí E, Martin N (2011) ExTTF-based dyes absorbing over the whole visible spectrum. *Org Lett* 13:604–607. doi:10.1021/ol102845m
12. Pastore M, De Angelis F (2013) Modeling materials and processes in dye-sensitized solar cells: understanding the mechanism, improving the efficiency. *Top Curr Chem* doi:10.1007/128_2013_468
13. Martinsovich N, Troisi A (2011) Theoretical studies of dye-sensitized solar cells: from electronic structure to elementary processes. *Energy Environ Sci* 4:4473–4495. doi:10.1039/c1ee01906f
14. Vittadini A, Selloni A, Rotzinger FP, Grätzel M (2000) Formic acid adsorption on dry and hydrated TiO₂ anatase (101) surfaces by DFT calculations. *J Phys Chem B* 104:1300–1306. doi:10.1021/jp993583b
15. Anselmi C, Mosconi E, Pastore M, Ronca E, De Angelis F (2012) Adsorption of organic dyes on TiO₂ surfaces in dye-sensitized solar cells: interplay of theory and experiment. *PCCP* 14:15963–15974. doi:10.1039/c2cp43006a
16. Ronca E, Pastore M, Belpassi L, Tarantelli F, De Angelis F (2013) Influence of the dye molecular structure on the TiO₂ conduction band in dye-sensitized solar cells: disentangling charge transfer and electrostatic effects. *Energy Environ Sci* 6:183–193. doi:10.1039/c2ee23170k
17. Pastore M, De Angelis F (2012) Computational modelling of TiO₂ surfaces sensitized by organic dyes with different anchoring groups: adsorption modes, electronic structure and implication for electron injection/recombination. *PCCP* 14:920–928. doi:10.1039/c1cp22663k
18. Pastore M, Angelis FD (2009) Aggregation of organic dyes on TiO₂ in dye-sensitized solar cells models: an ab initio investigation. *ACS Nano* 4:556–562. doi:10.1021/nn901518s
19. Pastore M, Angelis FD (2011) Computational modeling of stark effects in organic dye-sensitized TiO₂ heterointerfaces. *J Phys Chem Lett* 2:1261–1267. doi:10.1021/jz200443w
20. Mosconi E, Selloni A, De Angelis F (2012) Solvent effects on the adsorption geometry and electronic structure of dye-sensitized tio₂: a first-principles investigation. *J Phys Chem C* 116:5932–5940. doi:10.1021/jp209420h
21. Pastore M, Mosconi E, De Angelis F (2012) Computational investigation of dye–iodine interactions in organic dye-sensitized solar cells. *J Phys Chem C* 116:5965–5973. doi:10.1021/jp300095z
22. Mosconi E, Yum J-H, Kessler F, Gómez García CJ, Zuccaccia C, Cinti A, Nazeeruddin MK, Grätzel M, De Angelis F (2012) Cobalt electrolyte/dye interactions in dye-sensitized solar cells: a combined computational and experimental study. *J Am Chem Soc* 134:19438–19453. doi:10.1021/ja3079016
23. Martinsovich N, Troisi A (2011) High-throughput computational screening of chromophores for dye-sensitized solar cells. *J Phys Chem C* 115:11781–11792. doi:10.1021/jp2026847
24. Ambrosio F, Martinsovich N, Troisi A (2012) What is the best anchoring group for a dye in a dye-sensitized solar cell? *J Phys Chem Lett* 3:1531–1535. doi:10.1021/jz300520p
25. Maggio E, Troisi A (2013) Theory of the charge recombination reaction at the semiconductor–adsorbate interface in the presence of defects. *J Phys Chem C* 117:24196–24205. doi:10.1021/jp4080515
26. McMahon DP, Troisi A (2011) Persistence time of charge carriers in defect states of molecular semiconductors. *PCCP* 13:10241–10248. doi:10.1039/c1cp20192a
27. Frisch MJ, Trucks GW, Schlegel HB, Scuseria GE, Robb MA, Cheeseman JR, Scalmani G, Barone V, Mennucci B, Petersson GA, Nakatsuji H, Caricato M, Li X, Hratchian HP, Izmaylov AF, Bloino J, Zheng G, Sonnenberg JL, Hada M, Ehara M, Toyota K, Fukuda R, Hasegawa J, Ishida M, Nakajima T, Honda Y, Kitao O, Nakai H, Vreven T, Montgomery JA, Peralta JE, Ogliaro F, Bearpark M, Heyd JJ, Brothers E, Kudin KN, Staroverov VN, Kobayashi R, Normand J, Raghavachari K, Rendell A, Burant JC, Iyengar SS, Tomasi J, Cossi M, Rega N, Millam JM, Klene M, Knox JE, Cross JB, Bakken V, Adamo C, Jaramillo J, Gomperts R, Stratmann RE, Yazyev O, Austin AJ, Cammi R, Pomelli C, Ochterski JW, Martin RL, Morokuma K, Zakrzewski VG, Voth GA, Salvador P, Dannenberg JJ, Dapprich S, Daniels AD, Farkas, Foresman JB, Ortiz JV, Cioslowski J, Fox DJ (2009) Gaussian 09, Revision A.02. Gaussian, Inc, Wallingford
28. Francl MM, Pietro WJ, Hehre WJ, Binkley JS, Gordon MS, Defrees DJ, Pople JA (1982) Self-consistent molecular orbital methods. XXIII. A polarization-type basis set for second-row elements. *J Chem Phys* 77:3654–3665
29. Lee C, Yang W, Parr RG (1988) Development of the Colle-Salvetti correlation-energy formula into a functional of the electron density. *Phys Rev B* 37:785–789
30. Becke AD (1993) Density-functional thermochemistry. III. The role of exact exchange. *J Chem Phys* 98:5648–5652. doi:10.1063/1.464913
31. Stephens PJ, Devlin FJ, Chabalowski CF, Frisch MJ (1994) Ab initio calculation of vibrational absorption and circular dichroism spectra using density functional force fields. *J Phys Chem A* 98:11623–11627. doi:10.1021/j100096a001
32. Becke AD (1993) Density-functional thermochemistry. III. The role of exact exchange. *J Chem Phys* 98:5648–5652
33. Francl MM, Pietro WJ, Hehre WJ, Binkley JS, Gordon MS, Defrees DJ, Pople JA (1982) Self-consistent molecular-orbital methods.23. A polarization-type basis set for 2nd-row elements. *J Chem Phys* 77:3654–3665. doi:10.1063/1.444267
34. Chemcraft <http://www.chemcraftprog.com/>
35. Jamorski C, Casida ME, Salahub DR (1996) Dynamic polarizabilities and excitation spectra from a molecular implementation of time-dependent density-functional response theory: N[_{sub}2] as a case study. *J Chem Phys* 104:5134–5147
36. Petersilka M, Gossmann UJ, Gross EKV (1996) Excitation energies from time-dependent density-functional theory. *Phys Rev Lett* 76:1212–1215
37. Casida ME, Jamorski C, Casida KC, Salahub DR (1998) Molecular excitation energies to high-lying bound states from time-dependent density-functional response theory: characterization and correction of the time-dependent local density approximation ionization threshold. *J Chem Phys* 108:4439–4449
38. Dreuw A, Weisman JL, Head-Gordon M (2003) Long-range charge-transfer excited states in time-dependent density functional theory require non-local exchange. *J Chem Phys* 119:2943–2946. doi:10.1063/1.1590951
39. Dreuw A, Head-Gordon M (2005) Single-reference ab initio methods for the calculation of excited states of large molecules. *Chem Rev* 105:4009–4037. doi:10.1021/cr0505627
40. Tozer DJ (2003) Relationship between long-range charge-transfer excitation energy error and integer discontinuity in Kohn–Sham theory. *J Chem Phys* 119:12697–12699. doi:10.1063/1.1633756
41. Peach MJG, Benfield P, Helgaker T, Tozer DJ (2008) Excitation energies in density functional theory: an evaluation and a diagnostic test. *J Chem Phys* 128. doi:10.1063/1.2831900
42. Wiggins P, Williams JAG, Tozer DJ (2009) Excited state surfaces in density functional theory: a new twist on an old problem. *J Chem Phys* 131. doi:10.1063/1.3222641
43. Martinsovich N, Jones DR, Troisi A (2010) Electronic structure of TiO₂ surfaces and effect of molecular adsorbates using different DFT

- implementations. *J Phys Chem C* 114:22659–22670. doi:10.1021/jp109756g
44. Perdew JP, Burke K, Ernzerhof M (1996) Generalized gradient approximation made simple. *Phys Rev Lett* 77:3865–3868
45. Car R, Parrinello M (1985) Unified approach for molecular dynamics and density-functional theory. *Phys Rev Lett* 55:2471–2474. doi:10.1103/PhysRevLett.55.2471
46. Giannozzi P, Baroni S, Bonini N, Calandra M, Car R, Cavazzoni C, Ceresoli DL, Chiarotti G, Cococcioni M, Dabo I, Corso AD, de Gironcoli S, Fabris S, Fratesi G, Gebauer R, Gerstmann U, Gougousis C, Kokalj A, Lazzeri M, Martin-Samos L, Marzari N, Mauri F, Mazzarello R, Paolini S, Pasquarello A, Paulatto L, Sbraccia C, Scandolo S, Sclauzero G, Seitsonen AP, Smogunov A, Umari P, Wentzcovitch RM (2009) QUANTUM ESPRESSO: a modular and open-source software project for quantum simulations of materials. *J Phys Condens Matter* 21:395502
47. Cho MJ, Seo J, Oh HS, Jee H, Kim WJ, Kim KH, Hoang MH, Choi DH, Prasad PN (2012) Tricyanofuran-based donor–acceptor type chromophores for bulk heterojunction organic solar cells. *Sol Energy Mater Sol Cells* 98:71–77. doi:10.1016/j.solmat.2011.09.008
48. Patel DG, Bastianon NM, Tongwa P, Ieger JM, Timofeeva TV, Bartholomew GP (2011) Modification of nonlinear optical dyes for dye sensitized solar cells: a new use for a familiar acceptor. *J Mater Chem* 21:4242–4250. doi:10.1039/c0jm03774e
49. Perepichka DF, Bryce MR, Perepichka IF, Lyubchik SB, Christensen CA, Godbert N, Batsanov AS, Levillain E, McInnes EJJ, Zhao JP (2002) A (π -extended tetrathiafulvalene)–fluorene conjugate. Unusual electrochemistry and charge transfer properties: the first observation of a covalent D2⁺– σ –A⁻ Redox State1. *J Am Chem Soc* 124:14227–14238. doi:10.1021/ja012518o
50. Christensen CA, Batsanov AS, Bryce MR (2006) Extreme conformational constraints in π -extended tetrathiafulvalenes: unusual topologies and redox behavior of doubly and triply bridged cyclophanes. *J Am Chem Soc* 128:10484–10490. doi:10.1021/ja062358m
51. Martín N, Sánchez L, Seoane C, Ortí E, Viruela PM, Viruela R (1998) Synthesis, properties, and theoretical characterization of largely π -extended tetrathiafulvalene derivatives with quinonoid structures. *J Org Chem* 63:1268–1279. doi:10.1021/jo9719416
52. Diaz MC, Illescas BM, Martín N, Viruela R, Viruela PM, Ortí E, Brede O, Zilbermann I, Guldi DM (2004) Highly conjugated p-quinonoid π -extended tetrathiafulvalene derivatives: a class of highly distorted electron donors. *Chem Eur J* 10:2067–2077
53. García R, Herranz MÁ, Torres MR, Bouit P-A, Delgado JL, Calbo J, Viruela PM, Ortí E, Martín N (2012) Tuning the electronic properties of nonplanar exTTF-based push–pull chromophores by aryl substitution. *J Org Chem* 77:10707–10717. doi:10.1021/jo302047m
54. Tatay S, Haque SA, O'Regan B, Durrant JR, Verhees WJH, Kroon JM, Vidal-Ferran A, Gavina P, Palomares E (2007) Kinetic competition in liquid electrolyte and solid-state cyanine dye sensitized solar cells. *J Mater Chem* 17:3037–3044. doi:10.1039/b703750c
55. Ehret A, Stuhl L, Spitzer MT (2001) Spectral sensitization of TiO₂ nanocrystalline electrodes with aggregated cyanine dyes. *J Phys Chem B* 105:9960–9965. doi:10.1021/jp011952+
56. Wang Z-S, Cui Y, Dan-oh Y, Kasada C, Shinpo A, Hara K (2007) Thiophene-functionalized coumarin dye for efficient dye-sensitized solar cells: electron lifetime improved by coadsorption of deoxycholic acid. *J Phys Chem C* 111:7224–7230. doi:10.1021/jp067872t
57. Chen P, Yum JH, Angelis FD, Mosconi E, Fantacci S, Moon S-J, Baker RH, Ko J, Nazeeruddin MK, Grätzel M (2009) High open-circuit voltage solid-state dye-sensitized solar cells with organic dye. *Nano Lett* 9:2487–2492. doi:10.1021/nl901246g
58. Tian H, Yang X, Chen R, Zhang R, Hagfeldt A, Sun L (2008) Effect of different dye baths and dye-structures on the performance of dye-sensitized solar cells based on triphenylamine dyes. *J Phys Chem C* 112:11023–11033. doi:10.1021/jp800953s
59. Nunzi F, De Angelis F (2010) DFT investigations of formic acid adsorption on single-wall tio₂ nanotubes: effect of the surface curvature. *J Phys Chem C* 115:2179–2186. doi:10.1021/jp110132k
60. Rühle S, Greenshtein M, Chen SG, Merson A, Pizem H, Sukenik CS, Cahen D, Zaban A (2005) Molecular adjustment of the electronic properties of nanoporous electrodes in dye-sensitized solar cells. *J Phys Chem B* 109:18907–18913. doi:10.1021/jp0514123

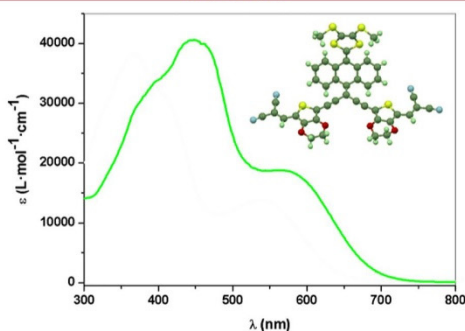
Efficient Light Harvesters Based on the
10-(1,3-Dithiol-2-ylidene)anthracene CorePierre-Antoine Bouit,[†] Lourdes Infantes,[§] Joaquín Calbo,^{||} Rafael Viruela,^{||}
Enrique Ortí,^{*||} Juan Luis Delgado,^{*†} and Nazario Martín^{*†,‡}

IMDEA-Nanociencia, Ciudad Universitaria de Cantoblanco, 28049 Madrid, Spain, Instituto de Química-Física “Rocasolano”, CSIC, 28006 Madrid, Spain, Instituto de Ciencia Molecular, Universidad de Valencia, 46980 Paterna, Spain, and Departamento de Química Orgánica, Facultad de Ciencias Químicas, Universidad Complutense de Madrid, 28040 Madrid, Spain

juanluis.delgado@imdea.org; enrique.orti@uv.es; nazmar@quim.ucm.es

Received July 1, 2013

ABSTRACT



Three new push–pull chromophores based on the 10-(1,3-dithiol-2-ylidene)anthracene core were synthesized and fully characterized. The new chromophores display broad absorption spectra, nearly covering the whole visible region, with high extinction coefficients. Electrochemistry and theoretical calculations allowed the understanding of these singular electronic properties. The molecular structures were unambiguously confirmed by X-ray diffraction.

Solar energy currently represents one of the most realistic alternatives to the use of fossil fuels. Photovoltaic devices based on organic compounds (OPV) have experienced tremendous development in the past years,¹ and recently efficiencies around 8–10% have been reported.² One of the crucial points to understanding this improvement is the careful election of suitable organic materials

able to fulfill some energetic and electronic requirements. Among these requisites, the ability of the material to harvest sunlight in a broad range of the visible and NIR spectrum is essential in order to obtain a suitable photo-response. In this regard, organic chromophores such as push–pull systems, displaying outstanding absorption properties, are promising materials to obtain highly efficient OPV³ and hybrid cells.⁴

In this communication, we report the synthesis and the optical and electrochemical properties of new push–pull

[†]Imdea Nanociencia.[§]CSIC.^{||}Universidad de Valencia.[‡]Universidad Complutense de Madrid.

(1) (a) Thompson, B. C.; Frechet, J. M. J. *Angew. Chem., Int. Ed.* **2008**, *47*, 58–77. (b) Delgado, J. L.; Bouit, P.-A.; Filippone, S.; Herranz, M. A.; Martin, N. *Chem. Commun.* **2010**, *46*, 4853–4865. (c) Li, C.-Z.; Yip, H.-L.; Jen, A. K.-Y. *J. Mater. Chem.* **2012**, *22*, 4161–4177. (d) Lin, Y.; Li, Y.; Zhan, X. *Chem. Soc. Rev.* **2012**, *41*, 4245–4272.

(2) (a) Huo, L.; Zhang, S.; Guo, X.; Xu, F.; Li, Y.; Hou, J. *Angew. Chem., Int. Ed.* **2011**, *50*, 9697–9702. (b) Mishra, A.; Bäuerle, P. *Angew. Chem., Int. Ed.* **2012**, *51*, 2020–2068.

(3) (a) Kronenberg, N. M.; Deppish, M.; Würthner, F.; Ledemann, H. V. A.; Deing, K.; Meerholz, K. *Chem. Commun.* **2008**, 6489–6491. (b) Roquet, S.; Cravino, A.; Leriche, P.; Alévèque, O.; Frère, P.; Roncali, J. *J. Am. Chem. Soc.* **2006**, *128*, 3459–3466. (c) Lin, L.-Y.; Chen, Y.-H.; Huang, Z.-Y.; Lin, H.-W.; Chou, S.-H.; Lin, F.; Chen, C.-W.; Liu, Y.-H.; Wong, K.-T. *J. Am. Chem. Soc.* **2011**, *133*, 15822–15825. (d) Bouit, P.-A.; Villegas, C.; Delgado, J. L.; Viruela, P.; Pou-Américo, R.; Ortí, E.; Martín, N. *Org. Lett.* **2011**, *13*, 604–607.

molecules based on the 10-(1,3-dithiol-2-ylidene)anthracene core (see Scheme S1 in the Supporting Information (SI)), absorbing in a broad region of the visible spectrum. The chemical structures of the new push–pull materials have been unambiguously confirmed by single-crystal X-ray diffraction, and their electrochemical and optical properties have been characterized with the help of density functional theory (DFT) calculations. Recently, we have described the preparation of 10-(1,3-dithiol-2-ylidene)anthracene derivatives for their application in dye-sensitized solar cells.⁵ Molecular engineering of this appealing core allows the design of materials with improved light-harvesting properties. The new dyes synthesized here bear the same electron-donor unit, the 10-(1,3-dithiol-2-ylidene)anthracene group, but a different conjugated π -bridge, 3,4-ethylenedioxythiophene (EDOT) for **6** or phenyl for **4** and **5**, as well as two kinds of electro-accepting units, an ester group for **4** and a dicyanovinylene group for **5** and **6** (Figure 1).

The synthesis of the key synthon **1**, featuring two terminal alkyne groups (Scheme S1), was carried out in four steps in good yield.⁶ The conjugated bridges were then introduced by the Sonogashira cross-coupling reaction using $\text{PdCl}_2(\text{PPh}_3)_2$ and CuI as catalysts. The introduction of the accepting units was achieved by 2-fold Knoevenagel condensation of aldehydes **2** and **3** with malononitrile, to afford the new dyes **5** and **6** in good to moderate yields (75% and 50%, respectively; see the SI). Dye **4**, with the two decyl chains, displays excellent solubility in the main

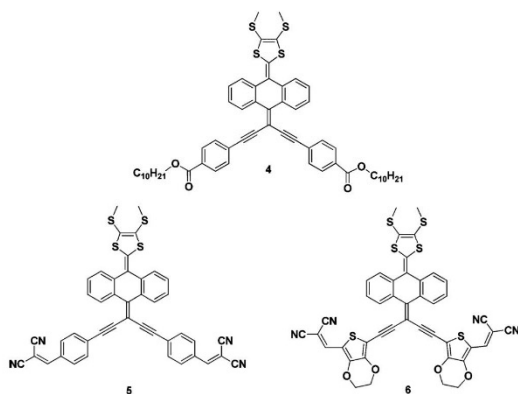


Figure 1. Push–pull systems **4**, **5**, and **6**.

(4) (a) Kim, S.; Lee, J. K.; Kang, S. O.; Ko, J.; Yum, J. H.; Fantacci, S.; De Angelis, F.; Di Censo, D.; Nazeeruddin, M. K.; Grätzel, M. *J. Am. Chem. Soc.* **2006**, *128*, 16701–16707. (b) Wenger, S.; Bouit, P.-A.; Chen, Q.; Teuscher, J.; Di Censo, D.; Humphry-Baker, R.; Moser, J. E.; Delgado, J. L.; Martin, N.; Zakeeruddin, S. M.; Grätzel, M. *J. Am. Chem. Soc.* **2010**, *132*, 5164–5169.

(5) Bouit, P.-A.; Marszałek, M.; Humphry-Baker, R.; Viruela, R.; Ortí, E.; Zakeeruddin, S.-M.; Grätzel, M.; Delgado, J. L.; Martin, N. *Chem.—Eur. J.* **2012**, *18*, 11621–11629.

(6) Chen, G.; Wang, L.; Thompson, D. W.; Zhao, Y. *Org. Lett.* **2008**, *10*, 657–660.

organic solvents. The structures of all the new compounds and the new sensitizers were confirmed by ^1H , ^{13}C NMR, and high resolution mass spectrometry.

Slow evaporation of chloroform solutions of **2**, **5**, and **6** allowed the obtention of single crystals suitable for its study by X-ray diffraction (Figures 2 as well as S10 and S11 in the SI).⁷ The compounds adopt the typical butterfly- or saddle-like shape observed for exTTF (2-[9-(1,3-dithiol-2-ylidene)anthracen-10(9*H*)-ylidene]-1,3-dithiole) derivatives.⁸ The existence of several $\text{C}-\text{H}\cdots\pi$ and $\pi\cdots\pi$ stacking interactions plus other weaker $\text{C}-\text{H}\cdots\text{N}\equiv\text{C}$ and $\text{C}-\text{H}\cdots\text{S}$ hydrogen bonds led to the formation of supra-molecular networks of compounds **2**, **5**, and **6**.

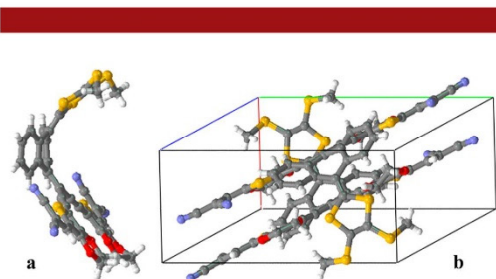


Figure 2. (a) X-ray crystal structure of **6**. (b) Unit cell.

The molecular geometries of the three push–pull systems were optimized using DFT calculations at the B3LYP/6-31G** level (see the SI for computational details). The decyl chains in **4** were replaced by a simple methyl group to simplify the calculation. As obtained from X-ray analysis, theoretical calculations predict concave saddle-like structures, in which the central ring of the anthracene unit folds up in a boat conformation and the dithiole rings are tilted down. The planes defined by the external benzene rings of the anthracene unit are predicted to form an angle of 40.5° for **5** and 38.6° for **6** slightly overestimating the angles obtained by X-ray diffraction (36.2° and 34.5° , respectively) due to the packing forces present in the crystal that tend to reduce the folding. The dihedral angles of 35.5° computed for the dithiole tilting in **5** and **6** nicely fit the X-ray values of 34.2° (**5**) and 34.1° (**6**). The same considerations apply for the tilting of the acceptor moiety (see Table S1 in the SI). The acceptor arms remain mostly planar in all dyes thus favoring the π -electron communication along the acceptor moiety. This planarity is even more pronounced in the crystal due to the efficient π - π coplanar interactions in the packing (see Figure 2b and Table S1).

Figure 3 shows the atomic orbital (AO) composition of the highest-occupied (HOMO–2 to HOMO) and

(7) CCDC 900353 (**2**), CCDC 890337 (**5**), and CCDC 890785 (**6**) contain the supplementary crystallographic data for this paper. These data can be obtained free of charge from The Cambridge Crystallographic Data Centre via http://www.ccdc.cam.ac.uk/data_request/cif.

(8) Batsanov, A. S.; Bryce, M. R.; Coffin, M. A.; Green, A.; Hester, R. E.; Howard, J. A. K.; Lednev, I. K.; Martin, N.; Moore, A. J.; Moore, J. N.; Ortí, E.; Sánchez, L.; Savirón, M.; Viruela, P. M.; Viruela, R.; Ye, T.-Q. *Chem.—Eur. J.* **1998**, *4*, 2580–2592.

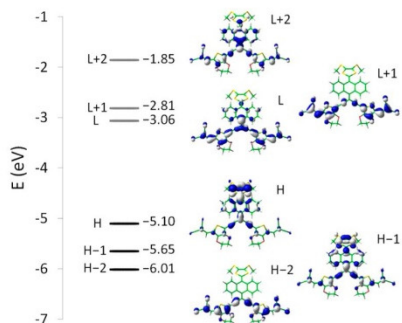


Figure 3. Electron-density contours ($0.03 e \text{ bohr}^{-3}$) and orbital energies calculated for the frontier molecular orbitals of **6** at the B3LYP/6-31G** level. H and L denote HOMO and LUMO, respectively.

lowest-unoccupied (LUMO to LUMO+2) molecular orbitals of **6**, as a representative example. The HOMO (-5.10 eV) and HOMO-1 (-5.65 eV) are localized on the electron-donor 10-(1,3-dithiol-2-ylidene)anthracene unit, hereafter named hemi-exTTF, whereas the HOMO-2 (-6.01 eV) spreads over the electron-acceptor moiety with no hemi-exTTF participation. The LUMO (-3.06 eV) and LUMO+1 (-2.81 eV) are located on the electron-acceptor arms, and the LUMO+2 (-1.85 eV) comprises both the hemi-exTTF moiety and the acceptor fragment. Identical topologies are predicted for the frontier molecular orbitals of **4** and **5** (see Figure S13). A pronounced stabilization of the LUMO is predicted in passing from **4** (-2.46 eV) to **5** (-3.01 eV) and **6** (-3.06 eV) due to the higher electronegative character of the dicyanovinylene group compared to the ester unit. The presence of the electron-donor EDOT fragment in **6** slightly increases the energy of the HOMO (-5.10 eV) compared to **5** (-5.17 eV). Theoretical calculations therefore predict small HOMO-LUMO energy gaps of -2.64 , -2.16 , and -2.04 eV for **4**, **5**, and **6**, respectively, and suggest the presence of low-energy charge-transfer (CT) absorption bands in the electronic spectrum.

The redox properties of **4–6** were examined by cyclic voltammetry (CV) (Table 1). The anodic region of dye **4** is characterized by one reversible wave ($E^{\circ}_{\text{ox}} = 0.27 \text{ V}$) attributed to the hemi-exTTF unit, whereas no reduction is observed in the experimental conditions. The presence of the stronger electron-accepting dicyanovinylene groups in **5** shifts the reduction potential to -1.31 V , whereas the oxidation potential is only weakly affected ($E^{\circ}_{\text{ox}} = 0.29 \text{ V}$). This trend nicely correlates with the slight stabilization of the HOMO (0.07 eV) and the significant stabilization of the LUMO (0.55 eV) predicted by theoretical calculations in passing from **4** to **5** (Figure S13). The presence of the auxiliary electron-donor EDOT groups in **6** slightly reduces the oxidation ($E^{\circ}_{\text{ox}} = 0.25 \text{ V}$) and reduction ($E^{\circ}_{\text{red}} = -1.26 \text{ V}$) potentials. CV measurements therefore obtain a decrease of the electrochemical gap along the series **4**

($> 2.07 \text{ V}$), **5** (1.60 V), and **6** (1.51 V), which is in perfect agreement with theoretical predictions and with the trend observed from optical data (see below).

Table 1. Electrochemical and Optical Data for **4–6**

compd	E°_{ox} (V) ^a	E°_{red} (V) ^b	E°_{g} ^{cv} (V) ^b	λ_{max} (nm) ^c	ϵ ($\text{L} \cdot \text{mol}^{-1} \cdot \text{cm}^{-1}$)
4	0.27	< -1.80	> 2.07	491	19 000
5	0.29	-1.31	1.60	536	14 000
6	0.25	-1.26	1.51	590	19 000

^a Measured by CV (CH_3CN , $0.1 \text{ M Bu}_4\text{ClO}_4$, $v = 100 \text{ mV} \cdot \text{s}^{-1}$, V vs Ag/AgNO₃). ^b Electrochemical gap determined as $E_{\text{ox}} - E_{\text{red}}$. ^c Measured in DCM, $10^{-5} \text{ mol} \cdot \text{L}^{-1}$.

The absorption properties of compounds **4–6** were measured in dichloromethane solution (Figure 4a). **4** displays two main absorption bands in the UV and visible range ($\lambda_1 = 364 \text{ nm}$; $\lambda_2 = 491 \text{ nm}$). Both transitions are red-shifted, first when a better acceptor is inserted in the molecule (**5**, $\lambda_1 = 366 \text{ nm}$; $\lambda_2 = 536 \text{ nm}$), then with the

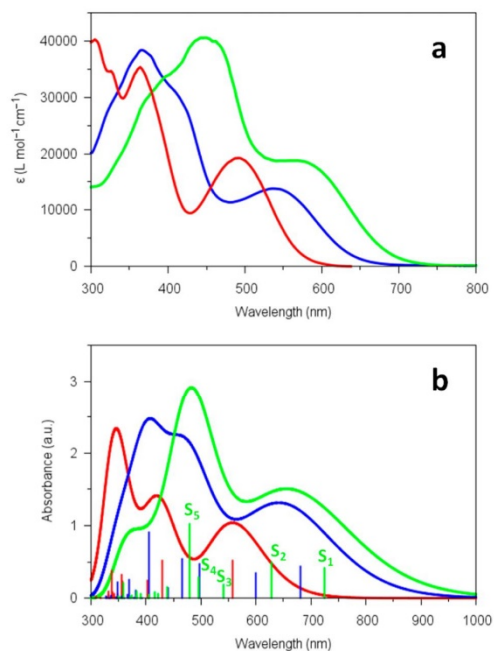


Figure 4. (a) Absorption spectra of **4** (red), **5** (blue), and **6** (green) recorded in dichloromethane at room temperature. (b) Theoretical simulation of the UV-vis absorption spectra for push-pull compounds **4–6**. Vertical lines indicate the vertical excitation energies and oscillator strengths calculated for the electronic transitions to the different singlet excited states S_n . States S_1 to S_5 are explicitly denoted for compound **6**.

presence of the EDOT units (**6**, $\lambda_1 = 443$ nm; $\lambda_2 = 590$ nm). As expected, a decrease of the optical band gap is observed when the push–pull effect in the compound is reinforced.

To investigate the nature of the electronic transitions that give rise to the absorption bands observed in the electronic spectra, the lowest-energy singlet excited states (S_n) were calculated for **4–6** using the time-dependent DFT (TD-DFT) approach. TD-DFT calculations predict that the lowest-energy absorption band observed for **5** and **6** above 500 nm is due to electronic transitions to the first two excited singlets S_1 and S_2 (see Table S2 and Figure 4b). These states originate from the HOMO→LUMO and HOMO→LUMO+1 monoexcitations, respectively, and imply an electron density transfer from the hemi-exTTF moiety, where the HOMO resides, to the acceptor moiety, where the LUMO and LUMO+1 are mainly located (Figure 3). In compound **4**, S_2 stands higher in energy (2.89 eV) due to the higher energy of the LUMO+1 (Figure S13) and does not contribute to the lowest-energy band at 491 nm (Figure 4b). Calculations therefore confirm the CT nature of the lowest-energy absorption band of **4–6**. The moderately high intensities observed for this band are in agreement with the oscillator strengths (f) around 0.4–0.5 calculated for S_1 and S_2 (Table S2) and are due to the significant overlap between the HOMO and the LUMO/LUMO+1.

The intense absorption band observed at higher energies mainly results from the HOMO–2→LUMO excitation (state S_6 for **5** and S_5 for **6**, Table S2 and Figure 4b), which mainly implies the electron-acceptor part of the molecule (Figure 3). This electronic transition is predicted to have a high intensity ($f \approx 1.00$) and shifts to lower energies in passing from **5** to **6** due to the EDOT groups that destabilize the HOMO–2 from –6.46 (**5**) to –6.01 eV (**6**). For compound **4**, the transition is calculated to show a lower intensity ($f = 0.33$) in good agreement with the experimental spectra (Figure 4a). The HOMO→LUMO+2 excitation involving the hemi-exTTF moiety and the CT HOMO–1→LUMO and HOMO–1→LUMO+1 excitations also contribute to this intense absorption band (Table S2).

In summary, a new family of anthracene-based chromophores has been synthesized and fully characterized. The new dyes capture light in a broad range of the solar spectrum, compound **6** being the best light-harvesting chromophore, absorbing in the UV and visible spectrum (from 300 to 750 nm). The outstanding absorption properties stem from the efficient electronic communication between the donor and acceptor moieties, giving rise to very intense charge-transfer bands. The remarkable electronic and optical properties exhibited by the new compounds make them promising materials for their further incorporation in molecular solar cells.^{9,10}

Acknowledgment. This work has been supported by the MINECO of Spain (CTQ 2011-27934, CTQ2011-24652, CTQ2012-31914, and Consolider-Ingenio CSD 2007-00010 on Molecular Nanoscience), the Comunidad de Madrid (MADRISOLAR-2, S2009/PPQ-1533), the Generalitat Valenciana (Prometeo/2012/053), and the EU project (FUNMOLS FP7-212942-1). J.L.D. thanks the MINECO for a Ramón y Cajal Fellowship. P.-A.B. thanks IMDEA-Nanociencia for a postdoctoral research grant. J.C. acknowledges MECD (Spanish Ministry of Education, Culture, and Sport) for a FPU grant. L.I. thanks Comunidad de Madrid (Spain) for support (BIPEDD-2: S2010-BMD-2457).

Supporting Information Available. Synthetic procedure, chemical characterization, X-ray structures, and computational details (geometrical data and TD-DFT results). This material is available free of charge via the Internet at <http://pubs.acs.org>.

(9) (a) Silvestri, F.; Irwin, M. D.; Beverina, L.; Facchetti, A.; Pagani, G. A.; Marks, T. J. *J. Am. Chem. Soc.* **2009**, *130*, 17640–17641. (b) Rousseau, T.; Cravino, A.; Bura, T.; Ulrich, G.; Ziessel, R.; Roncali, J. *Chem. Commun.* **2009**, 1673–1675.

(10) (a) Roncali, J. *Acc. Chem. Res.* **2009**, *42*, 1719–1730. (b) Bouit, P.-A.; Rauh, D.; Neugebauer, S.; Delgado, J. L.; Di Piazza, E.; Rigaut, S.; Maury, O.; Andraud, C.; Dyakonov, V.; Martin, N. *Org. Lett.* **2009**, *11*, 4806–4809.

The authors declare no competing financial interest.

Computational modeling of single- versus double-anchoring modes in di-branched organic sensitizers on TiO₂ surfaces: structural and electronic properties†

Cite this: *Phys. Chem. Chem. Phys.*, 2014, 16, 4709

Joaquín Calbo,^a Mariachiara Pastore,^{*b} Edoardo Mosconi,^b Enrique Orti^{*a} and Filippo De Angelis^{*b}

We present a first-principles DFT investigation of the adsorption geometry on the anatase (101) surface of a prototypical di-branched organic dye based on the extended tetrathiafulvalene moiety, incorporating two anchoring cyanoacrylic acid units. Reduced model systems with one and two anchoring groups have been initially studied to investigate the vibrational frequencies related to TiO₂ dye adsorption. Our calculations confirm that the reduced systems can be used as reliable models to study the anchoring modes and that the conclusions extracted from the reduced systems can be extrapolated to the entire molecule. A series of molecular structures have been investigated to simulate the anchoring environment in monodentate- and bidentate-like adsorption modes. The comparison between the theoretical results and the available experimental data suggests a di-anchored monodentate adsorption mode as the most probable adsorption structure. Geometry optimizations of the di-branched model system adsorbed on a periodic slab of anatase (101) allowed us to compare the relative stability of different adsorption conformations and led to a di-anchored monodentate mode as the most stable adsorption structure. Furthermore, *ab initio* molecular dynamics simulations confirmed this structure as the preferred one, providing additional stabilization by effective hydrogen-bonding to surface oxygens and structure distortion from planarity. The analysis of the partial density of states for the prototypical models confirms that the doubly anchored adsorption provides improved electronic properties compared to the singly anchored structures for dye-sensitized solar cell purposes.

Received 25th November 2013,
Accepted 13th January 2014

DOI: 10.1039/c3cp54970d

www.rsc.org/pccp

1. Introduction

Dye-sensitized solar cells (DSCs) have attracted increasing attention in the last decade as promising alternatives to the traditional silicon-based photovoltaics.^{1–3} In these devices, a dye-sensitizer absorbs the solar radiation and the photoexcited electron is transferred to the conduction band (CB) of a semiconductor, typically TiO₂ nanoparticles. Then, a redox mediator, commonly based on the iodide/triiodide couple, regenerates the oxidized dye thus completing the circuit.

Since the discovery of the highly efficient Ru(II)-based complexes, such as N3 and N719 dyes,^{2,4} much effort has been made to synthesize new and more efficient push-pull organic dyes, due to their lower-cost synthesis, tunable optical properties and environmental friendliness.^{5,6} However, few organic dyes with the standard I[−]/I₃[−] electrolyte show efficiencies that can directly compete with those of the most prominent Ru complexes.^{7–9} Organic dyes in conjunction with mono-electronic metallorganic redox couples, such as Co(II)/Co(III) complexes, usually showing simpler kinetics and requiring less dye regeneration overpotentials, have led to efficiencies exceeding those of Ru(II)-based sensitizers.^{10–14}

First-principles computer simulations have been shown to successfully provide new insights into the structural, electronic and optical properties of the hybrid dye/semiconductor interface in DSCs,¹⁵ in particular providing crucial information on the preferred adsorption modes of the dye onto the semiconductor surface.^{16,17} In previous work, some of us demonstrated that the highly efficient N719 exploits three of its four carboxylic acid anchoring groups in the linkage to the semiconductor surface.^{18,19} This coordination through three carboxylic acids provides not

^a Instituto de Ciencia Molecular, Universidad de Valencia, 46980 Paterna, Spain. E-mail: enrique.orti@uv.es

^b Computational Laboratory for Hybrid Organic Photovoltaics (CLHYO), Istituto CNR di Scienze e Tecnologie Molecolari, via Elce di Sotto 8, I-06123, Perugia, Italy. E-mail: chiara@thch.unipg.it, filippo@thch.unipg.it

† Electronic supplementary information (ESI) available: Chemical structures of several di-branched dyes; calculated B3LYP and PBE0 IR spectra in the gas phase and in acetonitrile solution for compound 1; calculated bond distances for the different models of 1; PBE0 infrared frequencies of the main vibrational modes present in the dye@semiconductor system; electrostatic potential averages plots; and PDOS for 2@TiO₂. See DOI: 10.1039/c3cp54970d

only high stability to the device, but also high open-circuit voltage (V_{OC}) and efficient electron injection. Thus, the design of new purely organic dyes bearing more than one anchoring group appears to be the next natural step.

In this perspective, several di-anchoring dyes have been very recently synthesized and characterized providing a general improvement in the photovoltaic performance compared to the single-anchoring homologues. Some examples of these novel di-branched dyes are the Zn-based porphyrin ZnPDCA dye,²⁰ and triarylamine-based absorbers such as KS-5,²¹ DB-1 and DB-2²² (see Scheme S1 in the ESI† for chemical structures). These dyes provided not only much higher short-circuit photocurrent densities (J_{SC}) and slightly higher V_{OC} than the single-branched homologues, but also improved and red-shifted incident photon-to-current efficiencies (IPCEs).

In the context of organic sensitizers, a number of push-pull π -extended tetrathiafulvalene (exTTF)-based systems (exTTF stands for 2-[9-(1,3-dithiol-2-ylidene)anthracen-10(9H)-ylidene]-1,3-dithiole) have emerged as novel promising dyes, which absorb light in a wide range of the UV-Vis and NIR spectrum.²³ This is mainly due to the improved donor ability of the exTTF unit, which produces a notable increase in the energy of the highest-occupied molecular orbital (HOMO). Encouraged by these results, two new di-anchoring dyes containing the exTTF-related donor unit 10-(1,3-dithiol-2-ylidene)anthracene²⁴ have been synthesized.²⁵ The only difference between these two novel dyes relies on the π -spacer separating the donor unit and the anchoring cyanoacrylic acid group: a simple benzene ring for **A** and the 3,4-ethylenedioxythiophene (EDOT) unit for **B** (Fig. 1). The use of EDOT spacers has been inspired by previous work, where the EDOT was shown to yield a red-shift in the spectroscopic response and an enhancement of the molar extinction coefficient in triphenylamine and exTTF-based sensitizers.^{23,26,27} However, the lower performance of **B** in the device, in line with previous findings, suggests fast recombination processes as a consequence of I₂-EDOT interactions that do not occur in **A**.²⁸ From the FTIR spectra recorded for **A** and **B**, a di-anchoring adsorption mode on the TiO₂ surface was found on the basis of

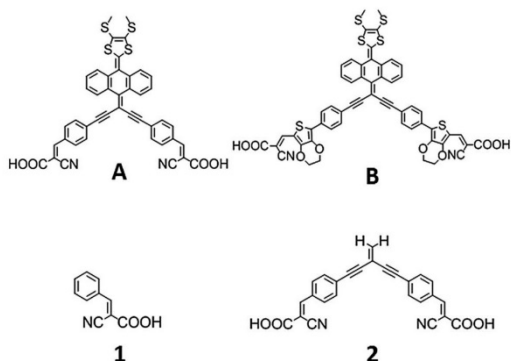


Fig. 1 Dyes **A** and **B** and the two size-reduced systems, with one (**1**) and two (**2**) anchoring groups, used as models of dye **A**.

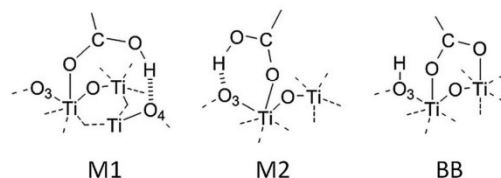


Fig. 2 Graphical representation of the three main carboxylic/carboxylate binding modes in DSCs: two different monodentate (M1 and M2) and one bridged bidentate (BB) adsorptions.

the disappearance of the stretching vibration of the carbonyl group at around 1700 cm^{-1} in passing from the powder spectra to the dye-adsorbed spectra.²⁵ However, the adsorption mode of each anchoring group to the semiconductor surface is much more difficult to determine.

We recall that the anchoring mechanism of a carboxylic-based dye onto the TiO₂ surface can be simplified by the different coordination modes of the carboxylic acid/carboxylate unit (COOH/COO⁻) to the metal ions.²⁹ Thus, it is possible to differentiate between three anchoring modes: monodentate (M), chelated (CB) and bridged bidentate (BB). Among them, the monodentate and especially the bridged bidentate modes displayed in Fig. 2 are the most common modes found in the field of organic sensitizers attached to the TiO₂ anatase (101) surface.^{16,30–34} In the case of the monodentate, two binding modes, M1 and M2, are distinguishable due to the oxygen atom (O₄ or O₃, respectively) to which the carboxylic hydrogen is linked.²⁹ A distinction between the monodentate and bidentate modes can be obtained by means of the empirical rule derived by Deacon and Philips, which correlates the difference between the asymmetric and symmetric stretching wavenumbers ($\Delta\nu_{as}$) of COO⁻ to the type of coordination.³⁵ In broad terms, a measurement of $\Delta\nu_{as}$ close or smaller than the reference value for the neat salt (usually about 200 cm^{-1}) indicates a bridged bidentate coordination, whereas a value of $\Delta\nu_{as}$ larger than the reference value is related to a monodentate adsorption. Experimentally, the identification of the symmetric and asymmetric stretching COO⁻ frequencies is only feasible for simple acids, due to the overlap of new and intense bands in the $1400\text{--}1600\text{ cm}^{-1}$ region occurring for aromatic and conjugated systems. For the two novel di-branched sensitizers **A** and **B**, a value of $\Delta\nu_{as} = 220\text{--}260\text{ cm}^{-1}$ was preliminarily proposed thus sitting at the edge of a possible assignment.

In this contribution, we theoretically investigate the relative stabilities of the different anchoring modes for sensitizer **A**. First, a comprehensive determination of the vibrational features of the sensitizer by varying the nature of the carboxylic anchorage allows for the understanding on how the anchorage of the dye to the TiO₂ surface modifies the fundamental frequencies of the carboxylic/carboxylate group. The theoretical characterization of the typical vibrational modes in a dye@TiO₂-like system enables us to unequivocally assign the symmetric and asymmetric CO modes in the available experimental FTIR spectrum. In a second step, a reduced model system of **A** is used to compare the relative

stabilities of the different considered anchoring modes. The geometry of all the systems is carefully examined and a long *ab initio* molecular dynamics is carried out for the conformer with the most stable adsorption mode. Finally, the role of the adsorption topology in influencing the electronic properties of the system is discussed on the basis of a detailed analysis of the density-of-states profiles. To our knowledge, this study represents the first investigation of the anchoring mode for a di-branched organic dye, opening the way to a full exploitation of this class of potential highly efficient dyes.

2. Methodology

To limit the computational cost, two simpler models of dye A incorporating one and two cyanoacrylic acid groups (compounds 1 and 2, respectively, in Fig. 1) were used. Density functional theory (DFT) calculations were performed at the B3LYP/6-31G* level,^{36,37} in conjunction with the polarizable continuum model (PCM)^{38,39} approach using acetonitrile as solvent. The vibrational frequencies obtained were corrected according to the vibrational scaling factor of 0.960 reported in the literature.^{40–43} Geometry optimizations and frequency calculations for the systems under study were carried out using the Gaussian 09 program package (version C.01).⁴⁴

To model the adsorption of the dye to the anatase (101) surface, a periodic slab of (TiO₂)_n with *n* = 64 was employed, being large enough to accommodate the dye in a di-branched monodentate mode. It has been recently shown that TiO₂ anatase slabs of thickness similar to our modeled slab (two-layer fashion) nicely reproduce the electronic structure of thicker films.⁴⁵ Because of the molecular rigidity of the dye, a transversal analogue with *n* = 72 was necessary to allow a di-anchoring bridged bidentate mode. The other possible adsorption modes were modeled using the *n* = 64 slab to reduce the computational cost, still maintaining the reliability of the results. The energy difference between the *n* = 64 and *n* = 72 periodic slabs was used to rescale the absolute energy of the investigated configurations in order to compare the relative stability computed on different-sized slabs.

Periodic calculations were performed using DFT within the generalized gradient approximation (GGA) by means of the PBE exchange–correlation functional.⁴⁶ The Car–Parrinello (CP) algorithm⁴⁷ was employed as implemented in the Quantum-Espresso 5.0 package⁴⁸ for both geometry optimizations and *ab initio* dynamics simulations. Electron–ion interactions were described by ultrasoft pseudopotentials with electrons from O, N and C 2s, 2p, H 1s, and Ti 3s, 3p, 3d, 4s shells explicitly included in the calculations. Plane-wave basis set cutoffs for the smooth part of the wave functions and the augmented density were 25 and 200 Ry, respectively. The dye molecules were adsorbed only on one side of the slab and the vacuum between the top of the molecule and the adjacent upper slab was ~6 Å for the largest extended single-anchored conformer. Molecular dynamics simulations were carried out with an integration time step of 10 au for a total of *ca.* 3 ps. The fictitious mass used for the electronic degrees of freedom is 1000 au, and the atomic

masses for the different elements were set to 5 amu. This set-up allows us to achieve a fast equilibration of the system and to speed-up the Car–Parrinello dynamics. A randomization of the atomic positions was used to increase the potential energy and raise the temperature of the system over 150 degrees. Afterwards, a Nose–Hoover thermostat was applied to increase and maintain the temperature between 300 and 350 degrees. Using the optimized geometries for the different adsorption modes, electronic structure calculations were also performed to obtain the projected density-of-states (PDOS) profiles. The contribution to the total DOS for the lowest-unoccupied molecular orbital (LUMO) of each branch in 2@TiO₂ was separated and the interaction between the dye and the semiconductor was analyzed following the Newns–Anderson model.^{49,50} The normalized contribution, *p_i*, to the PDOS relative to the dye's LUMO is defined as the portion of the ψ_i molecular orbital located on the sensitizer, evaluable by the relation:

$$p_i = \frac{\sum_{A \in \text{dye}} \left(c_{ij}^A \right)^2}{\sum_j \left(c_{ij}^A \right)^2} \quad (1)$$

where c_{ij}^A values are the expansion coefficients when ψ_i is expressed as a linear combination of *n* atomic orbitals centered on atom A.

To ensure that the PDOS belongs to the sensitizer's LUMO we selected a number of abduct orbitals so that the $\sum p_i \approx 1$. Since there are two nearly degenerate LUMOs due to the presence of two branches in the 2@TiO₂ system, only the contribution to the DOS of the branch “better” linked to the semiconductor surface was taken into account for the fitting. The center of this distribution corresponds to the energy of the LUMO of the dye adsorbed on TiO₂, $E_{\text{LUMO(ads)}}$, and it can be calculated as

$$E_{\text{LUMO(ads)}} = \sum_i p_i \varepsilon_i \quad (2)$$

where ε_i values are the orbital energies of the combined system for the selected energy range. The LUMO broadening has been then obtained as a mean deviation of a distribution centered at the $E_{\text{LUMO(ads)}}$:

$$h\Gamma = \sum_i p_i |\varepsilon_i - E_{\text{LUMO(ads)}}| \quad (3)$$

The energetic distribution of the LUMO for the dye adsorbed on the TiO₂ has been fitted using a Lorentzian function:

$$\rho_{\text{LUMO}}(E) = \frac{1}{\pi} \frac{\left(\frac{h\Gamma}{2} \right)}{(E - E_{\text{LUMO(ads)}})^2 + \left(\frac{h\Gamma}{2} \right)^2} \quad (4)$$

In this model, the LUMO broadening gives a direct estimation of the electron-transfer time by the relation:

$$\tau(\text{fs}) = \frac{658}{\Gamma(\text{meV})} \quad (5)$$

3. Results and discussion

3.1. Molecular calculations: simple models

To evaluate the possibility of reducing the molecular size of the dye to study the adsorption mode on the semiconductor, frequency calculations were first performed at the B3LYP/6-31G* level for the entire dye under study (**A**) and for the two size-reduced molecular models **1** and **2**, which incorporate one and two anchoring groups, respectively (see Fig. 1). The 10-(1,3-dithiol-2-ylidene)anthracene moiety, the donor part of dye **A**, is fully suppressed in **1** and **2**. These preliminary calculations allow us to assess how the vibrational modes that characterize the anchoring region evolve in passing from the reduced systems to the entire molecule. The vibrational frequencies calculated for **1** and **2** are compared to those obtained for **A** in Fig. 3.

An overall correspondence is found for the vibrational modes calculated in the 1000–1800 cm⁻¹ range, which increase in intensity passing from **1** to **2** and to **A** (Fig. 3). The peak above 1700 cm⁻¹ corresponds to the C=O stretching mode and the intense transition around 1570 cm⁻¹ is associated with a C=C stretching. For **A**, a relative intense transition is computed at 1480–1500 cm⁻¹ which corresponds to C=C stretching modes in the donor moiety. Less intense bands can be found for **1**, **2** and **A** in the 1400–1500 cm⁻¹ region which are assigned to aromatic C–C–H bendings. The peak computed at 1340 cm⁻¹ results from the intense stretching of the C–OH bond plus some weaker aromatic C–C–H bending modes. A low intense transition appears for **A** at around 1260 cm⁻¹ that corresponds to C–C–H bendings of the anthracene part. Finally, the high-intense peak at 1140 cm⁻¹ is due to the C–O–H bending. Therefore, the characteristic modes of the carboxylic group in the IR spectrum are repeated along the series of compounds **1**, **2** and **A** in their neutral form. The same behavior is expected for different anchoring modes, so that it is possible to extrapolate the vibrational properties of **A** in a particular adsorption mode from those of **1**, except for some low-intense transitions that are associated with the donor moiety.

To investigate the adsorption coordination of compound **1** onto the TiO₂ surface, six possible structural environments

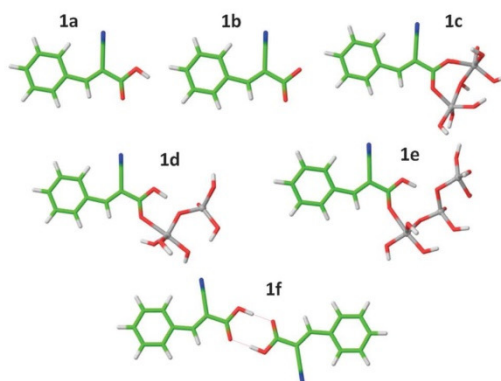


Fig. 4 Optimized geometries of compound **1** in different structural environments. Atom colors: C in green, O in red, H in white, N in blue and Ti in grey.

were modeled taking into account the nature of the carboxylic group: neutral (**1a**), anion (**1b**), linked to a Ti₂O₇-H₆ cluster in BB- (**1c**) and M2-like (**1d**) adsorption modes, linked to a Ti₃O₁₀H₈ cluster in an M1-like coordination (**1e**) and as a dimer (**1f**). The comparison of the frequencies calculated for these structures allows the determination of general trends for the IR bands associated with the COOH/COO⁻ group in passing from the isolated system (**1a** and **1b**) through a monodentate linkage (**1d** and **1e**) to a bidentate-like (**1c**) mode. The optimized structures computed in the gas phase for structures **1a–1f** are shown in Fig. 4.

The main differences concerning the vibration modes of the anchoring group between systems **1a–1f** are found in the 1000–1800 and 3000–3600 cm⁻¹ regions (see Fig. S1 in the ESI† for the 1000–1800 cm⁻¹ region). The O–H stretching appears beyond 3500 cm⁻¹, except for **1b**, and it drops around 500 cm⁻¹ in **1d**, **1e** and **1f** due to the formation of hydrogen bonds. As far as CO characteristic modes are concerned, the symmetric and asymmetric stretching of the COOH/COO⁻ group are fairly intense in the IR spectrum and their position, as stated in the introduction, represents an indication of the anchoring topology. The symmetric stretching is predicted in the 1250–1450 cm⁻¹ region and there is no clear trend passing from monodentate- to bidentate-like anchorages (Table 1). The asymmetric stretching

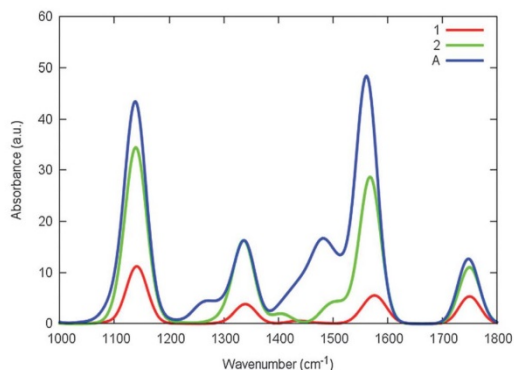


Fig. 3 IR spectra computed for the neutral species of system **A** and subsystems **1** and **2**.

Table 1 Infrared frequencies (in cm⁻¹) calculated for the main vibrational modes of structures **1a–1f** at the B3LYP/6-31G* level of theory (gas phase), and obtained from the experimental IR spectra of dye **A** as a powder and adsorbed onto TiO₂

System	CO asymm	CO symm	C=C	C–C–H	$\Delta\nu_{as}^a$
1a	1750	1340	1570	1340	410
1b	1710	1260	1590	1330	450
1c	1550	1390	1590	1350	150
1d	1650	1440	1570	1360	210
1e	1660	1400	1570	1360	260
1f	1700	1420	1570	1360	280
Exp. A powder ^b	1710	1420	1590	1350	290
Exp. A @TiO ₂ ^b	1620	1390	1590	1350	230

^a $\Delta\nu_{as} = \nu(\text{CO asymm}) - \nu(\text{CO symm})$. ^b IR spectra from ref. 25.

is computed at larger wavenumbers, in the 1550–1750 cm^{-1} region. Calculations indicate that the more monodentate character of the linkage, the higher the energy of the asymmetric mode. This leads to a $\Delta\nu_{\text{as}} > 200 \text{ cm}^{-1}$ for monodentate coordinations (**1d** and **1e**) whereas a value below 200 cm^{-1} is obtained for the bidentate anchorage (**1c**). Intense vibrational transitions associated with the aromatic backbone of the dye grow in the same region as the CO stretchings and constitute a difficulty in the correct experimental assignment of the symmetric and asymmetric CO modes. C=C stretchings are computed around at 1550–1600 cm^{-1} and can compete in intensity and position with the asymmetric CO stretching, especially for the bidentate coordinations (see Table 1). Moreover, an aromatic C–C–H bending mode is predicted at around 1350 cm^{-1} and its position is well preserved over all the models. This vibration may overlap the symmetric CO stretching in both monodentate- and bidentate-like anchoring environments, but it is computed at lower energies in all cases except for the non-representative **1b**. Theoretical frequency calculations therefore allow the unequivocal assignment of the characteristic CO modes in the experimental IR spectrum reported by Bouit *et al.*,²⁵ leading to the values shown in Table 1 for **A** as a powder and adsorbed on TiO_2 . The theoretical frequencies calculated for **1f** nicely fit the experimental data for the dye as a powder suggesting that the dye forms dimers in the powder as occurs in other cyanoacrylic acid-based compounds.⁵¹ The experimental value of $\Delta\nu_{\text{as}} = 290 \text{ cm}^{-1}$ inferred for the dye as a powder compared to the 280 cm^{-1} value predicted for **1f** supports this assumption. In turn, vibrational assignment of the **A@TiO₂** modes opens the door to more than one model. The experimental value of $\Delta\nu_{\text{as}} = 230 \text{ cm}^{-1}$ resulting from the theoretical assignment suggests that monodentate coordinations ($\Delta\nu_{\text{as}}$ of 210 and 260 cm^{-1} for **1d** and **1e**, respectively) are more likely to provide the real coordination in the **A@TiO₂** system than a bidentate adsorption mode (**1c**, $\Delta\nu_{\text{as}} = 150 \text{ cm}^{-1}$). Moreover, a better match of the CO symmetric mode calculated for **1e** (1400 cm^{-1}) with the corresponding **A@TiO₂** mode (1390 cm^{-1}) points to the M1 adsorption as the more likely coordination mode.

A parallel series of calculations was also performed using the PBE0 functional and the scaled results (scaling factor of 0.986) were almost identical to the B3LYP calculations (Fig. S2, ESI†). Therefore, no qualitative or quantitative difference upon changing the functional for the analysis of the vibrational modes in our systems is expected. PCM calculations in acetonitrile solution were also performed showing the same qualitative trends with a general increase in intensity for the CO and C=C stretching transitions (Fig. S3 and S4, ESI†).

3.2. Periodic calculations

(a) **Geometry analysis.** Having established the relationship between the characteristic normal modes of the COOH/COO[−] group and its environment, we can now move to model the di-branched system **2** (Fig. 1) anchored to the anatase (101) surface. Four single-anchored adsorption configurations, *i.e.* three monodentate (M1, M2 and MN) and one bidentate (BB)

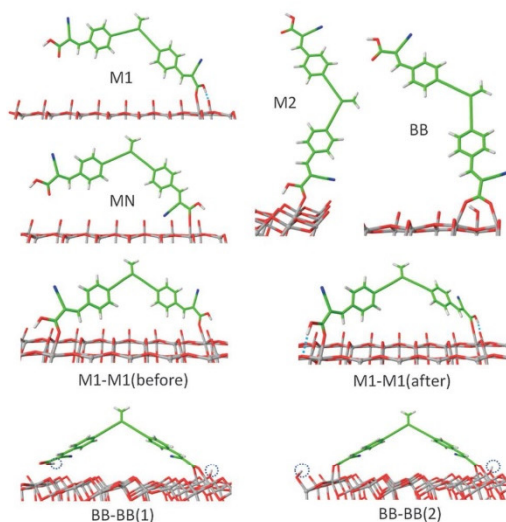


Fig. 5 Adsorption conformations modeled for system **2**. M1–M1(before) and M1–M1(after) correspond to minimum-energy conformations optimized before and after the *ab initio* molecular dynamics simulation.

structures, and two di-anchored conformations, *i.e.* one monodentate (M1–M1) and one bidentate (BB–BB) structures, were considered (Fig. 5). All the conformations were fully optimized using the Car–Parrinello algorithm and the most relevant geometrical parameters are given in Table 2. The M1–M1 conformation was optimized before and after running a long *ab initio* molecular dynamics simulation (termed M1–M1(before) and M1–M1(after) in Fig. 5).

Among the single-anchored systems, it is worth differentiating between the monodentate and the bidentate systems: while in the M1, M2 and MN adsorptions a different length is calculated for the C–O₁ and C–O₂ bonds, in the BB adsorption the situation is completely symmetric (Table 2). M1 and M2 only differ in the

Table 2 Selected bond distances (in Å) for the different conformations of **2@TiO₂**

Structure	Ti ₁ –O ₁ (Ti ₂ –O ₂)	C–O ₁	C–O ₂	O ₂ –H	H···O _{3/4}	N–Ti ₂	N–H
M1	2.248	1.249	1.321	1.030	1.546	—	—
M2	2.239	1.250	1.333	1.019	1.687	—	—
MN	2.129	1.231	1.347	0.983	—	2.616	—
BB	2.157 (2.254)	1.285	1.285	—	0.980	—	—
M1–M1(before) ^a	2.364	1.237	1.346	0.988	2.335	—	—
	2.228	1.242	1.343	0.986	3.202	—	—
M1–M1(after) ^a	2.256	1.245	1.331	1.012	1.731	—	—
	2.171	1.251	1.334	1.003	1.889	—	—
BB–BB(1) ^a	2.152 (2.317)	1.289	1.287	—	0.976	—	—
	2.713 (2.862)	1.225	1.366	0.988	2.160	—	2.448
BB–BB(2) ^a	2.127 (2.116)	1.282	1.298	—	0.974	—	—
	2.626 (2.074)	1.254	1.319	—	0.978	—	—

^a Values corresponding to each anchoring branch of **2** are given in different rows.

oxygen type (O_4 and O_3 , respectively) to which the carboxylic acid is H-bonded. The shorter value calculated for the bond length between the carboxylic hydrogen and the O_3/O_4 atoms ($H \cdots O_{3/4}$) suggests a stronger hydrogen bond interaction in the case of M1. In both cases, the hydrogen is retained by the carboxylate group and it is not transferred to the TiO_2 surface. A recent work has demonstrated that the inclusion of solvent effects slightly modifies the H-transfer scenario: more polar solvents favor the H-transfer to the semiconductor.²⁹ The MN structure was included in the analysis because here it competes in energy with M1 and M2 (*vide infra*), although it is usually computed higher in energy.^{16,18,19,31,33,45,52–63} As shown in Table 2, this conformation presents a relatively small N–Ti distance of 2.62 Å, which contributes to the relative stabilization of the adsorption mode. A comparison of the relative energies for the different adsorption modes will be discussed below.

The doubly anchored conformations deserve particular attention since, in line with previous findings on di-branched dyes,²² the experimental FTIR spectra suggest that our di-branched dye is attached to the TiO_2 surface by means of both anchoring groups.²⁵ In the optimized M1–M1(after), the $C-O_1$ bond lengthens and the $C-O_2$ bond shortens compared to M1–M1(before), thus the carboxylate group attains a more symmetric disposition. This is due to the formation of a hydrogen bond with the $O_{3/4}$ as a consequence of the rearrangement of the molecule after the dynamics. The $H \cdots O_{3/4}$ distance shortens in passing from M1–M1(before) to M1–M1(after) clearly pointing to the formation of a hydrogen bond. Moreover, the distortion from planarity to form the H-bond suggests that the energy stabilization due to the formation of the H-bond is much higher than the energy destabilization due to the partial breaking of planarity. The longer $H \cdots O_{3/4}$ distance predicted for M1–M1(after) compared to M1 and M2 is a signal of the geometrical constraints that M1–M1 suffers to be anchored adequately by its two cyanoacrylic acid groups forming two stabilizing H-bonds. Fig. 6 displays the evolution of the O_2 –H and $H \cdots O_{3/4}$ distances over time during the CP molecular dynamics. As shown, the temperature is high enough to break and form again the bonds involving the carboxylic hydrogen, thus giving flexibility to the system to explore a huge zone of the potential energy surface. At around 1.25–1.50 ps, the $H \cdots O_{3/4}$

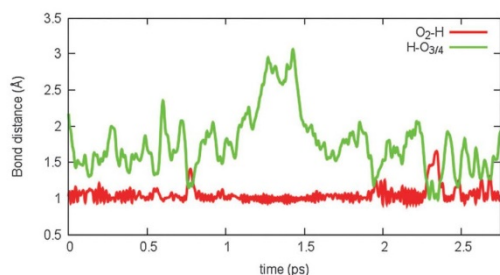


Fig. 6 Time evolution of the characteristic O_2 –H and $H \cdots O_{3/4}$ bond distances during the Car–Parrinello molecular dynamics simulation.

distance presents large values indicating a breaking of the H-bond (Fig. 6), whereas at 0.75 and 2.30 ps, the shorter distance predicted for $H \cdots O_{3/4}$ than for O_2 –H suggests a proton transfer from the carboxylic acid to the semiconductor oxygen. The exploration of the possible conformations of the di-branched dye therefore shows that, on average, the M1–M1 adsorption structure is the most visited disposition.

An additional geometrical distortion from planarity has to be made in order to obtain the BB–BB adsorption conformation, in which the dye is lying along the semiconductor surface. To generate this conformation, the two anchoring branches of the molecule need to adopt a perpendicular orientation with respect to the central $C=CH_2$ unit and lose the π -connection between them (see Fig. 5). Depending on the position of the carboxylic hydrogen of one branch in the semiconductor surface, we distinguish two clearly different situations: BB–BB(1), where the H is kept bonded to the anchoring group of the dye, and BB–BB(2), where the H is displaced to be linked to a further $O_{3/4}$ of the semiconductor. Whereas distance parameters are mostly equal in the purely BB branch for both situations, a significant difference is observed in the other branch where a competition between an M1 and a BB mode appears due to the relative position of the hydrogen atom (Table 2). In BB–BB(1), the H remains linked to the carboxylic acid and forms a kind of double H-bond with the N atom of the cyano group (N–H distance: 2.448 Å) and the $O_{3/4}$ atom ($H \cdots O_{3/4}$ distance: 2.16 Å). This mode possesses an asymmetric situation for the C–O bonds (1.225 and 1.366 Å) resembling a monodentate mode. For BB–BB(2), both anchoring groups provide a BB chelation but while one group is well bonded to the surface (2.127 and 2.116 Å for Ti–O distances), the other group has only a strong interaction through one oxygen (2.626 and 2.074 Å for Ti–O distances) due to the rigidity of the system.

(b) Relative stabilities. To shed light on the energetics of the different possible structures for the combined dye@ TiO_2 system, we calculated the relative energy of the modeled conformations with different adsorption modes (Table 3) using the Car–Parrinello optimized geometries. Two different periodic slabs were used to model the conformations here compared, and the energies between conformations held on different slabs have been related through the energy difference between the two isolated TiO_2 slabs. The reliability of this approach was confirmed by calculating the same conformation (structure M1) on the two $(TiO_2)_n$ slabs ($n = 64$ and 72). The energy difference

Table 3 Relative stabilities of the modeled adsorption conformations for 2@ TiO_2

Structure	Relative energy (kcal mol ⁻¹)
M1	4.98
M2	3.70
MN	9.70
BB	14.16
M1–M1(before)	0.00
M1–M1(after)	–9.39
BB–BB(1)	30.27
BB–BB(2)	38.55

obtained between the two calculations using the energy difference between the isolated slabs was as small as $0.30 \text{ kcal mol}^{-1}$.

The energy calculated for the M1–M1(before) structure is taken as a reference. Among the four single-anchored conformations, M2 is calculated to be the most stable adsorption mode, with the M1 structure being quite close in energy ($1.28 \text{ kcal mol}^{-1}$). However, taking into account the spatial arrangement of the COOH groups (Fig. 5), a di-anchored M2–M2 conformation is not feasible due to the geometric rigidity of the dye and it was therefore not modeled. The MN adsorption mode also gives a relatively small energy and is found to be $6.00 \text{ kcal mol}^{-1}$ less stable than M2. The bridging bidentate (BB) mode is computed to be more than 10 kcal mol^{-1} higher in energy than M2, in good agreement with previous theoretical studies employing Car–Parrinello calculations using periodic boundary conditions.^{17,64} Moving to the di-anchoring conformations, M1–M1(before) stands much more stable than BB–BB (30 kcal mol^{-1}). Furthermore, after the molecular dynamics simulation and the corresponding reoptimization procedure, M1–M1(after) gains an extra stabilization of more than 9 kcal mol^{-1} compared to M1–M1(before). This additional stability is a consequence of the formation of two H-bonds upon deformation of the dye structure from planarity. BB–BB(1) and BB–BB(2) therefore lie much higher in energy than M1–M1. In fact, the di-anchored BB structures are less stable than the single-anchored BB conformation by more than 15 kcal mol^{-1} . This huge destabilization is due to the inefficient bond interactions caused by the rigid structure of the dye, the fixed topology of the TiO₂ surface and the additional π -conjugation breaking experienced by the dye to adopt the di-anchored BB structures. In passing from M1 to M1–M1(after) a stabilization of around 14 kcal mol^{-1} is obtained for the di-anchored conformation, which mostly corresponds to the energy gain associated with the anchorage of a carboxylic acid group to the anatase (101) surface ($\sim 18.5 \text{ kcal mol}^{-1}$).⁶⁴ Based on the present calculations, which might however overstabilize the monodentate anchoring, dye **A** is therefore found to adsorb on the TiO₂ surface in a di-anchored monodentate M1–M1 manner in good agreement with experimental suggestions based on IR spectra.²⁵

(c) Electronic structure. To gain insight into the influence of the anchoring process on the electronic features of the final DSC device, we studied the density of states (DOS) for both the bare periodic slab and the dye@TiO₂ models using the PBE functional. Calculations were performed on the M1, M1–M1, BB and BB–BB structures optimized for **2**, which should provide a reliable description of the adsorbed systems because it contains both anchoring groups at the relative distance they have in the entire dye. Special attention must be paid to the relative energy position of the conduction band and the LUMO, whereas no concluding remarks should be taken from the valence band (VB) and the HOMO positions due to the lack of the donor moiety in model **2**. The presence of the donor moiety might also influence the CB position because it modulates the charge transfer (CT) in the ground state to the semiconductor as recently proved.⁶⁵ However, since theoretical calculations demonstrated negligible donor–acceptor CT in the ground state

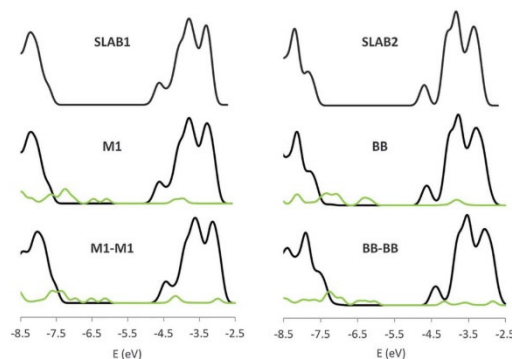


Fig. 7 Projected density of states (PDOS) calculated for the M1, M1–M1, BB and BB–BB adsorption models of **2**@TiO₂ and for their respective bare periodic slabs. Black and green lines represent the contribution of the semiconductor surface and the adsorbed molecule, respectively, to the density of states.

for the isolated compounds **A** and **B**,²⁵ and we are interested in relative changes for the different adsorption modes in the same system, no special concern has been shown to include the donor moiety. The absolute energy of the bands in the DOS diagram was calculated by referring the Kohn–Sham eigenvalues to the vacuum level, as determined from the value of the electrostatic potential in the vacuum region of the supercell. Electrostatic potentials along the direction normal to the surface for the dye-sensitized TiO₂ slab are included in the ESI† (Fig. S5 and S6).

Fig. 7 shows the projected density of states (PDOS) decomposition of the total DOS to highlight the role of the adsorption mode in the energy level distribution, and Table 4 collects the most relevant energy data. A band gap of 2.6 eV is computed for both bare model slabs, which is slightly underestimated compared to the experimental value of $\sim 3.0 \text{ eV}$ reported elsewhere.^{66,67} This result evidences the well-established shortcoming of standard DFT calculations leading to the underestimation of the band gap in semiconductors.⁶⁸

Single-anchoring modes such as M1 and BB maintain unchanged the position of the CB in the bare slab (-4.9 eV),

Table 4 Energy (eV) for the main bands close to the Fermi level obtained from the periodic calculations

	SLAB1	M1	M1–M1	SLAB2	BB	BB–BB
LUMO(1) ^a	—	−4.1	−4.2	—	−3.8	−3.6
LUMO(2) ^a	—	−4.0	−4.1	—	−3.8	−4.1
CB	−4.9	−4.9	−4.7	−4.9	−4.9	−4.6
VB	−7.5	−7.5	−7.4	−7.5	−7.5	−7.2
Band gap	2.6	2.6	2.7	2.6	2.6	2.6
LUMO–CB ^b	—	0.8	0.5	—	1.1	1.0

^a LUMO(1) and LUMO(2) refer to the PDOS contribution to the total DOS for the better-anchored branch and the worse- or non-anchored branch of **2** in the **2**@TiO₂ system, respectively. ^b The LUMO(1) is used in the difference since it is the one which most participates in the electron injection process into the semiconductor.

whereas di-anchored adsorptions M1–M1 and BB–BB slightly shift the CB to higher energies by 0.2 and 0.3 eV, respectively (Table 4). As previously described, the sensitizer's dipole component normal to the surface induces a shift in the TiO₂ CB energy.^{31,69} Actually, the situation is more entangled and some of us have recently shown that the CB shift is the result of a combined effect of (i) the amount of electron density transferred in the ground state from the dye to the semiconductor and (ii) the electric field generated by the dye on the TiO₂ surface.⁶⁵ Therefore, di-anchored models, where the two branches are linked to the semiconductor, show larger CT and electric field effects with respect to the single-anchored systems thus shifting the CB at a larger extent. An even sustained shift for the CB is expected when considering the entire dye due to an enhancement of the above-mentioned electronic features provoked by the donor group.

As far as the PDOS corresponding to the molecule adsorbed is concerned, special care must be taken since the two identical branches of the dye present different environments, thus leading to non-degenerate LUMO energy levels (see Table 4 and Fig. S7, ESI†). A splitting in the degeneracy in LUMO(1) and LUMO(2) is computed for M1 where the carboxylic acid of the anchoring group binds to the semiconductor surface, whereas near-degeneracy is predicted for M1–M1 due to the almost equivalent anchoring topology. Accidentally, these bands are almost degenerate in energy for BB (see Table 4) but the different width computed for each one unequivocally determines the contribution (LUMO(1)) of the anchored branch (Fig. S7, ESI†). Finally, the energy difference between the two LUMOs is computed to be 0.6 eV (see Table 4), due to the completely different arrangement of the COOH/COO[−] groups on the TiO₂ surface (*vide supra* in the Geometry Analysis). In the same geometrical environments, a slight decrease in energy is predicted for the LUMO band corresponding to the better interacting branch (from −4.0 and −4.1 to −4.2 in M1 and M1–M1, respectively). This trend does not apply to the dissociative bridged bidentate adsorptions due to the different COOH/COO[−] nature in the two branches.

Since the system under study possesses two near-degenerate unoccupied molecular orbitals (LUMO(1) and LUMO(2) in Table 4) in the 2@TiO₂ association, the PDOS corresponding to the better anchored branch LUMO(1) was extracted due to its relevant role on the electron injection into the semiconductor. The PDOS for the LUMO(1) was fitted to a Lorentzian peak function in order to quantify the interaction of the dye with the semiconductor. As shown in Fig. 8, the BB adsorption provides a wider band width (0.184 eV) compared to M1 (0.147 eV). The broadening of the LUMO of the dye is directly related to its interaction with the CB states of the TiO₂. Thus, the BB adsorption would be expected to provide a faster electron injection into the semiconductor.⁵⁷ Likewise, the BB–BB adsorption fit computes a broader LUMO band than M1–M1 thus favoring the electron injection. According to expression (5), we calculate electron-transfer times of 4.5, 3.6, 4.7 and 4.2 fs for M1, BB, M1–M1 and BB–BB, respectively. Obviously, the width of the LUMO band in the singly anchored conformations

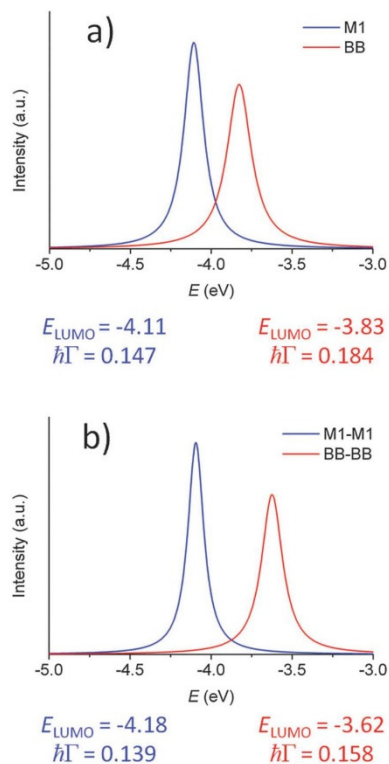


Fig. 8 Lorentzian fitting of the PDOS corresponding to the LUMO of the better anchored branch in the system 2@TiO₂ for the singly (a) and doubly (b) anchored adsorption modes. The corresponding fitting parameters E_{LUMO} (center of the peak) and $\hbar\Gamma$ (full width at half-peak height) of the Lorentzian function according to the expression (4) are displayed.

is wider than in the doubly anchored ones since the branch we are analyzing is better accommodated on the TiO₂ surface in the former. However, notice that this broadening effect is doubled in M1–M1 and BB–BB adsorption modes thus resulting in an enhanced electron injection into the semiconductor.

A rule of thumb for obtaining efficient electron injections in DSCs is to have a dye that provides an energy difference between LUMO and CB of around 0.5 eV. In this way, M1 and especially M1–M1 offer good LUMO–CB gaps (0.7 and 0.5 eV, respectively) for efficient electron injection. Therefore, the doubly anchored M1–M1 structure has two positive effects on the electronic properties: (i) it produces an increase in the CB energy, which should be beneficial for the DSCs performance in terms of an increase of the open circuit voltage, and (ii) it enhances the dye–semiconductor interaction leading to a broadening of the LUMOs and an adequate LUMO–CB gap, which favors electron injection into the semiconductor. It is thus evidenced that multi-anchored systems better fulfill the electronic requirements for DSCs and offer the possibility of modulating the LUMO–CB energy difference in a systematic way depending on the number of anchoring groups.

4. Conclusions

A first-principles investigation has been performed to determine the anchoring mode of an exTTF-based, di-branched, donor-acceptor dye to the anatase (101) surface. Considering two reduced but still reliable dye subsystems, a number of different anchoring environments were designed to determine not only the position of the symmetric and asymmetric CO stretching modes but also other vibrations appearing at similar energies, which may hinder the assignment of the diagnostic COOH/COO⁻ modes. The theoretical characterization of the typical vibrational modes in a dye@TiO₂-like system enabled the firm assignment of the symmetric and asymmetric CO modes in the available experimental FTIR spectrum. The comparison of the $\Delta\nu_{\text{as}}$ values inferred from the experiment and those theoretically obtained for the 1a–1f models suggests that, whereas the dye forms dimers in the powder, it adsorbs on the semiconductor surface most likely in an M1 monodentate coordination.

The reduced system 2, which contains the two anchoring groups present in the entire dye A, was used to perform optimizations of the most relevant COOH/COO⁻ coordinations over a periodic slab of anatase (101). Singly anchored monodentate adsorptions (M1, M2 and MN) are computed lower in energy than the bridging bidentate (BB) adsorption, in line with previous Car–Parrinello PBC results.¹⁷ Doubly anchored monodentate M1–M1 structures provide a gain in stability with respect to the singly anchored analogue. Exploring the potential energy surface by means of a Car–Parrinello molecular dynamics along 3 ps, we arrive at an M1–M1 structure in which the carboxylic anchoring groups are better positioned on the TiO₂ surface and form two stabilizing H-bonds. This structure, being about 14 kcal mol⁻¹ lower in energy than the monodentate M1 structure, corresponds to the most stable adsorption conformation. BB–BB adsorptions have been shown to be much higher in energy than M1–M1 not only because of the total breaking of the π -conjugation between the two acceptor branches but especially for the inadequate match of the carboxylic groups with respect to the anatase (101) topology. Therefore, the doubly anchored, monodentate M1–M1 structure is predicted as the energetically favored adsorption in good agreement with experimental evidences.

The projected density of states calculated for M1, BB, M1–M1 and BB–BB adsorption modes predict that the doubly anchored systems shift the conduction band of TiO₂ to slightly higher energies compared to the singly anchored analogues. This shift allows for an increase in the open-circuit voltage permitting higher conversion efficiencies for DSC purposes. Moreover, an extensive analysis of the PDOS for the different branches in the 2@TiO₂ system allowed the understanding of the inner role for the two nearly degenerate LUMO bands corresponding to the two identical branches of the dye in the total DOS. Although the singly anchored M1 adsorption provides a slightly broader LUMO band due to the better anchoring disposition onto TiO₂, the broadening in M1–M1 is doubled since the two branches are well interacting with the semiconductor surface. Overall, the energetically favored

M1–M1 structure provides appropriate LUMO–CB energy differences with two broad and intense LUMO bands, which favor the electron injection into the semiconductor and explains the good performance experimentally achieved in the device.

Acknowledgements

MP, EM and FDA thank CNR Projects EFOR and RADIUS, and FP7-ENERGY-2010 project 261920 “ESCORT” for financial support. JC and EO thank the MINECO of Spain and European FEDER funds (project CTQ2012-31914) and the Generalitat Valenciana (Prometeo/2012/053). JC acknowledges the Ministry of Education, Culture and Sport (MECS) of Spain for a FPU grant.

References

- 1 A. Hagfeldt, G. Boschloo, L. Sun, L. Kloo and H. Pettersson, *Chem. Rev.*, 2010, **110**, 6595–6663.
- 2 M. K. Nazeeruddin, F. De Angelis, S. Fantacci, A. Selloni, G. Viscardi, P. Liska, S. Ito, B. Takeru and M. Grätzel, *J. Am. Chem. Soc.*, 2005, **127**, 16835–16847.
- 3 B. O'Regan and M. Grätzel, *Nature*, 1991, **353**, 737–740.
- 4 M. K. Nazeeruddin, A. Kay, I. Rodicio, R. Humphry-Baker, E. Mueller, P. Liska, N. Vlachopoulos and M. Grätzel, *J. Am. Chem. Soc.*, 1993, **115**, 6382–6390.
- 5 A. Mishra, M. K. R. Fischer and P. Bäuerle, *Angew. Chem., Int. Ed.*, 2009, **48**, 2474–2499.
- 6 M. Pastore, E. Mosconi, S. Fantacci and F. De Angelis, *Curr. Org. Chem.*, 2012, **9**, 215–232.
- 7 D. P. Hagberg, J.-H. Yum, H. Lee, F. De Angelis, T. Marinado, K. M. Karlsson, R. Humphry-Baker, L. Sun, A. Hagfeldt, M. Grätzel and M. K. Nazeeruddin, *J. Am. Chem. Soc.*, 2008, **130**, 6259–6266.
- 8 H. Choi, C. Baik, S. O. Kang, J. Ko, M.-S. Kang, M. K. Nazeeruddin and M. Grätzel, *Angew. Chem., Int. Ed.*, 2008, **47**, 327–330.
- 9 G. Zhang, Y. Bai, R. Li, D. Shi, S. Wenger, S. M. Zakeeruddin, M. Grätzel and P. Wang, *Energy Environ. Sci.*, 2009, **2**, 92–95.
- 10 J.-H. Yum, E. Baranoff, F. Kessler, T. Moehl, S. Ahmad, T. Bessho, A. Marchioro, E. Ghadiri, J.-E. Moser, C. Yi, M. K. Nazeeruddin and M. Grätzel, *Nat. Commun.*, 2012, **3**, 631.
- 11 E. Mosconi, J.-H. Yum, F. Kessler, C. J. Gómez García, C. Zuccaccia, A. Cinti, M. K. Nazeeruddin, M. Grätzel and F. De Angelis, *J. Am. Chem. Soc.*, 2012, **134**, 19438–19453.
- 12 A. Yella, H.-W. Lee, H. N. Tsao, C. Yi, A. K. Chandiran, M. K. Nazeeruddin, E. W.-G. Diao, C.-Y. Yeh, S. M. Zakeeruddin and M. Grätzel, *Science*, 2011, **334**, 629–634.
- 13 T. Daeneke, T.-H. Kwon, A. B. Holmes, N. W. Duffy, U. Bach and L. Spiccia, *Nat. Chem.*, 2011, **3**, 211–215.
- 14 S. M. Feldt, E. A. Gibson, E. Gabrielsson, L. Sun, G. Boschloo and A. Hagfeldt, *J. Am. Chem. Soc.*, 2010, **132**, 16714–16724.
- 15 M. Pastore and F. De Angelis, *Top. Curr. Chem.*, 2013, DOI: 10.1007/128_2013_468.

- 16 A. Vittadini, A. Selloni, F. P. Rotzinger and M. Grätzel, *J. Phys. Chem. B*, 2000, **104**, 1300–1306.
- 17 C. Anselmi, E. Mosconi, M. Pastore, E. Ronca and F. De Angelis, *Phys. Chem. Chem. Phys.*, 2012, **14**, 15963–15974.
- 18 F. De Angelis, S. Fantacci, A. Selloni, M. K. Nazeeruddin and M. Grätzel, *J. Phys. Chem. C*, 2010, **114**, 6054–6061.
- 19 F. De Angelis, S. Fantacci, A. Selloni, M. Grätzel and M. K. Nazeeruddin, *Nano Lett.*, 2007, **7**, 3189–3195.
- 20 C. Y. Lee, C. She, N. C. Jeong and J. T. Hupp, *Chem. Commun.*, 2010, **46**, 6090–6092.
- 21 R. Sirohi, D. H. Kim, S.-C. Yu and S. H. Lee, *Dyes Pigm.*, 2012, **92**, 1132–1137.
- 22 A. Abbotto, N. Manfredi, C. Marinzi, F. De Angelis, E. Mosconi, J.-H. Yum, Z. Xianxi, M. K. Nazeeruddin and M. Grätzel, *Energy Environ. Sci.*, 2009, **2**, 1094–1101.
- 23 S. Wenger, P.-A. Bouit, Q. Chen, J. Teuscher, D. D. Censo, R. Humphry-Baker, J.-E. Moser, J. L. Delgado, N. Martín, S. M. Zakeeruddin and M. Grätzel, *J. Am. Chem. Soc.*, 2010, **132**, 5164–5169.
- 24 A. S. Batsanov, M. R. Bryce, M. A. Coffin, A. Green, R. E. Hester, J. A. K. Howard, I. K. Lednev, N. Martín, A. J. Moore, J. N. Moore, E. Ortí, L. Sánchez, M. Savirón, P. M. Viruela, R. Viruela and T.-Q. Ye, *Chem.–Eur. J.*, 1998, **4**, 2580–2592.
- 25 P.-A. Bouit, M. Marszalek, R. Humphry-Baker, R. Viruela, E. Ortí, S. M. Zakeeruddin, M. Grätzel, J. L. Delgado and N. Martín, *Chem.–Eur. J.*, 2012, **18**, 11621–11629.
- 26 M. Xu, S. Wenger, H. Bala, D. Shi, R. Li, Y. Zhou, S. M. Zakeeruddin, M. Grätzel and P. Wang, *J. Phys. Chem. C*, 2009, **113**, 2966–2973.
- 27 G. Zhang, H. Bala, Y. Cheng, D. Shi, X. Lv, Q. Yu and P. Wang, *Chem. Commun.*, 2009, 2198–2200.
- 28 M. Planells, L. Pelleja, J. N. Clifford, M. Pastore, F. De Angelis, N. Lopez, S. R. Marder and E. Palomares, *Energy Environ. Sci.*, 2011, **4**, 1820–1829.
- 29 M. Nara, H. Torii and M. Tasumi, *J. Phys. Chem. A*, 1996, **100**, 19812–19817.
- 30 M. Pastore and F. D. Angelis, *ACS Nano*, 2009, **4**, 556–562.
- 31 P. Chen, J. H. Yum, F. D. Angelis, E. Mosconi, S. Fantacci, S.-J. Moon, R. H. Baker, J. Ko, M. K. Nazeeruddin and M. Grätzel, *Nano Lett.*, 2009, **9**, 2487–2492.
- 32 H. Tian, X. Yang, R. Chen, R. Zhang, A. Hagfeldt and L. Sun, *J. Phys. Chem. C*, 2008, **112**, 11023–11033.
- 33 M. Pastore and F. D. Angelis, *J. Phys. Chem. Lett.*, 2011, **2**, 1261–1267.
- 34 F. Nunzi and F. De Angelis, *J. Phys. Chem. C*, 2010, **115**, 2179–2186.
- 35 G. B. Deacon and R. J. Phillips, *Coord. Chem. Rev.*, 1980, **33**, 227–250.
- 36 A. D. Becke, *J. Chem. Phys.*, 1993, **98**, 5648–5652.
- 37 P. J. Stephens, F. J. Devlin, C. F. Chabalowski and M. J. Frisch, *J. Phys. Chem. A*, 1994, **98**, 11623–11627.
- 38 J. Tomasi and M. Persico, *Chem. Rev.*, 1994, **94**, 2027–2094.
- 39 C. S. Cramer and D. G. Thrular, *Solvent Effects and Chemical Reactivity*, Kluwer, Dordrecht, 1996.
- 40 C. A. Jimenez-Hoyos, B. G. Janesko and G. E. Scuseria, *Phys. Chem. Chem. Phys.*, 2008, **10**, 6621–6629.
- 41 J. P. Merrick, D. Moran and L. Radom, *J. Phys. Chem. A*, 2007, **111**, 11683–11700.
- 42 A. P. Scott and L. Radom, *J. Phys. Chem. A*, 1996, **100**, 16502–16513.
- 43 G. Rauhut and P. Pulay, *J. Phys. Chem. A*, 1995, **99**, 3093–3100.
- 44 M. J. Frisch, G. W. Trucks, H. B. Schlegel, G. E. Scuseria, M. A. Robb, J. R. Cheeseman, G. Scalmani, V. Barone, B. Mennucci, G. A. Petersson, H. Nakatsuji, M. Caricato, X. Li, H. P. Hratchian, A. F. Izmaylov, J. Bloino, G. Zheng, J. L. Sonnenberg, M. Hada, M. Ehara, K. Toyota, R. Fukuda, J. Hasegawa, M. Ishida, T. Nakajima, Y. Honda, O. Kitao, H. Nakai, T. Vreven, J. A. Montgomery, J. E. Peralta, F. Ogliaro, M. Bearpark, J. J. Heyd, E. Brothers, K. N. Kudin, V. N. Staroverov, R. Kobayashi, J. Normand, K. Raghavachari, A. Rendell, J. C. Burant, S. S. Iyengar, J. Tomasi, M. Cossi, N. Rega, J. M. Millam, M. Klene, J. E. Knox, J. B. Cross, V. Bakken, C. Adamo, J. Jaramillo, R. Gomperts, R. E. Stratmann, O. Yazyev, A. J. Austin, R. Cammi, C. Pomelli, J. W. Ochterski, R. L. Martin, K. Morokuma, V. G. Zakrzewski, G. A. Voth, P. Salvador, J. J. Dannenberg, S. Dapprich, A. D. Daniels, Ö. Farkas, J. B. Foresman, J. V. Ortiz, J. Cioslowski and D. J. Fox, *Gaussian, Inc.*, Wallingford CT, 2009.
- 45 N. Martsinovich, D. R. Jones and A. Troisi, *J. Phys. Chem. C*, 2010, **114**, 22659–22670.
- 46 J. P. Perdew, K. Burke and M. Ernzerhof, *Phys. Rev. Lett.*, 1996, **77**, 3865–3868.
- 47 R. Car and M. Parrinello, *Phys. Rev. Lett.*, 1985, **55**, 2471–2474.
- 48 P. Giannozzi, S. Baroni, N. Bonini, M. Calandra, R. Car, C. Cavazzoni, D. Ceresoli, G. L. Chiarotti, M. Cococcioni, I. Dabo, A. D. Corso, S. d. Gironcoli, S. Fabris, G. Fratesi, R. Gebauer, U. Gerstmann, C. Gougousis, A. Kokalj, M. Lazzeri, L. Martin-Samos, N. Marzari, F. Mauri, R. Mazzarello, S. Paolini, A. Pasquarello, L. Paulatto, C. Sbraccia, S. Scandolo, G. Sclauzero, A. P. Seitsonen, A. Smogunov, P. Umari and R. M. Wentzcovitch, *J. Phys.: Condens. Matter*, 2009, **21**, 395502.
- 49 J. P. Muscat and D. M. Newns, *Prog. Surf. Sci.*, 1978, **9**, 1–43.
- 50 P. Persson, M. J. Lundqvist, R. Ernstorfer, W. A. Goddard and F. Willig, *J. Chem. Theory Comput.*, 2006, **2**, 441–451.
- 51 A. D. Khalaji, K. Fejfarova and M. Dusek, *Acta Crystallogr., Sect. E: Struct. Rep. Online*, 2011, **67**, o3508–o3509.
- 52 J. M. Azpiroz, E. Mosconi and F. D. Angelis, *J. Phys. Chem. C*, 2011, **115**, 25219–25226.
- 53 P. Persson, R. Bergström and S. Lunell, *J. Phys. Chem. B*, 2000, **104**, 10348–10351.
- 54 S. Manzhos, H. Segawa and K. Yamashita, *Phys. Chem. Chem. Phys.*, 2012, **14**, 1749–1755.
- 55 F. Labat and C. Adamo, *J. Phys. Chem. C*, 2007, **111**, 15034–15042.
- 56 F. De Angelis, *Chem. Phys. Lett.*, 2010, **493**, 323–327.
- 57 N. Martsinovich and A. Troisi, *J. Phys. Chem. C*, 2011, **115**, 11781–11792.

- 58 D. Rocca, R. Gebauer, F. De Angelis, M. K. Nazeeruddin and S. Baroni, *Chem. Phys. Lett.*, 2009, **475**, 49–53.
- 59 F. De Angelis, S. Fantacci, E. Mosconi, M. K. Nazeeruddin and M. Grätzel, *J. Phys. Chem. C*, 2011, **115**, 8825–8831.
- 60 F. Schiffrmann, J. VandeVondele, J. r. Hutter, R. Wirz, A. Urakawa and A. Baiker, *J. Phys. Chem. C*, 2010, **114**, 8398–8404.
- 61 F. De Angelis, S. Fantacci, A. Selloni, M. K. Nazeeruddin and M. Grätzel, *J. Am. Chem. Soc.*, 2007, **129**, 14156–14157.
- 62 F. Ambrosio, N. Martsinovich and A. Troisi, *J. Phys. Chem. Lett.*, 2012, **3**, 1531–1535.
- 63 K. Srinivas, K. Yesudas, K. Bhanuprakash, V. J. Rao and L. Giribabu, *J. Phys. Chem. C*, 2009, **113**, 20117–20126.
- 64 E. Mosconi, A. Selloni and F. De Angelis, *J. Phys. Chem. C*, 2012, **116**, 5932–5940.
- 65 E. Ronca, M. Pastore, L. Belpassi, F. Tarantelli and F. De Angelis, *Energy Environ. Sci.*, 2013, **6**, 183–193.
- 66 M. Landmann, E. Rauls and W. G. Schmidt, *J. Phys.: Condens. Matter*, 2012, **24**, 195503.
- 67 N. Martsinovich and A. Troisi, *Energy Environ. Sci.*, 2011, **4**, 4473–4495.
- 68 J. P. Perdew, *Int. J. Quantum Chem.*, 1985, **28**, 497–523.
- 69 S. Rühle, M. Greenshtein, S. G. Chen, A. Merson, H. Pizem, C. S. Sukenik, D. Cahen and A. Zaban, *J. Phys. Chem. B*, 2005, **109**, 18907–18913.



Chapter 5. Supramolecular donor–acceptor complexes

5.1. Introduction

The construction of artificial photoactive devices capable of mimicking the photosynthetic process by transforming sunlight into chemical potential is one of the most pursued objectives in the quest for new sources of energy.^[136] For this purpose, chemists have developed a wide variety of donor–acceptor systems, in which photon energy is used to produce a photoinduced electron transfer from the donor to the acceptor.^[137] Among them, porphyrins and fullerenes (Figure 25a,b) have extensively been combined due to their respective notable electron-rich and electron-withdrawing properties.^[138] Fullerenes have been widely employed in molecular switches, receptors, photoconductors, photoactive dyads, and as *n*-type semiconducting materials in organic solar cells.^[139] The excellent electron-accepting properties of fullerenes and their derivatives together with their low reorganization energy make them good candidates as building block systems for the light-to-power conversion. On the other hand, porphyrin dyes have been extensively incorporated in prototype dye-sensitized solar cells,^[140] reaching power conversion efficiencies as high as 13%,^[141] exceeding the performance of state-of-the-art ruthenium-based chromophores.

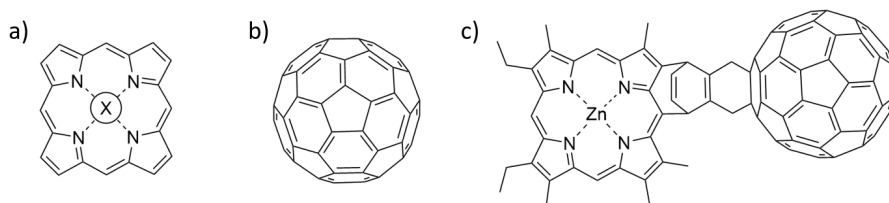


Figure 25. a) Simplest porphyrin chemical structure; X may refer either to a metal atom or two H atoms. b) Chemical structure of the Buckminsterfullerene C₆₀. c) The first reported porphyrin–fullerene dyad.^[142]

The initial report of the synthesis and photophysical study of a fullerene linked to a porphyrin pigment was accomplished in 1994 by Liddell and coworkers (Figure 25c).^[142] Thenceforth, a large list of porphyrin–fullerene push–pull chromophores have been designed either through the covalent chemistry or the chemistry governed by the noncovalent interactions—the supramolecular chemistry—.^[143] In contrast to the already well-known fundamentals of covalent donor–acceptor dyads, deep knowledge is still required in the versatile supramolecular chemistry counterpart. For example, although a variety of supramolecular ensembles involving both fullerene and porphyrin electroactive moieties interacting by π - π forces have been reported,^[30, 144] the nature of this affinity, which challenges the traditional belief that a curved guest (fullerene) requires curved hosts for effective complexation, is not yet fully understood (Figure 26).^[139] Rational comprehension of the supramolecular forces governing the assembly of fullerenes and porphyrins would enable further development and application of these building blocks in supramolecular chemistry and advanced materials science.

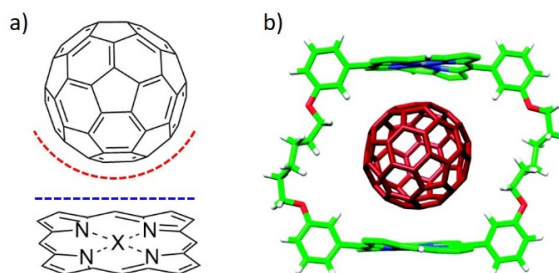


Figure 26. a) Convex–planar mismatch between the fullerene and porphyrin supramolecular recognition. b) X-ray crystal structure of a bis-porphyrin macrocycle•C₆₀ inclusion complex, showing that the distorted structure of the porphyrins is adopted to maximize interactions with C₆₀.^[145]

In contrast to fullerenes (or buckyballs in general), bowl-shaped polycyclic aromatic hydrocarbons (buckybowls) represent a novel and fascinating less-known class of compounds that can serve as models for the investigation of their analogous carbon nanoforms. Figure 27a shows the chemical structure of the simplest buckybowl: the well-known corannulene. The development of practical, gram-scale synthetic methods has allowed for systematic studies of the buckybowls chemistry with the added value of their synthetic availability in pure form with a well-defined molecular structure.^[146] The coordination of metal cations by fullerene fragments has been thoroughly studied (Figure 27b),^[146b] and they have also been used to construct receptors for fullerenes owing to their shape complementarity (e.g., the so-called buckycatcher shown in Figure 27c,d).^[147] The association of buckybowls by other organic hosts has, however, not been investigated thus far. A comprehensive elucidation on how these carbon-based buckybowls self-assemble with complementary electroactive organic compounds would undoubtedly help advance in the understanding of the noncovalent forces governing the supramolecular chemistry of carbon nanoforms. Additionally, the supramolecular orientation might give deep insight into the fundamental aspects of the electron-transfer processes occurring in these novel and unexplored donor–acceptor systems.

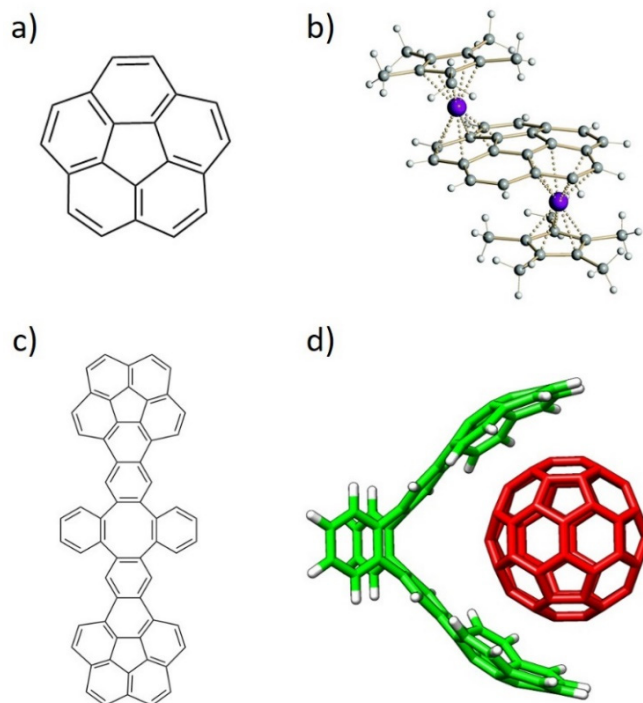


Figure 27. a) Chemical structure of one of the most used fullerene fragments: the corannulene. b) $[(\text{Cp}^*\text{Ru})_2(\mu_2\text{-}\eta^6,\eta^6\text{-C}_{20}\text{H}_{10})]^{2+}$: an example of a coordination complex involving the corannulene moiety. c) Chemical structure of the buckycatcher incorporating two corannulene units. d) 3D representation of the buckycatcher•C₆₀ supramolecular complex.

In this Chapter, a series of monotopic and ditopic porphyrin-based receptors are theoretically investigated to help rationalize the origin of the supramolecular recognition of these novel hosts to bind a fullerene derivative guest in an atypical convex–planar mismatch. In addition, the electron-donor truxTTF derivative has been used as host in the supramolecular recognition of fullerene fragments of increasing size for the generation of donor–acceptor assemblies that undergo charge-transfer phenomena upon photoexcitation. The nature of the forces

giving rise to the association and the origin of the charge-transfer process upon light absorption are disentangled by means of first-principles calculations.

5.2. Results and discussion

5.2.1. Metal-atom effect: monotopic porphyrin•C₆₀ assemblies

To shed light on the nature and strength of the noncovalent interactions governing the supramolecular assembly of fullerene derivatives with metal-substituted porphyrins, we thoroughly investigated a series of novel cup-and-ball metalloporphyrin–fullerene conjugates in collaboration with the experimental groups of Profs. Nazario Martín and Jean-François Nierengarten. Target complexes **2-M•1** were obtained by mixing the corresponding porphyrin–crown ether conjugates (**2-M**; **M** = 2H, Co, Ni, Cu or Zn) and the methano[60]fullerene derivative **1**^[148] (Figure 28). Note that chemical nomenclature slightly differs from the original work to simplify the reading. The complexation was first evidenced by experimentalists through ¹H-NMR spectroscopy, and the measurement of the binding constant of **2-M•1** was undertaken by monitoring the changes in the UV–Vis absorption spectra. The logarithmic binding constants (log *K*_a) for porphyrins **2-M** with the methanofullerene derivative **1** at 25 °C in dichloromethane were: 5.5, 6.3, 5.9, 6.3 and 6.9 for **2-2H•1**, **2-Co•1**, **2-Ni•1**, **2-Cu•1** and **2-Zn•1**, respectively.

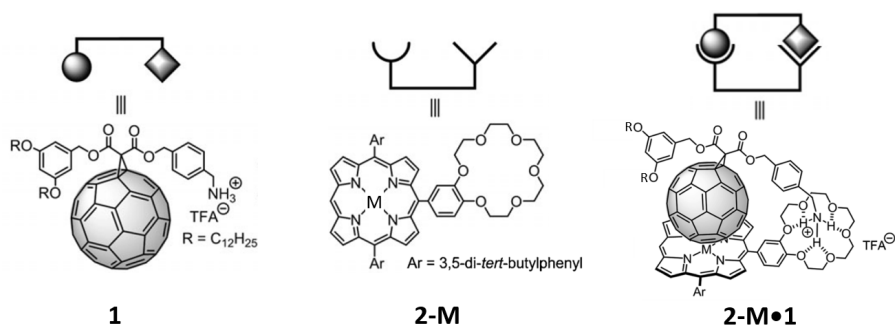


Figure 28. Chemical structure of the methano[60]fullerene guest **1** (left), the metalloporphyrin host **2-M** (centre), and the host–guest supramolecular complex **2-M•1** (right). **M** refers to either 2H, Co, Ni, Cu or Zn.

In order to better understand the nature of the different interactions governing the associates and gain insight into the experimental ordering found for K_a , a comprehensive theoretical investigation of these supramolecular complexes was carried out in a multi-level approach. Geometry optimizations were initially performed at the semiempirical PM7 level and showed that, after full geometry relaxation, the ammonium group of the methanofullerene interacts with the crown ether of the porphyrin by H-bond formation (Figure 29). Otherwise, the fullerene ball recognizes the centre of the porphyrin system interacting by noncovalent forces. Subsequent DFT reoptimizations at the B97-D/6-31G* level of theory led to the supramolecular parameters summarised in Table 2.

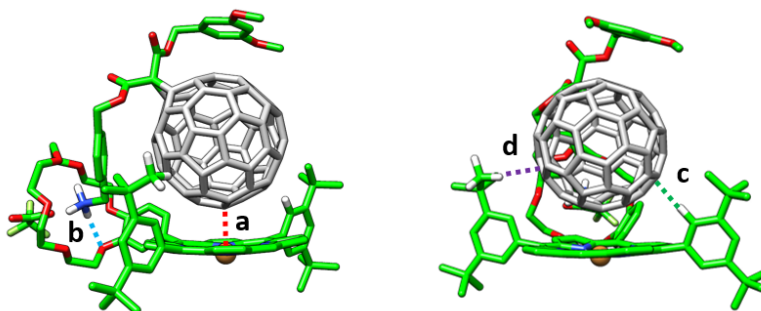


Figure 29. Minimum-energy structure calculated for the **2-Cu•1** complex at the PM7 level. Side (left) and front (right) views are displayed. The different types of intermolecular contacts are denoted with labels a–d. Only relevant hydrogen atoms are displayed for clarity.

Table 2. DFT-optimized (B97-D/6-31G*) intermolecular distances (a–d, in Å) characterizing the **2-M•1** associates, and binding energies (E_{bind} , in kcal mol⁻¹) computed at the PBE0-D3/cc-pVTZ level.^a

Complex	M–C ₆₀ (a)	NH···O (b)	CH···C ₆₀ (c)	CH···C ₆₀ (d)	E_{bind}
2-2H•1	2.756	1.848	2.679	2.577	–92.4
2-Co•1	2.119	1.850	2.642	2.573	–93.8
2-Ni•1	2.793	1.842	2.623	2.610	–88.7
2-Cu•1	2.754	1.846	2.662	2.599	–91.3
2-Zn•1	2.701	1.845	2.689	2.591	–92.8

^a See Figure 29 for the definition of the geometric parameters. For further details, the reader is referred to the original work (**Publication 4** below).

The main interactions governing the supramolecular association are represented by the M–C₆₀ (a) and NH···O (b) distances given in Table 2 (see Figure 29 for labelling). In addition, CH···π dispersion interactions (c and d) between the *tert*-butyl substituted benzene rings of the porphyrin and the π-cloud of the fullerene also contribute to the supramolecular complexation.

The association or binding energy (E_{bind}) for the **2-M•1** associates, defined as the energy difference between the complex and its constituting monomers at their respective minimum-energy geometries, was calculated at the PBE0-D3/cc-pVTZ level of theory using the B97-D/6-31G*-optimized geometries (Table 2). Passing from Ni to Zn, E_{bind} rises from -88.7 to -92.8 kcal mol $^{-1}$ due to the more stabilizing M–C $_{60}$ interaction that takes place in moving to electron-richer metal atoms. The stabilization in the formation of the nonmetalated **2-2H•1** complex amounts to -92.4 kcal mol $^{-1}$, and the largest association energy is computed for **2-Co•1** (-93.8 kcal mol $^{-1}$). Theoretical calculations show that the noncovalent interaction between the fullerene ball and the phenyl-substituted porphyrin amounts to -22.5 kcal mol $^{-1}$, and the presence of the *tert*-butyl groups at the meta position of the phenyl rings (interaction d) produces an additional stabilization of ~ 4 kcal mol $^{-1}$ (-26.3 kcal mol $^{-1}$ in total), in agreement with previous theoretical studies.^[149] The ammonium–crown ether NH \cdots O contacts have been found to be the main stabilizing driving force, with an interaction energy of -64.9 kcal mol $^{-1}$, which is three times the stabilization of the porphyrin–C $_{60}$ interaction.

Keeping in mind that C $_{60}$ interacts with the porphyrin moiety mainly through one electron-rich [6,6] double bond,^[150] we modelled a simplified system (**MP•C $_2$ H $_4$**), in which the pristine porphyrin (**MP**) interacts with a molecule of ethylene (Figure 30). This reduced model allows performing more accurate calculations to better understand the relative stabilization of the different associates when varying the metal in the porphyrin. A clear correlation between the calculated binding energies and metal–ethylene distances is obtained: the shorter the distance along the series **NiP•C $_2$ H $_4$** (3.18 Å) > **CuP•C $_2$ H $_4$** (3.00 Å) > **ZnP•C $_2$ H $_4$** (2.75 Å) > **CoP•C $_2$ H $_4$**

(2.62 Å), the larger the stabilization of the complex (Table 3). The net charge calculated for the metal atom increases in going from **CoP**·**C₂H₄** (+0.720 e) to **ZnP**·**C₂H₄** (+1.223 e) —Table 3— and, in a first approach, this can be related with the stabilizing electrostatic interaction between the porphyrin and the fullerene guest.

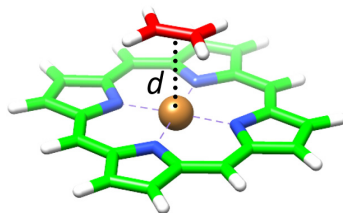


Figure 30. Porphyrin·**C₂H₄** model (**MP**·**C₂H₄**) used to understand the nature of the interaction between the porphyrin host **2** and the fullerene guest **1**.

Table 3. Binding energy (kcal mol⁻¹), metal–ethylene distance *d* (Å), and natural population analysis (NPA) charge of the porphyrin central atom (M = 2H, Co, Ni, Cu, Zn) calculated at the PBE0-D3/cc-pVTZ level of theory for the simplified porphyrin–ethylene associates.

Complex	E_{bind}	<i>d</i>	M charge
2HP · C₂H₄	−4.636	2.986	+0.942
CoP · C₂H₄	−8.534	2.619	+0.720
NiP · C₂H₄	−4.530	3.177	+0.733
CuP · C₂H₄	−5.965	2.997	+1.006
ZnP · C₂H₄	−8.047	2.749	+1.223

Symmetry-adapted perturbation theory (SAPT) calculations based on the Hartree–Fock wavefunction were performed for **2HP**·**C₂H₄**, **NiP**·**C₂H₄** and **ZnP**·**C₂H₄** to decompose the total binding energy into electrostatic, exchange, induction and dispersion energy components (Table 4). A stabilization in the electrostatic term of more than 10 kcal mol⁻¹ is

predicted in passing from **NiP·C₂H₄** to **ZnP·C₂H₄**, whereas the exchange interaction is computed positive, and much larger for **ZnP·C₂H₄** than for **2HP·C₂H₄** and **NiP·C₂H₄**. The induction term is meant to decay with the distance between the two interacting moieties as R^{-n} where $n = 2-4$, and thus it is computed non-negligible only in the case of the best interacting **ZnP·C₂H₄** (Table 4). Finally, the dispersion energy is predicted to be the largest stabilizing contribution in **2HP·C₂H₄** and **NiP·C₂H₄**, and it also largely stabilizes **ZnP·C₂H₄** in more than 10 kcal mol⁻¹. Theoretical calculations therefore suggest that the energy term that mainly contributes to the stabilization of the **2HP·C₂H₄** assembly is the dispersion component, whereas the electrostatic contribution acquires a major role in the metal-based porphyrin complexes, especially in **ZnP·C₂H₄**, for which M–ethylene distances are computed shorter and the metal bears a larger positive charge.

Table 4. Energy decomposition (in kcal mol⁻¹) calculated at the SAPT0/def2-TZVP level for closed-shell porphyrin-ethylene systems with M = 2H, Ni, Zn.

	2HP·C₂H₄	NiP·C₂H₄	ZnP·C₂H₄
electrostatic	-2.794	-5.277	-16.212
exchange	7.046	8.605	22.101
induction	-0.690	-0.728	-3.900
dispersion	-7.033	-7.055	-10.521
TOTAL	-3.472	-4.455	-8.532

5.2.2. Cooperativity in ditopic porphyrin•C₆₀ complexes

Whereas the supramolecular chemistry involving porphyrin and fullerene has been extensively explored through the generation of associates involving porphyrin tweezers and cages,^[151] metal–ligand

bonds,^[152] hydrogen bonds,^[153] electrostatic interactions,^[154] mechanical bonds,^[155] or a combination of several of these interactions,^[156] supramolecular arrays involving conjugated multiporphyrin systems are, however, scarce in the literature. Taking advantage of the knowledge gained in the work described above on the monotopic metalloporphyrin–fullerene conjugates, we have undertaken a collaborative study for the complexation of two analogous ditopic porphyrin receptors: *meso-meso* **3** and tape **4** (Figure 31), with the methano[60]fullerene compound **1** (Figure 28). A 1:2 stoichiometry was foreseen for both **3** and **4** when coupled to **1** based on the design of the host molecules, which was further corroborated by ElectroSpray Ionization (ESI) Mass Spectroscopy experiments.

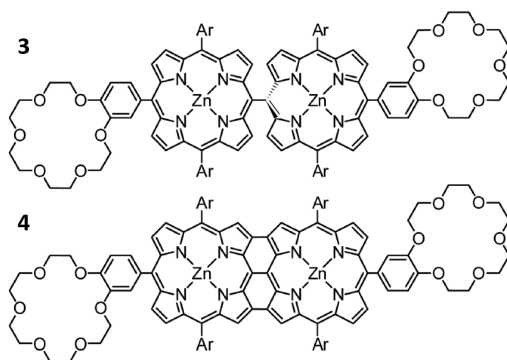


Figure 31. Chemical structure of the novel ditopic porphyrin-based hosts **3** and **4**.

Theoretical calculations were carried out to shed light into the nature and strength of the interactions controlling the different association processes taking place in the formation of the supramolecular assemblies, with special attention to the negative cooperative effects experimentally evidenced for these systems (see the original **Publication 5** below for further details). Minimum-energy geometries

were computed for supramolecular complexes **3•1** and **3•1₂** at the B97-D3/(6-31G**+LANL2DZ) level of theory (Figure 32). In analogy to the monotopic porphyrin supramolecular arrangements discussed in the previous Section, compound **1** in **3•1** interacts with the crown ether through the positively-charged ammonium group, forming three NH...O(ether) hydrogen-bond interactions in the 1.83–2.00 Å range. Additional short H...C contacts between the peripheral *tert*-butyl-substituted phenyl rings and C₆₀ are computed in the range of 2.5–3.2 Å, which add approximately 1 kcal mol⁻¹ of stabilization per each interaction. Importantly, the vicinal porphyrin, linked to the porphyrin that interacts with **1**, approaches the fullerene fragment and gives rise to additional interactions: short H...C contacts in the 2.7–3.2 Å range and a weak π–π interaction between the peripheral benzene ring and the fullerene.

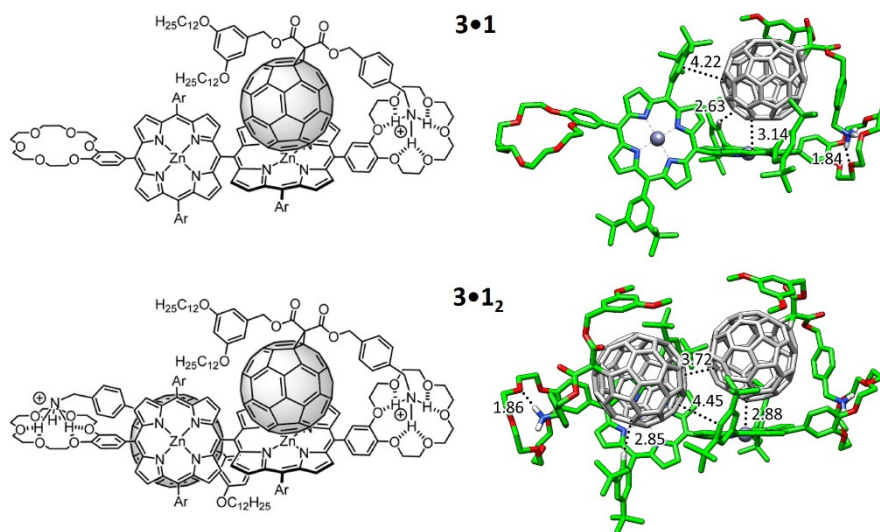


Figure 32. Chemical structure (left) and minimum-energy geometry calculated at the B97-D3/(6-31G**+LANL2DZ) level (right) of the supramolecular assembly of ditopic host **3** with one and two molecules of guest **1**.

Moving to **3•1₂**, the second molecule of **1** enters the empty porphyrin core and defines similar interactions to those described for **3•1**. The minimum-energy geometry shows that the two fullerenes tend to approximate each other in order to stabilize the resulting complex (Figure 32), with close C...C contacts between the two C₆₀ of 3.7 Å. This is at the expense of distortions out from orthogonality between the two porphyrin moieties. The peripheral di-*tert*-butylphenyl groups placed on the vicinal porphyrin moieties play an active role in the stabilization of the complex with short H...C(C₆₀) contacts around 2.8 Å and π–π interactions at 4.4 Å.

The association between porphyrin tape **4** and **1** (Figure 33) follows the same pattern as previously described for **3•1**. Here, the introduction of the second fullerene-based guest **1** into the **4•1** complex can be achieved in two different ways: the two fullerene balls standing in the same side in a *syn* disposition (**4•1₂-syn**), or the two balls located in opposite sides with respect to the plane generated by the porphyrin tape dimer in an *anti* disposition (**4•1₂-anti**) (Figure 33). By comparing the *anti* with the *syn* complex, an important π–π stabilization arises for the latter due to the fullerene–fullerene proximity. Experiments showed that the complexation of the first molecule of **1** in porphyrin hosts **3** and **4** leads to a complex where it is more difficult to complex a second equivalent of **1** (negative cooperativity). The relevant π–π contacts between the buckyballs calculated for **4•1₂-syn** therefore confers an additional stabilizing interaction that would reduce the negative cooperativity with respect to **3•1₂**, as experimentally evidenced for the tape assembly.

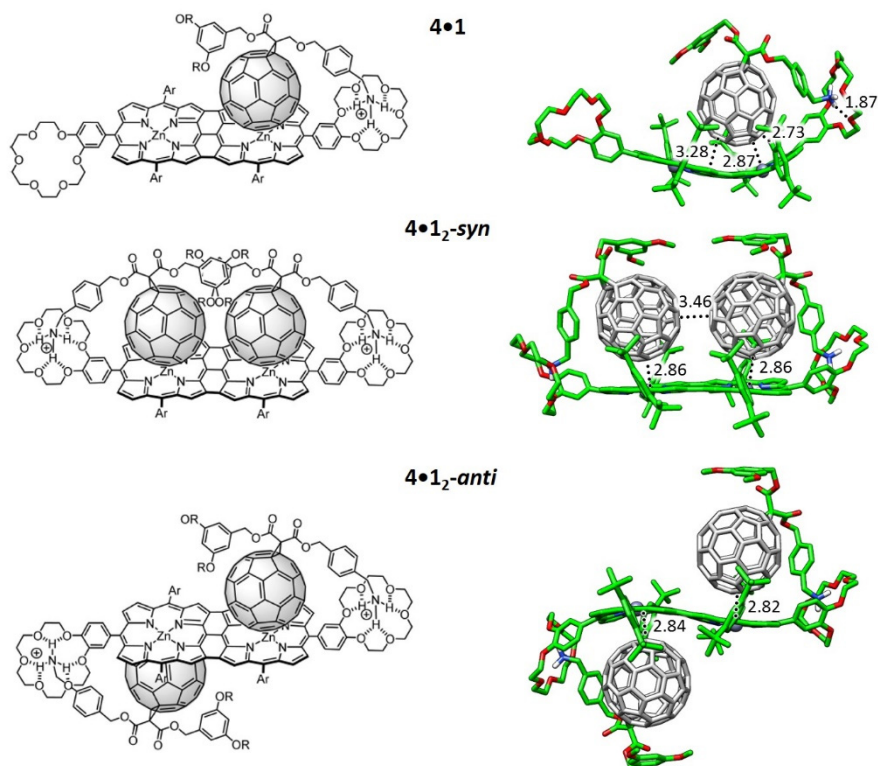


Figure 33. Chemical structure (left) and minimum-energy geometry calculated at the B97-D3/(6-31G**+LANL2DZ) level (right) of the supramolecular assembly of ditopic host **4** with one and two molecules of guest **1**.

Single-point energy B97-D3 calculations were performed on the optimized geometries by using the more extended cc-pVTZ+LANL2DZ basis set to estimate the binding energy (E_{bind}) for all the supramolecular complexes (Table 5). The association of one molecule of **1** by the *meso-meso* porphyrin dimer **3** leads to a large net stabilization of -108.19 kcal mol $^{-1}$, rising especially from the NH \cdots O(ether) contacts and the porphyrin core–C $_{60}$ interaction. Upon inclusion of the second molecule of **1**, E_{bind} is approximately doubled, reaching a value of -211.05 kcal mol $^{-1}$ for **3•1₂**. The theoretical values predicted for E_{bind} (Table 5) indicate that

the incorporation of the first guest molecule leads to a more stable complex for **3** than for **4**, and suggest that the entrance of the second molecule of **1** is relatively more favoured for **4** than for **3** (binding energy differences per **1** unit between 1:2 and 1:1 complexes of +5.33 and –3.4 kcal mol⁻¹ for **3** and **4**, respectively; Table 5). These trends are in accord with the higher association constant K_1 obtained for *meso-meso* porphyrin **3** ($\log K_1 = 8.7$) compared to tape porphyrin **4** ($\log K_1 = 6.8$), and with the smaller decrease it experiences for **4** in passing from the 1:1 to the 1:2 stoichiometry ($\log K_2 = 5.4$ for both **3•1₂** and **4•1₂**).

Table 5. Binding energies computed at the B97-D3/(cc-pVTZ+LANL2DZ) level for the host–guest supramolecular associates with stoichiometry 1:1 and 1:2.

Complex	E_{bind} (kcal mol ⁻¹)
3•1	–108.19
3•1₂	–211.05
4•1	–98.40
4•1_{2-anti}	–195.40
4•1_{2-syn}	–200.20

To help rationalize the experimental values of the association constants for both the 1:1 and 1:2 complexes, net electronic charges were calculated at the B97-D3/(6-31G**+LANL2DZ) level for **3•1** and **4•1** using the Natural Population Analysis (NPA). Upon formation of complexes **3•1** and **4•1**, the electron-donor porphyrin dimer transfers 0.19e and 0.26e to the fullerene-based acceptor, respectively. In **3•1**, the porphyrin moiety interacting with the C₆₀ ball accumulates a positive charge of +0.16e, whereas the vicinal empty porphyrin bears a residual positive charge of only +0.03e. Moving to **4•1**, the C₆₀-interacting porphyrin moiety bears a smaller positive charge of +0.11e compared to the empty

porphyrin fragment (+0.15e). The efficient π -conjugation between the two porphyrin moieties in tape **4** explains the charge transfer from one fragment to the other. Theoretical calculations therefore predict a notable decrease in the electron density for both *meso-meso* and tape porphyrin dimers in the ground state upon complexation of the first acceptor molecule of **1**. The decrease of electronic density disfavours the entrance of the second guest molecule, and contributes to the remarkable change of the association constant ($\log K_a$), from 8.7 to 5.4 in **3•1₂** and from 6.8 to 5.4 in **4•1₂**, when the second molecule of **1** is included to form the stoichiometric 1:2 complex. For complex **4•1₂**, the stabilizing interaction between the C₆₀ units found for the more stable *syn* disposition partially compensates for the negative effect provoked by the lowered electronic density, inducing a reduction of the negative cooperativity as evidenced by experiments.

During the research carried out along the PhD period, the supramolecular assembly of fullerene C₆₀ with crown ether-decorated exTTF^[157] and bis-exTTF-macrocyclic^[158] receptors has also been theoretically inspected. The latter were already found to bind efficiently carbon-based nanotubes.^[159] A protocol to elucidate binding constants between small-molecule derivatives and insoluble carbon nanotubes has also been developed through pyrene-based hosts in a collaborative investigation with the group of Prof. Emilio M. Pérez.^[160] The reader is referred to the original publications for further information on these studies (articles 17–18 in the List of publications).

5.2.3. The truxTTF•hemifullerene supramolecular complex

In contrast to the ubiquitous electron-acceptor buckminsterfullerene C_{60} , other kind of carbon nanoforms have gained an increasing attention in the last decade. Based on the alternation of 5- and 6-member fused rings, fullerene fragments (also known as buckybowls) have attracted the interest of the scientific community as models of their parent buckyball, nanotube and graphene materials. Buckybowls have the added value of a richer chemistry and their pure synthetic availability with a well-defined molecular structure (e.g., see Figure 34a for the chemical structure of the hemifullerene $C_{30}H_{12}$).^[161]

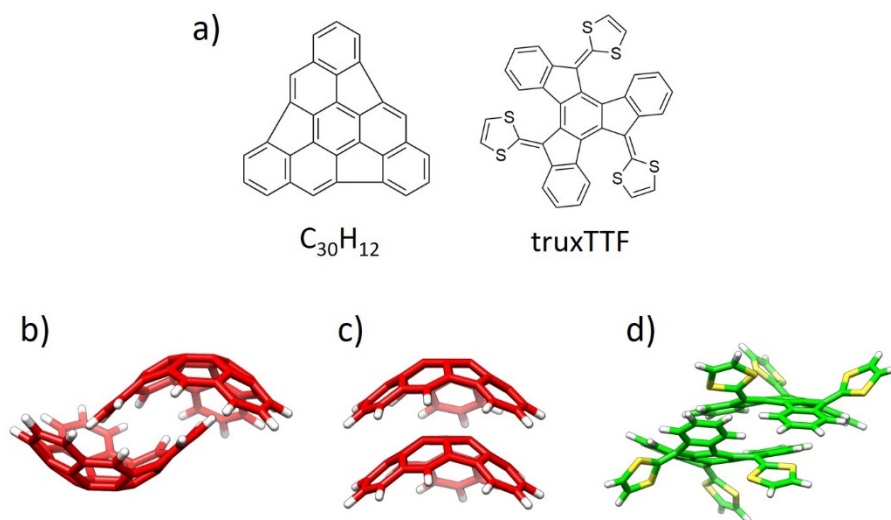


Figure 34. a) Chemical structure of hemifullerene $C_{30}H_{12}$ and truxTTF. b,c) Structure of the dimers formed by $C_{30}H_{12}$ (carbon atoms in red) in its trigonal and orthorhombic crystal polymorphs, respectively. d) Structure of the dimer formed by truxTTF in its crystal packing (carbons in green, sulphurs in yellow).

Among the different carbon-based nanofragments, the truxene structure has attracted a great deal of interest due to its exceptional solubility, high thermal stability and ease to be modified.^[162] Over the last years, and thanks to the advances in the synthesis of truxene derivatives, the scope of applications of this attractive heptacyclic polyarene building block, initially limited to synthesis and photoluminescence, has been extended to organic electronics.^[163]

Particularly interesting is the modification of the truxene core through the incorporation of three dithiole ring units in the generation of the so-called truxene-TTF (truxTTF) compound (Figure 34a).^[164] In analogy to the extended TTF derivative (exTTF), the truxTTF structure is distorted out of planarity due to short dithiole–benzene contacts, giving rise to a double-concave unit that presents the structural requirements as an electron-donor host for the recognition of fullerene derivatives.^[164-165] Considering the ability of the truxTTF to associate fullerenes promoted by the concave–convex complementarity together with its appealing electron-donating character, we reasoned that this electron-rich moiety should also be able to bind small fullerene fragments, such as hemifullerene C₃₀H₁₂, forming heteromolecular donor–acceptor bowl-to-bowl complexes. To explore this possibility, we carried out density functional theory (DFT) calculations on four different supramolecular truxTTF•C₃₀H₁₂ models, which were rationally constructed based on the crystallographic information on both C₃₀H₁₂^[166] and truxTTF^[164] (Figure 34b–d).

Figure 35 displays the minimum-energy structures (**A1–4**) computed for the truxTTF•C₃₀H₁₂ heterodimer at the revPBE0-D3/cc-pVTZ level. In structures **A1** and **A2**, the convex surface of the C₃₀H₁₂ bowl perfectly

matches the two concave cavities of the truxTTF host; that is, either through the cavity formed by the carbon backbone (structure **A1**) or through the cavity formed by the central benzene ring and the three dithiole rings (structure **A2**). Both structures can thus be seen as bowl-in-bowl arrangements where π - π interactions are maximized. The concave cavities of truxTTF and $C_{30}H_{12}$ can also interact, giving rise to heterodimers in which either a benzene or a dithiole ring of the truxTTF molecule is placed inside the concave cavity of the hemifullerene bowl (structures **A3** and **A4**, respectively).

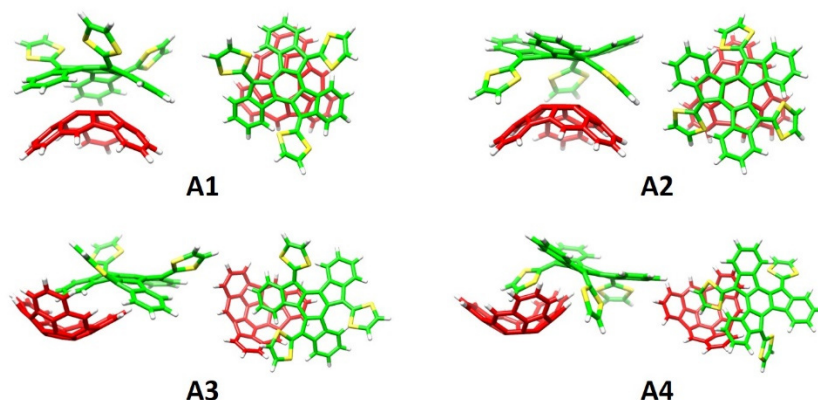


Figure 35. Minimum-energy structures (**A1–4**) computed for the truxTTF• $C_{30}H_{12}$ heterodimer at the revPBE0-D3/cc-pVTZ level.

To assess the strength of the interaction between the truxTTF and $C_{30}H_{12}$ bowls, association energies of the previously-optimized heterodimers were also calculated at the revPBE0-D3/cc-pVTZ level. The four supramolecular structures **A1–4** exhibit significant gas-phase association energies, ranging from -21.0 and -19.4 kcal mol $^{-1}$ for **A1** and **A2**, respectively, to -25.2 and -28.5 kcal mol $^{-1}$ for **A3** and **A4**, respectively. Recent high-level theoretical calculations at the DLPNO-CCSD(T) level of

accuracy carried out in our group confirm the stabilization ordering obtained at the DFT-D3 level for the four possible arrangements.^[167]

Encouraged by the theoretical results, the group of Prof. Nazario Martín carried out a titration of truxTTF with C₃₀H₁₂ in chloroform at room temperature. Experimentalists observed a decrease in the intensity of the truxTTF absorption at $\lambda = 450$ nm, accompanied by the increase of a broad band in the 500–600 nm region (Figure 36a). UV–Vis experiments showed an association constant of $\log K_a = 3.6 \pm 0.3$ for the truxTTF•C₃₀H₁₂ supramolecular complex in chloroform at room temperature.

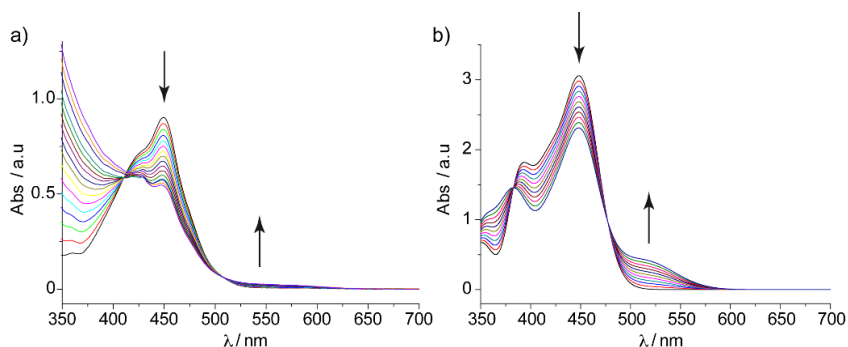


Figure 36. a) Experimental UV–Vis spectra, as obtained during the titration of truxTTF (1.7×10^{-4} M) with C₃₀H₁₂ (0.8×10^{-3} M) in CHCl₃ at room temperature. b) TDDFT simulation of the absorption spectrum of truxTTF as the ratio of truxTTF•C₃₀H₁₂ increases from 0 to 100 % (B3LYP/cc-pVDZ calculations including CHCl₃ as solvent for the structure **A4**).

To gain insight into the electronic nature of the absorption bands observed experimentally, and their evolution during the titration experiment, the electronic structure and the lowest-lying singlet excited states (S_n) of the truxTTF•C₃₀H₁₂ heterodimer and the constituting monomers were computed using the time-dependent DFT (TDDFT)

approach, taking into account solvent effects. Only the results obtained for the most stable structure of $\text{truxTTF}\cdot\text{C}_{30}\text{H}_{12}$ (**A4**) are discussed.

TDDFT calculations predict the first two excited states S_1 and S_2 at 537 nm (2.31 eV) and 516 nm (2.40 eV), respectively, above the ground state S_0 . The $S_0 \rightarrow S_1$ and $S_0 \rightarrow S_2$ electronic transitions have moderate oscillator strengths (f) of 0.036 and 0.046, respectively, and are mainly described by one-electron promotions from the HOMO to the LUMO and LUMO+1, respectively. These transitions therefore imply a charge transfer from the electron-donor truxTTF , where the HOMO is located, to the electron-acceptor $\text{C}_{30}\text{H}_{12}$, where the LUMO and LUMO+1 are spread (Figure 37), and are the major contribution to the band experimentally recorded in the 500–600 nm range. Calculations predict several transitions (S_9 – S_{11}) in the 450 nm region giving rise to the truxTTF centred band originated from HOMO, HOMO–1 \rightarrow LUMO+3, LUMO+4 one-electron excitations. A TDDFT simulation of the experimental titration was performed by increasing the % of the $\text{truxTTF}\cdot\text{C}_{30}\text{H}_{12}$ absorption spectrum with respect to that of the isolated truxTTF compound (see Figure 36). The theoretical simulation is in sound agreement with the experimental evolution of the absorption spectra, therefore supporting the formation of the supramolecular donor–acceptor $\text{truxTTF}\cdot\text{C}_{30}\text{H}_{12}$ heterodimer and the appearance of a low-lying charge-transfer band in the region of 500–550 nm.

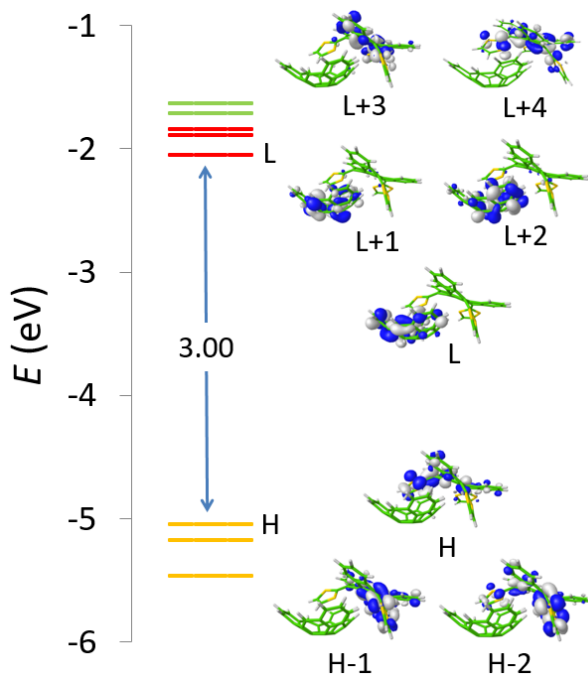


Figure 37. Isovalue contours (± 0.03 a.u.) and energies calculated for the HOMOs and LUMOs of structure **A4** at the revPBE0-D3/cc-pVTZ level. H and L denote HOMO and LUMO, respectively.

The formation of the charge-separated $\text{truxTTF}^+\cdot\text{C}_{30}\text{H}_{12}^-$ species upon photoexcitation was further confirmed by femtosecond pump–probe experiments carried out by the group of Prof. Dirk M. Guldi. The time-evolution analysis of the spectroscopic data afforded rate constants of 6.6×10^{11} and $1.0 \times 10^{10} \text{ s}^{-1}$ for the charge separation and charge recombination dynamics, respectively.

This work reports on the first evidence in which a fullerene fragment mimics the charge transfer behaviour of the parent Buckminster C_{60} buckyball in a donor–acceptor supramolecular assembly (see **Publication 6**).

5.2.4. Buckybowls for donor–acceptor assemblies

In order to further explore the buckybowl properties evidenced in the study of the $\text{truxTTF}\cdot\text{C}_{30}\text{H}_{12}$ complexation, a combined theoretical and experimental investigation was undertaken for similar carbon-based buckybowls of increasing size. In contrast to hemifullerene $\text{C}_{30}\text{H}_{12}$, the recently reported larger $\text{C}_{32}\text{H}_{12}$ and $\text{C}_{38}\text{H}_{14}$ buckybowls are corannulene-based fragments of [60] and [70]fullerene, respectively (Figure 38).^[168] Such a difference in the aromatic core might likely be accompanied by fundamental differences in terms of electronic properties and/or supramolecular complexation.

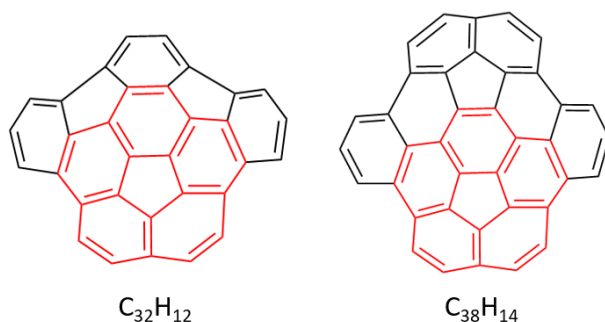


Figure 38. Chemical structure of corannulene-based buckybowls of $\text{C}_{32}\text{H}_{12}$ and $\text{C}_{38}\text{H}_{14}$. The corannulene skeleton is highlighted in red.

Based on our previous experience with hemifullerene $\text{C}_{30}\text{H}_{12}$,^[169] we expected that the larger $\text{C}_{32}\text{H}_{12}$ and $\text{C}_{38}\text{H}_{14}$ fragments associate truxTTF in a similar fashion. To test this hypothesis, we began by studying the supramolecular interaction *in silico*, by means of dispersion-corrected DFT calculations (see Figure 39 for the case of $\text{truxTTF}\cdot\text{C}_{32}\text{H}_{12}$). In analogy to that previously obtained for $\text{C}_{30}\text{H}_{12}$, the corannulene-based $\text{C}_{32}\text{H}_{12}$ and $\text{C}_{38}\text{H}_{14}$ buckybowls may interact either through concave–convex bowl-in-bowl arrangements —structures **B1–2** for $\text{C}_{32}\text{H}_{12}$, and

C1–2 for $C_{38}H_{14}$ — with a maximization of π – π interactions, or through a concave–concave staggered disposition, implying a mixture of π – π and $CH\cdots\pi$ noncovalent interactions —structures **B3–4** for $C_{32}H_{12}$, and **C3–6** for $C_{38}H_{14}$ —. The chemical nomenclature slightly differs from the original work to simplify the discussion and further compare with the work described in the previous Section.

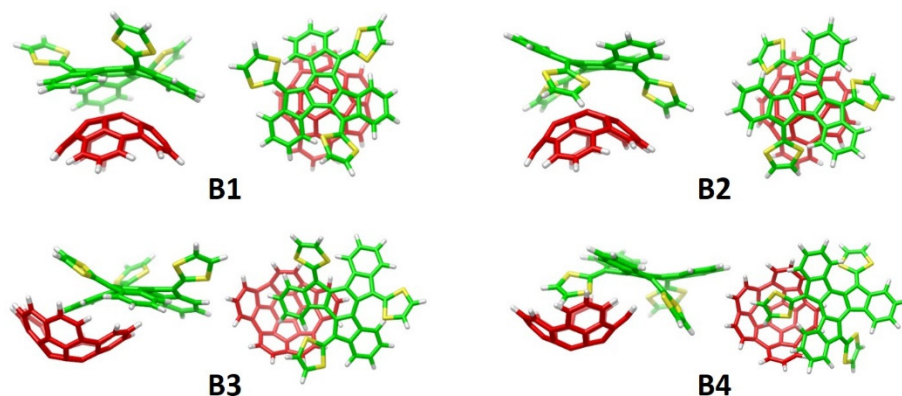


Figure 39. Minimum-energy structures (**B1–4**) computed at the revPBE0-D3/cc-pVTZ level for the most stable conformations of the heterodimer formed by the $C_{32}H_{12}$ fullerene fragment with truxTTF (truxTT• $C_{32}H_{12}$).

Briefly, the association or binding energy (E_{bind}) for the bowl-in-bowl structures was computed to be several kcal mol^{-1} less stable than the staggered dispositions in all cases (Table 6). Among them, the arrangements in which the dithiole is placed inside the basin of the buckybowl fragment were computed the most stable heterodimers ranging from $-28.5 \text{ kcal mol}^{-1}$ in $C_{30}H_{12}$, to $-29.9 \text{ kcal mol}^{-1}$ in $C_{32}H_{12}$ and to $-34.2 \text{ kcal mol}^{-1}$ in $C_{38}H_{14}$. It therefore seems that upon increasing the buckybowl size, the supramolecular interaction with the electron-donor exTTF is reinforced due to the increasing number of weak noncovalent interactions originated from π – π forces and $CH\cdots\pi$ contacts.

In order to provide a more realistic description reflecting the strength of complexation at room temperature and in solution, the free energy of the dimerization process was theoretically estimated for all the possible conformers of $\text{truxTTF}\cdot\text{C}_{32}\text{H}_{12}$ and $\text{truxTTF}\cdot\text{C}_{38}\text{H}_{14}$, and compared with that computed for $\text{truxTTF}\cdot\text{C}_{30}\text{H}_{12}$. Enthalpy and entropy corrections to the free energy were calculated at the B3LYP/cc-pVDZ level of theory. For the entropic part, the rigid-rotor harmonic-oscillator approximation (RRHO) was used as described by Grimme.^[75] Solvent effects were included at the same level of theory using the Universal Solvation Model based on Solute Electron Density (so-called SMD). The reader is referred to **Publication 7** for further details.

Free energies in gas phase show that entropic effects are similar for both bowl-in-bowl and staggered dimers (compare E_{bind} and ΔG_{gas} in Table 6). Upon inclusion of solvent effects (chloroform), the ΔG_{theor} values obtained indicate the same trends for the relative stabilities of the different supramolecular arrangements as predicted by the association energy (Table 6). Interestingly, only the staggered conformers provide negative values of ΔG_{theor} , suggesting that bowl-in-bowl arrangements might not be formed in solution. For the three buckybowls, the staggered dimers in which the dithiole ring is placed inside the bowl basin are computed as the most stable structures, with ΔG_{theor} values of -4.29 , -4.93 and -5.00 kcal mol⁻¹ for $\text{truxTTF}\cdot\text{C}_{32}\text{H}_{12}$, $\text{truxTTF}\cdot\text{C}_{38}\text{H}_{14}$ and $\text{truxTTF}\cdot\text{C}_{30}\text{H}_{12}$, respectively. Theoretical log K_{a} values are predicted in the range of 3–4, showing a perfect matching in the case of $\text{truxTTF}\cdot\text{C}_{30}\text{H}_{12}$ (log $K_{\text{a,theor}} = 3.7$) with respect to the experimental value previously reported (log $K_{\text{a,exp}} = 3.6 \pm 0.3$).^[169]

Table 6. Thermodynamic parameters (in kcal mol⁻¹) including association energy (E_{bind}), free energy in gas phase (ΔG_{gas}), and free energy including solvent effects (ΔG_{theor}) for the dimerization process. Theoretical and experimental K_{a} values are also included.^a

Heterodimer	E_{bind}	ΔG_{gas}	ΔG_{theor}	$\log K_{\text{a,theor}}$	$\log K_{\text{a,exp}}$	
truxTTF•C ₃₀ H ₁₂	A1	-21.02	-8.27	1.13		
	A2	-19.38	-5.98	2.64		
	A3	-25.23	-10.88	-2.96	3.7	3.6
	A4	-28.52	-14.34	-5.00		
truxTTF•C ₃₂ H ₁₂	B1	-20.44	-3.87	5.07		
	B2	-19.97	-4.24	3.67		
	B3	-24.69	-6.95	0.97	3.2	2.9–3.3
	B4	-29.91	-12.84	-4.29		
truxTTF•C ₃₈ H ₁₄	C1	-23.37	-4.32	5.81		
	C2	-21.63	-3.46	4.80		
	C3	-29.09	-9.72	0.51		
	C4	-33.48	-14.39	-3.75	3.6	3.4–3.5
	C5^b	-31.57	-11.71	-2.65		
	C6^b	-34.24	-14.94	-4.93		

^aThe reader is referred to the original work (**Publication 7** below) for further computational details and experimental specifications. ^b**C5** and **C6** conformers are analogous to **C3** and **C4**, respectively, in which the buckybowl is rotated by $\sim 90^\circ$ with respect to the truxTTF.

Encouraged by the theoretical results, the association of the truxTTF with the C₃₂H₁₂ and C₃₈H₁₄ buckybowls was further assessed by the

experimentalists through absorption titrations in several solvents at room temperature. Overall, the absorption features in the UV–Vis spectrum upon titration led to similar band evolution as that previously found in $\text{truxTTF}\cdot\text{C}_{30}\text{H}_{12}$ (Figure 36a). For $\text{C}_{32}\text{H}_{12}$ and $\text{C}_{38}\text{H}_{14}$, however, the low-lying charge-transfer (CT) band was found very weak but detected in the 500–600 nm range. Theoretical calculations of the electronic structure in these heterodimers confirm unequivocally the existence of weak low-lying charge-transfer bands in the 500–650 nm range, corresponding to CT excitations from the HOMO and HOMO–1, located on the electron-donor truxTTF , to the LUMO and LUMO+1, centred over the buckybowl. Multiwavelength analysis of the titration experiments led to association constants of $\log K_a = 2.9\text{--}3.3$ for $\text{C}_{32}\text{H}_{12}$ and $\log K_a = 3.4\text{--}3.5$ for $\text{C}_{38}\text{H}_{14}$. As can be seen in Table 6, the theoretical values estimated for $\log K_a$ are in very good agreement with the experimental results, giving support to the formation of the staggered structures predicted theoretically as the preferred conformation.

Although carried out by the experimental group of Prof. Nazario Martín, it is convenient to recall the ^1H -NMR experiments performed for the $\text{C}_{32}\text{H}_{12}$ and $\text{C}_{38}\text{H}_{14}$ heterodimers in order to shed light on the structure of these associates in solution. Figure 40a shows the ^1H -NMR of truxTTF (black), $\text{C}_{32}\text{H}_{12}$ (blue) and $\text{truxTTF}\cdot\text{C}_{32}\text{H}_{12}$ (red). Upon complexation, all the signals of $\text{C}_{32}\text{H}_{12}$ suffer slight and quantitatively similar upfield shifts. Meanwhile, the signals corresponding to the truxene core of truxTTF (b–e in Figure 40a) appear unaltered, and only the dithiole ring signals (a + a' in Figure 40a) are shifted upfield by ca. 0.02 ppm. These changes support the formation of the structure depicted as **B4** in Figure 39, which was calculated to be the only thermodynamically favourable arrangement in chloroform solution for $\text{truxTTF}\cdot\text{C}_{32}\text{H}_{12}$ (*vide supra*).

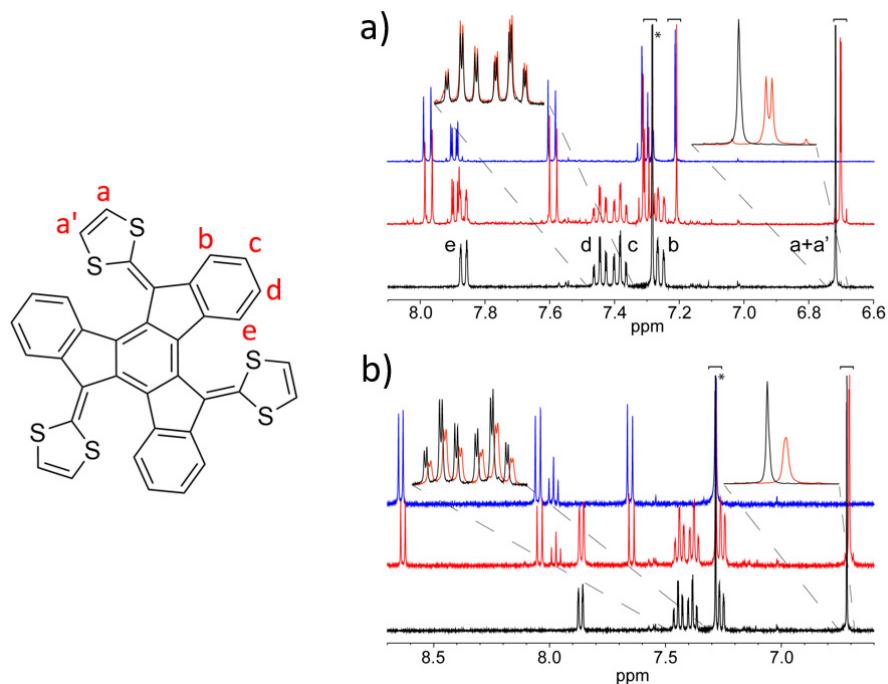


Figure 40. $^1\text{H-NMR}$ (CDCl_3 , 400 MHz, 298K, all species at ca. 5 mM) of: a) truxTTF (black), $\text{C}_{32}\text{H}_{12}$ (blue) and truxTTF + $\text{C}_{32}\text{H}_{12}$ (red), and b) truxTTF (black), $\text{C}_{38}\text{H}_{14}$ (blue) and truxTTF + $\text{C}_{38}\text{H}_{14}$ (red). The insets shows an overlay of the spectra of truxTTF and the complexes in the region between 6.74 and 6.68 ppm (a + a') and 7.48–7.34 ppm (c + d).

The case of truxTTF• $\text{C}_{38}\text{H}_{14}$ is not so straightforward though (Figure 40b). All the signals of the corannulene-based buckybowls are shifted slightly upfield. However, experimentalists detected a shielding of both the truxene-core and the dithiole signals of truxTTF upon association. These spectroscopic changes point to a coexistence in solution of the staggered structures, with predominance of those in which the dithiole rings are inside the cavity of $\text{C}_{38}\text{H}_{14}$ (similarly to **B4** in Figure 39 for truxTTF• $\text{C}_{32}\text{H}_{12}$), again in perfect agreement with the relevant calculations (Table 6). These outcomes turn out to be the first evidences

that buckybowls, in contrast to fullerenes, are able to bind electron-donor organic molecules in dispositions other than the typical concave–convex arrangements, maximizing both $\text{CH}\cdots\pi$ and $\pi\text{--}\pi$ interactions. It is also to be noted that the structures implying the dithiole rings always result more stable than those only involving the carbon backbones, thus indicating the important role played by $\text{S}\cdots\text{C}\pi\text{--}\pi$ interactions.

Finally, femtosecond transient absorption studies carried out by the group of Dirk M. Guldi shed light onto excited-state interactions in these associates. In the case of $\text{truxTTF}\cdot\text{C}_{38}\text{H}_{14}$, photoexcitation yielded the charge-separated state $\text{truxTTF}^{+\bullet}\cdot\text{C}_{38}\text{H}_{14}^{\bullet-}$ with a lifetime of ~ 160 ps in the most polar benzonitrile. For $\text{truxTTF}\cdot\text{C}_{32}\text{H}_{12}$, the assignment of the charge-separated state rendered extremely difficult, but is, based on earlier findings, regarded to be very likely.

5.3. Summary

The supramolecular arrays studied in this Chapter constitute singular examples that have helped a better understanding of the supramolecular recognition of fullerenes and fullerene fragments by electron-rich hosts, either with concave–concave or convex–planar mismatch.

Firstly, the different parameters influencing the stability of the supramolecular ensembles formed by porphyrins and fullerene C_{60} , with special attention to the nature of the metal in the porphyrin moiety, have been rationalized with the help of theoretical calculations thus providing new insights into the fullerene–porphyrin interaction. In the case of the bis-porphyrin adducts, theoretical calculations evidence a significant

decrease of the electron density in both ditopic *meso-meso* and tape porphyrin dimers upon complexation of the first C₆₀-related molecule, in good agreement with the negative cooperativity found experimentally in these systems. This negative effect is partially compensated by the stabilizing C₆₀–C₆₀ interactions that take place in the more stable *syn* disposition of the tape porphyrin:methanofullerene 1:2 aggregate.

Secondly, the association of a series of fullerene fragments —C₃₀H₁₂, C₃₂H₁₂ and C₃₈H₁₄— with an electron-donating bowl-shaped tetrathiafulvalene derivative (truxTTF) reveal that the counterintuitive concave–concave conformation in which the 1,3-dithiole ring of truxTTF is placed inside the concave cavity of the bucky bowl is the most stable arrangement. This structure was confirmed experimentally by NMR measurements, and implies the combination of π – π and CH \cdots π interactions as the driving force for association. Time-dependent DFT calculations provide a detailed understanding of the UV–Vis spectral changes observed upon titration, giving support to the existence of a photoinduced charge-transfer from the electron-donor truxTTF to the electron-acceptor bucky bowl. The charge-separated state resulting from this CT transition was detected experimentally by means of femtosecond pump–probe spectroscopic techniques for the supramolecular assembly of truxTTF with C₃₀H₁₂ and C₃₈H₁₄. These supramolecular complexes constitute the first examples of donor–acceptor assemblies involving fullerene fragments that mimic the electronic behaviour of their parent buckyballs.

5.4. Publications

Publication 4 L. Moreira, J. Calbo, B. M. Illescas, J. Aragón, I. Nierengarten, B. Delavaux-Nicot, E. Ortí, N. Martín, J.-F. Nierengarten, “Metal-Atom Impact on the Self-Assembly of Cup-and-Ball Metalloporphyrin–Fullerene Conjugates”, *Angew. Chem. Int. Ed.* **2015**, *54*, 1255–1260.

Publication 5 L. Moreira, J. Calbo, J. Aragón, B. M. Illescas, I. Nierengarten, B. Delavaux-Nicot, E. Ortí, N. Martín, and J.-F. Nierengarten. “Conjugated Porphyrin Dimers: Cooperative Effects and Electronic Communication in Supramolecular Ensembles with C₆₀”, *J. Am. Chem. Soc.* **2016**, *138*, 15359–15367.

Publication 6 M. Gallego, J. Calbo, J. Aragón, R. M. Krick Calderon, F. H. Liquido, T. Iwamoto, A. K. Greene, E. A. Jackson, E. M. Pérez, E. Ortí, D. M. Guldi, L. T. Scott, N. Martín, “Electron Transfer in a Supramolecular Associate of a Fullerene Fragment”, *Angew. Chem. Int. Ed.* **2014**, *53*, 2170–2175.

Publication 7 M. Gallego, J. Calbo,† R. M. Krick Calderon, P. Pla, Y.-C. Hsieh, E. M. Pérez, Y.-T. Wu, E. Ortí, D. M. Guldi, N. Martín, “Complexation and Electronic Communication between Corannulene-Based Buckybowls and a Curved Truxene-TTF Donor”, *Chem. Eur. J.* (accepted, DOI: 10.1002/chem.201604921).

Reproduced with permission of Wiley and American Chemical Society.

Metal-Atom Impact on the Self-Assembly of Cup-and-Ball Metalloporphyrin–Fullerene Conjugates**

Luis Moreira, Joaquín Calbo, Beatriz M. Illescas, Juan Aragón, Iwona Nierengarten, Béatrice Delavaux-Nicot, Enrique Ortí,* Nazario Martín,* and Jean-François Nierengarten*

Dedicated to Professor Jean-Pierre Sauvage on the occasion of his 70th birthday

Abstract: A fullerene ammonium derivative has been combined with different metalloporphyrin–crown ether receptors to generate very stable supramolecules. The combination of fullerene–porphyrin and ammonium–crown ether interactions leads to a strong chelate effect as evidenced by a high effective molarity (3.16 M). The different parameters influencing the stability of the supramolecular ensembles, in particular the nature of the metal in the porphyrin moiety, have been rationalized with the help of theoretical calculations thus providing new insights into fullerene–porphyrin interactions.

The construction of artificial photoactive devices capable of mimicking photosynthesis by transforming sunlight into chemical potential is one of the most sought objectives in the quest for new sources of energy.^[1] For this purpose, chemists have developed a wide variety of donor–acceptor systems, in which photon energy is used to produce a photo-induced electron transfer from the donor to the acceptor.^[2]

Among them, porphyrins and fullerenes have extensively been combined due to their respective notable electron-donor and electron-acceptor properties.^[3]

Most research on porphyrin–fullerene conjugates has been based on covalent chemistry.^[4] However, considering the versatility of noncovalent interactions, a variety of supramolecular ensembles involving both chromophores has been reported.^[5] Surprisingly, although many of these examples involve π – π interactions between both components, the nature of this affinity, which challenges the traditional belief that a curved guest requires curved hosts for effective complexation,^[6] is not yet fully understood. Crystallographic data suggests that it stems from the attraction between the higher electron density of a [6,6] double bond of the fullerene sphere and the protic center of a free-base porphyrin or the metal of a metalloporphyrin, therefore confronting the general notion of fullerenes as molecular acceptors.^[7] In addition, little is known on the role of the metal atom.^[8] To the best of our knowledge, there are few examples dealing with this issue in solution: the porphyrin sandwiches developed by Aida and co-workers^[9] and the “jaws porphyrins”^[10] and the calix[4]arene-linked bisporphyrins^[11] developed by Reed, Boyd, and co-workers. None of these papers fully rationalized the binding or association constants (K_a) for the different metals beyond pointing to the existence of an electrostatic component as free-base porphyrins bind fullerenes with a similar strength than their Zn^{II} analogues.^[8a] One of them even suggests that the high binding constants obtained in the complexation of fullerenes can be ascribed to their desolvation rather than to electronic effects.^[11] Computational studies mainly point to the presence of dispersion forces in the complex and do not provide an accurate analysis of the interaction.^[8a,12]

Furthermore, supramolecular complexes presenting a single porphyrin–fullerene π – π interaction are readily dissociated in solution, given their low thermodynamic stability, making their study more challenging. However, as previously reported in our group, the inclusion of additional supramolecular recognition motifs can lead to a cooperative stabilization of the complex, in which the introduction of an additional ammonium–crown ether interaction dramatically stabilized the resulting complex.^[13] Therefore, understanding and quantifying the cooperative interplay between different noncovalent interactions and the structure of the supramolecular complexes obtained remain a major challenge.^[14] For this, the effective molarity (EM) is a key parameter, as it assesses the chelate effect of a system by accounting for the easier

[*] Dr. L. Moreira, Dr. I. Nierengarten, Prof. Dr. J.-F. Nierengarten
 Laboratoire de Chimie des Matériaux Moléculaires
 Université de Strasbourg et CNRS (UMR 7509)
 ECPM, 25 rue Becquerel, 67087 Strasbourg (France)
 E-mail: nierengarten@unistra.fr

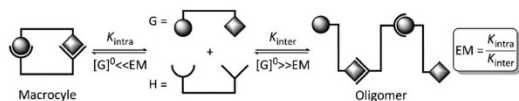
Dr. L. Moreira, Dr. B. M. Illescas, Prof. Dr. N. Martín
 Departamento de Química Orgánica, Fac. C.C. Químicas
 Universidad Complutense de Madrid
 Av. Complutense s/n, 28040 Madrid (Spain)
 E-mail: nazmar@ucm.es

J. Calbo, Dr. J. Aragón, Prof. Dr. E. Ortí
 Instituto de Ciencia Molecular, Universidad de Valencia
 Catedrático José Beltrán 2, 46980 Paterna (Spain)
 E-mail: enrique.orti@uv.es

Dr. B. Delavaux-Nicot
 Laboratoire de Chimie de Coordination du CNRS (UPR 8241)
 Université de Toulouse (UPS, INPT)
 205 route de Narbonne, 31077 Toulouse Cedex 4 (France)

[**] This work was supported by the European Research Council (ERC-2012-ADG_20120216 (ChiralCarbon), the Ministerio de Economía y Competitividad (MINECO) of Spain (projects CTQ2011-24652 and CTQ2012-31914), the Comunidad Autónoma de Madrid (MADRI-SOLAR-2 project S2009/PPQ-1533), the Generalitat Valenciana (PROMETEO/2012/053), and the European FEDER funds (CTQ2012-31914). L.M. thanks the Obra Social “la Caixa” for a postgraduate fellowship. J.C. acknowledges the Spanish Ministry of Education, Culture, and Sport (MECD) for an FPU grant.

Supporting information for this article is available on the WWW under <http://dx.doi.org/10.1002/anie.201409487>.

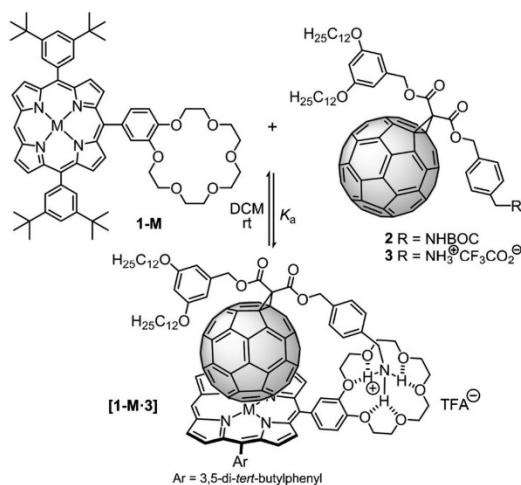


Scheme 1. EM quantifies the ease of cyclization versus oligomerization.

formation of an intramolecular reaction over its intermolecular analogues (Scheme 1).^[15]

To shed light on these topics, this work presents a complete study on the effect of different metals, namely Co, Ni, Cu, and Zn, on the binding constant of a series of novel metal-porphyrin-[60]fullerene cup-and-ball complexes. Their self-assembly is assessed through the EM of the Zn-based complex and their K_a values are rationalized with the help of electrochemical studies and quantum-chemical calculations.

Targeted complexes [**1-M-3**] were obtained by mixing the corresponding porphyrin-crown ether conjugates (**1-M**; M = 2H, Co, Ni, Cu, Zn) and the methano[60]fullerene derivative **3**^[16] as shown in Scheme 2.



Scheme 2. Formation of supramolecular complexes [**1-M-3**] from their corresponding building blocks **1-M** (M = 2H, Co, Ni, Cu, Zn) and **3**.

Complexation was first evidenced by ¹H NMR spectroscopy. Addition of 1 equiv of **3** to **1-Zn** resulted in a fast equilibrium leading to a shift of the signals particularly visible in the aromatic region (see Figure S1 in the Supporting Information, SI).

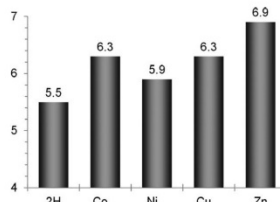
Measurement of the binding constant of [**1-M-3**] was undertaken by monitoring the changes in the UV/Vis absorption spectra of **1-M** after addition of increasing quantities of **3** in DCM at room temperature. A representative example is the formation of [**1-Zn-3**] (Figure S3). Addition of increasing quantities of **3** to **1-Zn** resulted in a redshift of the Soret band ($\lambda_{\max} = 416 \text{ nm} \rightarrow 423 \text{ nm}$), which

was observed in all complexes (see Figure S4). This shift has been accounted for by the charge transfer from the axial ligand to the porphyrin ring,^[17] and is widely used as an evidence of the presence of intermolecular π -stacking.^[5d]

The appearance of a single isosbestic point at 422 nm suggests a single equilibrium between the unbounded and the bounded species.^[18] Given the unlikely formation of a 1:2 complex by simultaneous collision of three molecules, this is most probably a 1:1 complex. This stoichiometry is in line with that found for a related system developed by our group^[13] and was also evidenced by positive ESI-MS. Thus, the mass spectrum obtained from an equimolar mixture of **1-Zn** and **3** in DCM displayed a single-charged ion peak at m/z 2461.00 ascribable to the 1:1 complex [**1-Zn-3**] after loss of the counteranion (calculated m/z 2461.00). In addition, the MS of a 1:4 mixture of **1-Zn:3** showed exclusively the peak corresponding to a 1:1 stoichiometry (see Figure S2). Finally, nonlinear curve fitting of the titration data using Specfit multivariate analysis software (see SI) fitted to a 1:1 model and led to the K_a values reported in Table 1.

Table 1: Calculated binding constants (K_a) for porphyrins **1-M** toward the methanofullerene derivative **3** at 25 °C in DCM.

Complex	$\log K_a \pm 3\sigma$
[1-2H-3]	5.5 ± 0.2
[1-Co-3]	6.3 ± 0.2
[1-Ni-3]	5.9 ± 0.1
[1-Cu-3]	6.3 ± 0.3
[1-Zn-3]	6.9 ± 0.2

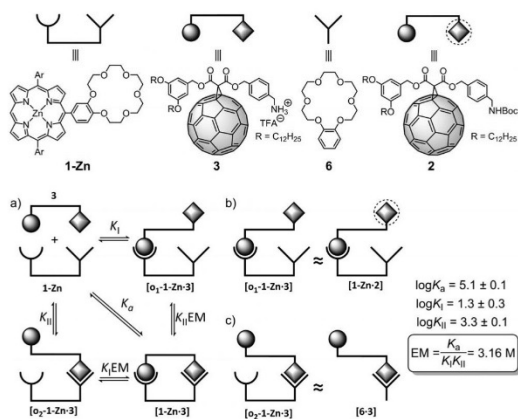


Interestingly, the pattern found for the binding constants of [**1-M-3**] complexes is very different from those reported in previous studies as [**1-2H-3**] does not bind fullerene with a similar strength than [**1-Zn-3**].^[9-11] Indeed, the values obtained in our series correlate with that expected for a porphyrin-C₆₀ associate governed by van der Waals forces, in which K_a becomes larger as the number of electrons in the porphyrin increases, with the sole exception of [**1-Co-3**]. Its different behavior can be attributed to the strong interaction between fullerenes and Group 9 metals (Co, Rh, Ir),^[9a] which has been related to the partial occupation of the Co-d_{z²} orbital, leading to less repulsive interactions.^[12b] Experimentally, this is evidenced by the fact that the Soret band of **1-Co** shows the largest redshift of all the series ($\Delta\lambda_{\max} = 24 \text{ nm}$) upon complexation, suggesting a larger charge transfer interaction (see SI).

It is crucial to note that all previous examples were based on the complexation of pristine C₆₀, whose low solubility limited the choice of solvents for the titration experiment

making its desolvation the driving force of the complexation, as already mentioned in the introduction.^[11] The use of methanofullerene **3** has elegantly circumvented this limitation, enabling us to have a better insight into the nature of this interaction, while basically retaining the original properties of the fullerene moiety.

The chelate effect in these self-assembled systems was assessed by estimating the EM of the reference complex [**1-Zn-3**]. For this purpose, each of the interactions leading to the complex was independently evaluated and compared to the overall stability, K_a (Scheme 3).^[19] The porphyrin conjugate **1-**



Scheme 3. a) The EM is obtained by evaluating each supramolecular interaction separately. b) The porphyrin–fullerene interaction was assessed by ¹H NMR titration of **1-Zn** with methanofullerene **2** in CDCl₃ at room temperature yielding K_I (Figures S5 and S6). c) The stability of the ammonium–crown ether association, K_{II} , was evaluated by ¹H NMR titration of **3** with crown ether **6**.^[20] The overall binding constant, K_a , was obtained by UV/Vis titration of **1-Zn** with **3** in CHCl₃ at room temperature (see Figure S7).

Zn was combined with methanofullerene **2**, whose ammonium moiety is protected to prevent any H-bonding interaction, to evaluate the porphyrin–fullerene interaction. The strength of the ammonium–crown ether motif was evaluated by titrating **3** with **6**.^[20] The high EM obtained (3.16 M) reflects how the introduction of the ammonium–crown ether association as an additional recognition motif increases the complementarity of the building blocks with a minimum cost in their preorganization.

The supramolecular complexes were further studied by Osteryoung square wave voltammetry (OSWV) and cyclic voltammetry (CV). Formation of [**1-M-3**] led to changes of the electrochemical signature of the **1-M** porphyrins suggesting donor–acceptor interactions in the ground state (see Table S1 and Figures S8–S10). Indeed, a slight shift of the first oxidation potential and a change in intensity are detected by OSWV upon interaction. In the case of **1-Co**, the first oxidation potential is centered on the metal and not on the π -system of the porphyrin ligand.^[21] In CV, for this particular association, an apparent anodic shift of the first oxidation potential ($\Delta E = 220$ mV) is observed (Figure S10). This is the

most important shift value in comparison with all the other cases and is in line with specific interactions of the metal center and the fullerene sphere (see above). As for the reduction, the significant anodic shift (ca. 50 mV) of the first reduction of the fullerene moiety upon addition of **3** to **1-Co** further evidences this phenomenon.

The molecular structures and binding energies of the [**1-M-3**] complexes were theoretically investigated to gain a better understanding of the different interactions governing the associates (see SI for full computational details). Geometry optimizations were first performed at the semiempirical PM7 level and show that, after full-geometry relaxation, the ammonium group of the methanofullerene interacts with the crown ether of the porphyrin by H-bond formation, whereas the fullerene ball recognizes the center of the porphyrin system by noncovalent forces (Figure 1).

Accurate density functional theory (DFT) optimizations of the [**1-M-3**] geometries were performed at the B97-D/6-31G* level starting from the PM7-optimized structures (see Figure S11 for the DFT-optimized geometries). The main interactions governing the supramolecular association are represented by the M–C₆₀ (**a**) and NH...O (**b**) distances given in Table 2 (see Figure 1 for labeling). In addition, C–H... π dispersion interactions (**c** and **d**) between the *tert*-butyl-substituted benzene rings of the porphyrin and the π -cloud of the fullerene also contribute to the supramolecular complex. The increase in the electron density on the metal atom

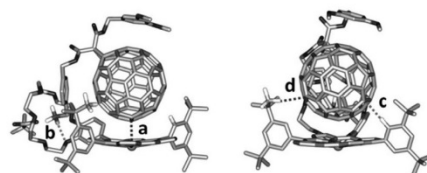


Figure 1. Minimum-energy structure calculated for the [**1-Cu-3**] complex at the PM7 level. Side (left) and front (right) views are displayed. The different types of intermolecular noncovalent interactions are denoted with labels **a–d**. Only relevant hydrogen atoms are displayed for clarity.

Table 2. DFT-optimized (B97-D/6-31G*) intermolecular distances (**a–d**, in Å) characterizing the [**1-M-3**] associates, and binding energies (E_{bind}) computed at the PBE0-D3/cc-pVTZ level.

Complex	M–C ₆₀ (a) ^[a]	NH...O (b) ^[b]	CH...C ₆₀ (c) ^[c]	CH...C ₆₀ (d) ^[d]	E_{bind} (kcal mol ⁻¹)
[1-2H-3]	2.756	1.848	2.679	2.577	–92.4
[1-Co-3]	2.119	1.850	2.642	2.573	–93.8
[1-Ni-3]	2.793	1.842	2.623	2.610	–88.7
[1-Cu-3]	2.754	1.846	2.662	2.599	–91.3
[1-Zn-3]	2.701	1.845	2.698	2.591	–92.8

[a] Distance between the center of the porphyrin (the metal atom) and the center of the closest [6,6] bond of C₆₀. [b] Shortest distance between the hydrogen atoms of the ammonium group and the oxygen atoms of the crown ether. [c] Shortest distance between the hydrogen atoms of the peripheral benzene rings of the porphyrin and the closest C₆₀ carbon atom. [d] Shortest distance between the hydrogen atoms of the *tert*-butyl groups and the closest C₆₀ carbon atom.

determines a shortening in the M–C₆₀ distance from 2.79 Å in **[1-Ni-3]** to 2.70 Å in **[1-Zn-3]**, and the nonmetalated **[1-2H-3]** associate presents an intermediate value of 2.76 Å identical to **[1-Cu-3]**. Calculations predict an M–C₆₀ distance of only 2.12 Å for **[1-Co-3]** underestimating the value of 2.60–2.80 Å recorded for neutral Co^{II} metalloporphyrin complexes.^[22] However, as discussed below, this underestimation is presumably due to the relatively small basis set employed in the geometry optimization. The hydrogen bond NH...O lengths (**b**) that account for the ammonium–crown ether interaction do not vary along the series of porphyrin–fullerene associates (Table 2). The CH...C₆₀ interactions **c** and **d** are all around 2.60 Å and determine a slight folding of the porphyrin macrocycle to better wrap the fullerene surface.

The association or binding energy (E_{bind}) of the **[1-M-3]** associates was calculated at the PBE0-D3/cc-pVTZ level of theory using the B97-D/6-31G*–optimized geometries (Table 2). Passing from Ni to Zn, E_{bind} rises from –88.7 to –92.8 kcal mol^{–1} due to the more stabilizing M–C₆₀ interaction that takes place in moving to electron-richer metal atoms. The stabilization in the formation of the nonmetalated **[1-2H-3]** complex amounts to –92.4 kcal mol^{–1}, and the largest association energy is computed for **[1-Co-3]** (–93.8 kcal mol^{–1}). The differences found between the calculated E_{bind} and the experimental trends found for K_a may arise from the solvent and entropic effects, which are not taken into account in the calculations.

To quantify the contribution of the main interactions governing the formation of the **[1-M-3]** complexes, binding energies at the PBE0-D3/cc-pVTZ//B97-D/6-31G* level were computed for simplified model systems of **[1-Zn-3]** (see Figure S12 and Table S2). The noncovalent interaction between the fullerene ball and the phenyl-substituted porphyrin amounts to –22.5 kcal mol^{–1}, and the presence of the *tert*-butyl groups at the *meta* position of the phenyl rings (interaction **d**) produces an additional stabilization of approximately 4 kcal mol^{–1} (–26.3 kcal mol^{–1}) in agreement with previous theoretical studies.^[12a,23] The ammonium–crown ether NH...O contacts are computed to be the main stabilizing interaction and provide an interaction energy of –64.9 kcal mol^{–1}, which is three times the stabilization of the porphyrin–C₆₀ interaction in good accord with the experimental trends discussed above (Scheme 3). The binding energy obtained from the sum of these three supramolecular interactions (–91.2 kcal mol^{–1}) is pretty close to the total association energy computed for **[1-Zn-3]** (–92.8 kcal mol^{–1}) supporting the validity of the analysis performed.

Calculations evidence the charge transfer from the axial C₆₀ ligand to the metal center since the positive charge of the metal decreases in passing from **1-M** to **[1-M-3]** (see Table S3). This effect is especially important for **[1-Co-3]** (0.20e) due to the participation of the Co-d_{z²} orbital in the half-filled HOMO (see Figure S15), and determines the larger red shift observed for this complex in the UV/Vis spectrum (see above). The fullerene guest is therefore acting as a donor, giving electron density to the metal and, at the same time, it is also acting as an acceptor receiving electron density from the porphyrin macrocycle through the π–π interaction between both fragments (see Table S3).

Keeping in mind that C₆₀ interacts with the porphyrin moiety mainly through the electron-rich [6,6] double bonds,^[8a] we modeled a simplified system (**MP-C₂H₄**) in which the pristine porphyrin (**MP**) interacts with a molecule of ethylene (Figure S13). This reduced model allows performing more accurate calculations to better understand the relative stabilization of the different associates when varying the metal in the porphyrin.

Geometry relaxation of the porphyrin–ethylene complex at the PBE0-D3/cc-pVTZ level led to a minimum-energy conformation in which the ethylene stands parallel to the porphyrin plane with a C_{2v} molecular symmetry (Figure S13). A clear correlation between the calculated binding energies and metal–ethylene distances is now obtained, because the shorter the distance along the series **NiP-C₂H₄** (3.18 Å) > **CuP-C₂H₄** (3.00 Å) > **ZnP-C₂H₄** (2.75 Å) > **CoP-C₂H₄** (2.62 Å) is, the larger is the stabilization of the complex (Table 3). In comparing the **2HP-C₂H₄** and **CuP-C₂H₄** com-

Table 3: Binding energies, metal–ethylene distances, and natural population analysis (NPA) charges of the porphyrin central atom (M = 2H, Co, Ni, Cu, Zn) calculated at the PBE0-D3/cc-pVTZ level of theory for the simplified porphyrin–ethylene associates.

Complex	E_{bind} [kcal mol ^{–1}]	M–ethylene distance [Å]	M net charge [e]
2HP-C₂H₄	–4.636	2.986	+ 0.942
CoP-C₂H₄	–8.534	2.619	+ 0.720
NiP-C₂H₄	–4.530	3.177	+ 0.733
CuP-C₂H₄	–5.965	2.997	+ 1.006
ZnP-C₂H₄	–8.047	2.749	+ 1.223

plexes, which have similar M–ethylene distances, the larger association energy computed for the latter suggests that the presence of the metal favors the stabilization of the complex by approximately 1.5 kcal mol^{–1}. The M–C₂H₄ distance computed for the **CoP-C₂H₄** associate (2.62 Å) is significantly longer than that obtained for the **[1-Co-3]** complex at the B97-D/6-31G* level, and is in good accord with previously reported M–C₆₀ distances for Co-based porphyrin–fullerene associates.^[22]

The net charge calculated for the metal atom increases in going from **CoP-C₂H₄** (+0.720e) to **ZnP-C₂H₄** (+1.223e) (Table 3) and, in a first approach, can be related with the stabilizing electrostatic interaction between the porphyrin and the fullerene guest. However, as discussed here in the following, additional contributions to the binding energy provoke a nonlinear correlation between the net charge of the porphyrin central atom and the total association energy.

Symmetry-adapted perturbation theory (SAPT)^[24] calculations were performed for **2HP-C₂H₄**, **NiP-C₂H₄**, and **ZnP-C₂H₄** to decompose the total binding energy into electrostatic, exchange, induction, and dispersion energy components (Table 4). SAPT decomposition was not performed for **CoP-C₂H₄** and **CuP-C₂H₄** because it is not available for open-shell systems. A stabilization in the electrostatic term of more than 10 kcal mol^{–1} is predicted in passing from **NiP-C₂H₄** to **ZnP-C₂H₄** because of the shorter M–ethylene distance and the larger positive charge held by

Table 4: Energy decomposition (in kcal mol⁻¹) calculated at the SAPTO/def2-TZVP level for closed-shell porphyrin–ethylene systems with M = 2H, Ni, Zn.

	2HP-C ₂ H ₄	NiP-C ₂ H ₄	ZnP-C ₂ H ₄
electrostatic	-2.794	-5.277	-16.212
exchange	7.046	8.605	22.101
induction	-0.690	-0.728	-3.900
dispersion	-7.033	-7.055	-10.521
TOTAL ^[a]	-3.472	-4.455	-8.532

[a] Total SAPTO energy is corrected according to the spin-component scaling approach.

the metal atom in **ZnP-C₂H₄** (Table 4). The same reasoning cannot be applied to **2HP-C₂H₄**, for which the large positive charge accumulated in the H atoms is not translated into a high electrostatic stabilization due to the comparatively small size of the H atoms. The exchange interaction contributes positively to the final association energy and is computed to be much larger for **ZnP-C₂H₄** than for **2HP-C₂H₄** and **NiP-C₂H₄** (Table 4). The shorter metal–ethylene distance and especially the larger atomic size of Zn magnify the value of this repulsive interaction. The induction term is meant to decrease exponentially with the distance between the two interacting moieties. In **ZnP-C₂H₄**, for which the M–ethylene distance is significantly smaller and the Zn atom bears a relatively large positive charge of +1.22e, the induction term is computed to be non-negligible (−4 kcal mol⁻¹). For the other two systems, this stabilizing term is less than 1 kcal mol⁻¹.

Finally, the dispersion energy is computed to be the largest stabilizing contribution in **2HP-C₂H₄** and **NiP-C₂H₄**, and it stabilizes the **ZnP-C₂H₄** complex in more than 10 kcal mol⁻¹ (Table 4). Absolute binding energies at the SAPTO level (**2HP-C₂H₄**: −3.472 kcal mol⁻¹, **NiP-C₂H₄**: −4.455 kcal mol⁻¹, **ZnP-C₂H₄**: −8.532 kcal mol⁻¹) nicely match the values obtained at the PBE0-D3/cc-pVTZ level (Table 3) except for **2HP-C₂H₄**, which is now computed to be slightly less stable than **NiP-C₂H₄** in better accord with the experimental evidences. Theoretical calculations therefore suggest that the energy term that mainly contributes to the stabilization of the **2HP-C₂H₄** associate is the dispersion component. In the metal-based porphyrin complexes, the electrostatic contribution acquires a major role, especially for **ZnP-C₂H₄**, for which M–ethylene distances are shorter and the metal bears a larger positive charge.

In conclusion, a new series of supramolecular cup-and-ball complexes has been prepared to evaluate the impact of the metal moiety in the porphyrin–fullerene interaction. The high binding constants obtained for **[1-M-3]** and the large EM of **[1-Zn-3]** (3.16 M) evidence the nice complementarity of π–π and ammonium–crown ether interactions in the self-assembly of the dyads. Further electrochemical and computational studies were also performed. The combination of the experimental and in silico results clearly show that, whereas π–π interactions are governed by dispersion forces in free base porphyrins, they arise both from electrostatic and dispersion interactions in metalloporphyrins.

Received: September 25, 2014
 Published online: November 27, 2014

Keywords: crown compounds · fullerenes · molecular modeling · porphyrins · supramolecular chemistry

- [1] V. Balzani, A. Credi, M. Venturi, *Molecular Devices and Machines*, Wiley-VCH, Weinheim, 2008, pp. 171–207.
- [2] a) S. Berardi, S. Drouet, L. Francas, C. Gimbert-Surinach, M. Guttentag, C. Richmond, T. Stoll, A. Llobet, *Chem. Soc. Rev.* 2014, 0, 0; b) M. D. Kärkäs, E. V. Johnston, O. Verho, B. Åkermark, *Acc. Chem. Res.* 2013, 46, 100–111.
- [3] S. Fukuzumi, *Functional Organic Materials*, Wiley-VCH, Weinheim, 2007, pp. 465–510.
- [4] a) C. Villegas, J. L. Delgado, P.-A. Bouit, B. Grimm, W. Seitz, N. Martín, D. M. Guldi, *Chem. Sci.* 2011, 2, 1677–1681; b) C. A. Wijesinghe, M. E. El-Khouly, M. E. Zandler, S. Fukuzumi, F. D'Souza, *Chem. Eur. J.* 2013, 19, 9629–9638; c) H. Imahori, *Org. Biomol. Chem.* 2004, 2, 1425–1433.
- [5] a) N. Martín, J.-F. Nierengarten, *Supramolecular Chemistry of Fullerenes and Carbon Nanotubes*, Wiley-VCH, Weinheim, 2012; b) M. Kimura, Y. Saito, K. Ohta, K. Hanabusa, H. Shirai, N. Kobayashi, *J. Am. Chem. Soc.* 2002, 124, 5274–5275; c) K. Yoosaf, J. Iehl, I. Nierengarten, M. Hmadeh, A.-M. Albrecht-Gary, J.-F. Nierengarten, N. Armaroli, *Chem. Eur. J.* 2014, 20, 223–231; d) F. D'Souza, O. Ito, *Chem. Commun.* 2009, 4913–4928.
- [6] E. M. Pérez, N. Martín, *Chem. Soc. Rev.* 2008, 37, 1512–1519.
- [7] a) M. M. Olmstead, D. A. Costa, K. Maitra, B. C. Noll, S. L. Phillips, P. M. Van Calcar, A. L. Balch, *J. Am. Chem. Soc.* 1999, 121, 7090–7097; b) P. D. W. Boyd, M. C. Hodgson, C. E. F. Rickard, A. G. Oliver, L. Chaker, P. J. Brothers, R. D. Bolskar, F. S. Tham, C. A. Reed, *J. Am. Chem. Soc.* 1999, 121, 10487–10495.
- [8] a) P. D. W. Boyd, C. A. Reed, *Acc. Chem. Res.* 2004, 37, 235–242; b) G. W. Gokel, J. J. Barbour, R. Ferdani, J. Hu, *Acc. Chem. Res.* 2002, 35, 878–886.
- [9] a) J.-Y. Zheng, K. Tashiro, Y. Hirabayashi, K. Kinbara, K. Saigo, T. Aida, S. Sakamoto, K. Yamaguchi, *Angew. Chem. Int. Ed.* 2001, 40, 1857–1861; *Angew. Chem.* 2001, 113, 1909–1913; b) K. Tashiro, T. Aida, *Chem. Soc. Rev.* 2007, 36, 189–197.
- [10] D. Sun, F. S. Tham, C. A. Reed, L. Chaker, P. D. W. Boyd, *J. Am. Chem. Soc.* 2002, 124, 6604–6612.
- [11] A. Hosseini, S. Taylor, G. Accorsi, N. Armaroli, C. A. Reed, P. D. W. Boyd, *J. Am. Chem. Soc.* 2006, 128, 15903–15913.
- [12] a) Y.-B. Wang, Z. Lin, *J. Am. Chem. Soc.* 2003, 125, 6072–6073; b) M.-S. Liao, J. D. Watts, M.-J. Huang, *J. Phys. Chem. B* 2007, 111, 4374–4382.
- [13] N. Solladié, M. E. Walther, M. Gross, T. M. Figueira Duarte, C. Bourgoigne, J.-F. Nierengarten, *Chem. Commun.* 2003, 2412–2413.
- [14] E. Chekmeneva, C. A. Hunter, M. J. Packer, S. M. Turega, *J. Am. Chem. Soc.* 2008, 130, 17718–17725.
- [15] a) G. Ercolani, L. Schiaffino, *Bioinspiration and Biomimicry in Chemistry*, Wiley, Weinheim, 2012, pp. 47–69; b) P. Ballester, A. I. Oliva, A. Costa, P. M. Deyà, A. Frontera, R. M. Gomila, C. A. Hunter, *J. Am. Chem. Soc.* 2006, 128, 5560–5569.
- [16] D. Bonifazi, G. Accorsi, N. Armaroli, F. Song, A. Palkar, L. Echevoyen, M. Scholl, P. Seiler, B. Jaun, F. Diederich, *Helv. Chim. Acta* 2005, 88, 1839–1884.
- [17] M. Nappa, J. S. Valentine, *J. Am. Chem. Soc.* 1978, 100, 5075–5080.
- [18] K. A. Connors, *Binding Constants: The Measurement of Molecular Complex Stability*, Wiley, Weinheim, 1987.
- [19] H. J. Hogben, J. K. Sprafke, M. Hoffmann, M. Pawlicki, H. L. Anderson, *J. Am. Chem. Soc.* 2011, 133, 20962–20969.

- [20] N. Solladié, M. E. Walther, H. Herschbach, E. Leize, A. V. Dorselaer, T. M. Figueira Duarte, J.-F. Nierengarten, *Tetrahedron* **2006**, *62*, 1979–1987.
- [21] M. L'Her, A. Pondaven in *The Porphyrin Handbook* (Eds.: K. M. Kadish, K. M. Smith, R. Guilard), Academic, Amsterdam, **2003**, pp. 117–169.
- [22] D. V. Konarev, S. S. Khasanov, G. Saito, R. N. Lyubovskaya, *J. Porphyrins Phthalocyanines* **2003**, *7*, 801–806.
- [23] M. Nishio, M. Hirota, Y. Umezawa, *The CH/π Interaction: Evidence, Nature and Consequences*, Wiley, Weinheim, **1998**.
- [24] E. G. Hohenstein, R. M. Parrish, C. D. Sherrill, J. M. Turney, H. F. Schaefer, *J. Chem. Phys.* **2011**, *135*, 174107.
-



Conjugated Porphyrin Dimers: Cooperative Effects and Electronic Communication in Supramolecular Ensembles with C₆₀

Luis Moreira,^{†,||} Joaquín Calbo,[‡] Juan Aragón,[‡] Beatriz M. Illescas,^{||} Iwona Nierengarten,[†] Béatrice Delavaux-Nicot,[§] Enrique Ortí,^{*,‡} Nazario Martín,^{*,||,⊥} and Jean-François Nierengarten^{*,†}

[†]Laboratoire de Chimie des Matériaux Moléculaires, Université de Strasbourg et CNRS (UMR 7509), ECPM, 67087 Strasbourg, Cedex 2, France

[‡]Instituto de Ciencia Molecular, Universidad de Valencia, 46100 Burjassot, Spain

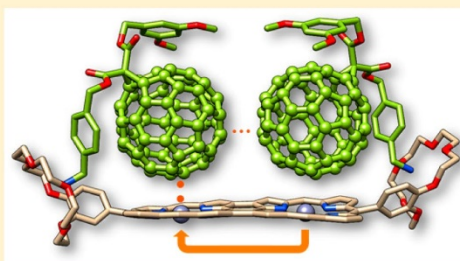
^{||}Departamento de Química Orgánica, Facultad de Ciencias Químicas, Universidad Complutense de Madrid, 28040 Madrid, Spain

[§]Laboratoire de Chimie de Coordination du CNRS (UPR 8241), Université de Toulouse (UPS, INPT), 31077 Toulouse, Cedex 4, France

[⊥]Imdea-Nanoscience, Campus Cantoblanco, 28049 Madrid, Spain

Supporting Information

ABSTRACT: Two new conjugated porphyrin-based systems (dimers 3 and 4) endowed with suitable crown ethers have been synthesized as receptors for a fullerene-ammonium salt derivative (1). Association constants in solution have been determined by UV-vis titration experiments in CH₂Cl₂ at room temperature. The designed hosts are able to associate up to two fullerene-based guest molecules and present association constants as high as $\sim 5 \times 10^8 \text{ M}^{-1}$. Calculation of the allosteric cooperative factor α for supramolecular complexes [3•1₂] and [4•1₂] showed a negative cooperative effect in both cases. The interactions accounting for the formation of the associates are based, first, on the complementary ammonium-crown ether interaction and, second, on the π - π interactions between the porphyrin rings and the C₆₀ moieties. Theoretical calculations have evidenced a significant decrease of the electron density in the porphyrin dimers 3 and 4 upon complexation of the first C₆₀ molecule, in good agreement with the negative cooperativity found in these systems. This negative effect is partially compensated by the stabilizing C₆₀-C₆₀ interactions that take place in the more stable *syn*-disposition of [4•1₂].



INTRODUCTION

In recent years, a large variety of porphyrin-fullerene dyads has been studied in the search for efficient charge- and energy-transfer processes of interest in the area of artificial photosynthesis and organic photovoltaics.¹ Although greater efforts have been devoted to the study of covalent hybrids, supramolecular approaches have also been developed. Thus, supramolecular porphyrin-fullerene associates have been built up by π - π interactions,² in particular with porphyrin tweezers and cages,³ metal-ligand bonds,⁴ hydrogen bonds,⁵ electrostatic interactions,⁶ mechanical bonds,⁷ or a combination of several of these interactions.⁸ Supramolecular arrays involving conjugated multiporphyrin systems are, however, scarce in the literature. Some of us have studied different conjugated polytopic porphyrin receptors with two up to 10 porphyrin subunits.⁹ In those systems, a positive cooperative supramolecular effect was encountered and rationalized by the existence of favorable π - π interactions between the different fullerene moieties interacting with the porphyrin rings. However, in such systems the porphyrin subunits behaved independently, as demon-

strated by comparison of the absorption and emission spectra of the polytopic receptors with those of the corresponding monotopic porphyrin system. On the other hand, Tashiro and Aida studied the supramolecular interaction of a cyclic receptor formed by two fused porphyrin dimers and C₆₀.¹⁰ This receptor was able to complex one unit of C₆₀, while the introduction of a second fullerene moiety was hindered by a strong negative cooperative effect. In this case, the electronic communication between the two fused porphyrins causes a decrease of the affinity of the receptor toward the second C₆₀ unit.

Herein we report the synthesis of two new ditopic porphyrin receptors for C₆₀ (3 and 4), appended with crown ether moieties, to study their complexation with the ammonium salt C₆₀ derivative 1¹¹ (Figure 1). The ammonium-crown ether interaction provides a recognition motif for the supramolecular complexation of two fullerene moieties. While in system 3 the two porphyrins are almost orthogonal, they are fully conjugated

Received: July 18, 2016

Published: September 17, 2016

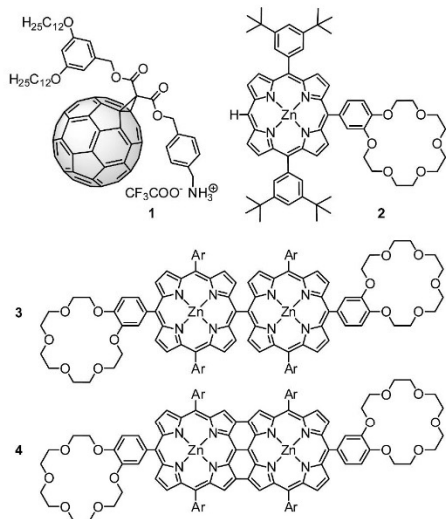


Figure 1. Monoporphyrin **2** was used to obtain host molecules **3** and **4**, which were then complexed with guest molecule **1**.

in the planar fused compound **4**. Theoretical calculations were carried out to understand the nature of the interactions controlling the association processes with special attention to the cooperative effects experimentally evidenced for these systems. For both porphyrinic receptors, the combination of ammonium-crown ether interactions with fullerene-porphyrin interactions provided very stable supramolecular ensembles and negative cooperative effects have been evidenced for the binding of the second fullerene-ammonium salt **1**. Actually, the intramolecular C₆₀-porphyrin interactions of the first guest molecule substantially reduce the electron density in the porphyrin dimers **3** and **4** and thus intramolecular interactions of the second fullerene guest with its porphyrinic receptor are less favorable. Interestingly, this effect is however stronger for compound **3**, despite the reduced electronic communication between the two porphyrinic moieties when compared to porphyrin tape **4**. The negative cooperativity resulting from the fullerene-porphyrin interactions may be partially compensated by additional stabilizing interactions between the guest C₆₀ units in the complex formed with **4**.

RESULTS AND DISCUSSION

Synthesis. Porphyrin dimer **3** was obtained by Ag(I)-promoted oxidative *meso-meso* coupling of monoporphyrin **2**^{2a} in CHCl₃. The proposed mechanism for this reaction is based on the initial one-electron oxidation of a porphyrin unit by AgPF₆ followed by the nucleophilic attack of another neutral porphyrin molecule and its subsequent dehydrogenation.¹² ¹H NMR analysis of the crude reaction mixture after the reaction evidenced the appearance of a signal at -2.92 ppm, corresponding to the partial demetalation of the porphyrin subunits. Therefore, the mixture was treated with a Zn(II) salt to ensure full metalation. Purification of the product was easily achieved by gravity-fed chromatography and gel permeation chromatography due to the good solubility of this derivative,

with an orthogonal conformation hampering aggregation by π - π stacking between molecules.

Triply fused porphyrin tape **4** was obtained in an efficient manner using more oxidative conditions, i.e., Sc(III)-catalyzed oxidation of porphyrin **2** with 2,3-dichloro-5,6-dicyanobenzoquinone. As in the previous case, the reaction was followed by treatment with a Zn(II) salt to ensure full metalation of the product (Scheme S1 in the Supporting Information).

NMR Characterization. ¹H NMR spectroscopic analysis of the aromatic region of dimer **3** provided valuable information on its structure. To start with, the characteristic *meso* proton signal of porphyrin **2** at ~ 10.3 ppm, strongly deshielded by the aromatic ring current, was no longer present (Figures 2a,b).

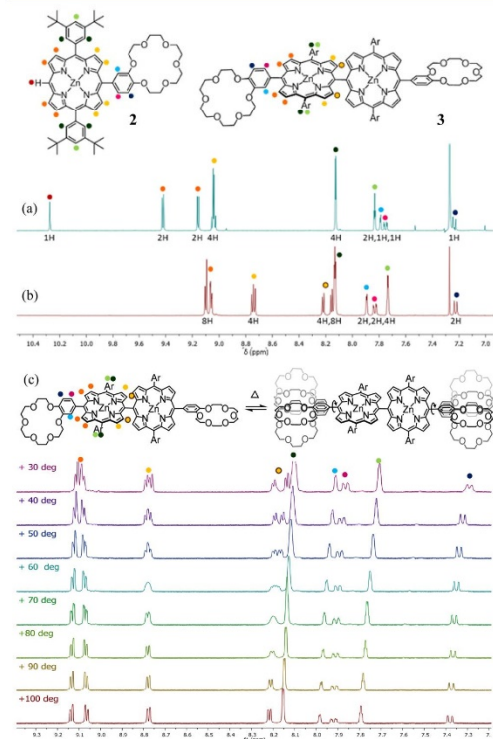


Figure 2. NMR characterization of compound **3**. ¹H NMR (CDCl₃, 400 MHz, 298 K) of monoporphyrin **2** (a) versus *meso-meso* dimer **3** (b) and (c) ¹H NMR variable temperature experiments (ClCD₂CD₂Cl, 400 MHz, 30–100 °C).

Also, inner pyrrolic protons were shifted upfield by 0.85 ppm, in good agreement with an approximate perpendicular arrangement of both subunits, where the ring current of one porphyrin moiety affects the protons of the other moiety.^{12a} Additional through-space correlation NOESY experiments enabled full assignment of all the protons in the aromatic region (Figure S1, Supporting Information).

Variable temperature ¹H NMR studies of **3** (Figure 2c) evidenced the presence of a chiral axis across the porphyrin-benzocrown ether bond. Heating the system led to an increase in its kinetic energy and, thus, the benzocrown ether moieties

started to rotate around the porphyrin-phenyl bonds, overcoming their steric hindrance. The rotational barrier was estimated to be ca. 17 kcal·mol⁻¹ (Figure S2) in line with other experimental measurements on phenyl porphyrins.¹³ As a result of the heating, all pyrrolic protons in the porphyrin were then equally affected by the crown ether, changing the apparent symmetry of the system and reducing the complexity of the spectra. This is evidenced by the appearance of two clear AB systems in the pyrrolic region. A similar effect was observed in the signals corresponding to the crown ether moiety (Figure S3). Rotation around the porphyrin-porphyrin bond is not possible at the measurement conditions due to the higher steric hindrance as will be further demonstrated with UV-vis spectra.

NMR characterization was not possible for molecule 4 due to the appearance of very broad signals, probably as a result of the formation of aggregates. However, its characteristic absorption spectrum, together with its MS spectrum, allowed us to unambiguously characterize the product.

UV-Vis Characterization. The UV-vis absorption spectrum of molecule 3 corresponds to that of a typical *meso-meso* dimer,^{11,14} with a large splitting of the Soret band due to exciton coupling and a Q-band modestly shifted toward the red in comparison with 2, suggesting that each of the porphyrin subunits retains its monomeric electronic character.¹⁵ In contrast, dimer 4 exhibits the characteristic absorption spectrum of a triply fused porphyrin tape, with no splitting of the Soret band and the appearance of a low-lying broad band reaching the 1000 nm region (Figure 3).

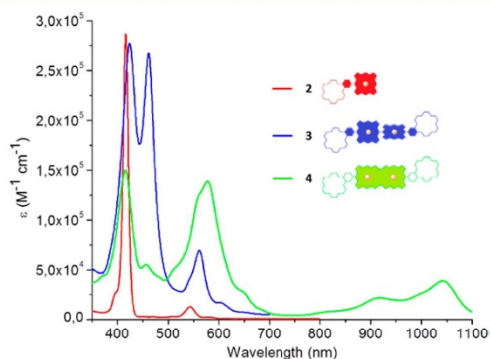


Figure 3. UV-vis spectra of 2 (1.9×10^{-6} M, red), 3 (4.7×10^{-6} M, blue), and 4 (1.1×10^{-5} M, green) in CH_2Cl_2 .

Variable temperature absorption measurements (25–95 °C in PhCl) on porphyrin dimer 3 did not show any clear evidence of rotation around the porphyrin-porphyrin bond (Figure S4).¹⁶

In order to rationalize the changes observed in the UV-vis spectra in passing from 2 to 3 and 4, singlet excited states (S_1) were computed at the B3LYP/(6-31G**+LANL2DZ) level¹⁷ using time-dependent density functional theory (TD-DFT)¹⁸ (see the Supporting Information for full computational details). Table S1 summarizes the most relevant electronic transitions that give shape to the absorption spectra of 2–4. For 2, the electronic transitions to the two low-lying singlet excited states (S_1 and S_2) are computed about 550 nm. These transitions are weak, with oscillator strengths (f) of 0.045 and 0.025,

respectively, correspond to electronic excitations locally centered on the porphyrin core, and give rise to the Q-band observed experimentally at 548 nm. In addition, states S_5 and S_6 computed around 380 nm are responsible for the Soret band observed at 400 nm. The electronic transitions to S_5 and S_6 possess high oscillator strengths of 1.565 and 0.831, respectively, and also imply electronic excitations mainly located on the porphyrin core (Table S1 and Figure S8).

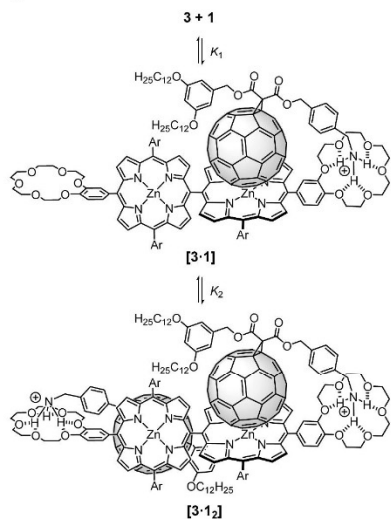
Moving to the porphyrin *meso-meso* dimer 3, the electronic transitions to the S_1 and S_2 states associated with the Q-band are computed at slightly higher wavelengths (in the 570 nm region) due to the small electronic interaction between the two porphyrin moieties that causes a narrowing of the HOMO-LUMO energy gap from 2.71 eV in 2 to 2.55 eV in 3 (Figure S8 and S10). The Soret band, originating now in the S_{17} state ($f = 1.577$), is also red-shifted in comparison with 2. Interestingly, TD-DFT calculations predict an intense S_{11} excited state ($f = 1.022$) lower in energy than S_{17} and computed at 475 nm, which reproduces the splitting of the Soret band and the peak experimentally observed at 460 nm. This state originates in an electronic excitation of the porphyrin moieties with no implication of the peripheral benzene rings or the crown ether groups.

For porphyrin tape dimer 4, the two lowest-lying electronic transitions associated with the S_1 and S_2 states are computed in the 960–970 nm range (Table S1). These two moderately intense transitions ($f = 0.312$ and 0.089, respectively) originate in porphyrin-centered excitations and give rise to the new broad band observed for 4 in the 800–1100 nm range. Their low energy is due to the complementarity of the two fused porphyrin moieties with an efficient π -conjugation between them, which results in a destabilization/stabilization of the HOMOs/LUMOs and, therefore, in a drastic decrease of the HOMO-LUMO gap (1.55 eV, Figure S10). States S_7 and S_{10} computed in the 520–560 nm range give rise to the typical Q-band, which is notoriously more intense than in 2 and 3 as predicted by the oscillator strengths obtained for S_7 (1.150) and S_{10} (0.874). The peripheral benzene rings participate in these states that mainly correspond to the excitation of the porphyrin cores (Table S1 and Figure S9). Finally, several intense transitions are computed in the 385–395 nm region, which give rise to the broad peak observed at 400 nm for the Soret band (Figure 3).

Complexation Studies. Supramolecular ensembles were built up by adding increasing quantities of fullerene derivative 1 over the corresponding porphyrin dimers 3 and 4 in CH_2Cl_2 at room temperature (Schemes 1 and 2). Complexation was followed by monitoring the induced UV-visible spectroscopic changes. In the case of dimer 3, it resulted in a red shift of the Soret bands ($\lambda_{1,\text{max}} = 422 \rightarrow 427$ nm; $\lambda_{2,\text{max}} = 458 \rightarrow 463$ nm), evidencing the presence of intermolecular π - π interactions between the host and the guest (Figure 4).^{8a} A similar behavior was found for the Soret band ($\lambda_{1,\text{max}} = 416 \rightarrow 426$ nm), the Q-band ($\lambda_{2,\text{max}} = 578$ nm \rightarrow 581 nm), and also the red-shifted absorption bands ($\lambda_{3,\text{max}} = 917 \rightarrow 941$ nm; $\lambda_{4,\text{max}} = 1042 \rightarrow 1063$ nm) of porphyrin tape 4 (Figure 5).

A 1:2 stoichiometry was foreseen for both 3 and 4 based on the design of the host molecules and the results previously obtained for the analogous monoporphyrin system [2·1].^{8a} This was further corroborated by ESI MS for a 1:2 mixture of porphyrin dimer 3 and methanofullerene 1 in CH_2Cl_2 , which exhibited a double charged ion peak at m/z 2461.0, ascribed to the 1:2 complex after loss of the trifluoroacetate (TFA)

Scheme 1. Supramolecular Complexes Obtained from Building Blocks 3 and 1



counteranions (Figure S5). A similar result was obtained in the ESI-MS analysis of a 1:2 mixture of porphyrin tape 4 and 1 (Figure S6). The peak corresponding to the 1:1 complex was not detected under these conditions in any case, suggesting that 1:2 complexes are the most abundant species in the analyzed solutions.

It is important to note that, in spite of being formed by a myriad of internal micro equilibria leading to semicomplexed species (Scheme S2), the complexation of 3 and 4 by 1 can be simplified in the two-steps processes sketched in Schemes 1 and 2 (see also Scheme S2b). This is possible due to the high effective molarity found for the analogous [2·1] system (3.16 M^{-1}) evidencing its tendency toward ring-closing under the conditions employed.^{8a} Nonlinear curve fitting to a 1:2 model yields the association constants (K_a) summarized in Table 1. In the case of the complexes formed with porphyrin tape 4, curve fitting was better when performed over the region around 750–1100 nm than over the Soret bands region.

Analysis of the Cooperativity. First evidence of cooperative behavior in the supramolecular complexes formed by 3–4 and 1 arise from the shape of the binding isotherms found for both systems, which are not the rectangular hyperbola expected for a noncooperative system (insets in Figures 4 and 5). Further quantitative analysis can be made if we consider that, even if each of the porphyrin subunits exhibits chelate cooperativity, interactions between subunits can be considered as allosteric (Scheme S2). Therefore, an approximation to the allosteric cooperative factor α can be calculated for these systems.

For [3·1₂], α was estimated by eq 1, where $K \approx K_1$. The value obtained (0.0005) was much lower than unity, thus clearly pointing to a negative cooperativity, i.e., the complexation of the first molecule of 1 leads to a complex where it is more difficult to complex a second equivalent of 1. This result can be in principle explained by invoking the electronic communication between porphyrin moieties, according to

Scheme 2. Supramolecular Complexes Obtained from Building Blocks 4 and 1

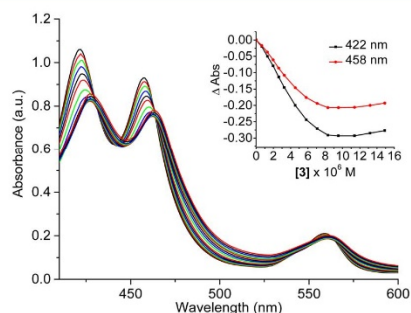
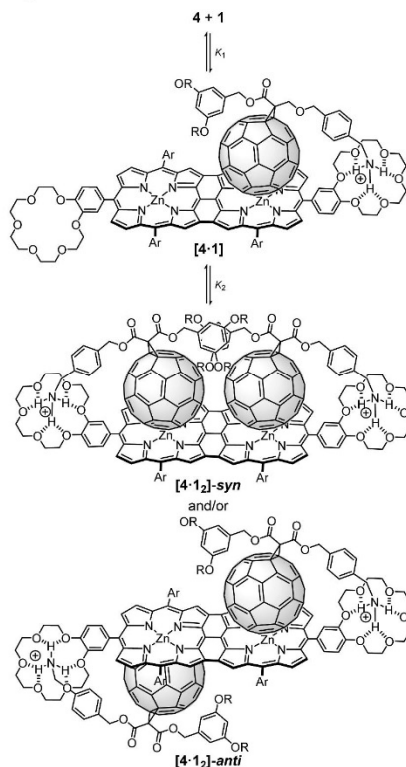


Figure 4. UV-vis spectral changes observed during the complexation of porphyrin dimer 3 ($4.72 \times 10^{-6} \text{ M}$) by addition of 1 (0–3.4 equiv) in CH_2Cl_2 at room temperature. Inset shows the binding isotherm of the Soret bands.

which complexation of a first fullerene molecule by a porphyrin subunit would deplete the electronic density of that porphyrin and its neighbor's, thus decreasing the affinity of the latter toward fullerenes. However, the electronic communication between the porphyrin moieties in 3 is low due to their orthogonal disposition as evidenced above by the UV-vis spectra and the theoretical calculations.

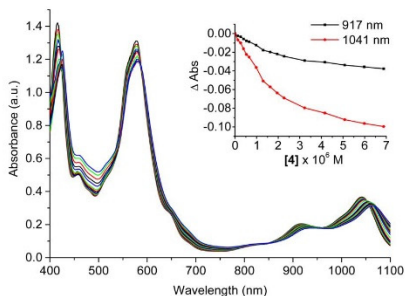


Figure 5. UV-vis spectral changes observed during the complexation of porphyrin tape **4** (1.18×10^{-8} M) by addition of **1** (0–10.5 equiv by 0.7 equiv steps) in CH_2Cl_2 at room temperature. Inset shows the binding isotherm of the low-energy bands.

Table 1. Stepwise Association Constants for $[\mathbf{3}\cdot\mathbf{1}_2]$ and $[\mathbf{4}\cdot\mathbf{1}_2]$

log $K_i \pm 3\sigma$		
3	log K_1	8.7 ± 1.4
	log K_2	5.4 ± 0.9
4	log K_1'	6.8 ± 0.5
	log K_2'	5.4 ± 0.3

$$[\mathbf{3}\cdot\mathbf{1}_2] \quad \alpha = \frac{K_1 K_2}{K^2} = \frac{K_2}{K_1} = \frac{10^{5.4}}{10^{8.7}} = 0.0005 \quad (1)$$

The allosteric cooperativity factor obtained for $[\mathbf{4}\cdot\mathbf{1}_2]$ (eq 2) also evidences a negative cooperativity in the system. In this case, a very efficient electronic communication exists between the porphyrin moieties, and a significant electronic depletion can be expected for the empty porphyrin unit upon complexation of one fullerene guest.

$$[\mathbf{4}\cdot\mathbf{1}_2] \quad \alpha = \frac{K_2}{K_1} = \frac{10^{5.4}}{10^{6.8}} = 0.04 \quad (2)$$

Interestingly, the cooperativity factor obtained for $[\mathbf{4}\cdot\mathbf{1}_2]$ is 80 times larger than that found for $[\mathbf{3}\cdot\mathbf{1}_2]$, suggesting the existence of other interactions that overcome the electronic depletion of the porphyrin tape upon complexation of the first equivalent of **1**. As depicted in Scheme 2, complex $[\mathbf{4}\cdot\mathbf{1}_2]$ can yield two different complexes, $[\mathbf{4}\cdot\mathbf{1}_2]$ -*syn* and $[\mathbf{4}\cdot\mathbf{1}_2]$ -*anti*. Although it is not possible to ascertain which disposition is preferred in solution by spectroscopic measurements, and steric hindrance could be expected to be larger for the *syn* configuration, the possibility of having additional π - π interactions between fullerene moieties in $[\mathbf{4}\cdot\mathbf{1}_2]$ -*syn*, not existent in $[\mathbf{4}\cdot\mathbf{1}_2]$ -*anti*, could explain the larger α value obtained, thus pointing to the *syn* disposition as the one preferred in solution. The relative stability of $[\mathbf{4}\cdot\mathbf{1}_2]$ -*syn* and $[\mathbf{4}\cdot\mathbf{1}_2]$ -*anti* associates is discussed below on the basis of theoretical calculations.

Electrochemical Study. The redox potentials of compounds **2–4** and their supramolecular complexes with **1** have been studied by cyclic voltammetry (CV) and Osteryoung square wave voltammetry (OSWV) measurements in CH_2Cl_2 at room temperature. Results are summarized in Table S2 and Figures S11–S16. For compound **2**, two quasireversible one-electron oxidation processes lead to the formation of the

corresponding radical-cation, in which an electron is delocalized over the porphyrin, and also to the corresponding dication.

Dimer **3** seems to display a behavior close to that of the corresponding monomer **2** (Table S2 and Figures S11 and S14). Indeed, the two porphyrin rings are poorly conjugated and, as a result, the dimer nearly behaves as the juxtaposition of two monomers. Notwithstanding, some electronic communication exists between the two porphyrin moieties because the first two oxidation waves split in two peaks in passing from **2** to **3**.

In contrast, the conjugation of the two porphyrin units has a huge effect on the redox potentials of tape **4** (Table S2 and Figure S14). Conjugation induces an important lowering of the first oxidation ($E_{\text{ox}}^1 = 0.55$ V) and first reduction ($E_{\text{red}}^1 = -0.58$ V) potentials as compared to monomer **2** ($E_{\text{ox}}^1 = 0.87$ V and $E_{\text{red}}^1 = -1.31$ V) and to porphyrin dimer **3** ($E_{\text{ox}}^1 = 0.83$ V and $E_{\text{red}}^1 = -1.28$ V). This trend is supported by theoretical calculations which predict that the HOMO/LUMO increases/decreases drastically in energy in passing from **2** ($-4.73/-2.02$ eV) and **3** ($-4.63/-2.07$ eV) to **4** ($-4.31/-2.77$ eV). Since the porphyrin rings are efficiently conjugated in tape dimer **4**, the resulting unpaired electron is delocalized over the two rings, giving rise to a completely delocalized π radical cation or anion. Dimer **4** therefore constitutes a single redox entity, and the HOMO–LUMO energy gap can be associated with the difference between the first oxidation and first reduction processes: $\Delta'E = E_{\text{ox}}^1 - E_{\text{red}}^1$. Thus, dimer **4** provides a significant decrease in the HOMO–LUMO energy gap as compared to that of monomer **2** ($\Delta'E(\text{monomer } 2) - \Delta'E(\text{tape } 4) = 1.05$ V), due to the lowering of the first oxidation potential by 320 mV and of the first reduction potential by 730 mV. The low electrochemical gap is a direct result of the more extended π -conjugation in the planar triply fused system than in the simply fused **3** or monomer **2**. Calculations predict a decrease of 1.16 eV for the HOMO–LUMO energy gap in passing from **2** to **4**, in good accord with the value obtained from electrochemical data and literature.¹⁹

In OSWV, complexation-induced changes are observed in the porphyrin host molecules **2–4** upon complexation with guest molecule **1** (see Figures S14–S16). Specifically, a significant decrease of the intensity of the oxidation waves below 1.5 V is detected.

It has been previously observed that porphyrins may influence C_{60} reduction potentials, especially its first wave, upon complexation.^{2c,8a,11,20} In the particular case of $[\mathbf{4}\cdot\mathbf{1}_2]$, the C_{60} moiety becomes less favorable to reduction upon complexation, as evidenced by a cathodic shift of 60 mV in the first fullerene-centered reduction (Table S2 and Figure S16), thus suggesting an intramolecular fullerene-porphyrin interaction in $[\mathbf{4}\cdot\mathbf{1}_2]$. Even though the first apparent reduction potential of **4** is close to that of the C_{60} , the change observed in Figure S16 after addition of 2 equiv of C_{60} clearly evidences this interaction: two different peaks at -0.56 V and -0.62 V are clearly distinguishable. The magnitude of the potential shift observed for **4** after guest complexation (60 mV) is similar to that found in other supramolecular complexes such as the Zn-porphyrin sandwich designed by Aida and Saigo.^{20a} However, these strong shifts are not always present. Indeed, redox potentials of fullerene–donor conjugates are generally very weakly affected by intramolecular π - π interactions, even in cyclic systems in which the two components are forced to be at the van der Waals contact.^{2c,21} In our systems, no significant

electrochemical changes are detected for **1** upon complexation with **2** and **3** (Table S2).

The different electrochemical behavior can be explained on the basis of tape **4** being a better donor molecule than **2** and **3**, with an E_{ox}^1 300 mV lower. This is most likely due to the electronic conjugation across the whole molecule, which may render the donor–acceptor electron transfer to the C_{60} easier, something in full agreement with the calculation of the net electronic charges of the [3•1] and [4•1] species (vide infra). Moreover, the analysis of the cooperativity, which emphasizes the role of other interactions, indicates a much higher cooperativity factor for [4•1₂] than for [3•1₂].

Computational Modeling. Theoretical calculations performed at the DFT B97-D3/(6-31G**+LANL2DZ) level of theory^{17b,c,22} were used to provide deeper understanding of the origin and nature of the intermolecular forces driving the supramolecular assembly of dimers **3** and **4** with the fullerene-based compound **1** (see the SI for computational details).

In [3•1], compound **1** interacts with the crown ether through the positively charged ammonium group forming three N–H⋯O(ether) hydrogen-bond interactions in the 1.83–2.00 Å range (Figure 6a). This interaction has been recently demonstrated to

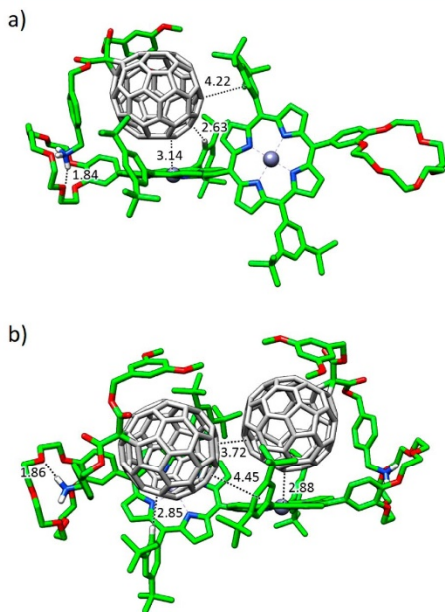


Figure 6. Minimum-energy geometry computed for supramolecular complexes [3•1] (a) and [3•1₂] (b) at the B97-D3/(6-31G**+LANL2DZ) level of theory. Selected intermolecular distances are given in Å. Hydrogen atoms are omitted for clarity.

be the promoting force in the supramolecular assembly between guest **1** and related metalloporphyrin-based hosts with a net stabilizing energy that amounts to -64.9 kcal/mol.^{8a} The fullerene ball of **1** favorably interacts with the porphyrin core of **3** with short metal⋯C(C_{60}) contacts of 3.14 Å. This interaction originates not only from dispersion forces arising from long-range electron correlation effects but also from

strong electrostatic effects when considering metal-substituted porphyrins.^{8a} Furthermore, short H⋯C contacts between the peripheral *tert*-butyl-substituted phenyl rings and C_{60} are computed in the range of 2.5–3.2 Å, which add approximately 1 kcal/mol per each interaction to the final stabilization energy of the complex. More importantly, the vicinal porphyrin, linked to the porphyrin that interacts with **1**, approaches the fullerene fragment and gives rise to additional interactions: short H⋯C contacts in the 2.7–3.2 Å range and a weak π – π interaction between the peripheral benzene ring and the fullerene. In fact, the empty porphyrin core is distorted from linearity with respect to the occupied porphyrin core by approximately 8° to maximize the interaction with C_{60} (Figure 6a). These additional interactions, which are not present in [2•1], can be a plausible explanation for the higher experimental association constant found for porphyrin dimer **3** ($\log K_1 = 8.7 \pm 1.4$) in comparison with monoporphyrin **2** ($\log K_1 = 6.9 \pm 0.2$).^{8a}

Moving to [3•1₂], the second molecule of **1** enters the empty porphyrin core and defines similar interactions to those described for [3•1]. The minimum-energy geometry shows that the two fullerenes tend to approximate each other in order to stabilize the resulting complex (Figure 6b). Close C⋯C contacts between the two C_{60} are computed at 3.7 Å. Again, the peripheral di-*tert*-butylphenyl groups placed on the vicinal porphyrin moieties play an active role in the stabilization of the complex with short H⋯C(C_{60}) contacts around 2.8 Å and π – π interactions at 4.4 Å.

The association between porphyrin tape **4** and **1** (Figure 7a) follows the same pattern as previously described for [3•1]. The ammonium group is bound to the crown ether forming efficient short N–H⋯O(ether) contacts in the 1.94–1.97 Å range. The fullerene interacts with the porphyrin core and with the di-*tert*-butylphenyl groups through metal⋯ C_{60} contacts of 2.87 Å and H⋯ C_{60} distances in the range of 2.7–3.1 Å, respectively. Oddly, the dimer porphyrin tape becomes curved to better embrace the fullerene ball and further stabilize the complex. In contrast to that previously described in [3•1], the di-*tert*-butylphenyl groups of the vicinal porphyrin core are not close enough to interact with C_{60} (closest H⋯C(C_{60}) contact calculated at 3.80 Å) and, therefore, they do not contribute in the stabilization of the [4•1] complex (Figure 7a).

The introduction of the second fullerene-based guest **1** into the [4•1] complex can be achieved in two different ways: the two fullerene balls standing in the same side in a *syn* disposition ([4•1]-*syn*), or the two balls located in opposite sides with respect to the plane generated by the porphyrin tape dimer in an *anti* disposition ([4•1]-*anti*) (Figure 7b and c). In both cases, all the previous intermolecular interactions described for [4•1] exist in the stoichiometric complex 1:2 with short metal⋯ C_{60} contacts in the range of 2.82–2.99 Å and di-*tert*-butylphenyl– C_{60} H⋯C contacts of 2.7–3.1 Å. However, by comparing the *anti* with the *syn* complex, an important π – π stabilizing interaction arises for the latter due to the fullerene–fullerene proximity (ring-to-ring distance calculated at 3.46 Å). A recent study on related fullerene-based adducts showed the key importance of the stabilizing C_{60} – C_{60} interactions, resulting in an energy differentiation between the *syn* and *anti* dispositions of more than 5 kcal/mol in favor of *syn*.²³

Single-point energy B97-D3 calculations were performed on the B97-D3/(6-31G**+LANL2DZ)-optimized geometries by using the more extended cc-pVTZ+LANL2DZ basis set to estimate the binding energy (E_{bind}) for all the supramolecular complexes (Table 2). The association of one molecule of **1** to

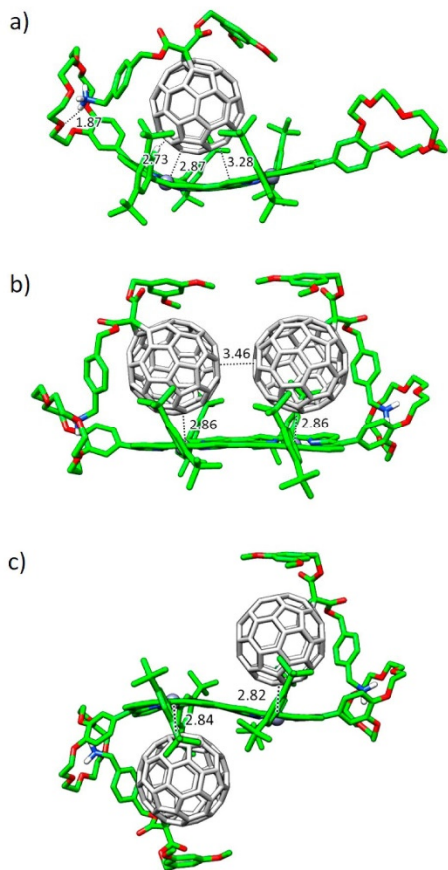


Figure 7. Minimum-energy geometry computed for $[4\cdot 1]$ (a) $[4\cdot 1_2]$ -*syn* (b) and $[4\cdot 1_2]$ -*trans* (c) at the B97-D3/(6-31G**+LANL2DZ) level of theory. Selected intermolecular distances are given in Å. Hydrogen atoms are omitted for clarity.

Table 2. Binding Energies Computed at the B97-D3/(cc-pVTZ+LANL2DZ) Level for the Host–Guest Supramolecular Associates with Stoichiometry 1:1 and 1:2

complex	E_{bind} (kcal/mol)
$[3\cdot 1]$	−108.19
$[3\cdot 1_2]$	−211.05
$[4\cdot 1]$	−98.40
$[4\cdot 1_2]$ - <i>anti</i>	−195.46
$[4\cdot 1_2]$ - <i>syn</i>	−200.20

the *meso*–*meso* porphyrin dimer **3** leads to a large net stabilization of −108.19 kcal/mol rising especially from the N–H⋯O(ether) contacts and the porphyrin core– C_{60} interaction. Additionally, the di-*tert*-butylphenyl groups contribute to the final stabilization of the complex by approximately 1 kcal/mol per H⋯ C_{60} contact (total number of contacts = 6). Upon the inclusion of the second molecule of **1**, E_{bind} is approximately doubled, reaching a value of −211.05

kcal/mol for $[3\cdot 1_2]$. The additional fullerene–fullerene stabilizing interactions in $[3\cdot 1_2]$ with respect to $[3\cdot 1]$ are counteracted by the poorer disposition of the balls to interact with the di-*tert*-butylphenyl groups of the vicinal porphyrin moiety that contribute to the stabilization of $[3\cdot 1]$.

For $[4\cdot 1]$, the binding energy is computed to be −98.40 kcal/mol. This value is 10 kcal/mol lower than in $[3\cdot 1]$ due to the less-efficient interaction with the vicinal empty porphyrin (compare Figures 6a and 7a). Upon addition of the second molecule of **1** in an *anti* disposition ($[4\cdot 1_2]$ -*anti*), E_{bind} is computed at −195.46 kcal/mol, almost twice the binding energy of $[4\cdot 1]$ (Table 2). Finally, a slightly larger stabilization of −200.20 kcal/mol is obtained for the $[4\cdot 1_2]$ -*syn* complex. As suggested above, the additional C_{60} – C_{60} interaction with a short π – π contact calculated at 3.46 Å overcomes the steric hindrance between the two balls and makes the *syn* complex 5 kcal/mol more stable than the *anti*. This value is in good accord with the energy difference of 6.36 kcal/mol recently reported in favor of the *cis* configuration in a related pentacene- C_{60} derivative.²³

The theoretical values predicted for E_{bind} (Table 2) therefore indicate that the incorporation of the first guest molecule leads to a more stable complex for **3** than for **4**, and suggest that the entrance of the second molecule of **1** is more favored for **4** than for **3**. These trends are in accord with the higher association constant K_1 obtained for **4**, and with the smaller decrease it experiences for **4** in passing from the 1:1 to the 1:2 stoichiometry (Table 1). A direct correlation between the theoretical values predicted for E_{bind} and the experimental values of K_n is however not straightforward because calculations do not take into account the desolvation energy needed to form the complexes in solution.

To help in the rationalization of the experimental values of the association constants for both the 1:1 and 1:2 complexes (Table 1), net electronic charges were calculated at the B97-D3/(6-31G**+LANL2DZ) level for $[3\cdot 1]$ and $[4\cdot 1]$ using the natural population analysis (NPA) approach.²⁴ Upon inclusion of the first **1** molecule, the electron-donor porphyrin dimer **3** transfers 0.19e to the fullerene-based acceptor. The porphyrin moiety interacting with the C_{60} ball accumulates a positive charge of +0.16e, whereas the vicinal empty porphyrin bears a residual positive charge of only +0.03e. Moving to $[4\cdot 1]$, the fullerene-based **1** system borrows 0.26e from the porphyrin dimer. In contrast to $[3\cdot 1]$, the C_{60} -interacting porphyrin moiety bears a smaller positive charge of +0.11e compared to the empty porphyrin fragment (+0.15e). The efficient π -conjugation between the two porphyrin moieties in porphyrin type **4** explains the charge transfer from one fragment to the other. Theoretical calculations therefore predict a notable decrease in the electron density for both *meso* and *tape* porphyrin dimers in the ground state upon complexation of the first **1** acceptor molecule. The decrease of electronic density disfavors the entrance of the second guest molecule and contributes to the remarkable change of the association constant ($\log K_n$), from 8.7 to 5.4 in $[3\cdot 1_2]$ and from 6.8 to 5.4 in $[4\cdot 1_2]$, when the second **1** molecule is included to form the stoichiometric 1:2 complex. For complex $[4\cdot 1_2]$, the stabilizing interactions between the C_{60} units found for the more stable *cis* disposition partially compensate for the negative effect provoked by the lowered electronic density. However, other factors such as the steric hindrance provoked by the long alkyl chains born by the guest molecules should be considered

to fully justify these trends and the higher negative cooperativity shown by **3** compared to **4**.

CONCLUSION

In conclusion, we have studied the supramolecular interaction of porphyrin dimer **3** and porphyrin tape **4**, endowed with crown ether rings, with C_{60} derivative **1**. The formation of the complexes is driven by the complementary ammonium-crown ether H-bonding interactions and the π - π interactions between the porphyrin rings and the C_{60} moieties. Both porphyrin systems form complexes with 1:1 and 1:2 stoichiometries, and present a negative cooperativity, showing a decrease of the binding constants for the complexation of the second fullerene unit. This fact is justified by the decrease of the donating ability of the second porphyrin moiety once the first fullerene unit has been added. In the case of compound **4**, the two porphyrins moieties present a very effective π -conjugation that allows for a larger charge transfer between them upon the inclusion of the first guest molecule. However, this negative effect is partially compensated by the favorable π - π interaction between the two fullerene guests in the more stable *syn* disposition of [4 \cdot 1 $_2$] and, therefore, the decrease of the binding constant for the addition of the second fullerene unit in [4 \cdot 1 $_2$] is not as large as observed for [3 \cdot 1 $_2$]. The supramolecular arrays studied in this work constitute singular examples that will help one to better understand the supramolecular recognition of fullerenes by porphyrin-based hosts, in the quest for efficient charge- and energy-transfer architectures potentially useful in artificial photosynthesis and organic photovoltaics.

ASSOCIATED CONTENT

Supporting Information

The Supporting Information is available free of charge on the ACS Publications website at DOI: 10.1021/jacs.6b07250.

Experimental and computation details. Figures S1–S16. Tables S1–S2. Schemes S1–S2. (PDF)

AUTHOR INFORMATION

Corresponding Authors

*enrique.orti@uv.es

*nazmar@ucm.es

*nierengarten@unistra.fr

Notes

The authors declare no competing financial interest.

ACKNOWLEDGMENTS

Financial support by the European Research Council (ERC-320441-Chiralcarbon), the Ministerio de Economía y Competitividad (MINECO) of Spain (projects CTQ2014-52045-R, CTQ2015-71154-P, CTQ2015-71936-REDT, and Unidad de Excelencia María de Maeztu MDM-2015-0538), the Comunidad Autónoma de Madrid (PHOTOCARBON project S2013/MIT-2841), the Generalitat Valenciana (PROMETEO/2016/135), European FEDER funds (CTQ2015-71154-P), the International Center for Frontier Research in Chemistry (icFRC) and the Labex Chimie des Systèmes Complexes is acknowledged. L.M. thanks the Obra Social "la Caixa" for a postgraduate fellowship. J.C. acknowledges the Spanish Ministry of Education, Culture, and Sport (MECD) for a FPU grant. N.M. thanks to Alexander von Humboldt Foundation. The authors thank to Prof. J. F. Nierengarten for the cover art design.

REFERENCES

- (1) (a) Garg, V.; Kodis, G.; Chachivili, M.; Hambourger, M.; Moore, A. L.; Moore, T. A.; Gust, D. *J. Am. Chem. Soc.* **2011**, *133*, 2944. (b) Guldi, D. M. *Chem. Soc. Rev.* **2002**, *31*, 22. (c) Kuramochi, Y.; Sandanayaka, A. S. D.; Satake, A.; Araki, Y.; Ogawa, K.; Ito, O.; Kobuke, Y. *Chem. - Eur. J.* **2009**, *15*, 2317. (d) Kuhri, S.; Charalambidis, G.; Angaridis, P. A.; Lazarides, T.; Pagona, G.; Tagmatarchis, N.; Coutsolelos, A. G.; Guldi, D. M. *Chem. - Eur. J.* **2014**, *20*, 2049. (e) Umeyama, T.; Imahori, H. *Photosynth. Res.* **2006**, *87*, 63. (f) Wielopolski, M.; Molina-Ontoria, A.; Schubert, C.; Margraf, J. T.; Krokos, E.; Kirschner, J.; Gouloumis, A.; Clark, T.; Guldi, D. M.; Martin, N. *J. Am. Chem. Soc.* **2013**, *135*, 10372. (g) Fukuzumi, S.; Ohkubo, K.; D'Souza, F.; Sessler, J. L. *Chem. Commun.* **2012**, *48*, 9801.
- (2) (a) Boyd, P. D. W.; Hodgson, M. C.; Rickard, C. E. F.; Oliver, A. G.; Chaker, L.; Brothers, P. J.; Bolskar, R. D.; Tham, F. S.; Reed, C. A. *J. Am. Chem. Soc.* **1999**, *121*, 10487. (b) Kimura, M.; Saito, Y.; Ohta, K.; Hanabusa, K.; Shirai, H.; Kobayashi, N. *J. Am. Chem. Soc.* **2002**, *124*, 5274. (c) Saegusa, Y.; Ishizuka, T.; Kojima, T.; Mori, S.; Kawano, M.; Kojima, T. *Chem. - Eur. J.* **2015**, *21*, 5302.
- (3) (a) Hosseini, A.; Taylor, S.; Accorsi, G.; Armaroli, N.; Reed, C. A.; Boyd, P. D. W. *J. Am. Chem. Soc.* **2006**, *128*, 15903. (b) Durot, S.; Taesch, J.; Heitz, V. *Chem. Rev.* **2014**, *114*, 8542. (c) Garcia-Simon, C.; Costas, M.; Ribas, X. *Chem. Soc. Rev.* **2016**, *45*, 40. (d) Nakamura, T.; Ube, H.; Miyake, R.; Shionoya, M. *J. Am. Chem. Soc.* **2013**, *135*, 18790. (e) Song, J.; Aratani, N.; Shinokubo, H.; Osuka, A. *J. Am. Chem. Soc.* **2010**, *132*, 16356. (f) Meng, W.; Breiner, B.; Rissanen, K.; Thoburn, J. D.; Clegg, J. K.; Nitschke, J. R. *Angew. Chem., Int. Ed.* **2011**, *50*, 3479.
- (4) (a) Stangel, C.; Schubert, C.; Kuhri, S.; Rotas, G.; Margraf, J. T.; Regulska, E.; Clark, T.; Torres, T.; Tagmatarchis, N.; Coutsolelos, A. G.; Guldi, D. M. *Nanoscale* **2015**, *7*, 2597. (b) Garg, V.; Kodis, G.; Liddell, P. A.; Terazono, Y.; Moore, T. A.; Moore, A. L.; Gust, D. J. *Phys. Chem. B* **2013**, *117*, 11299. (c) D'Souza, F.; Smith, P. M.; Zandler, M. E.; McCarty, A. L.; Itou, M.; Araki, Y.; Ito, O. *J. Am. Chem. Soc.* **2004**, *126*, 7898. (d) Trabolsi, A.; Elhabiri, M.; Urbani, M.; Delgado de la Cruz, J. L.; Ajamaa, F.; Solladie, N.; Albrecht-Gary, A.-M.; Nierengarten, J.-F. *Chem. Commun.* **2005**, 5736. (e) Lee, C. Y.; Jang, J. K.; Kim, C. H.; Jung, J.; Park, B. K.; Park, J.; Choi, W.; Han, Y.-K.; Joo, T.; Park, J. T. *Chem. - Eur. J.* **2010**, *16*, 5586.
- (5) (a) Dordevic, L.; Marangoni, T.; De Leo, F.; Papagiannouli, I.; Aloukos, P.; Couris, S.; Pavoni, E.; Monti, F.; Armaroli, N.; Prato, M.; Bonifazi, D. *Phys. Chem. Chem. Phys.* **2016**, *18*, 11858. (b) Xenogiannopoulou, E.; Medved, M.; Iliopoulos, K.; Couris, S.; Papadopoulos, M. G.; Bonifazi, D.; Soombar, C.; Mateo-Alonso, A.; Prato, M. *ChemPhysChem* **2007**, *8*, 1056. (c) Aloukos, P.; Iliopoulos, K.; Couris, S.; Guldi, D. M.; Soombar, C.; Mateo-Alonso, A.; Nagaswaran, P. G.; Bonifazi, D.; Prato, M. *J. Mater. Chem.* **2011**, *21*, 2524. (d) Sánchez, L.; Sierra, M.; Martín, N.; Myles, A. J.; Dale, T. J.; Rebek, J.; Seitz, W.; Guldi, D. M. *Angew. Chem., Int. Ed.* **2006**, *45*, 4637. (e) Wessendorf, F.; Grimm, B.; Guldi, D. M.; Hirsch, A. *J. Am. Chem. Soc.* **2010**, *132*, 10786. (f) Maligaspe, E.; Tkachenko, N. V.; Subbaiyan, N. K.; Chitta, R.; Zandler, M. E.; Lemmetyinen, H.; D'Souza, F. *J. Phys. Chem. A* **2009**, *113*, 8478. (g) D'Souza, F.; Wijesinghe, C. A.; El-Khouly, M. E.; Hudson, J.; Niemi, M.; Lemmetyinen, H.; Tkachenko, N. V.; Zandler, M. E.; Fukuzumi, S. *Phys. Chem. Chem. Phys.* **2011**, *13*, 18168. (h) D'Souza, F.; Venukadasula, G. M.; Yamanaka, K.-i.; Subbaiyan, N. K.; Zandler, M. E.; Ito, O. *Org. Biomol. Chem.* **2009**, *7*, 1076. (i) Wessendorf, F.; Gnichwitz, J.-F.; Sarova, G. H.; Hager, K.; Hartnagel, U.; Guldi, D. M.; Hirsch, A. *J. Am. Chem. Soc.* **2007**, *129*, 16057. (j) D'Souza, F.; Maligaspe, E.; Ohkubo, K.; Zandler, M. E.; Subbaiyan, N. K.; Fukuzumi, S. *J. Am. Chem. Soc.* **2009**, *131*, 8787.
- (6) (a) Balbinot, D.; Atalick, S.; Guldi, D. M.; Hatzimarinaki, M.; Hirsch, A.; Jux, N. *J. Phys. Chem. B* **2003**, *107*, 13273. (b) Grimm, B.; Kamas, E.; Brettreich, M.; Ohta, K.; Hirsch, A.; Guldi, D. M.; Torres, T.; Sessler, J. L. *J. Phys. Chem. B* **2010**, *114*, 14134.
- (7) (a) Megiatto, J. D.; Schuster, D. I.; de Miguel, G.; Wolfrum, S.; Guldi, D. M. *Chem. Mater.* **2012**, *24*, 2472. (b) Megiatto, J. D.; Schuster, D. I.; Abwandner, S.; de Miguel, G.; Guldi, D. M. *J. Am. Chem. Soc.* **2010**, *132*, 3847. (c) Jakob, M.; Berg, A.; Rubin, R.

Levanon, H.; Li, K.; Schuster, D. I. *J. Phys. Chem. A* **2009**, *113*, 5846.
(d) Megiatto, J. D.; Li, K.; Schuster, D. I.; Palkar, A.; Herranz, M. Á.; Echegoyen, L.; Abwandner, S.; de Miguel, G.; Guldi, D. M. *J. Phys. Chem. B* **2010**, *114*, 14408. (e) Sasabe, H.; Sandanayaka, A. S. D.; Kihara, N.; Furusho, Y.; Takata, T.; Araki, Y.; Ito, O. *Phys. Chem. Chem. Phys.* **2009**, *11*, 10908. (f) Li, K.; Schuster, D. I.; Guldi, D. M.; Herranz, M. Á.; Echegoyen, L. *J. Am. Chem. Soc.* **2004**, *126*, 3388. (g) Watanabe, N.; Kihara, N.; Furusho, Y.; Takata, T.; Araki, Y.; Ito, O. *Angew. Chem., Int. Ed.* **2003**, *42*, 681.

(8) (a) Moreira, L.; Calbo, J.; Illescas, B. M.; Aragó, J.; Nierengarten, J.; Delavaux-Nicot, B.; Orti, E.; Martín, N.; Nierengarten, J.-F. *Angew. Chem., Int. Ed.* **2015**, *54*, 1255. (b) Calderon, R. M. K.; Valero, J.; Grimm, B.; de Mendoza, J.; Guldi, D. M. *J. Am. Chem. Soc.* **2014**, *136*, 11436. (c) Wu, Z.-Q.; Shao, X.-B.; Li, C.; Hou, J.-L.; Wang, K.; Jiang, X.-K.; Li, Z.-T. *J. Am. Chem. Soc.* **2005**, *127*, 17460. (d) Solladie, N.; Walther, M. E.; Gross, M.; Figueira Duarte, T. M.; Bourgogne, C.; Nierengarten, J.-F. *Chem. Commun.* **2003**, 2412. (e) D'Souza, F.; Chitta, R.; Gadde, S.; Zandler, M. E.; McCarty, A. L.; Sandanayaka, A. S. D.; Araki, Y.; Ito, O. *J. Phys. Chem. A* **2006**, *110*, 4338. (f) Fang, X.; Zhu, Y.-Z.; Zheng, J.-Y. *J. Org. Chem.* **2014**, *79*, 1184.

(9) Trabolsi, A.; Urbani, M.; Delgado, J. L.; Ajamaa, F.; Elhabiri, M.; Solladié, N.; Nierengarten, J.-F.; Albrecht-Gary, A.-M. *New J. Chem.* **2008**, *32*, 159.

(10) Sato, H.; Tashiro, K.; Shinmori, H.; Osuka, A.; Murata, Y.; Komatsu, K.; Aida, T. *J. Am. Chem. Soc.* **2005**, *127*, 13086.

(11) Bonifazi, D.; Accorsi, G.; Armaroli, N.; Song, F.; Palkar, A.; Echegoyen, L.; Scholl, M.; Seiler, P.; Jaun, B.; Diederich, F. *Helv. Chim. Acta* **2005**, *88*, 1839.

(12) (a) Osuka, A.; Shimidzu, H. *Angew. Chem., Int. Ed. Engl.* **1997**, *36*, 135. (b) Ogawa, T.; Nishimoto, Y.; Yoshida, N.; Ono, N.; Osuka, A. *Angew. Chem., Int. Ed.* **1999**, *38*, 176.

(13) Medforth, C. J.; Haddad, R. E.; Muzzi, C. M.; Dooley, N. R.; Jaquinod, L.; Shyr, D. C.; Nurco, D. J.; Olmstead, M. M.; Smith, K. M.; Ma, J.-G.; Shelnutz, J. A. *Inorg. Chem.* **2003**, *42*, 2227.

(14) Cho, H. S.; Jeong, D. H.; Cho, S.; Kim, D.; Matsuzaki, Y.; Tanaka, K.; Tsuda, A.; Osuka, A. *J. Am. Chem. Soc.* **2002**, *124*, 14642.

(15) Kim, Y. H.; Jeong, D. H.; Kim, D.; Jeoung, S. C.; Cho, H. S.; Kim, S. K.; Aratani, N.; Osuka, A. *J. Am. Chem. Soc.* **2001**, *123*, 76.

(16) Kim, D.; Osuka, A. *J. Phys. Chem. A* **2003**, *107*, 8791.

(17) (a) Becke, A. D. *J. Chem. Phys.* **1993**, *98*, 5648. (b) Francl, M. M.; Pietro, W. J.; Hehre, W. J.; Binkley, J. S.; Gordon, M. S.; DeFrees, D. J.; Pople, J. A. *J. Chem. Phys.* **1982**, *77*, 3654. (c) Hay, P. J.; Wadt, W. R. *J. Chem. Phys.* **1985**, *82*, 299.

(18) Casida, M. E.; Jamorski, C.; Casida, K. C.; Salahub, D. R. *J. Chem. Phys.* **1998**, *108*, 4439.

(19) Fendt, L.-A.; Fang, H.; Plonska-Brzezinska, M. E.; Zhang, S.; Cheng, F.; Braun, C.; Echegoyen, L.; Diederich, F. *Eur. J. Org. Chem.* **2007**, 4659.

(20) (a) Tashiro, K.; Aida, T.; Zheng, J.-Y.; Kinbara, K.; Saigo, K.; Sakamoto, S.; Yamaguchi, K. *J. Am. Chem. Soc.* **1999**, *121*, 9477. (b) Sutton, L. R.; Scheloske, M.; Pirner, K. S.; Hirsch, A.; Guldi, D. M.; Gisselbrecht, J.-P. *J. Am. Chem. Soc.* **2004**, *126*, 10370.

(21) (a) Bourgeois, J.-P.; Diederich, F.; Echegoyen, L.; Nierengarten, J.-F. *Helv. Chim. Acta* **1998**, *81*, 1835. (b) Figueira-Duarte, T. M.; Lloveras, V.; Vidal-Gancedo, J.; Delavaux-Nicot, B.; Duhayon, C.; Veciana, J.; Rovira, C.; Nierengarten, J.-F. *Eur. J. Org. Chem.* **2009**, 5779. (c) Mukherjee, S.; Banerjee, S.; Bauri, A. K.; Bhattacharya, S. *J. Mol. Struct.* **2011**, *1004*, 13. (d) Iehl, J.; Vartanian, M.; Holler, M.; Nierengarten, J.-F.; Delavaux-Nicot, B.; Strub, J.-M.; Van Dorsselaer, A.; Wu, Y.; Mohanraj, J.; Yoosaf, K.; Armaroli, N. *J. Mater. Chem.* **2011**, *21*, 1562.

(22) (a) Grimme, S.; Antony, J.; Ehrlich, S.; Krieg, H. *J. Chem. Phys.* **2010**, *132*, 154104. (b) Grimme, S.; Ehrlich, S.; Goerigk, L. *J. Comput. Chem.* **2011**, *32*, 1456.

(23) Zhang, J.; Dolg, M. *Chem. - Eur. J.* **2014**, *20*, 13909.

(24) Reed, A. E.; Weinstock, R. B.; Weinhold, F. *J. Chem. Phys.* **1985**, *83*, 735.

Fullerene Fragments

Electron Transfer in a Supramolecular Associate of a Fullerene Fragment**

María Gallego, Joaquín Calbo, Juan Aragón, Rafael M. Krick Calderon, Fernando H. Liquido, Takahiro Iwamoto, Allison K. Greene, Edward A. Jackson, Emilio M. Pérez, Enrique Ortí,* Dirk M. Guldi,* Lawrence T. Scott,* and Nazario Martín*

Abstract: Herein, we investigate the association of a fullerene fragment, hemifullerene $C_{30}H_{12}$, with an electron-donating bowl-shaped tetrathiafulvalene derivative (truxTTF). UV/Vis titrations and DFT calculations support formation of the supramolecular complex, for which an association constant of $\log K_a = 3.6 \pm 0.3$ in $CHCl_3$ at room temperature is calculated. Remarkably, electron transfer from truxTTF to $C_{30}H_{12}$ to form the fully charge-separated species takes place upon irradiation of the associate with light, constituting the first example in which a fullerene fragment mimics the electron-accepting behavior of fullerenes within a supramolecular complex.

The different nanoforms of carbon,^[1] namely fullerenes,^[2] carbon nanotubes,^[3] and graphene,^[4] each present distinct extraordinary properties that have attracted a great deal of attention in different areas of research. Fullerenes, in particular C_{60} and its derivatives, have been thoroughly studied as electron acceptors in fundamental investigations of photoinduced electron transfer (PET) processes, combined with a variety of electron donors in covalent and noncovalent dyads.^[5] From an application point of view, C_{60} and C_{70} derivatives are by far the most commonly utilized n-type semiconducting materials in organic solar cells.^[6] In the case of carbon nanotubes, both their mechanical and optoelectronic properties have been exploited to construct a variety of devices, including field-effect transistors and sensors.^[7] Finally, graphene is currently considered to have the potential to be the “balm of Fierabras” of carbon-based technologies. Transparent electrodes,^[8] extremely sensitive sensors,^[9] super-

capacitors,^[10] and lightweight high-performance materials^[11] have all been postulated as potential applications of graphene.^[12]

Molecular fragments of these carbon nanoforms^[13] can serve as model systems for their investigation, with the added value of their synthetic availability in pure form with a well-defined molecular structure. The coordination of metal cations by fullerene fragments has been thoroughly studied, and they have also been used frequently to construct receptors for fullerenes,^[14] but their binding by other organic hosts has not been investigated thus far. Herein, we present the first insights into the supramolecular association of a fullerene fragment (hemifullerene, $C_{30}H_{12}$) with a bowl-shaped electron donor molecule, based on a truxene core to which three dithiole rings are covalently attached (truxTTF).^[15] The chemical structures of $C_{30}H_{12}$ and truxTTF are shown in Figure 1 a.

Several syntheses^[16] and two crystal structures^[17] of hemifullerene $C_{30}H_{12}$ were reported a few years ago. In the solid state, two polymorphs were found, each of which showed a different packing motif, originating from the interaction between the $C_{30}H_{12}$ molecules. In the trigonal polymorph, bowl-in-bowl columnar stacks were found, an arrangement in which π - π interactions are maximized (Figure 1 b). In the orthorhombic polymorph, each hemifullerene inserts one of its six-membered rings into the cavity of a neighboring molecule, forming dimers in which both CH- π and π - π interactions play a primary role (Figure 1 c). On the other hand, in truxTTF, a bowl-in-bowl arrangement is prevented

[*] M. Gallego, Prof. Dr. N. Martín
Departamento de Química Orgánica, Fac. C.C. Químicas
Universidad Complutense de Madrid
Av. Complutense s/n, 28040 Madrid (Spain)
E-mail: nazmar@quim.ucm.es
Homepage: <http://www.ucm.es/info/fullerene/>

J. Calbo, Dr. J. Aragón, Prof. Dr. E. Ortí
Instituto de Ciencia Molecular, Universidad de Valencia
46980 Paterna (Spain)
E-mail: enrique.orti@uv.es

R. M. Krick Calderon, Prof. Dr. D. M. Guldi
Department of Chemistry and Pharmacy & Interdisciplinary Center
for Molecular Materials (ICMM), Friedrich-Alexander-Universität
Erlangen-Nürnberg, Egerlandstraße 3, 91058 Erlangen (Germany)
E-mail: guldi@chemie.uni-erlangen.de

F. H. Liquido, T. Iwamoto, A. K. Greene, E. A. Jackson,
Prof. Dr. L. T. Scott
Merkert Chemistry Center, Boston College
Chestnut Hill, MA-02467-3860 (USA)

E-mail: lawrence.scott@bc.edu

Dr. E. M. Pérez, Prof. Dr. N. Martín
IMDEA-nanociencia, C/Faraday 9, Ciudad Universitaria de
Cantoblanco, 28049 Madrid (Spain)

[**] This work was supported by the ERC (AdG ChiralCarbon ERC-2012-ADG_20120216), the MINECO of Spain (CTQ2011-24652, CTQ2011-25714, CTQ2012-31914, PIB2010P-00196, and Consolider-Ingenio CSD2007-00010), the CAM (MADRISOLAR-2 S2009/PPQ-1533), the Generalitat Valenciana (PROMETEO/2012/053), the European FEDER funds (CTQ2012-31914), and the Bavarian Initiative “Solar Technologies go Hybrid”. E.M.P. is thankful to the MINECO for a Ramón y Cajal research fellowship. M.G. and J.C. acknowledge the Spanish Ministry of Education, Culture and Sport (MECD) for FPU grants. T.I. is grateful to The Kyoto University Foundation for an overseas study fellowship.

Supporting information for this article is available on the WWW under <http://dx.doi.org/10.1002/anie.201309672>.

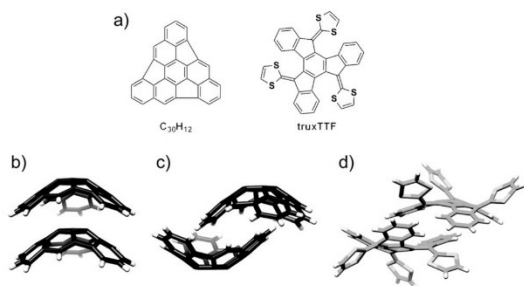


Figure 1. a) Chemical structures of hemifullerene $C_{30}H_{12}$ and truxTTF. b,c) Structures of the dimers formed by $C_{30}H_{12}$ (C black) in its trigonal and orthorhombic crystal polymorphs, respectively. d) Structure of the dimers formed by truxTTF (C gray, S light gray) in its crystal packing.

by the protruding dithiole rings and, consequently, only the dimeric form in which one of the aromatic rings of each monomer is placed inside the cavity of the other is found (Figure 1 d). Because of their concave shape, both $C_{30}H_{12}$ and truxTTF are inherently chiral,^[18] consequently, each is obtained as a racemic mixture of two enantiomers.

Considering the ability of truxTTF to associate fullerenes,^[15,19] and its electron-donating character, we reasoned that it should also be able to bind $C_{30}H_{12}$, forming heteromolecular bowl–bowl complexes. To explore this possibility, we first carried out density functional theory (DFT) calculations on four different supramolecular truxTTF- $C_{30}H_{12}$ models, which were rationally constructed from the crystallographic information on both $C_{30}H_{12}$ and truxTTF. All of the models proposed were fully optimized using the revPBE0-D3 functional,^[20] which is capable of capturing the dispersion effects and is one of the best density functionals to accurately describe supramolecular complexes governed by π - π interactions.^[21] The revPBE0-D3 functional has been successfully applied in the structural and energetic characterization of related supramolecular nanoarchitectures between a tetra-thiafulvalene derivative and a graphene sheet model.^[22]

Figure 2 displays the minimum-energy structures (**1–4**) computed for the truxTTF- $C_{30}H_{12}$ heterodimer at the revPBE0-D3/cc-pVTZ level. The most relevant intermolecular distances in **1–4** are given in Figure S1 in the Supporting Information. The truxTTF- C_{60} associate was also calculated at the same level of theory (Figure S2). In structures **1** and **2**, the convex surface of the $C_{30}H_{12}$ bowl perfectly matches the two concave cavities of the truxTTF host; that is, either through the cavity formed by the carbon backbone (structure **1**) or through the cavity formed by the central benzene ring and the three dithiole rings (structure **2**). Both structures can be thus seen as bowl-in-bowl arrangements where π - π interactions are maximized. The concave cavities of truxTTF and $C_{30}H_{12}$ can also interact, giving rise to heterodimers in which either a benzene or a dithiole ring of the truxTTF molecule is placed inside the concave cavity of the hemifullerene bowl (structures **3** and **4**, respectively). The optimized heterodimeric structures **1–4** all show close intermolecular contacts in the 2.5–3.7 Å range (Figure S1), which is indicative of the positive noncovalent interaction between both bowls.

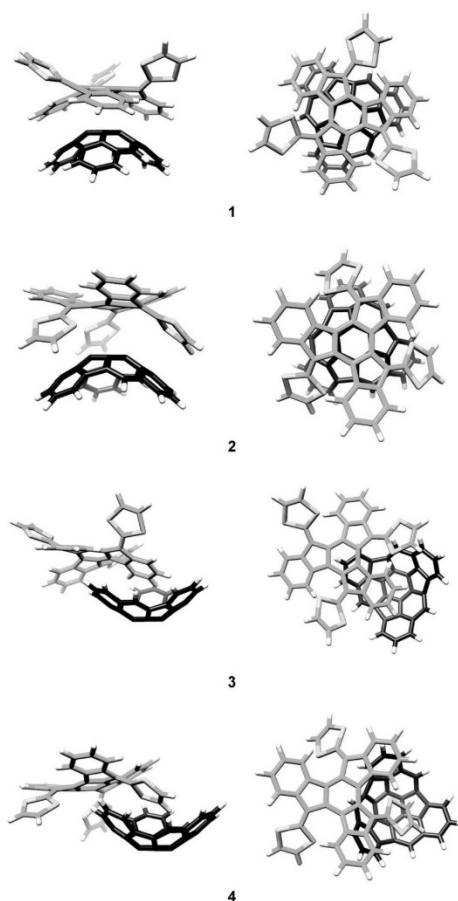


Figure 2. Minimum-energy structures (**1–4**) computed for the truxTTF- $C_{30}H_{12}$ heterodimer at the revPBE0-D3/cc-pVTZ level. For truxTTF: C gray, S light gray, H white. For $C_{30}H_{12}$: C black, H white.

To assess the strength of the interaction between the truxTTF and $C_{30}H_{12}$ bowls, association energies for the previously optimized heterodimers were also calculated at revPBE0-D3/cc-pVTZ. The four supramolecular structures **1–4** exhibit significant gas-phase association energies, ranging from -21.0 and -19.4 kcal mol⁻¹ for **1** and **2**, respectively, to -25.2 and -28.5 kcal mol⁻¹ for **3** and **4**, respectively. The bowl-in-bowl arrangements are therefore significantly less stable than the staggered ones. The truxTTF- C_{60} model system, for which we have experimentally calculated association constants in the range of $\log K_a = 3–4$ in a variety of solvents at room temperature,^[15,19] presents an association energy of -22.1 kcal mol⁻¹, which is very close to that computed for structure **1**, owing to the similarity in the concave–convex interaction.

The electronic properties of the truxTTF- $C_{30}H_{12}$ associate have also been theoretically investigated. Figure S3a sketches

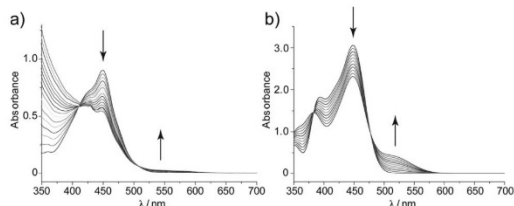


Figure 3. a) Experimental UV/Vis spectra, as obtained during the titration of truxTTF (1.7×10^{-4} M) with $C_{30}H_{12}$ (0.8×10^{-3} M) in $CHCl_3$ at room temperature. Each addition corresponds to 0.2 equiv. b) TDDFT simulation of the absorption spectra of truxTTF as the ratio of truxTTF- $C_{30}H_{12}$ increases from 0 to 100% (B3LYP/cc-pVDZ calculations including $CHCl_3$ as solvent).

the highest occupied (HOMO-2 to HOMO) and lowest unoccupied (LUMO to LUMO + 4) molecular orbitals computed at the revPBE0-D3/cc-pVTZ level for the most stable structure (**4**) of truxTTF- $C_{30}H_{12}$. Similar molecular orbital distributions are found for the rest of supramolecular structures **1–3** (Figure S3b). The HOMO, HOMO-1, and HOMO-2 spread over the electron-donating truxTTF moiety. In contrast, the LUMO, LUMO+1, and LUMO+2 are localized on the electron-accepting $C_{30}H_{12}$ bowl, with LUMO + 1 and LUMO + 2 being almost degenerate. Above LUMO + 2, LUMO + 3 and LUMO + 4 are again concentrated on the truxTTF bowl. The nature and energies calculated for the HOMOs and LUMOs of truxTTF- $C_{30}H_{12}$ therefore suggest that photoinduced charge-transfer processes from truxTTF to $C_{30}H_{12}$ should take place in the UV/Vis range.

Encouraged by the results of the theoretical calculations, we titrated truxTTF (1.7×10^{-4} M) with $C_{30}H_{12}$ (0.8×10^{-3} M) in $CHCl_3$ at room temperature. The electronic absorption spectra resulting from this titration experiment are depicted in Figure 3a. We observed a decrease in the intensity of the truxTTF absorption at $\lambda = 450$ nm, accompanied by the increase of a broad charge-transfer band in the 500–600 nm region. These spectral changes are analogous to those found in the titration of truxTTF vs. C_{60} , albeit with a significantly less intense charge-transfer feature.^[19] The results of three separate titration experiments were analyzed with Reactlab Equilibria software, affording a binding constant of $\log K_a = 3.6 \pm 0.3$.

To gain more insight into the electronic nature of the absorption bands observed experimentally, and their evolution during the titration experiment, the lowest-energy singlet excited states (S_n) of the truxTTF- $C_{30}H_{12}$ heterodimer and of isolated truxTTF were computed using the time-dependent DFT (TDDFT) approach, taking into account the solvent effects (see the Computational Details in the Supporting Information). Only the results obtained for the most stable structure (**4**) of truxTTF- $C_{30}H_{12}$ are discussed. TDDFT calculations predict the first two excited states S_1 and S_2 at 537 nm (2.31 eV) and 516 nm (2.40 eV) above the ground state S_0 with moderate oscillator strengths (*f*) of 0.036 and 0.046, respectively. The $S_0 \rightarrow S_1$ and $S_0 \rightarrow S_2$ electronic transitions are mainly described by one-electron promotions from

the HOMO to the LUMO and LUMO + 1, respectively. These transitions therefore imply a charge transfer from the electron-donor, truxTTF, where the HOMO is located, to the electron-acceptor, $C_{30}H_{12}$, where the LUMO and LUMO + 1 are spread (Figure S3a), and are the major contribution to the charge-transfer band experimentally recorded in the 500–600 nm range. Other charge-transfer transitions are computed around 500 nm, but they are less intense (Supporting Information, Table S1). At higher energies, the S_9 (454 nm, 2.73 eV), S_{10} (452 nm, 2.75 eV), and S_{11} (445 nm, 2.78 eV) states are calculated to be very close in energy and present higher oscillator strengths (0.178, 0.178, and 0.093, respectively). The $S_0 \rightarrow S_9$, $S_0 \rightarrow S_{10}$, and $S_0 \rightarrow S_{11}$ electronic transitions mainly originate from the HOMO, HOMO-1 \rightarrow LUMO + 3, LUMO + 4 one-electron excitations localized on truxTTF (Figure S3a), and give rise to the absorption band observed at 450 nm. The oscillator strengths calculated for these transitions are significantly smaller than those computed for isolated truxTTF (0.277, 0.320, and 0.145, respectively).

A TDDFT simulation of the absorption spectra of the truxTTF chromophore as the amount of truxTTF- $C_{30}H_{12}$ increases from 0 (spectrum of truxTTF) to 100% is shown in Figure 3b. The simulation clearly reveals that the truxTTF band decreases in intensity as truxTTF- $C_{30}H_{12}$ forms. This decrease is due to the smaller oscillator strengths computed for the truxTTF-centered transitions in the truxTTF- $C_{30}H_{12}$ complex. The charge-transfer band associated with the formation of truxTTF- $C_{30}H_{12}$ simultaneously increases in intensity. The theoretical simulation is in notable agreement with the experimental evolution of the absorption spectra, and supports the formation of the supramolecular donor-acceptor truxTTF- $C_{30}H_{12}$ heterodimer.

In addition to the ground-state interactions, we turned to pump probe absorption measurements to unravel the processes following photoexcitation of truxTTF- $C_{30}H_{12}$ and their references, truxTTF and $C_{30}H_{12}$. Upon 470 nm excitation of truxTTF, a new transient immediately develops (Figure S4). Characteristics of the latter are a marked maximum in the visible at 530 nm and a broad, featureless transition that spans all throughout the near infrared. Furthermore, a marked ground-state bleaching is observed around 450 nm. This excited state decays rapidly, as in other sulfur-rich electron donors, with a lifetime of only 1.0 ± 0.1 ps. The short lifetime is rationalized by the presence of the sulfur atoms, with a strong second-order vibronic spin-orbit coupling, as it transforms into a much weaker absorbing state, for which a lifetime of 20 ± 1 ps is detected.

For $C_{30}H_{12}$, the singlet and triplet excited states upon 387 nm excitation include transient maxima at 515 and 586 nm (Figure S5). These reflect the singlet excited state that decays within 11 ns through intersystem crossing to the energetically low-lying triplet excited state.

Following 470 nm photoexcitation of truxTTF- $C_{30}H_{12}$ (1:5 ratio), the differential absorption changes are dominated by truxTTF-centered features (Figure 4). Within approximately 1.5 ± 0.5 ps, the latter give place, however, to a new transient with characteristics that include maxima at 440, 475, 495, 530 (sh), and 615 nm, as well as a minimum at 450 nm. Neither photoexcited $C_{30}H_{12}$ nor photoexcited truxTTF exhibit differ-

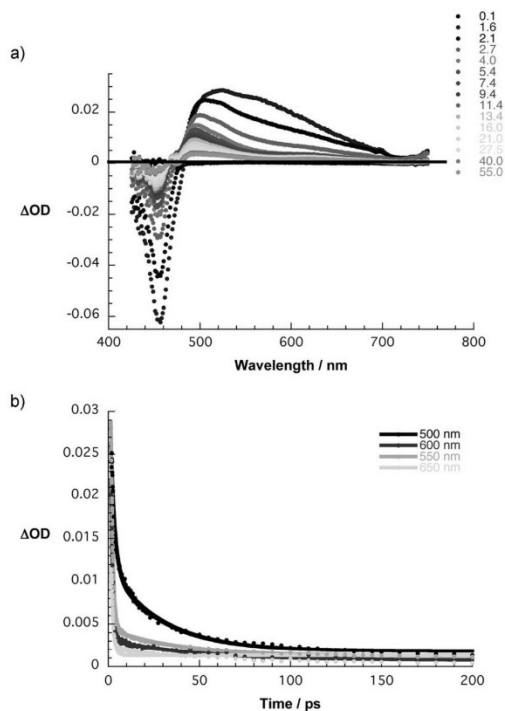


Figure 4. a) Differential absorption spectra (visible) obtained upon femtosecond pump probe experiments (470 nm) of truxTTF- $C_{30}H_{12}$ (1:5 ratio) in chlorobenzene with time delays of 0.1–55.0 ps at room temperature. b) Time absorption profiles of the spectra shown in (a) at 500 (black spectrum), 550 (gray spectrum), 600 (dark-gray spectrum), and 650 nm (light-gray spectrum) monitoring the charge transfer.

ential absorption changes that bear any significant resemblance to these data (Figure S4 and S5). Thus, a tentative assignment of these features implies the formation of a charge-separated state.

Support for this interpretation comes from spectroelectrochemical oxidation and reduction experiments with truxTTF and $C_{30}H_{12}$ in *ortho*-dichlorobenzene, respectively. For the former, upon applying a potential of +0.8 V versus Ag wire, maxima at 500 and 615 nm and a minimum at 450 nm are noted (Figure 5a). Importantly, resetting the potential back to 0 V led to a quantitative recovery of the starting spectrum. In the context of the latter, a potential of –1.0 V was chosen, and the differential absorption changes for the reduced $C_{30}H_{12}$ include maxima at 445, 475, 530, and 640 nm, which are accompanied by a 455 nm minimum (Figure 5b). Again, these changes were reversed upon resetting the applied potential back to 0 V. As such, the differential absorption changes upon photoexciting truxTTF- $C_{30}H_{12}$ (Figure 4) are in sound agreement with the superimposition of the spectroelectrochemically initiated oxidation and reduction of the truxTTF and hemifullerene, respectively. From multiwavelength analyses we derive rate constants of $6.6 \times$

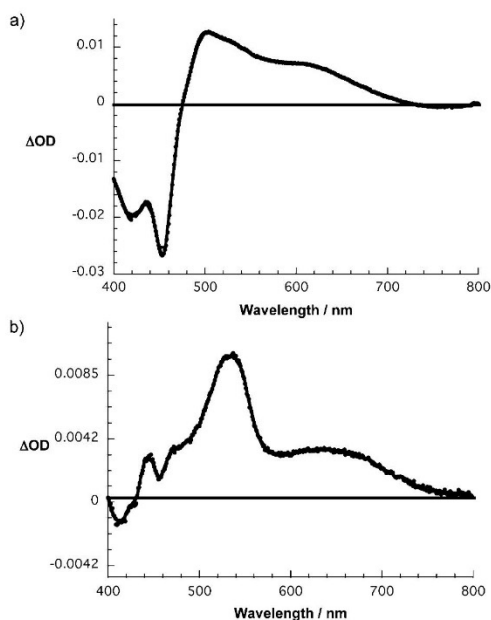


Figure 5. Differential absorption spectra (visible) obtained upon spectroelectrochemical oxidation of truxTTF (a) and reduction of $C_{30}H_{12}$ (b) in deoxygenated *ortho*-dichlorobenzene containing TBAPF₆ (0.1 M) with potentials vs. Ag wire of +0.8 and –1.0 V, respectively.

10^{11} and $1.0 \times 10^{10} \text{ s}^{-1}$ for the charge separation and charge recombination dynamics, respectively.

To better understand the spectroelectrochemical data recorded for the truxTTF and $C_{30}H_{12}$ fragments, the theoretical absorption spectra of the singly oxidized truxTTF⁺ and singly reduced $C_{30}H_{12}^-$ species were computed. The spectra calculated for the neutral species were subtracted from the spectra of the oxidized/reduced systems to obtain a theoretical simulation of the differential absorption spectra (Figure S6). For the truxTTF fragment, the predicted spectrum (Figure S6a) is in excellent agreement with the experimental spectrum (Figure 5a). The long tail over 550–800 nm originates from electron promotions from high-energy, doubly occupied molecular orbitals to the single-occupied molecular orbital (SOMO) (doublet states D_5 to D_9). The peak observed at 500 nm is due to higher-energy excitations (states D_{12} to D_{15}), where SOMO \rightarrow LUMOs transitions are involved. The steep slope experimentally recorded at around 480 nm is nicely reproduced by the theoretical simulation and originates from the proximity in energy of the intense excitation to the doublet state D_{17} in the cation and the excitation to the singlet state S_2 in the neutral species. The two-peak bleaching in the 400–450 nm region is due to the intense transitions (S_5 – S_6 and S_7 – S_8) of neutral truxTTF counterbalanced between them by the intense doublet excitation (D_{24}) in the cation. For the hemifullerene fragment, the theoretical simulation (Figure S6b) is in worse agreement with the experimental spectrum (Figure 5b) because the most intense band is

calculated too high in energy. The lower-energy band appearing at 600–700 nm corresponds to doublet excitations (D_3 – D_5) from the SOMO to higher-unoccupied molecular orbitals. The near-degeneracy of the LUMOs in neutral $C_{30}H_{12}$ is the origin of these low-energy transitions. Otherwise, the main features experimentally observed above 420 nm are assigned to doublet transitions (D_8 to D_{20}) implying electron excitations from doubly occupied molecular orbitals to the SOMO.

In summary, we have corroborated the association of a fullerene fragment, namely hemifullerene $C_{30}H_{12}$, with a bowl-shaped electron-donor, truxTTF. The association was investigated experimentally through UV/Vis titrations. To this end, changes in the absorption spectra, most notably a decrease in the truxTTF absorption and the formation of a weak charge transfer band, are clearly indicative for the truxTTF- $C_{30}H_{12}$ heterodimer in solution. Quantitatively, we calculated a binding constant of $\log K_a = 3.6 \pm 0.3$ in $CHCl_3$ at room temperature, which is comparable to that found for the association of truxTTF with C_{60} . Calculations at the revPBE0-D3/cc-pVTZ level of theory supported the noncovalent interactions between truxTTF and $C_{30}H_{12}$; providing insight into the possible structure of the heterodimer and the nature of the changes observed during the UV/Vis titration.

Remarkably, femtosecond pump-probe experiments reveal the formation of a transient species that corresponds to a charge-separated truxTTF $^{+}$ - $C_{30}H_{12}^{-}$ state. Overall, the latter assignment was backed by both spectroelectrochemical measurements and theoretical calculations. Analysis of the time evolution of these features afforded rate constants of 6.6×10^{11} and $1.0 \times 10^{10} \text{ s}^{-1}$ for the charge separation and charge recombination dynamics, respectively. This is the first example of a fullerene fragment mimicking the charge transfer behavior of C_{60} , which paves the way to the study of other related known fullerene fragments, thus opening a new avenue for these electronically less-known carbon-based materials.

Received: November 6, 2013

Published online: January 22, 2014

Keywords: density functional calculations · donor-acceptor systems · fullerenes · photoinduced electron transfer · supramolecular chemistry

- [1] J. L. Delgado, M. A. Herranz, N. Martín, *J. Mater. Chem.* **2008**, *18*, 1417–1426.
- [2] a) N. Martín, *Chem. Commun.* **2006**, 2093–2104; b) J. Delgado, S. Filippone, F. Giacalone, M. Herranz, B. Illescas, E. M. Pérez, N. Martín, *Top. Curr. Chem.* **2013**, *320–331*, 1–64.
- [3] *Carbon Nanotubes And Related Structures: Synthesis Characterization, Functionalization, And Applications* (Eds.: D. M. Guldi, N. Martín), Wiley-VCH, Weinheim, **2010**.
- [4] a) M. J. Allen, V. C. Tung, R. B. Kaner, *Chem. Rev.* **2010**, *110*, 132–145; b) C. N. R. Rao, A. K. Sood, K. S. Subrahmanyam, A. Govindaraj, *Angew. Chem.* **2009**, *121*, 7890–7916; *Angew. Chem. Int. Ed.* **2009**, *48*, 7752–7777; c) A. K. Geim, *Science* **2009**, *324*, 1530–1534; d) A. K. Geim, K. S. Novoselov, *Nat. Mater.* **2007**, *6*, 183–191.
- [5] a) N. Martín, L. Sánchez, M. A. Herranz, B. Illescas, D. M. Guldi, *Acc. Chem. Res.* **2007**, *40*, 1015–1024; b) D. Wróbel, A. Graja, *Coord. Chem. Rev.* **2011**, *255*, 2555–2577; c) S. Fukuzumi, T. Kojima, *J. Mater. Chem.* **2008**, *18*, 1427–1439; d) H. Imahori, *Org. Biomol. Chem.* **2004**, *2*, 1425–1433.
- [6] a) G. Dennler, M. C. Scharber, C. J. Brabec, *Adv. Mater.* **2009**, *21*, 1323–1338; b) M. Helgesen, R. Søndergaard, F. C. Krebs, *J. Mater. Chem.* **2010**, *20*, 36–60; c) C. J. Brabec, S. Gowrisanker, J. J. M. Halls, D. Laird, S. Jia, S. P. Williams, *Adv. Mater.* **2010**, *22*, 3839–3856; d) H. Hoppe, N. S. Sariciftci, *J. Mater. Chem.* **2006**, *16*, 45–61; e) J. L. Delgado, P.-A. Bouit, S. Filippone, M. A. Herranz, N. Martín, *Chem. Commun.* **2010**, *46*, 4853–4865.
- [7] a) J. M. Schnorr, T. M. Swager, *Chem. Mater.* **2011**, *23*, 646–657; b) C. Wang, K. Takei, T. Takahashi, A. Javey, *Chem. Soc. Rev.* **2013**, *42*, 2592–2609; c) S. Park, M. Vosguerichian, Z. Bao, *Nanoscale* **2013**, *5*, 1727–1752; d) S. N. Kim, J. F. Rusling, F. Papadimitrakopoulos, *Adv. Mater.* **2007**, *19*, 3214–3228.
- [8] a) S. Bae, H. Kim, Y. Lee, X. Xu, J.-S. Park, Y. Zheng, J. Balakrishnan, T. Lei, H. R. Kim, Y. I. Song, Y.-J. Kim, K. S. Kim, B. Oezylmaz, J.-H. Ahn, B. H. Hong, S. Iijima, *Nat. Nanotechnol.* **2010**, *5*, 574–578; b) X. Li, Y. Zhu, W. Cai, M. Borysiak, B. Han, D. Chen, R. D. Piner, L. Colombo, R. S. Ruoff, *Nano Lett.* **2009**, *9*, 4359–4363; c) K. S. Kim, Y. Zhao, H. Jang, S. Y. Lee, J. M. Kim, K. S. Kim, J.-H. Ahn, P. Kim, J.-Y. Choi, B. H. Hong, *Nature* **2009**, *457*, 706–710; d) X. Wang, L. Zhi, K. Müllen, *Nano Lett.* **2008**, *8*, 323–327.
- [9] a) C.-H. Lu, H.-H. Yang, C.-L. Zhu, X. Chen, G.-N. Chen, *Angew. Chem.* **2009**, *121*, 4879–4881; *Angew. Chem. Int. Ed.* **2009**, *48*, 4785–4787; b) J. T. Robinson, F. K. Perkins, E. S. Snow, Z. Wei, P. E. Sheehan, *Nano Lett.* **2008**, *8*, 3137–3140; c) F. Schedin, A. K. Geim, S. V. Morozov, E. W. Hill, P. Blake, M. I. Katsnelson, K. S. Novoselov, *Nat. Mater.* **2007**, *6*, 652–655.
- [10] a) Y. Zhu, S. Murali, M. D. Stoller, K. J. Ganesh, W. Cai, P. J. Ferreira, A. Pirkle, R. M. Wallace, K. A. Cychoz, M. Thommes, D. Su, E. A. Stach, R. S. Ruoff, *Science* **2011**, *332*, 1537–1541; b) K. Zhang, L. L. Zhang, X. S. Zhao, J. Wu, *Chem. Mater.* **2010**, *22*, 1392–1401; c) Y. Wang, Z. Shi, Y. Huang, Y. Ma, C. Wang, M. Chen, Y. Chen, *J. Phys. Chem. C* **2009**, *113*, 13103–13107.
- [11] H. Hu, Z. Zhao, W. Wan, Y. Gogotsi, J. Qiu, *Adv. Mater.* **2013**, *25*, 2219–2223.
- [12] X. Huang, Z. Yin, S. Wu, X. Qi, Q. He, Q. Zhang, Q. Yan, F. Boey, H. Zhang, *Small* **2011**, *7*, 1876–1902.
- [13] M. A. Petrukhina, L. T. Scott, *Fragments of Fullerenes and Carbon Nanotubes: Designed Synthesis, Unusual Reactions, and Coordination Chemistry*, Wiley, Hoboken, **2012**, p. 413.
- [14] a) S. Mizyed, P. Georghiou, M. Bancu, B. Cuadra, A. K. Rai, P. Cheng, L. T. Scott, *J. Am. Chem. Soc.* **2001**, *123*, 12770–12774; b) P. E. Georghiou, A. H. Tran, S. Mizyed, M. Bancu, L. T. Scott, *J. Org. Chem.* **2005**, *70*, 6158–6163; c) L. N. Dawe, T. A. AlHujran, H.-A. Tran, J. I. Mercer, E. A. Jackson, L. T. Scott, P. E. Georghiou, *Chem. Commun.* **2012**, *48*, 5563–5565.
- [15] E. M. Pérez, M. Sierra, L. Sánchez, M. R. Torres, R. Viruela, P. M. Viruela, E. Ortí, N. Martín, *Angew. Chem.* **2007**, *119*, 1879–1883; *Angew. Chem. Int. Ed.* **2007**, *46*, 1847–1851.
- [16] a) G. Mehta, G. Panda, P. V. V. S. Sarma, *Tetrahedron Lett.* **1998**, *39*, 5835–5836; b) S. Hagen, M. S. Bratcher, M. S. Erickson, G. Zimmermann, L. T. Scott, *Angew. Chem.* **1997**, *109*, 407–409; *Angew. Chem. Int. Ed. Engl.* **1997**, *36*, 406–408; c) A. H. Abdourazak, Z. Marciniow, A. Sygula, R. Sygula, P. W. Rabideau, *J. Am. Chem. Soc.* **1995**, *117*, 6410–6411.
- [17] M. A. Petrukhina, K. W. Andreini, L. Peng, L. T. Scott, *Angew. Chem.* **2004**, *116*, 5593–5597; *Angew. Chem. Int. Ed.* **2004**, *43*, 5477–5481.
- [18] A. Dalla Cort, L. Mandolini, C. Pasquini, L. Schiaffino, *New J. Chem.* **2004**, *28*, 1198–1199.

- [19] H. Isla, B. Grimm, E. M. Pérez, M. Rosario Torres, M. A. Herranz, R. Viruela, J. Aragó, E. Ortí, D. M. Guldi, N. Martín, *Chem. Sci.* **2012**, *3*, 498–508.
- [20] a) Y. Zhang, W. Yang, *Phys. Rev. Lett.* **1998**, *80*, 890–890; b) S. Grimme, J. Antony, S. Ehrlich, H. Krieg, *J. Chem. Phys.* **2010**, *132*, 154104–154118.
- [21] W. Hujo, S. Grimme, *J. Chem. Theory Comput.* **2011**, *7*, 3866–3871.
- [22] F. G. Brunetti, H. Isla, J. Aragó, E. Ortí, E. M. Pérez, N. Martín, *Chem. Eur. J.* **2013**, *19*, 9843–9848.
-

Complexation and Electronic Communication between Corannulene-Based Buckybowls and a Curved Truxene-TTF Donor

María Gallego,^{[a],†} Joaquín Calbo,^{[b],†} Rafael M. Crick Calderon,^{[c],†} Paula Pla,^[b] Ya-Chu Hsieh,^[d] Emilio M. Pérez,^[e] Yao-Ting Wu,^{*,[d]} Enrique Orti,^{*,[b]} Dirk M. Guldi,^{*,[c]} and Nazario Martín^{*,[a,e]}

Dedicated to the memory of Prof. José Barluenga, for his outstanding contributions to the progress of science in Spain

Abstract: The association behavior of an electron-donating, bowl-shaped, truxene-based tetrathiafulvalene (truxTTF) with two corannulene-based fullerene fragments –C₃₂H₁₂ and C₃₈H₁₄– is investigated in several solvents. Formation of 1:1 complexes is followed by absorption titrations and complemented by density functional theory (DFT) calculations. The binding constants are in the range of log K_a 2.9–3.5. DFT calculations reveal that the conformation in which the 1,3-dithiole ring of truxTTF is placed inside the concave cavity of the corannulene derivative is the most stable arrangement. This arrangement is confirmed experimentally by NMR measurements and implies the combination of π–π and CH–π interactions as the driving force for association. Time-dependent DFT calculations reproduce the experimental UV-vis titrations and provide a detailed understanding of the spectral changes observed. Femtosecond transient absorption studies reveal the processes occurring after photoexcitation of either C₃₂H₁₂ or C₃₈H₁₄ and their supramolecular associates with truxTTF. In the case of truxTTF·C₃₈H₁₄, photoexcitation yielded the charge-separated state truxTTF⁺·C₃₈H₁₄[–] with a lifetime of ~160 ps.

Introduction

Polycyclic aromatic hydrocarbons (PAHs) represent a large family of molecular building blocks based on multiple fused aromatic rings.^[1–3] When PAHs are formed solely by fused benzene rings, their structure remains planar, except in helicenes^[4–6] or highly strained cyclic derivatives.^[7–11] When PAHs feature five-membered rings as part of their structure, they adopt non-planar equilibrium geometries. In an extreme scenario, spherical fullerenes evolve upon embedding twelve five-membered rings into a PAH structure. Notably, any number of five-membered rings below twelve produces bowl-shape molecules, or "buckybowls",^[12–13]

The fact that the concave and convex surfaces of buckybowls, on one hand, and their edges, on the other hand, are readily available for reactions offers intriguing possibilities in chemistry. The convex surface often shares reactivity patterns similar to those seen for fullerenes. For example, when C₂₆H₁₂, the smallest fullerene fragment featuring a [6,6] double bond, is treated under 1,3-dipolar cycloaddition conditions, carbene additions or nucleophilic addition of MeLi, it exhibits reactions as found for [60]fullerene, that is, addition reactions at the central [6,6] ring junction. If it is subjected to Friedel-Crafts alkylation conditions, C₂₆H₁₂ behaves like an ordinary PAH, namely reacting at the double bonds located at the edges.^[14] More complex is the scenario when more than a single type of [6,6] double bond is present in the bucky bowl. For example, when the larger circumtrindene (C₃₆H₁₂)^[15] undergoes 1,3 dipolar cycloaddition conditions, the process is site-selective for [6,6] bonds located at the point of greatest curvature.^[14] As a matter of fact, this chemical reactivity resembles that observed for C₇₀. C₇₀ shows five types of [6,6] bonds, but only α and β isomers are typically detected under Prato reaction conditions, with a large preference for the α isomer. In some rare cases, traces of the γ isomer are also observed.^[16]

Buckybowls also show very rich coordination chemistry. It may take place at either the concave or the convex face yielding *endo* and *exo* complexes, respectively.^[17] The first structurally characterized corannulene complex was [(Cp⁺Ru)₂μ²-η⁶, η⁶-C₂₀H₁₀]²⁺, reported by Rabideau and co-workers.^[18] To this end, two (Cp⁺Ru)⁺ are bound to non-adjacent arene rings on opposite sides of the corannulene. Notably, η⁶-coordination causes reduction of the curvature and, in turn, a flattening of the corannulene. Concave-selective coordination is also possible – [CpFe(sumanene)]⁺ was the first example reported.^[19]

Buckybowls have been targeted as molecular building blocks towards more complex carbon nanoforms, like carbon

- [a] Dr. M. Gallego, Prof. Dr. N. Martín
Departamento de Química Orgánica
Fac. C. C. Químicas, Universidad Complutense de Madrid
Av. Complutense s/n, 28040 Madrid, Spain
E-mail: nazmar@ucm.es
- [b] J. Calbo, P. Pla, Prof. Dr. E. Orti
Instituto de Ciencia Molecular
Universidad de Valencia
46980 Paterna, Spain
E-mail: enrique.orti@uv.es
- [c] Dr. R. M. Crick-Calderon, Prof. Dr. D. M. Guldi
Department of Chemistry and Pharmacy and Interdisciplinary Center
for Molecular Materials(ICMM)
Friedrich-Alexander-Universität
Erlangen-Nürnberg, 91058 Erlangen, Germany
E-mail: dirk.guldi@fau.de
- [d] Dr. Y.-C. Hsieh, Prof. Dr. Y.-T. Wu
Department of Chemistry
National Cheng Kung University
70101 Tainan, Taiwan
E-mail: ytwuchem@mail.ncku.edu.tw
- [e] Dr. E. M. Pérez
IMDEA Nanociencia
Faraday 9, Campus UAM
28049 Madrid, Spain

[†]These authors contributed equally

Supporting information for this article is given via a link at the end of the document. ((Please delete this text if not appropriate))

nanotubes.^[20] In particular, buckybowls serve as seeds, from which carbon nanotubes of a specific chirality are grown.^[21] Finally, and most importantly, buckybowls show unique electronic properties, often in between those of flat PAHs and fullerenes, which can be skillfully exploited for organic electronics applications.^[22-23]

With regards to supramolecular chemistry, buckybowls have been thoroughly studied as hosts for fullerenes owing to their shape complementarity.^[24-26] The association of buckybowls by other organic hosts has, however, hardly been investigated. We recently described the association of a fullerene fragment, hemifullerene C₃₀H₁₂, by an electron-donating, bowl-shaped tetrathiafulvalene derivative (truxTTF) in which three 1,3-dithiole rings are attached to a truxene core (Chart 1).^[27] The stability of the associate was remarkable, with an association constant of $\log K_a = 3.6 \pm 0.3$ in CHCl₃ at room temperature. Moreover, we demonstrated photoinduced electron transfer from truxTTF to C₃₀H₁₂ to form the fully charge-separated species, which constituted the first example in which a buckybowl mimicked the electron accepting properties of fullerenes within supramolecular complexes.^[27]

In contrast to hemifullerene C₃₀H₁₂, the recently reported larger C₃₂H₁₂ and C₃₈H₁₄ buckybowls (Chart 1) are corannulene-based fragments of [60] and [70]fullerene, respectively.^[28-29] Such a difference in core aromatic structure is likely to be accompanied by fundamental differences in terms of electronic properties.

Here, we demonstrate that truxTTF forms heteromolecular associates ($\log K_a \approx 3$) with C₃₂H₁₂ and C₃₈H₁₄ in a variety of organic solvents. Density functional theory (DFT) calculations showed several different approximations of the heteromolecular complexes, all with favourable interaction energies, but only one, the staggered arrangement, with a significant negative free energy of complexation. NMR experiments confirmed the formation of staggered structures for both heterodimers in solution. Spectroelectrochemical and transient absorption studies reveal that photoinduced electron transfer (PET) takes place in truxTTF-C₃₈H₁₄, thus showing that corannulene π -extended derivatives resemble the electronic behaviour of [60]fullerene.

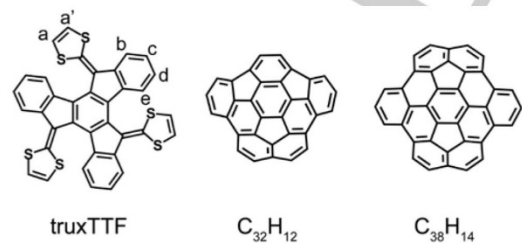


Chart 1. Chemical structure of truxTTF, C₃₂H₁₂ and C₃₈H₁₄.

Results and Discussion

The synthesis and the comprehensive characterization of truxTTF,^[30] C₃₂H₁₂,^[31] and C₃₈H₁₄^[28-29] have been reported elsewhere. Very briefly, truxTTF was synthesized from commercially available truxenone via a three-fold Horner-Wadsworth-Emmons olefination with the adequate dithiole phosphonate ylide. The highly strained C₃₂H₁₂ and C₃₈H₁₄ were synthesized from the adequate planar fluoroanthene derivatives through Pd-catalyzed C-C coupling reactions.

Based on our previous experience with hemifullerene C₃₀H₁₂, we expected the larger C₃₂H₁₂ and C₃₈H₁₄ to associate with truxTTF in a similar fashion. To test this hypothesis, we began by investigating the supramolecular interaction in silico, through dispersion-corrected DFT calculations. There are four different ways in which truxTTF and C₃₂H₁₂ can interact with each other. These four-modeled configurations are depicted in Figure 1.

In **1** and **2**, the convex surface of C₃₂H₁₂ perfectly matches the two concave cavities of the truxTTF host. In particular, either through the cavity formed by the truxene core –structure **1**– or through the cavity formed by the three 1,3-dithiole rings and the central benzene ring of the truxene core –structure **2**. Both are best described as bowl-in-bowl arrangements, where π - π interactions are maximized. The concave cavities of truxTTF and C₃₂H₁₂ can also interact giving rise to heterodimers in which either a benzene or a dithiole ring of truxTTF is placed inside the concave cavity of the corannulene-based bowl, resulting in **3** and **4**, respectively. These two dispositions resemble the arrangement found in the crystal packing for the homodimers of truxTTF and the related C₃₀H₁₂, implying a mixture of π - π and CH- π interactions.^[30, 32] All the optimized heterodimeric structures (**1**–**4**) show close intermolecular contacts in the 2.5–3.7 Å range (Figure S1 in the Supporting Information), indicative of stabilizing non-covalent interactions between both bowls.

To assess the strength of the interaction between the truxTTF and C₃₂H₁₂ bowls, association energies for the previously optimized heterodimers were calculated at the revPBE0-D3/cc-pVTZ level of theory, including the three-body correction (E_{ABC}) to the dispersion interaction (see the Supporting Information for full computational details). **1**–**4** exhibit significant gas-phase association energies ranging from –20.4 and –20.0 kcal/mol for **1** and **2**, respectively, to –24.7 and –29.9 kcal/mol for **3** and **4**, respectively (Table 1). The bowl-in-bowl structures are therefore significantly less stable than the staggered arrangements.

The supramolecular complexes formed by truxTTF and C₃₈H₁₄ were likewise modeled in several conformations. Depending on the relative disposition of one moiety with respect to the other, two bowl-in-bowl (**5** and **6**) and four staggered (**7**–**10**) conformations were optimized at the revPBE0-D3/cc-pVTZ level of theory (Figure 2). **7** and **8** differ from **9** and **10** in a –90° rotation of the staggered arrangements. Bowl-in-bowl arrangements **5** and **6** offer an optimal disposition for maximizing π - π interactions, with short intermolecular contacts in the 3.2–3.8 Å range (Figure S2). Staggered arrangements **7**–**10** are governed by a mixture of π - π and CH- π interactions between the electron donating truxTTF and the electron accepting C₃₈H₁₄, with short intermolecular contacts ranging 2.7–3.9 Å (Figure S2).

The bowl-in-bowl arrangements, in which the convex surface of $C_{38}H_{14}$ perfectly matches the two concave cavities of the truxTTF host are represented in **5** and **6**. Either **5** –through the cavity formed by the carbon backbone– or **6** –through the cavity formed by the central benzene ring and the three dithiole rings– show favourable interactions with stabilizations of -23.4 and -21.6 kcal/mol, respectively. The staggered arrangements **7–10** show significantly larger interaction energies. The conformer in which a dithiole ring of truxTTF is placed inside the concave

cavity of $C_{38}H_{14}$ is computed to be the most stable arrangement with -33.5 kcal/mol for **8** and -34.2 kcal/mol for **10** (Table 1).

The interaction energy computed for the most stable structures of heterodimers truxTTF· $C_{32}H_{12}$ and truxTTF· $C_{38}H_{14}$ surpasses the association energy computed for the hemifullerene-truxTTF (truxTTF· $C_{30}H_{12}$) heterodimer (-28.5 kcal/mol) at the same level of theory.^[27] Theoretical calculations therefore suggest favourable arrangements in which truxTTF is merged with corannulene-based $C_{32}H_{12}$ and $C_{38}H_{14}$ carbon nanoforms in highly stable supramolecular heterodimers.

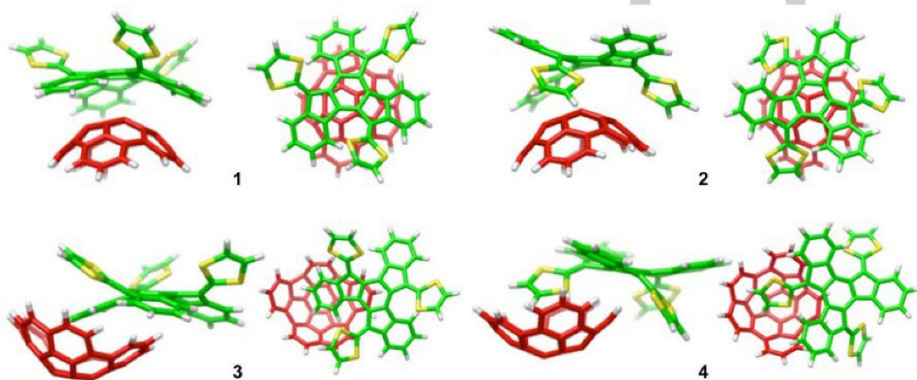


Figure 1. Minimum-energy structures (**1–4**) computed at the revPBE0-D3/cc-pVTZ level for the most stable conformations of the heterodimer formed by the $C_{32}H_{12}$ fullerene fragment with truxTTF (truxTTF· $C_{32}H_{12}$). Carbon atoms of the truxTTF are depicted in green, sulfur in yellow, and hydrogen in white. Carbon atoms of $C_{32}H_{12}$ are depicted in red and hydrogen in white.

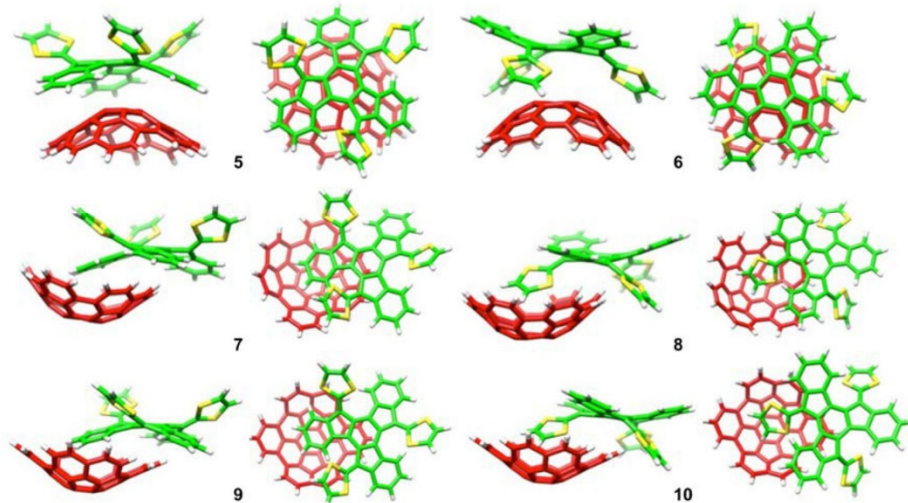


Figure 2. Minimum-energy structures (**5–10**) computed at the revPBE0-D3/cc-pVTZ level for the most stable conformations of the heterodimer formed by the $C_{38}H_{14}$ fullerene fragment with truxTTF (truxTTF· $C_{38}H_{14}$). Carbon atoms of the truxTTF are depicted in green, sulfur in yellow, and hydrogen in white. Carbon atoms of $C_{38}H_{14}$ are depicted in red and hydrogen in white.

Table 1. Table Caption. Thermodynamic parameters (in kcal/mol) including association energy (E_{assoc}), free energy in gas phase (ΔG_{gas}) and free energy including solvent effects (ΔG_{theor}) for the dimerization process. Theoretical and experimental $\log K_{\text{a}}$ values are also included.

Heterodimer	E_{assoc}	$\Delta G_{\text{gas}}^{[b]}$	$\Delta G_{\text{theor}}^{[c]}$	$\log K_{\text{a,theor}}^{[d]}$	$\log K_{\text{a,exp}}$	
truxTTF•C ₃₀ H ₁₂ ^[a]	1'	-21.02	-8.27	1.13		
	2'	-19.38	-5.98	2.64		
	3'	-25.23	-10.88	-2.96	3.7	3.6 ± 0.3 ^[e]
	4'	-28.52	-14.34	-5.00		
truxTTF•C ₃₂ H ₁₂	1	-20.44	-3.87	5.07		
	2	-19.97	-4.24	3.67	3.2	2.9 ± 0.4 ^[e] 3.2 ± 0.1 ^[f] 3.3 ± 0.2 ^[g]
	3	-24.69	-6.95	0.97		
	4	-29.91	-12.84	-4.29		
truxTTF•C ₃₈ H ₁₄	5	-23.37	-4.32	5.81		
	6	-21.63	-3.46	4.80		
	7	-29.09	-9.72	0.51	3.6	3.4 ± 0.1 ^[f] 3.5 ± 0.2 ^[g]
	8	-33.48	-14.39	-3.75		
	9	-31.57	-11.71	-2.65		
	10	-34.24	-14.94	-4.93		

[a] Minimum-energy geometries as used in Ref. 27. Notation 1'–4' refers to systems 1–4 in the original work. [b] Free energy of complexation including zero-point energy, thermal, enthalpy and entropy corrections. [c] Free energy of complexation after addition of solvent effects through SMD and chloroform as a solvent. [d] Theoretical $\log K_{\text{a}}$ calculated for the most stable conformer using the ΔG_{theor} value. [e] Determined in CHCl₃ as solvent. [f] PhCl as solvent. [g] THF as solvent.

In order to provide a more realistic description reflecting the strength of complexation at room temperature and in solution, the free energy of the dimerization process was theoretically estimated for all the possible conformers of truxTTF•C₃₂H₁₂ and truxTTF•C₃₈H₁₄, and compared with that computed for truxTTF•C₃₀H₁₂ (see the Supporting Information for full computational details). Free energies in gas phase show that entropic effects are similar for both bowl-in-bowl and staggered dimers (Table S1). Upon inclusion of solvent effects (chloroform), the ΔG_{theor} values obtained indicate the same trends for the relative stabilities of the different supramolecular arrangements as predicted by the association energy (Table 1). Interestingly, only the staggered conformers provide negative values of ΔG_{theor} , suggesting that bowl-in-bowl arrangements might not be formed in solution (Table 1). For the three buckybowls, the staggered dimers in which the dithiole ring is placed inside the bowl basin are computed as the most stable structures, with ΔG_{theor} values of -4.29, -4.93 and -5.00 kcal/mol for truxTTF•C₃₂H₁₂, truxTTF•C₃₈H₁₄ and truxTTF•C₃₀H₁₂, respectively. Theoretical $\log K_{\text{a}}$ values are predicted in the range of 3–4, showing a perfect matching in the case of truxTTF•C₃₀H₁₂ ($\log K_{\text{a,theor}} = 3.7$) with respect to the experiment value ($\log K_{\text{a,exp}} = 3.6 \pm 0.3$) previously

reported.²⁷ Calculations using chlorobenzene led to both qualitatively and quantitatively similar results (Table S1).

Considering these encouraging results, we studied the association in solution through absorption titrations in PhCl, CHCl₃ and THF at room temperature. Typical results for the titration of truxTTF with C₃₂H₁₂ are shown in Figure 3a. Overall, the spectral changes are very small. For example, the truxTTF band at 450 nm lacks any notable decrease in absorption despite the fact that C₃₂H₁₂ absorbs only very weakly in this spectral region.^[26] However, a very weak increase of absorption in the 500–600 nm region was observed, which is correctly reproduced by TDDFT calculations (vide infra) and parallels our previous observations with C₃₀H₁₂.²⁷ Indeed, multiwavelength analysis for three separate titration experiments in each solvent consistently afforded satisfactory results for the 1:1 binding model. In particular, we obtained $\log K_{\text{a,exp}} = 3.19 \pm 0.02$, 2.9 ± 0.4 and 3.3 ± 0.2 in PhCl, CHCl₃ and THF, respectively.

More pronounced were the spectral changes noted during the titration of truxTTF vs C₃₈H₁₄ as shown in Figure 3b. Here, we observed a significant decrease in the intensity of the truxTTF absorption band at around 450 nm, accompanied by the increase of a broad band and a charge-transfer band in the 500–600 nm region, with concomitant formation of an

isosbestic point at 490 nm. The isosbestic point is, however, buried upon addition of more than one equivalent of $C_{38}H_{14}$. Multiwavelength analysis afforded binding constants of $\log K_{a,exp} = 3.4 \pm 0.1$ and 3.5 ± 0.2 in PhCl and THF, respectively. As can be seen in Table 1, the theoretical values estimated for $\log K_a$ are in very good agreement with the experimental results, giving support to the formation of the staggered structures predicted theoretically as the preferred conformation.

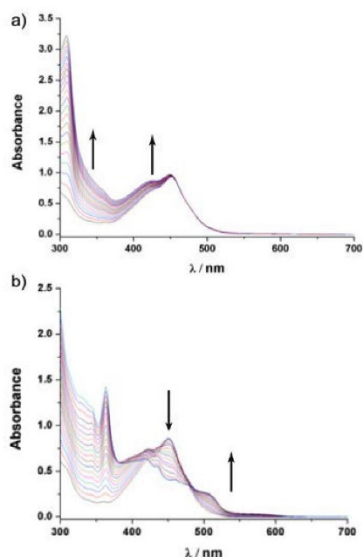


Figure 3. a) Experimental absorption spectra as obtained during the titration of truxTTF (1.76×10^{-4} M) with $C_{32}H_{12}$ (8.78×10^{-4} M) in PhCl at room temperature, up to 3.81 equivalents of $C_{32}H_{12}$ were added. b) Experimental absorption spectra as obtained during the titration of truxTTF (1.5×10^{-4} M) with $C_{38}H_{14}$ (7.7×10^{-4} M) in PhCl at room temperature, up to 3 equivalents of $C_{38}H_{14}$ were added.

Time-dependent DFT (TDDFT) calculations in the presence of the solvent (PhCl) were carried out for the most stable structures of truxTTF· $C_{32}H_{12}$ (**4**) and truxTTF· $C_{38}H_{14}$ (**10**) and for their corresponding monomeric units to disentangle the spectroscopic changes detected in the absorption spectra upon titration (see the Supporting Information for computational details). TDDFT calculations on truxTTF· $C_{32}H_{12}$ predict four singlet excited states S_1 – S_4 in the 500–650 nm range, with very low oscillator strengths ($f < 0.01$, Table S2). These electronic transitions correspond to charge-transfer excitations from the HOMO and HOMO–1, located on truxTTF, to the LUMO and LUMO+1, located on $C_{32}H_{12}$ (Figure S3), that relate to the hardly-observed band experimentally recorded above 500 nm (Figure 3a). Similarly, the lowest singlet excited states S_1 – S_4 for the truxTTF· $C_{38}H_{14}$ complex imply charge-transfer excitations and are computed

at 500–700 nm, with a moderate oscillator strength in the case of S_4 ($f = 0.016$). This state in conjunction with the larger interaction energy might explain the detection of the weak, broad CT band in the case of the $C_{38}H_{14}$ -based dimer (Figure 3b). The new absorption band rising at 500 nm in truxTTF· $C_{38}H_{14}$ is assigned to the electronic transition to the first excited state S_1 of $C_{38}H_{14}$ calculated at 489 nm, which appears at similar wavelength (492 nm) for truxTTF· $C_{38}H_{14}$ (Table S2). In contrast, $C_{32}H_{12}$ presents no significant absorption above 400 nm (Table S2† and Figure S4). In both dimers, the typical truxTTF band centered at 450 nm is predicted to slightly decrease in intensity but preserves its position upon complexation (Table S2† and Figure S5). Finally, the experimental peak rising at 360 nm in truxTTF· $C_{38}H_{14}$ (Figure 3b) is assigned to the intense electronic transition to S_8 ($f = 0.373$) predicted for the $C_{38}H_{14}$ fragment at 356 nm. Spectroscopic changes in absorption upon complexation are therefore easily understood by joining the absorption features of the constituting monomeric units.

1H NMR experiments helped to shed light on the structure of these associates in solution. Figure 4a shows the 1H NMR of truxTTF (black), $C_{32}H_{12}$ (blue) and truxTTF· $C_{32}H_{12}$ (red). The lettering is in accordance with Chart 1 and shows the assignment for truxTTF. Upon complexation, all the signals of $C_{32}H_{12}$ suffer slight and quantitatively similar upfield shifts. Meanwhile, the signals corresponding to the truxene core of truxTTF (b–e in Figure 4a) appear unaltered, and only the dithiole ring signals (a + a' in Figure 4a) are shifted upfield by ca. 0.02 ppm. Moreover, a change in multiplicity from a singlet to two doublets ($J = 6.8$ Hz) with very strong rooftop effect is also noticeable (see insets in Figure 4a). These changes support the structure depicted as **4** in Figure 1, which was calculated to be the only thermodynamically favourable arrangement in chloroform solution for truxTTF· $C_{32}H_{12}$ (vide supra).

The case of truxTTF· $C_{38}H_{14}$ is not so straightforward. The 1H NMR spectra are shown in Figure 4b with analogous colour coding. As in the previous example, all the signals of the corannulene-based buckybowl are shifted slightly upfield. However, we can see shielding of both the truxene-core and the dithiole signals of truxTTF upon association. The former are quantitatively smaller and mostly affect the d and c triplets, while the latter are larger, and in this case do not result in a change of multiplicity, but only in broadening (see insets in Figure 4b). These spectroscopic changes point to a coexistence in solution of the staggered structures (**7–10** in Figure 2), with predominance of those in which the dithiole rings are inside the cavity of $C_{38}H_{14}$ (**8** and **10** in Figure 2), again in perfect agreement with the relevant calculations.

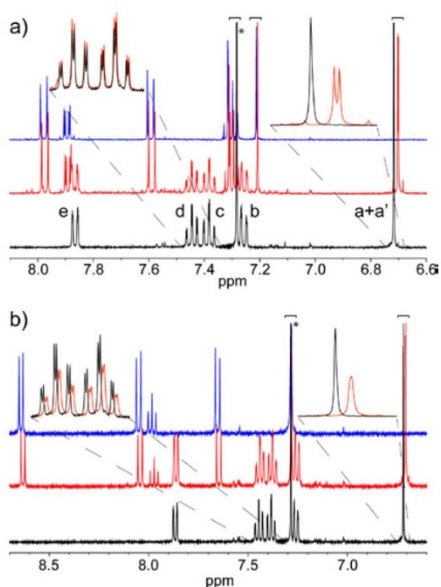


Figure 4. ^1H NMR (CDCl₃, 400 MHz, 298K, all species at ca. 5 mM) of: a) truxTTF (black), C₃₈H₁₂ (blue) and truxTTF + C₃₈H₁₂ (red), and b) truxTTF (black), C₃₈H₁₄ (blue) and truxTTF + C₃₈H₁₄ (red). The insets show an overlay of the spectra of truxTTF and the complexes in the region between 6.74 and 6.68 ppm (a + a') and 7.48–7.34 ppm (c + d).

To shed light onto the excited state properties of truxTTF, C₃₈H₁₄, and their supramolecular associate truxTTF·C₃₈H₁₄, transient absorption experiments were conducted. Upon 480 nm excitation of truxTTF in chlorobenzene, a new transient immediately develops.^[27] Characteristics of the latter are a marked maximum in the visible at 530 nm. Furthermore, a marked ground-state bleaching is observed around 450 nm. This excited state decays rapidly, as in other sulphur-rich electron donors, with a lifetime of 1.0 ± 0.5 ps. The short lifetime is rationalized by the presence of the sulfur atoms, with a strong second-order vibronic spin-orbit coupling, as it transforms into a much weaker absorbing state with maxima at 505 and 700 nm (Figure 5), for which a lifetime of 20 ± 5 ps is detected.

When exciting C₃₈H₁₄ at 480 nm in chlorobenzene, several strong transient maxima evolve with the completion of the laser pulse (Figure 6). Three sharp maxima at 450, 546 and 800 nm are accompanied by broad transients ranging from 625 to 725 nm. After excitation, a multiexponential deactivation of these features is observed. While the 546 nm maxima persists, the features at 450, 800 and from 625 to 725 nm deactivate within 46 ps (20%) and 3.5 ns (80%). The former is assigned to a non-radiative intrinsic deactivation. The latter reflects the intersystem crossing to the triplet excited state of C₃₈H₁₄. The triplet excited state shows a transient absorption maximum at 546 nm and one broad

transient around 670 nm that deactivate within 18 μs to the ground state. Experiments in toluene and benzonitrile gave similar results.

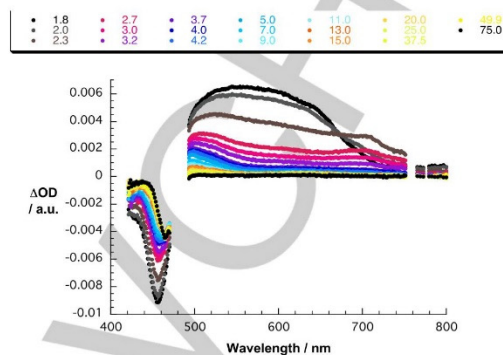


Figure 5. Differential absorption spectra obtained upon femtosecond pump probe experiments (480 nm) of truxTTF in argon-saturated chlorobenzene with time delays of 1.8–75 ps at room temperature.

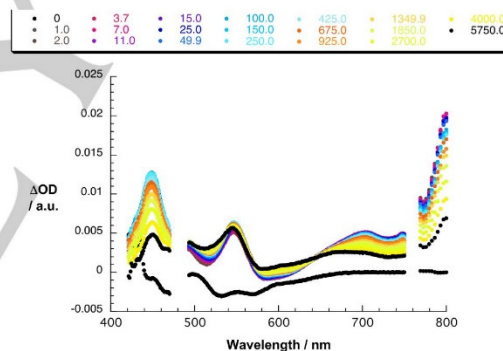


Figure 6. Differential absorption spectra obtained upon femtosecond pump probe experiments (480 nm) of C₃₈H₁₄ in argon-saturated chlorobenzene with time delays of 0–5750 ps at room temperature.

In order to gain insight into the processes occurring after photoexcitation, spectroelectrochemical measurements were conducted, that is, recording the differential absorption spectra upon electrochemical oxidation of truxTTF²⁷ and reduction of C₃₈H₁₄ (Figure 7). TDDFT calculations were performed on the anion species of C₃₈H₁₄, and the simulated differential absorption spectrum is shown in Figure S7. The broad band experimentally centered around 650 nm corresponds to the D₀ → D₄ excitation of C₃₈H₁₄[−] with oscillator strength of $f = 0.094$. Theoretical calculations nicely reproduce the crossing point around 550 nm, being the negative signal at 500 nm originated by the intense S₁ excited state of neutral C₃₈H₁₄.

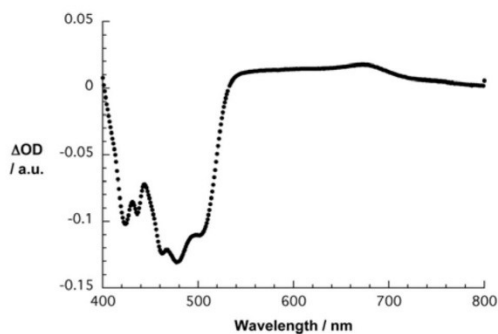


Figure 7. Differential absorption spectrum obtained upon electrochemical reduction of $C_{38}H_{14}$ in deoxygenated *ortho*-dichlorobenzene containing TBAPF₆ (0.1 M) with an applied potential of -1.1 V vs. Ag wire at room temperature.

When exciting $\text{truxTTF} \cdot C_{38}H_{14}$ (10:1) in either toluene, chlorobenzene or benzonitrile at 480 nm, truxTTF -centered transients dominate the spectra (Figure 8). In particular, the 530 nm marker is discernable at the conclusion of the excitation. With a lifetime of 0.8 ± 0.2 ps the latter transforms into a new transient species, that is, the charge-separated state featuring $\text{truxTTF}^{\bullet+}$ and $C_{38}H_{14}^{\bullet-}$. Of great importance are changes in the differential absorption in the range between 500 and 700 nm, where both the $\text{truxTTF}^{\bullet+}$ and the $C_{38}H_{14}^{\bullet-}$ species presents higher absorption (Figure 7), supporting the notion of electronic communications in the excited state is taking place.

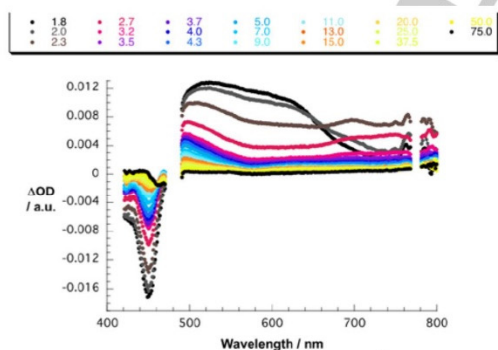


Figure 8. Differential absorption spectra obtained upon femtosecond pump probe experiments (480 nm) of $\text{truxTTF} \cdot C_{38}H_{14}$ (10:1) in argon-saturated toluene with time delays of 1.8–75 ps at room temperature.

A detailed kinetic analysis corroborates our hypothesis. To this end, multiwavelength analysis yields four major lifetime components. After excitation, a very short lifetime of 0.8 ± 0.2 is followed by a 15 ± 5 ps component. We assign

the shorter component to ultrafast charge separation yielding the $\text{truxTTF}^{\bullet+} \cdot C_{38}H_{14}^{\bullet-}$ charge-separated state. The longer component is most likely due to intrinsic deactivation of non-complexed truxTTF and $C_{38}H_{14}$. The third component of 160 ± 15 ps, which is neither observed for truxTTF nor for $C_{38}H_{14}$, reflects the charge recombination to yield $\text{truxTTF} \cdot C_{38}H_{14}$ in the ground state. Finally, the fourth component of >5.5 ns is likely due to the slow deactivation of the $C_{38}H_{14}$ triplet excited state as confirmed by the detection of the 450, 546, and 800 nm markers. The latter is populated by intersystem crossing within non-complexed $C_{38}H_{14}$ and, potentially, charge recombination.

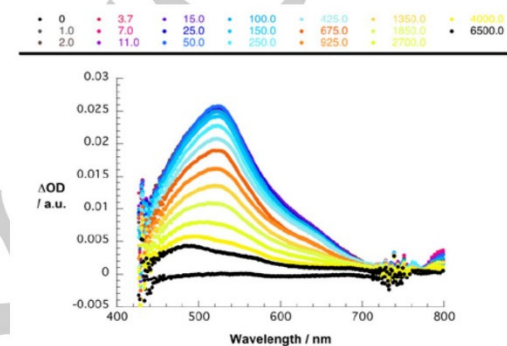


Figure 9. Differential absorption spectra obtained upon femtosecond pump probe experiments (500 nm) of $C_{32}H_{12}$ in argon-saturated chlorobenzene with time delays of 0–6500 ps at room temperature.

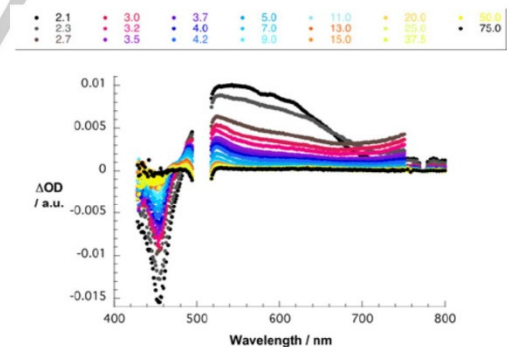


Figure 10. Differential absorption spectra obtained upon femtosecond pump probe experiments (500 nm) of $\text{truxTTF} \cdot C_{32}H_{12}$ (10:1) in argon-saturated *ortho*-dichlorobenzene with time delays of 1.8–75 ps at room temperature.

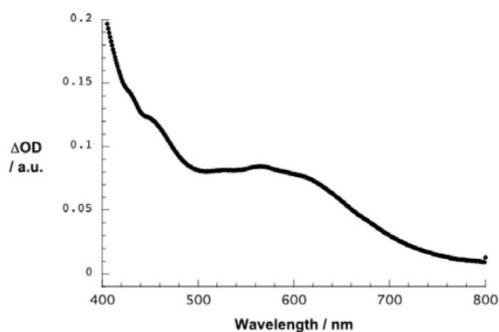


Figure 11. Differential absorption spectra obtained upon electrochemical reduction of $C_{32}H_{12}$ in deoxygenated *ortho*-dichlorobenzene containing TBAPF₆ (0.1 M) with an applied potential of -1.0 V vs. Ag wire at room temperature.

When exciting $C_{32}H_{12}$ at 500 nm in chlorobenzene, a transient centering on 520 nm is observed (Figure 9). This feature deactivates within 1.6 ns to the ground state or the lower-lying triplet excited state that is, however, not spectroscopically observed. Similar results were observed in toluene, anisole, *ortho*-dichlorobenzene, and benzonitrile.

In order to shed light into the excited state interactions between truxTTF and $C_{32}H_{12}$, mixtures of various molar ratios (10:1 – 1:10) in solvents of different polarities (anisole, toluene, chlorobenzene, *ortho*-dichlorobenzene and benzonitrile) were explored in transient absorption experiments exciting at 387 and 480 nm. Figure 10 exemplifies the differential absorption changes recorded in chlorobenzene. The spectral similarity between the excited state absorptions of truxTTF and $C_{32}H_{12}$, on one hand, and the radical cation of truxTTF as well as the radical anion of $C_{32}H_{12}$ (Figure 11), on the other hand, rendered an unambiguous characterization of the charge-separated state truxTTF^{•+}• $C_{32}H_{12}^{\bullet-}$ rather difficult. In fact, TDDFT simulations confirmed the absence of any characteristic feature for the anion species of $C_{32}H_{12}$ above 700 nm (Figure S6) that could help in identifying the charge-separated state. Based on the current investigation with $C_{38}H_{14}$ and the past investigation with $C_{30}H_{12}$, excited state interactions in terms of charge transfer with truxTTF are likely to occur.²⁷

Conclusions

To conclude, we have demonstrated the association of two corannulene-based fullerene fragments – $C_{32}H_{12}$ and $C_{38}H_{14}$ – with a bowl-shaped tetrathiafulvalene unit –truxTTF. Absorption titrations aided in following the complexation process. The most remarkable features are the depletion of intrinsic truxTTF absorption upon addition of $C_{32}H_{12}$ or $C_{38}H_{14}$, accompanied by the rise of a charge transfer band in the visible between 500 and 600 nm. Multiwavelength analysis

revealed association constants of $\log K_a = 2.9 - 3.5$. DFT calculations performed at the revPBE0-D3/cc-pVTZ level supported the supramolecular association. Here, different possible complex geometries were predicted, revealing either bowl-in-bowl or staggered arrangements, the latter offering the largest interaction energies, even surpassing the association energy obtained for the analogous truxTTF• $C_{30}H_{12}$ complex. Accurate calculations of the free energy of complexation suggested that only the staggered conformer in which one dithiole ring is placed inside the bowl basin could be formed in solution for truxTTF• $C_{32}H_{12}$, whereas a mixture of staggered conformers might be present for truxTTF• $C_{38}H_{14}$. NMR experiments gave confirmation to these theoretical predictions. Femtosecond transient absorption studies shed light onto excited state interactions in the associates. In the case of truxTTF• $C_{38}H_{14}$, photoexcitation yielded the charge-separated state truxTTF^{•+}• $C_{38}H_{14}^{\bullet-}$ with a lifetime of ~ 160 ps in the most polar benzonitrile. For truxTTF• $C_{32}H_{12}$, the assignment of the charge-separated state rendered extremely difficult, but is, based on earlier findings, regarded to be very likely.

These experimental and theoretical findings reveal π -extended corannulene derivatives as suitable systems to form 1:1 supramolecular complexes with bowl-shaped electron donor molecules, in which intermolecular PET processes occur, mimicking the related buckyballs.

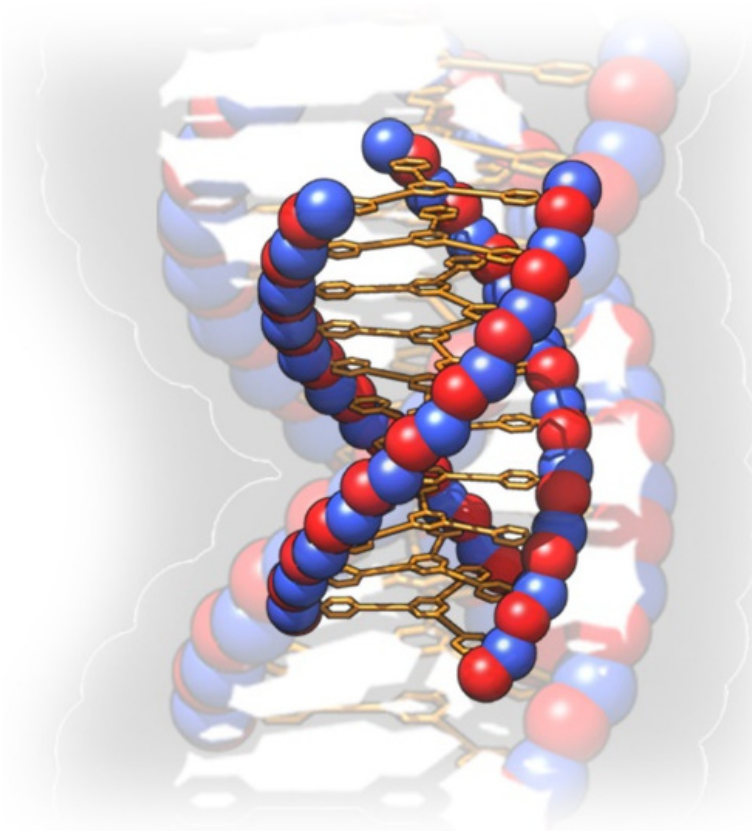
Acknowledgements

Financial support by the European Research Council (ERC-320441-Chiralcarbon and MINT, ERC-StG-307609), MINECO of Spain (CTQ2014-52045-R, CTQ2015-71154-P, CTQ2014-60541-P, and Unidad de Excelencia María de Maeztu MDM-2015-0538), the CAM (FOTOCARBON project S2013/MIT-2841), European Feder funds (CTQ2015-71154-P), and Generalitat Valenciana (PROMETEO/2016/135) is acknowledged. J.C. and M.G. thank the MECD of Spain for doctoral FPU grants. NM thanks Alexander von Humboldt Foundation. D.M.G. gratefully acknowledges funding from the Deutsche Forschungsgemeinschaft as part of the Collaborative Research Centre SFB 953 "Synthetic Carbon Allotropes" and of the Excellence Cluster "Engineering of Advanced Materials". The Bayerische Staatsregierung is acknowledged for funding granted as part of the "Solar Technologies go Hybrid" initiative.

Keywords: buckybowl • donor-acceptor • supramolecular complexes • association constants • photoinduced charge transfer

- [1] A. Narita, X.-Y. Wang, X. Feng, K. Müllen, *Chem. Soc. Rev.* **2015**, *44*, 6616-6643.
- [2] R. Rieger, K. Müllen, *J. Phys. Org. Chem.* **2010**, *23*, 315-325.
- [3] J. Wu, W. Pisula, K. Müllen, *Chem. Rev.* **2007**, *107*, 718-747.
- [4] M. Gingras, G. Felix, R. Peresutti, *Chem. Soc. Rev.* **2013**, *42*, 1007-1050.
- [5] M. Gingras, *Chem. Soc. Rev.* **2013**, *42*, 968-1006.
- [6] M. Gingras, *Chem. Soc. Rev.* **2013**, *42*, 1051-1095.

- [7] E. R. Darzi, R. Jasti, *Chem. Soc. Rev.* **2015**, *44*, 6401-6410.
- [8] J. Evans Paul, R. Darzi Evan, R. Jasti, *Nat Chem* **2014**, *6*, 404-408.
- [9] T. Matsuno, S. Sato, R. Iizuka, H. Isobe, *Chem. Sci.* **2015**, *6*, 909-916.
- [10] Y. Miyauchi, K. Johmoto, N. Yasuda, H. Uekusa, S. Fujii, M. Kiguchi, H. Ito, K. Itami, K. Tanaka, *Chem. Eur. J.* **2015**, *21*, 18900-18904.
- [11] K. Kato, Y. Segawa, L. T. Scott, K. Itami, *Chem. Asian J.* **2015**, *10*, 1635-1639.
- [12] M. A. Petrukhina and L. T. Scott, eds., *Fragments of Fullerenes and Carbon Nanotubes: Designed Synthesis, Unusual Reactions, and Coordination Chemistry*, John Wiley & Sons, **2012**.
- [13] Y.-T. Wu, J. S. Siegel, *Top. Curr. Chem.* **2014**, *349*, 63-120.
- [14] L. T. Scott, H. E. Bronstein, D. V. Preda, R. B. M. Ansems, M. S. Bratcher, S. Hagen, *Pure Appl. Chem.* **1999**, *71*, 209-219.
- [15] L. T. Scott, M. S. Bratcher, S. Hagen, *J. Am. Chem. Soc.* **1996**, *118*, 8743-8744.
- [16] E. E. Maroto, A. de Cozar, S. Filippone, A. Martin-Domenech, M. Suarez, F. P. Cossio, N. Martin, *Angew. Chem., Int. Ed.* **2011**, *50*, 6060-6064.
- [17] M. A. Petrukhina, L. T. Scott, *Dalton Trans.* **2005**, 2969-2975.
- [18] P. A. Vecchi, C. M. Alvarez, A. Ellern, R. J. Angelici, A. Sygula, R. Sygula, P. W. Rabideau, *Angew. Chem., Int. Ed.* **2004**, *43*, 4497-4500.
- [19] T. Amaya, H. Sakane, T. Hirao, *Angew. Chem., Int. Ed.* **2007**, *46*, 8376-8379.
- [20] U. H. F. Bunz, S. Menning, N. Martin, *Angew. Chem., Int. Ed.* **2012**, *51*, 7094-7101.
- [21] L. T. Scott, E. A. Jackson, Q. Zhang, B. D. Steinberg, M. Bancu, B. Li, *J. Am. Chem. Soc.* **2012**, *134*, 107-110.
- [22] K. Müllen, J. P. Rabe, *Acc. Chem. Res.* **2008**, *41*, 511-520.
- [23] J. Wu, W. Pisula, K. Müllen, *Chem. Rev.* **2007**, *107*, 718-747.
- [24] T. Kawase, H. Kurata, *Chem. Rev.* **2006**, *106*, 5250-5273.
- [25] E. M. Pérez, N. Martin, *Chem. Soc. Rev.* **2008**, *37*, 1512-1519.
- [26] E. M. Pérez, N. Martin, *Chem. Soc. Rev.* **2015**, *44*, 6425-6433.
- [27] M. Gallego, J. Calbo, J. Aragón, R. M. Krick Calderon, F. H. Liquido, T. Iwamoto, A. K. Greene, E. A. Jackson, E. M. Pérez, E. Ortí, D. M. Guldí, L. T. Scott, N. Martin, *Angew. Chem., Int. Ed.* **2014**, *53*, 2170-2175.
- [28] M.-K. Chen, H.-J. Hsin, T.-C. Wu, B.-Y. Kang, Y.-W. Lee, M.-Y. Kuo, Y.-T. Wu, *Chem. Eur. J.* **2014**, *20*, 598-608.
- [29] T.-C. Wu, M.-K. Chen, Y.-W. Lee, M.-Y. Kuo, Y.-T. Wu, *Angew. Chem., Int. Ed.* **2013**, *52*, 1289-1293.
- [30] E. M. Pérez, M. Sierra, L. Sánchez, M. R. Torres, R. Viruela, P. M. Viruela, E. Ortí, N. Martin, *Angew. Chem., Int. Ed.* **2007**, *46*, 1847-1851.
- [31] T.-C. Wu, H.-J. Hsin, M.-Y. Kuo, C.-H. Li, Y.-T. Wu, *J. Am. Chem. Soc.* **2011**, *133*, 16319-16321.
- [32] M. A. Petrukhina, K. W. Andreini, L. Peng, L. T. Scott, *Angew. Chem., Int. Ed.* **2004**, *43*, 5477-5481.



Chapter 6. Supramolecular polymers

6.1. Introduction

The incorporation of the noncovalent interactions to build up supramolecular constructs using electroactive building blocks lays the foundations of the so-called supramolecular polymer science.^[170] A supramolecular polymer can be defined as any type of assembly formed from one or more molecular components via reversible bonds, i.e., the constituting units are joint together by noncovalent forces.^[171] A rapidly developing interdisciplinary research avenue has emerged with the appearance of supramolecular polymers showing appealing functionalities, with potential interest as optoelectronic, self-healing, and biomedical materials.^[35b]

The first supramolecular polymer was reported in 1990 by Lehn and coworkers,^[172] and was constituted by the junction of bifunctional diamidopyridines and uracil derivatives through a H-bonded array (Figure 41). Subsequently, multiple-hydrogen-bonding arrays with a higher binding constant, such as quadruple-hydrogen-bonding arrays, were employed to achieve supramolecular polymers with high degree of polymerization.^[173]

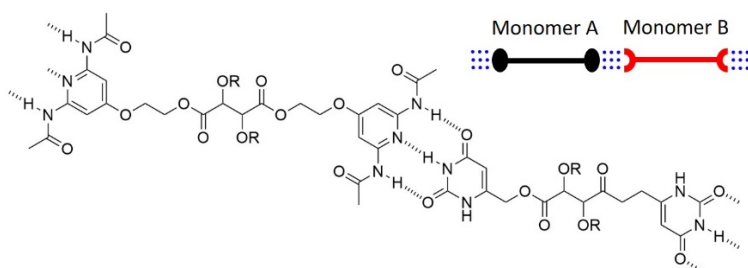


Figure 41. First supramolecular polymer reported by Lehn and coworkers in 1990 generated from a triple-hydrogen-bonding array between bifunctional diamidopyridine and uracil derivatives.^[172]

Apart from the highly-directional H-bonding interactions, a variety of noncovalent interactions (e.g., metal coordination, aromatic stacking, etc.) have also been exploited as driving forces to construct supramolecular polymers (Figure 42).^[37b] For example, metal-containing polymers,^[174] host-guest assemblies,^[175] as well as supramolecular polymers fabricated through strong aromatic donor-acceptor interactions^[176] have been reported. Additionally, chemists have fabricated supramolecular polymers driven by a combination of multiple noncovalent interactions (Figure 42).^[177] The combination of different and orthogonal supramolecular building blocks not only enriches the library of supramolecular polymers, but also allows control of the supramolecular polymerization, achieving supramolecular polymers with well-defined structure and tailor-made functionality.

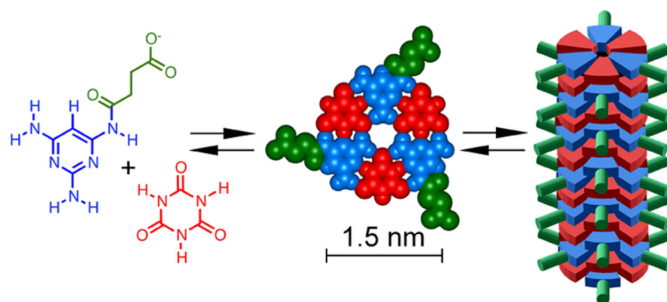


Figure 42. Chemical structures of succinate-conjugated 2,4,6-triaminopyrimidine and cyanuric acid in the generation of a supramolecular polymer governed by multiple noncovalent interactions.^[177b]

Supramolecular chemistry, on the other hand, stands a playground for understanding the ubiquitously-present-in-nature phenomenon of chirality.^[38a] Chirality in supramolecular chemistry implies the non-symmetric arrangement of molecular components in a noncovalent assembly. Chiral assemblies may arise in a supramolecular self-

assembled polymer if one of its component is chiral or if achiral components arrange in a nonsymmetrical way to produce a supermolecule that is chiral. Chiral structures has prompted the development of a number of significant research topics like asymmetric synthesis and catalysis,^[178] liquid crystals,^[179] conductive materials,^[180] and chiral recognition.^[181]

A particularly interesting family of π -conjugated compounds for the construction of functional supramolecular polymers are the so-called discotic molecules.^[182] These chemical entities are structures with a disc-shaped core and a periphery involving a number of interactions that eventually leads to the formation of highly ordered columns. Only at high concentrations, the intercolumnar interactions become prominent, and superstructure formation or gelation occurs followed by the liquid crystalline phase in the bulk. An archetypical example of discotic structure is the benzene-1,3,5-tricarboxamide (BTA) motif, comprising either three N-centred or three CO-centred amides attached to a benzene core (Figure 43).^[183] Such BTAs have attracted considerable attention in supramolecular chemistry in the last few years. Studies conducted on these systems shed light into the mechanism of the self-assembly and the origin of cooperativity, as well as in disentangling the transfer and amplification of chirality in stereospecific molecular units.^[38c, 183-184] The creation of new disc-like electroactive molecules that self-assemble in supramolecular polymers guided by weak and reversible noncovalent interactions will therefore be decisive for understanding the foundations of self-assembly, cooperativity and chirality amplification while creating functional materials to be exploited in optoelectronic, self-healing and biomedical applications.

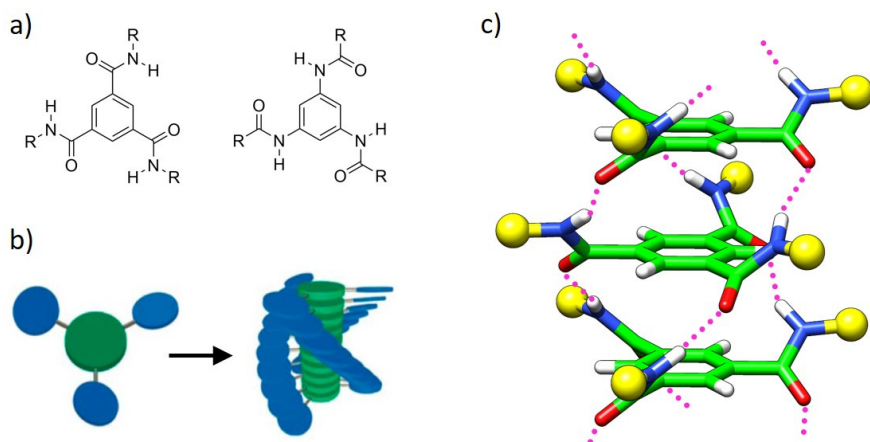


Figure 43. a) Structure of CO-centred (left) and N-centred (right) BTAs. b) Propeller-like shape of C₃-symmetric molecules and their assembly into a helical superstructure upon stacking in columns. c) Triple H-bonding array along the supramolecular arrangement of the CO-centred BTA polymer.

In this Chapter, a thorough theoretical characterization of the forces originating the supramolecular assembly of discotic-like trisamide derivatives has been performed in a multi-level approach. Molecular mechanics calculations are performed to give insight into the preferential helical orientation depending on the connectivity and the presence of stereogenic aliphatic peripheral chains. The factors promoting the cooperative polymerization regime are disentangled within the DFT framework. On the other hand, the self-assembly of peryleneimidazole derivatives presenting multiple noncovalent supramolecular interaction motifs is theoretically characterised. DFT calculations, in a nice synergy with the experimental evidences, give insight into the supramolecular interactions that guide the aggregation and explain the unexpected blue-emissive properties upon gelation.

6.2. Results and discussion

6.2.1. Tricarboxamide supramolecular polymers

Inspired by the structural motif of the BTA compounds, we study herein a series of oligo(phenyleneethynylene) (OPE) N-centred amides (or retroamides) in collaboration with the experimental group of Prof. Luis Sánchez, and compare them with the previously reported^[185] CO-centred tricarboxamide analogues (Figure 44). Experimentally, the supramolecular assembly of the OPE-based derivatives was followed by FTIR and ¹H-NMR. The registration of the circular dichroism (CD) unambiguously demonstrated the formation of enantiomeric helical structures. The helical sense of the columnar aggregates is determined by the absolute configuration of the stereogenic centre (*S* or *R*) allocated in the peripheral alkyl chains, and seems not to be affected by the connectivity of the amide functional groups.

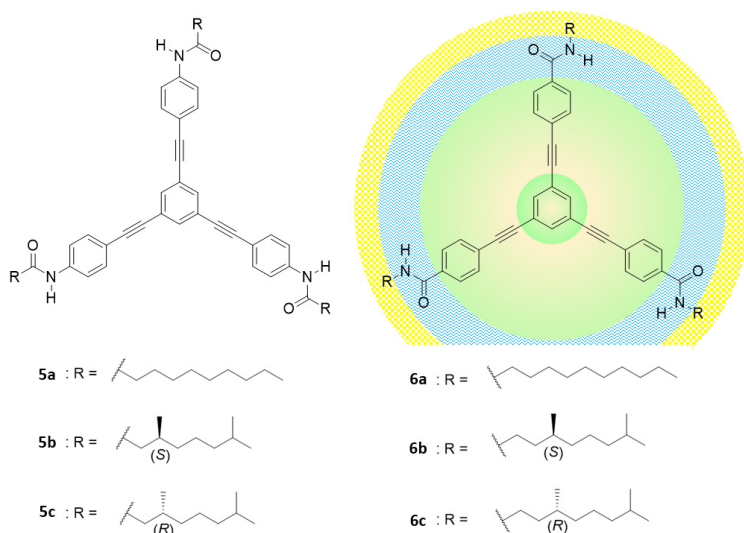


Figure 44. Chemical structures of discotic trisamides **5** and **6**.

To further investigate the role of the connectivity of the amide groups on the self-assembly mechanism, as well as on the chiroptical features of the aggregates, a computational study was performed using a multi-level theoretical approach. The theoretical CD spectra of the trimeric species of **5**, bearing no alkyl chain, in both helical right-handed (**5-*P***) and left-handed (**5-*M***) arrangements were computed at the B3LYP/6-31G* level using the time-dependent density functional theory. The CD spectrum calculated for **5-*M*** shows a positive and a negative peak centred at 290 and 330 nm, respectively, which nicely agrees with the CD spectrum recorded for **5c** (280 and 303 nm, Figure 45). Moreover, the relative intensities of the positive/negative peaks predicted theoretically reasonably match the experimental CD signals. The CD spectrum computed for **5-*P*** stands as the mirror image of the CD for **5-*M*** (Figure 45b), and matches the shape recorded experimentally for **5b** (Figure 45a). In addition, the CD spectrum computed for the trimer of **6** in a clockwise conformation (**6-*P***) presents the same signal pattern as for **5-*P***, which indicates that the origin of this intense CD signal pattern is ascribable to the helical disposition of the molecules in the columnar stack with minor contribution from the amide connectivity. The electronic transitions giving rise to the CD signal in the 260–360 nm region (vertical lines in Figure 45b) were computed to correspond with π - π^* monoexcitations and mainly involve the conjugated OPE units.^[186] Theoretical calculations therefore show that the preferred orientation of **5b** with *S*-stereogenic centres in the alkyl chains is a right-handed (*P*) helix, whereas it corresponds to a left-handed (*M*) helix for **5c** with *R*-stereogenic centres.

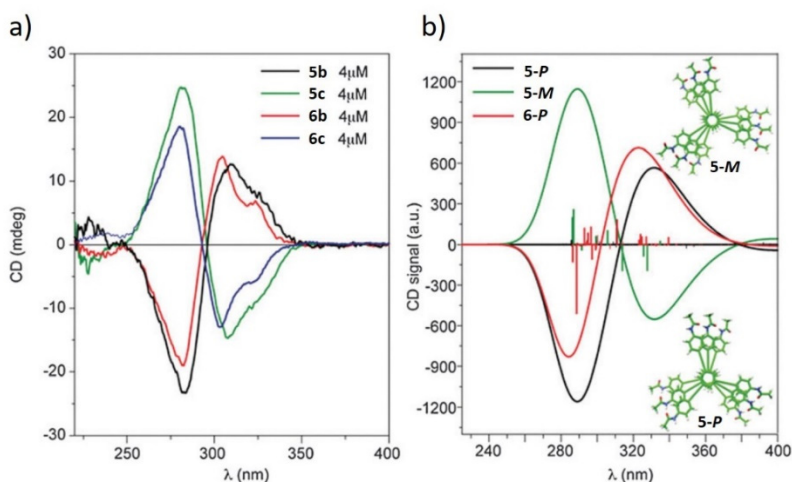


Figure 45. a) Experimental CD spectra of **5b-c** and **6b-c** (DNH/CHCl₃, 95/5, 4×10^{-6} M, 298 K). b) Theoretical simulations of the CD spectra calculated for the **5-M**, **5-P** and **6-P** trimers.

To shed light on the helical organization of the aggregates formed by trisamides **5** and **6**, theoretical molecular mechanics/molecular dynamics (MM/MD) simulations were performed using the MM3 force field. A π -stacked decamer of **5c** was firstly designed with both right- and left-handed helicities as a representative model to investigate the relative stability of the two possible columnar configurations. MD simulations of 100 ps were performed on infinite aggregates using periodic boundary conditions. Supramolecular arrangements of **5c** with *P* and *M* orientations endowed with short and long chains were considered. The values calculated for E_{bind} in the infinite aggregates of **5c** with $-C_5H_{11}$ chains are -44.8 ± 0.3 and -45.0 ± 0.2 kcal mol⁻¹ for the *P* and *M* configurations, respectively. Moving to the systems with longer $-C_9H_{19}$ chains, the difference in binding energy per monomeric unit increases to 1 kcal mol⁻¹ in favour of the *M*-type helix ($E_{\text{bind}} = -49.2 \pm 0.5$ and -50.1 ± 0.9 kcal mol⁻¹ for *P* and *M* aggregates, respectively). The theoretical

results therefore indicate that the energy difference between the two possible helical configurations significantly increases when increasing the length of the peripheral side chains, and predict that the left-handed (*M*) columnar stacking is the energetically preferred helical arrangement for the aggregation of **5c** bearing stereogenic *R* centres.

Supramolecular aggregates of **5b** with long $-C_9H_{19}$ chains containing stereogenic *S* centres were also calculated in both clock- and anticlockwise helicities, and now the *P*-helix is computed to be the more stable ($E_{\text{bind}} = -50.2 \pm 0.7$ and -49.1 ± 0.4 kcal mol⁻¹ for **5b-P** and **5b-M**, respectively). These results justify the occurrence of a preferred helicity for a given configuration (*S* or *R*) of the stereogenic centre placed on the peripheral alkyl chains of retroamides **5**. Further MM/MD simulations performed for the supramolecular assemblies of **6c** led to similar conclusions as those found for **5c**, being the anticlockwise **6c-M** ~ 1 kcal mol⁻¹ more stable than **6c-P** ($E_{\text{bind}} = -46.1 \pm 0.7$ and -47.1 ± 0.7 kcal mol⁻¹ for **6c-P** and **6c-M**, respectively). Theoretical calculations therefore show that the preference of a determined helical handedness in the trisamides under study depends on the chirality of the stereogenic group, and is not affected by the connectivity in which the amide group is linked to the discotic core. Furthermore, the E_{bind} values are computed lower for **6c** than for **5b-c**, which is in accordance with the higher cooperativity experimentally obtained for the supramolecular polymerization of retroamides **5**.

A representative snapshot of the MD simulation for the helical *M*-aggregate of **5c** was extracted to analyse the spatial disposition of the molecular units in the polymer (Figure 46). In the stack, the OPE cores remain mostly planar to maximize the π - π interactions, whereas the

amide groups are twisted out of the aromatic plane forming H-bonds with the vicinal monomer. These two types of interactions are the driving force that finally gives rise to perfectly-assembled columnar helices (see the original **Publication 8** for more details).

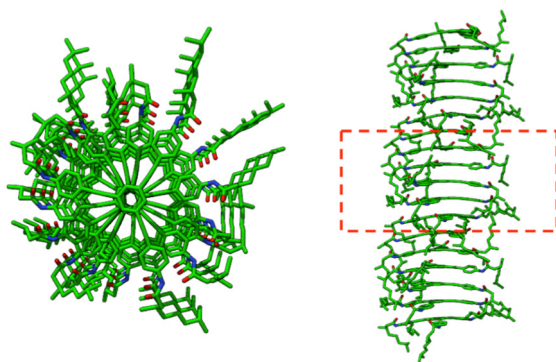


Figure 46. Top and side views of the most stable structure obtained from the MM/MD simulation for the left-handed *M*-helix of the *N*-centred retroamide **5c**. The unit cell containing six monomeric units is marked in dashed red lines. H atoms are omitted for clarity.

To gain deeper insight into the supramolecular polymerization mechanism of trisamides **5** and **6**, comparative DFT calculations at the MPWB1K/6-31G** level were performed for helical *P*-aggregates of increasing size of retroamide **5b** and carboxamide **6b**. To reduce the cost of the calculations, short $-C_5H_{11}$ and $-C_6H_{13}$ alkyl chains bearing the stereogenic *S* centre were used for **5b** and **6b**, respectively. Figure 47 shows the change, as *n* increases, of the association energy per monomeric unit ($E_{bind,n}$) for the $(\mathbf{5b})_n$ aggregate, and provides a clear indication of the cooperative character of the supramolecular polymerization. As the aggregate grows, the absolute value of $E_{bind,n}$ increases, due to the larger polarization of the stack that strengthens the H-bonding network, and the aggregate becomes more stable. The values

predicted for $E_{\text{bind},n}$ in $(\mathbf{5b})_n$ ($-31.0 \text{ kcal mol}^{-1}$ for $n = \infty$) are larger, in absolute value, than those obtained for $(\mathbf{6b})_n$ ($-25.2 \text{ kcal mol}^{-1}$ for $n = \infty$). Likewise, there is an increase of the dipole moment per monomer unit ($DM_{\text{mon},n}$) for $(\mathbf{5b})_n$, which is calculated larger (12.94 D for $n = \infty$) than that for $(\mathbf{6b})_n$ (11.04 D for $n = \infty$). The cooperativity in the trisamide helices, found larger for N-centred **5**, is therefore evidenced by the theoretical calculations through the evolution of both the binding energy and the dipole moment per monomeric unit upon increasing the polymer size.

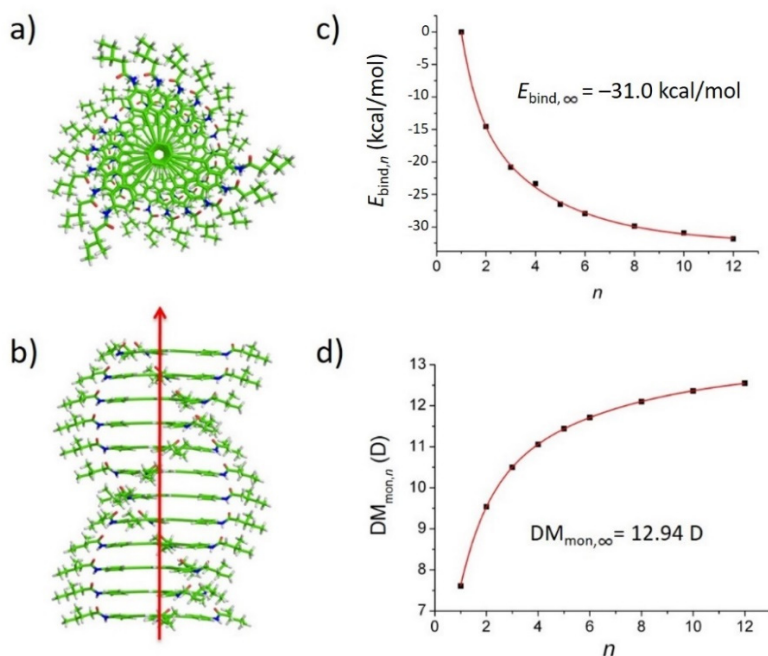


Figure 47. Top (a) and side (b) views of the right-handed helical arrangement of the $(\mathbf{5b})_{12}$ aggregate bearing S -stereogenic short alkyl chains. The direction of the dipole moment in the stack is shown in red. Asymptotic behaviour of the binding energy (c) and dipole moment (d) per monomer unit ($E_{\text{bind},n}$ and $DM_{\text{mon},n}$, respectively) upon increasing the number of monomer units in the $(\mathbf{5b})_n$ aggregate; values are fitted (red line) to a biexponential function.

Along the PhD period, other similar systems based on the subphthalocyanine core have been studied in a fruitful collaboration with the group of Profs. Tomás Torres and David González-Rodríguez.^[187] Cone-shaped SubPc units are demonstrated to self-assemble in helical supramolecular polymers with a combination of π - π , H-bond and highly polar B-F \cdots B interactions. The reader is referred to the original work for further details (see article 20 in the List of publications). Implications of mixing pure enantiomers in the resulting supramolecular polymer helicity, as well as the study of columnar vs. dimeric vs. dissociated regimes as a function of the solvent, is under writing process.^[188]

6.2.2. Pyreneimidazole-based oligomers

Since its discovery in 1837 by Laurent in the residue of the destructive distillation of coal tar,^[189] pyrene has become one of the most studied polycyclic aromatic hydrocarbons. The attractive electronic and photophysical properties of pyrene allowed its application as an active component in organic electronics.^[190] To improve the emissive properties of pyrene, great efforts have been devoted to its structural modification in order to avoid aggregation and to suppress the quenching effect of the π - π interactions.^[190b, 191] In the search for novel functional materials based on the π -conjugated core of pyrene connected supramolecularly by H-bond interactions, a pyreneimidazole structure and its supramolecular polymerization features have been investigated (Figure 48). Whereas supramolecular polymerization patterns usually follow a predictable motif based on the chemical groups introduced in the electroactive unit, the three-dimensional arrangement of supramolecular polymers sometimes leads to unexpected structures hard to elucidate. This work

constitutes a great example of a symbiotic study combining our first-principles calculations with the experiments carried out by the group of Prof. Luis Sánchez to shed light onto the odd self-assembly of blue-emitting pyrene-based supramolecular polymers.

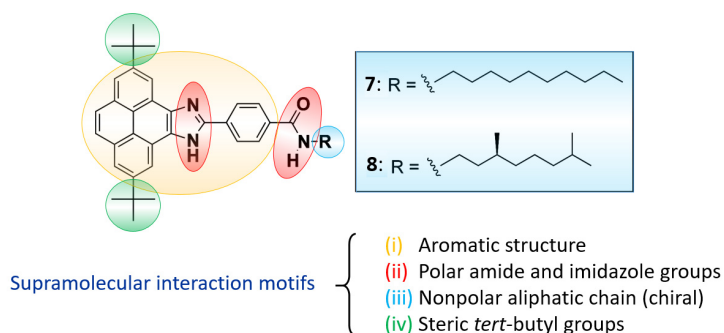


Figure 48. Chemical structure of pyreneimidazoles **7** and **8** and schematic representation of their supramolecular interaction motifs.

Experimental evidences of the supramolecular polymerization of the pyreneimidazole derivatives shown in Figure 48 were extracted from temperature-dependent UV-Vis spectroscopy measurements. These compounds show formation of gels in cyclohexane at low concentrations, exhibiting an unexpected blue emission under irradiation at 364 nm, and a low degree of cooperativity in the supramolecular polymerization. Circular dichroism measurements as well as sergeants-and-soldiers experiments were carried out by the group of Prof. Luis Sánchez for both the achiral **7** and chiral **8** derivatives in order to disentangle the supramolecular organization of the organogels. The formation of supramolecular helical arrangements for this family of pyreneimidazoles was ruled out due to the absence of any dichroic signal.

Theoretical calculations were performed on compound **7** within the density functional theory (DFT) framework to shed light on the structural

and energetic aspects of the pyreneimidazole system upon aggregation. A number of dimers, as minimal supramolecular units, were modelled for 7 owing to the variety of supramolecular interaction motifs present in the monomer: (i) the aromatic structure, (ii) the polar amide and imidazole groups, (iii) the nonpolar long aliphatic chain, and (iv) the steric *tert*-butyl groups (Figure 48). Besides the π - π recognition motif that gives rise to structures **A–C** with weak CO \cdots HN (**A** and **C**) or NH \cdots N (**B**) H-bond interactions, the polar imidazole and amide groups constitute high potential energy regions for the supramolecular stabilization of the dimers. Thereby, dimers **D–F**, in which the formation of strong H-bonds is the recognition driving force, were modelled (Figure 49).

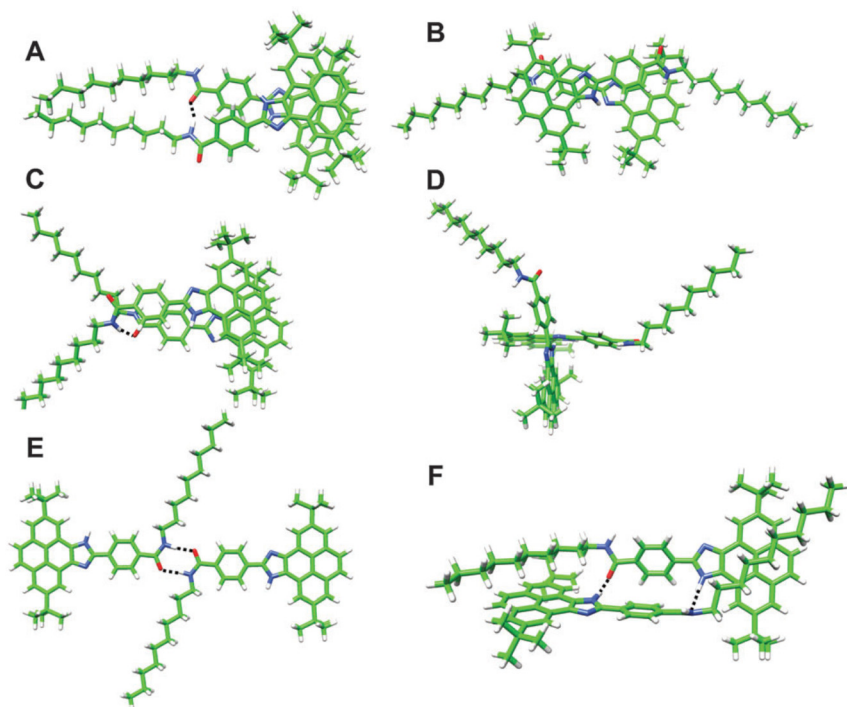


Figure 49. Minimum-energy geometries calculated for the different dimers postulated for the pyreneimidazole system at the B97-D3/6-31G** level of theory.

Table 7. Binding energy (E_{bind} , in kcal mol⁻¹), number of H-bond contacts (n_{HB}), distance of the closest H-bond contact (d_{HB} , in Å), and dominant dispersion interactions (π - π , CH \cdots π and CH \cdots CH) that characterise dimers **A-F**.

	E_{bind}	n_{HB}	d_{HB}	π - π	CH \cdots π	CH \cdots CH
A	-54.6	1	1.918	✓	-	-
B	-51.0	1	2.064	✓	-	-
C	-53.7	1	2.051	✓	-	-
D	-32.0	1	1.826	-	✓	-
E	-7.7	2	1.822	-	✓	-
F	-61.7	2	1.839	-	✓	-

Table 7 summarises the binding energy (E_{bind}) and the main intermolecular forces governing the self-assembly of dimers **A-F** calculated at the B97-D3/6-31G** level. For a detailed description of dimers **A-E**, the reader is referred to the original **Publication 9** below. Focusing on the most stable dimeric species, arrangement **F** combines H-bonding interactions between the imidazole and amide groups and CH \cdots π stabilizing interactions between the alkyl chains and the pyrene cores (Figure 49). Topological analysis of the electron density carried out by means of the NCI index allows visualizing the non-covalent interaction (NCI) surfaces, which provide additional information on the origin of the supramolecular aggregation. Green surfaces indicate weak nondirectional CH \cdots π interactions, whereas small bluish regions correspond to strong H-bond contacts (Figure 50). The additive effect of these interactions leads to the highest stability ($E_{\text{bind}} = -61.7$ kcal mol⁻¹) calculated among all the dimers modelled. The structure of dimer **F** allowed us to identify all the ROESY signals observed experimentally and, in particular, the short contacts between the alkyl chains and the pyrene cores. Additionally, taking into account that the formation of π - π dimers

quenches the emission properties of pyrene, the absence of these π - π interactions between the pyrene cores in dimer **F** would explain the blue emission obtained for the fibres.

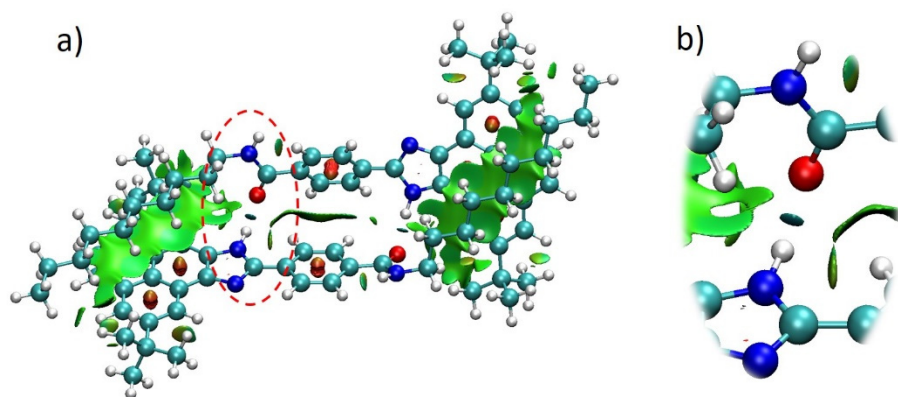


Figure 50. a) NCI surfaces representing H-bond interactions (in blue) and dispersion forces (in green) for dimer **F** of compound **7**. Intramolecular ring-centroid repulsions are drawn in brown. b) Amplified view of the bluish NCI surface corresponding to a well-formed H-bond interaction.

To rationalize how dimer **F** can grow up from such nonplanar, distorted disposition of the monomers, a tetramer shown in Figure 51 was built up through an imidazole–amide–imidazole H-bond sequence. After full geometry optimization at the B97-D3/6-31G** level, calculations reveal that the H-bonding motif is preserved along the monomeric pairs. The average NH(amide)–N(imidazole) contact is computed to be 2.18 Å, whereas the CO(amide)–HN(imidazole) interaction is calculated at 1.82 Å. The total association energy in the tetramer reaches -182.1 kcal mol $^{-1}$, which corresponds with an $E_{\text{bind}} = -60.7$ kcal mol $^{-1}$ per monomer pair. This value is very close to the E_{bind} computed for dimer **F** (-61.7 kcal mol $^{-1}$), suggesting that the oligomer can easily grow keeping the strong H-bond pattern and the stabilizing CH \cdots π forces. Besides, the alternated

H-bonding network upon self-assembly points towards a low degree of cooperativity in the supramolecular polymerization, in line with the experimental evidences.

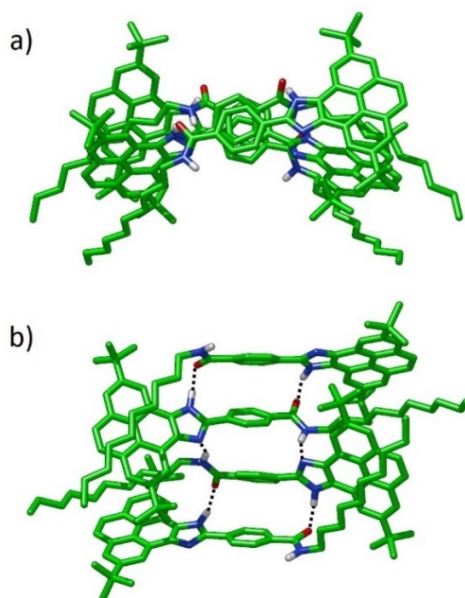


Figure 51. Top (a) and side (b) views of the B97-D3/6-31G**-optimized geometry calculated for the tetramer of **7** in an **F**-type assembly. Dotted lines emphasize the H-bonding array established between the imidazole and amide units. Only hydrogen atoms involved in H-bonding interactions are shown.

Recently, other family of derivatives based on the N-annulated perylenedicarboxamide have been investigated in collaboration with the group of Luis Sánchez.^[192] Interestingly, these compounds led to the formation of bundles of fibres that generate a spontaneous anisotropy in the environment. The supramolecular assembly of these derivatives was rationalized in terms of columnar superstructures with an oscillating helical orientation upon external stimuli (see article 22 in the List of publications).

6.3. Summary

We demonstrate herein the cooperative supramolecular polymerization of discotic N-centred trisamides based on the OPE unit to form helical aggregates. The inverted connectivity of the amide functional groups does not modify the helical sense of the aggregates in comparison with the previously reported CO-centred analogues. The handedness of the helical structures formed by the self-assembly depends on the absolute configuration (*S* or *R*) of the stereogenic centres located at the peripheral side chains. MM/MD simulations performed for infinite aggregates help to energetically discriminate between the *P* and *M* arrangements, and support the preference of a determined helical handedness depending on the chirality of the stereogenic group. The synergy of π - π interactions, the threefold H-bonding between the amides, and the weak dispersive forces between the peripheral alkyl chains exert a prominent role on the construction of the helical supramolecular structures. The cooperative character of the polymerization mechanism, higher for N-centred retroamides than CO-centred tricarboxamides, is furthermore supported by the dipole moment per monomeric unit that grows exponentially due to the enhancement of the polarization of the H-bonding network during the nucleation process.

On the other hand, pyreneimidazole derivatives have been designed with a variety of supramolecular interaction motifs that guide their self-assembly towards a supramolecular polymerization process. The organized supramolecular structures are able to immobilize apolar solvents like cyclohexane forming gels with apparently non-helical organization. The number and type of noncovalent interactions operating in these pyrene-type derivatives result in an amazing scenario of

possibilities for aggregation. Theoretical calculations demonstrate, in a nice synergy with the experimental data, that the formation of the aggregates is mainly governed by the H-bonding interactions between the amide functionality and the imidazole moiety, together with a number of relevant CH \cdots π interactions. The absence of π - π interactions between the pyrene cores further explains the preservation of the typical blue-emitting properties of pyrene upon aggregation in the fibrillar material.

6.4 Publications

Publication 8 J. Buendía, J. Calbo,† F. García, J. Aragón, P. M. Viruela, E. Ortí, L. Sánchez, "Helical supramolecular polymerization of C₃-symmetric amides and retroamides: on the origin of cooperativity and handedness", *Chem. Commun.* **2016**, *52*, 6907–6910.

Publication 9 J. S. Valera, J. Calbo,† R. Gómez, E. Ortí, L. Sánchez, "Blue-emitting pyrene-based aggregates", *Chem. Commun.* **2015**, *51*, 10142–10145.

Reproduced with permission of Royal Society of Chemistry.

Cite this: *Chem. Commun.*, 2016, 52, 6907Received 30th March 2016,
Accepted 22nd April 2016

DOI: 10.1039/c6cc02681h

www.rsc.org/chemcomm

Helical supramolecular polymerization of C_3 -symmetric amides and retroamides: on the origin of cooperativity and handedness†‡

Julia Buendía,§^a Joaquín Calbo,§^b Fátima García,^a Juan Aragón,^b Pedro M. Viruela,^b Enrique Orti*^b and Luis Sánchez*^a

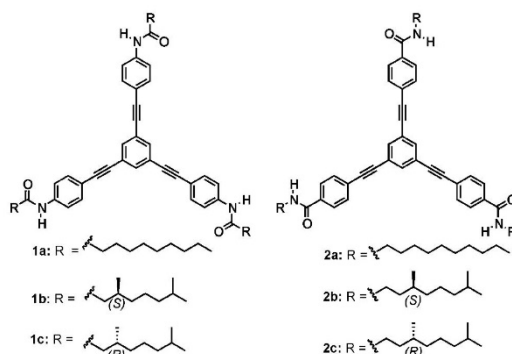
The cooperative supramolecular polymerization of **1 and **2** yields *P*- or *M*-type helical aggregates depending on the absolute configuration (*S* or *R*) of the stereogenic centres attached to the side chains. The connectivity of the amide group does not affect the handedness of the helical aggregates, but determines a larger cooperativity for retroamides **1**.**

Since the first example reported by Lehn in 1990,¹ the research on supramolecular polymers has established spectacular developments.² Considering the level of sophistication and functionality showed by natural helical structures, the rational generation of helical supramolecular polymers is one of the most exciting areas of investigation for this class of polymers.³ A key issue in the construction of helical structures is to control their handedness, which is directly related with the efficient transfer of the chiral information embedded in the constitutive chiral units. Although it is possible to achieve chiral supramolecular polymers by using elements of asymmetry like axial chirality,⁴ the sign and magnitude of the optical activity is usually conditioned by the stereogenic centres at peripheral chains linked to cores of different nature.⁵

We report herein on a joint experimental and theoretical investigation of the supramolecular polymerization of *N*-centred retroamides **1** in comparison with previously reported CO-centred tricarboxamides **2** (Fig. 1).⁶ We demonstrate that reversing the connectivity in retroamides **1** results in a cooperative supramolecular polymerization that yields helical aggregates with the same handedness for both self-assembling units. Theoretical calculations have been utilized to assign the handedness of the aggregates and to investigate the cooperative mechanism of the

supramolecular polymerization. Molecular mechanics/molecular dynamics (MM/MD) simulations find an energy difference between *P*- and *M*-type supramolecular helical structures, depending on the absolute configuration (*S* or *R*) of the stereogenic centres, that is large enough to determine a preferred handedness of the helical structure. This joint experimental-theoretical study yields information on the rules governing the transference of chirality from the constituting chiral molecular entities to the self-assembled helical supramolecular structures, and represents a useful complement to recent studies on *N*-centred benzene-1,3,5-tricarboxamides (BTAs) and related oligo(phenylene ethynylene) (OPE) retroamides.^{7,8}

The synthesis of trisamides **1a–c** has been accomplished in three synthetic steps for achiral **1a** and four synthetic steps for chiral **1b–c** (Scheme S1, ESI†). The FTIR spectra show well-defined bands at 3297, 1666 and 1585 cm^{-1} (Fig. S1, ESI†), corresponding to the *N*-H and amide I (C=O) stretching bands and to the amide II (C-N) bending band, respectively, which are indicative of the formation of an intermolecular triple array of H-bonds between the amide functional groups.⁶ The ¹H NMR spectra of **1c** show only three resonances ascribable to anisochronous aromatic

Fig. 1 Chemical structures of trisamides **1** and **2**.

^a Departamento de Química Orgánica, Facultad de Ciencias Químicas, Ciudad Universitaria s/n, 28040 Madrid, Spain. E-mail: lusamar@quim.ucm.es

^b Instituto de Ciencia Molecular, Universidad de Valencia, 46980 Paterna, Spain. E-mail: enrique.orti@uv.es

† Dedicated to Professor Nazario Martín on the occasion of his 60th birthday.

‡ Electronic supplementary information (ESI) available: Fig. S1–S14 and theoretical computational details. See DOI: 10.1039/c6cc02681h

§ These authors contributed equally.

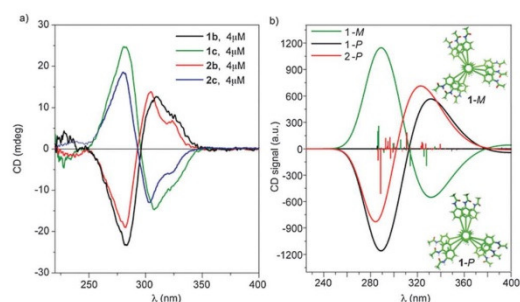


Fig. 2 (a) Experimental CD spectra of **1b–c** and **2b–c** (DHN/CHCl₃, 95/5, 4 × 10⁻⁶ M, 298 K). (b) Theoretical simulations of the CD spectra calculated for the **1-M**, **1-P** and **2-P** trimers.

protons (Fig. S2, ESI†). The three amides appear as a broad singlet at $\delta \sim 7.2$. As expected, increasing the concentration in the ¹H NMR results in deshielding of the amide resonance and in the concomitant upfield shift of the aromatic protons (Fig. S2, ESI†). The combination of both FTIR and ¹H NMR spectroscopic data suggests the ability of retroamides **1** to form helical supramolecular structures, as previously reported for **2**.⁶

Trisamides **1**, and especially achiral **1a**, are sparingly soluble in apolar solvents. Therefore, the use of mixtures of solvents is required to determine the chiroptical activity of the chiral retroamides **1b–c** and to study the mechanism of self-assembly. The circular dichroism (CD) spectra of **1b** and **1c** were recorded by using a mixture of decaline (DHN), as a poor solvent, with 5% of chloroform, as a good solvent. Similarly to the dichroic pattern previously reported for OPE-retroamides,⁷ a clear bisignated Cotton effect with negative and positive waves peaking at 280 and 303 nm, respectively, is visible for **1b**, and presents the opposite sign pattern for **1c** (Fig. 2a). The dichroic pattern of **1b** and **1c** coincides with that recorded using the same experimental conditions for **2b** and **2c**, respectively. This demonstrates the formation of enantiomeric helical structures, and that the connectivity of the amide functional group does not affect the helical sense of the columnar aggregate. The sense of the helix is determined by the absolute configuration of the stereogenic centre (*S* or *R*) allocated in the peripheral alkyl chains.

The thermodynamic parameters associated with the helical supramolecular polymerization of **1b–c** were investigated by variable-temperature experiments in a DHN/CHCl₃ (95/5) mixture as solvent. The cooling curves of **1b–c** show a non-sigmoidal shape characteristic of a cooperative nucleation–elongation mechanism (Fig. S3 and S4, ESI†).^{2,6} Fitting the curves to the equilibrium (EQ) model allows the derivation of the enthalpy of elongation, ΔH_e , the entropy of elongation, ΔS , the nucleation penalty, ΔH_n , and the temperature of elongation, T_e .⁹ Table 1 shows that the thermodynamic data derived for **1b** and **1c** are larger, in absolute value, than those obtained for **2b** (Fig. S5, ESI†), which indicates a higher stability of the N-centred retroamides **1**. This result contrasts with that reported for BTAs, for which the CO-centred aggregates are more stable than the N-centred congeners.^{7,10}

Table 1 Thermodynamic parameters of **1b–c** and **2b** in a DHN/CHCl₃ (95/5) solution

Compound	ΔH_e (kJ mol ⁻¹)	ΔS (J mol ⁻¹ K ⁻¹)	ΔH_n (kJ mol ⁻¹)
1b	-94.4 ± 0.8	-201 ± 2	-31.1 ± 8
1c	-92.6 ± 0.5	-197 ± 1	-22.4 ± 1
2b	-63.2 ± 0.7	-114 ± 2	-17.2 ± 0.2

To further investigate the role of the connectivity of the amide groups on the self-assembly mechanism, as well as on the chiroptical features of the aggregates, a computational study has been performed using a multi-level theoretical approach. The theoretical CD spectra of the trimer species of **1**, bearing no alkyl chain, in both helical right-handed (**1-P**) and left-handed (**1-M**) arrangements were first computed at the B3LYP/6-31G* level using time-dependent density functional theory (TD-DFT) (see ESI†).¹¹ The CD spectrum calculated for **1-M** shows a positive and a negative peak centred at 290 and 330 nm (Fig. 2b), respectively, which nicely agrees with the CD spectrum recorded for **1c** (280 and 303 nm, Fig. 2a). Moreover, the relative intensities of the positive/negative peaks predicted theoretically reasonably match with the experimental CD signals. The electronic transitions giving rise to the CD signal in the 260–360 nm region (vertical lines in Fig. 2b) correspond to $\pi \rightarrow \pi^*$ monoexcitations and mainly involve the conjugated OPE units.¹¹

The CD spectrum computed for **1-P** stands as the mirror image of the CD for **1-M** (Fig. 2b), and matches the shape recorded experimentally for **1b** (Fig. 2a). In addition, the CD spectrum computed for the trimer of **2** in a clockwise conformation (**2-P**) presents the same signal pattern as for **1-P**, which indicates that the origin of this intense CD signal pattern is ascribable to the helical disposition of the molecules in the columnar stack with minor contribution from the amide connectivity. In fact, the experimental CD measurements demonstrate that the difference between **1** and **2** with opposite amide connectivity is only a slight blue-shift of the CD signal (Fig. 2a), which is correctly predicted in the theoretical simulations (Fig. 2b). Theoretical calculations therefore show that the preferred orientation of **1b** with *S*-stereogenic centres in the alkyl chains is a right-handed (*P*) helix, whereas it corresponds to a left-handed (*M*) helix for **1c** with *R*-stereogenic centres.

To shed light on the helical organization of the aggregates formed by trisamides **1** and **2**, theoretical MM/MD simulations were performed using the well-tested MM3 force field (see ESI† for details). A π -stacked decamer of **1c** was firstly designed with both right- and left-handed helicity as a representative model to investigate the relative stability of the two possible columnar configurations. Two different sizes of peripheral alkyl chain were used in the calculations: short chains of -C₅H₁₁ and long chains of -C₉H₁₉, identical to those actually attached to the OPE core (Fig. S6, ESI†). After full geometry optimization using MM3 (Fig. S7, ESI†), both the right- and left-handed helical decamers are computed to be practically isoenergetic when using the short -C₅H₁₁ chains, with the *M*-helix being 0.8 kJ mol⁻¹ more stable. The energy difference between the *P* and *M* helices increases to 12.6 kJ mol⁻¹ in favour of the *M*-type helix for

the decamer bearing the long $-C_9H_{19}$ chains, which suggests that the size of the alkyl chain is relevant to the energy differentiation between a right- and a left-handed growth of the columnar stacks. The intermolecular distance between monomers along the stacking axis (Δz) is predicted to be very similar for all the decamers, ranging from 3.42 to 3.45 Å (Fig. S7, ESI†). The mean value for the rotational dihedral angle between adjacent monomers is $\sim 20^\circ$ in the four decamers with H-bond interactions in the range of 1.93–1.97 Å.

As a second step in the theoretical study of the relative stability of the helical *P* and *M* aggregates, MD calculations of 100 ps were performed on infinite aggregates using periodic boundary conditions. All the possible supramolecular arrangements of **1c**, that is, the *P* and *M* helices endowed with short and long chains, were considered. The unit cells contained six monomer units and were built up using the MM3-optimized values of Δz and a twisting angle between adjacent monomers of 20° . Since the monomer possesses C_3 symmetry, translational periodicity along the stacking axis was achieved after six rotations of 20° (Fig. S8, ESI†).

Fig. S9 (ESI†) shows the potential energy evolution over time for the different dynamics. The stabilizing binding energy due to the noncovalent interactions between adjacent molecules in the stack was calculated as a mean value per monomer unit (E_{bind}) using 200 random MM3-optimized structures over the last 50 ps of the MD trajectories and the following expression.

$$E_{\text{bind}} = (E_{\text{cell}} - nE_{\text{mon}})/n \quad (1)$$

In eqn (1), E_{cell} is the energy of the unit cell, E_{mon} is the energy of an isolated monomeric unit, and n is the number of molecules in the unit cell ($n = 6$). The values calculated for E_{bind} in the infinite aggregates of **1c** with $-C_5H_{11}$ chains are -187.4 ± 1.3 and -188.2 ± 0.7 kJ mol $^{-1}$ for the *P* and *M* configurations, respectively. Moving to the systems with the long $-C_9H_{19}$ chains, the difference in binding energy per monomeric unit increases to 4 kJ mol $^{-1}$ in favour of the *M*-type helix ($E_{\text{bind}} = -205.7 \pm 1.9$ and -209.7 ± 3.6 kJ mol $^{-1}$ for *P* and *M* aggregates, respectively). The theoretical results therefore show that the energy difference between the two possible helical configurations significantly increases when increasing the length of the peripheral side chains, and predict that the left-handed (*M*) columnar stacking is the energetically preferred helical arrangement for the aggregation of **1c** bearing stereogenic *R* centres.

In the stack, the OPE cores remain mostly planar to maximize the π - π interactions, whereas the amide groups are twisted out of the aromatic plane forming H-bonds with the vicinal monomer (see Fig. S11 for the most stable structure obtained from the MD simulation for the helical *M*-aggregate of **1c**, ESI†). These two types of interactions are the driving force that finally gives rise to perfectly assembled columnar helices.

Supramolecular aggregates of **1b** with long $-C_9H_{19}$ chains containing stereogenic *S* centres were modelled in both the clockwise **1b-P** and anticlockwise **1b-M** helicities. MM/MD calculations led to mean E_{bind} values of -205.6 ± 1.8 and -210.0 ± 3.1 kJ mol $^{-1}$ for **1b-M** and **1b-P**, respectively. These

values are similar to those obtained for **1c-M** (-209.7 ± 3.6 kJ mol $^{-1}$) and **1c-P** (-205.7 ± 1.9 kJ mol $^{-1}$), but now the *P*-helix is more stable for **1b**. The theoretical results therefore justify the occurrence of a preferred helicity for a given configuration (*S* or *R*) of the stereogenic centre placed on the peripheral alkyl chains of retroamides **1**.

MM/MD simulations were also performed for the supramolecular assemblies of **2c** following the same procedure as for the N-centred systems. Long dynamics of 100 ps were conducted for both aggregates and the mean E_{bind} values calculated were -193.0 ± 2.9 and -197.2 ± 3.1 kJ mol $^{-1}$, for **2c-P** and **2c-M**, respectively. Theoretical calculations therefore predict that the preferred helical sense for trisamide **2c** is left-handed, which coincides with the preferential helicity obtained for the *R*-stereogenic **1c** assembly. Furthermore, the E_{bind} values computed for **2c** are lower than those found for **1b-c**, which is in accordance with the higher cooperativity experimentally obtained for the supramolecular polymerization of retroamides **1** (Table 1).

To gain deeper insight into the supramolecular polymerization mechanism of trisamides **1** and **2**, comparative DFT calculations at the MPWB1K/6-31G** level were finally performed for the helical *P*-aggregates of increasing size of retroamide **1b** and carboxamide **2b**. To reduce the cost of the calculations, short $-C_5H_{11}$ and $-C_6H_{13}$ alkyl chains bearing the stereogenic *S* centre were used for **1b** and **2b**, respectively (Fig. S12, ESI†). Ideal columnar aggregates including $n = 1-6, 8, 10$, and 12 molecules were generated using the molecular geometry and the stacking parameters obtained at the MPWB1K/6-31G** level for the central molecule of a fully optimized pentamer (see ESI† and Fig. S13). In the (**1b**) $_n$ aggregates, adjacent molecules are separated by $\Delta z = 3.75$ Å and are rotated by $\theta = 18.2^\circ$ along the stack forming a triple H-bonding network with N-H...O=C distances of 1.85 Å. The amide groups are twisted out of the molecular plane by 43.4° to maximize the intermolecular interactions. Fig. 3a and b show the structure of the (**1b**) $_{12}$ aggregate as a representative example. Similar intermolecular parameters were used for the (**2b**) $_n$ aggregates (see ESI†).

The binding energy per monomer unit ($E_{\text{bind},n}$) depends on the number of monomer units (n) forming the aggregate and is calculated with eqn (1) using the total energy of the aggregate instead of the energy of the unit cell (Table S1, ESI†). Fig. 3c and Fig. S14 (ESI†) show the change, as n increases, of $E_{\text{bind},n}$ for the (**1b**) $_n$ aggregate and provides a clear indication of the cooperative character of the supramolecular polymerization. As the aggregate grows, the absolute value of $E_{\text{bind},n}$ increases due to the larger polarization of the stack that strengthens the H-bonding network, and the aggregate becomes more stable. It is worth noting that the asymptotic limit ($n = \infty$) is rapidly approached upon addition of 8–12 monomer units; the increase in stabilization being relatively small from then on. The stabilization of the columnar aggregate per monomer unit predicted for the decamer (-123.70 kJ mol $^{-1}$) is indeed very close to the value obtained from the extrapolation to $n = \infty$ (-129.87 kJ mol $^{-1}$).¹² The increase of $E_{\text{bind},n}$ indicates an initial nucleation process, in which the stability of the aggregate rapidly increases with n , followed by an elongation process, in which the incorporation of new monomeric units has no additional effect. This supports the

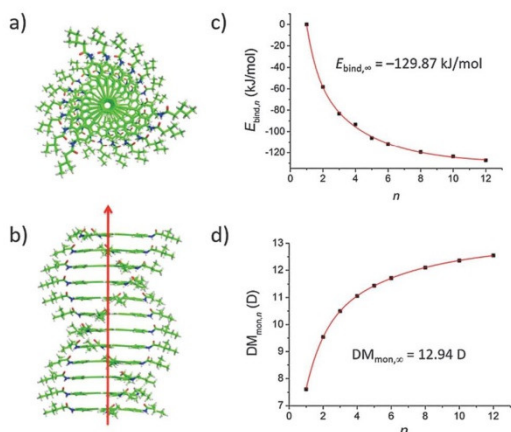


Fig. 3 Top (a) and side (b) views of the right-handed helical columnar arrangement of the $(\mathbf{1b})_{12}$ aggregate bearing *S*-stereogenic short alkyl chains. The direction in which the dipole moment grows in the stack is shown in red. Asymptotic behavior of the binding energy (c) and dipole moment (d) per monomer unit ($E_{\text{bind},n}$ and $DM_{\text{mon},n}$, respectively) upon increasing the number of monomer units in the $(\mathbf{1b})_n$ aggregate; values are fitted (red line) to a biexponential function as explained in the ESI.†

cooperative polymerization mechanism proposed above from the experimental data. The cooperative character of the supramolecular polymerization is additionally evidenced by the increase of the dipole moment per monomer unit ($DM_{\text{mon},n}$) calculated for $(\mathbf{1b})_n$. As shown in Fig. 3d, $DM_{\text{mon},n}$ increases exponentially with the number of monomeric units along the growing direction, evidencing the enhancement of the polarization of the H-bonding network during the nucleation process.¹³

The binding energies and dipole moments per monomer unit calculated for $(\mathbf{2b})_n$ show the same increase discussed for $(\mathbf{1b})_n$ (Fig. S15, ESI†). The values predicted for $E_{\text{bind},n}$ ($-105.33 \text{ kJ mol}^{-1}$ for $n = \infty$) are smaller, in absolute value, than those obtained for $(\mathbf{1b})_n$ ($-129.87 \text{ kJ mol}^{-1}$ for $n = \infty$). This agrees with the experimental trends deduced from the thermodynamic data in Table 1, and suggests a lower degree of cooperativity in the supramolecular polymerization of tricarboxamides **2**. This idea is also supported by the values obtained for $DM_{\text{mon},n}$ which are significantly larger for $(\mathbf{1b})_n$ (12.94 D for $n = \infty$) than for $(\mathbf{2b})_n$ (11.04 D for $n = \infty$), indicating a higher polarization of the H-bonding network in the former.

In summary, we demonstrate herein the cooperative supramolecular polymerization of the *N*-centred trisamides **1** to form helical aggregates in which the inverted connectivity of the amide functional groups does not modify the helical sense of the aggregates in comparison to previously reported tricarboxamides **2**. The handedness of the helical structures formed by the self-assembly of **1** and **2** depends on the absolute configuration (*S* or *R*) of the stereogenic centres located at the peripheral side chains.

MM/MD simulations performed for infinite aggregates help to energetically discriminate between the *P* and *M* arrangements and support the preference of a determined helical handedness depending on the chirality of the stereogenic group. The synergy of π - π interactions, the threefold H-bonding between the amides and the weak dispersive forces between the peripheral alkyl chains exert a prominent role on the construction of the helical supramolecular structures. The cooperative character of the polymerization mechanism, higher for retroamides **1** in comparison to amides **2**, is furthermore supported by the dipole moment per monomeric unit that grows exponentially due to the enhancement of the polarization of the H-bonding network during the nucleation process. The results presented in this work exemplify the remarkable synergy between experimental and theoretical data to extract valuable information about the supramolecular polymerization process of self-assembling molecules.

Financial support by the MINECO of Spain (CTQ2014-53046-P, CTQ2015-71154-P, and Unidad de Excelencia María de Maeztu MDM-2015-0552), Generalitat Valenciana (PROMETEO/2012/053) and Comunidad de Madrid (NanoBIOSOMA, S2013/MIT-2807) is acknowledged. J. B. and J. C. thank the MECED for a doctoral FPI and FPU grants, respectively.

Notes and references

- C. Fouquey, J.-M. Lehn and A.-M. Levelut, *Adv. Mater.*, 1990, **2**, 254.
- (a) T. F. A. de Greef, M. M. J. Smulders, M. Wolfs, A. P. H. J. Schenning, R. P. Sijbesma and E. W. Meijer, *Chem. Rev.*, 2009, **109**, 5687; (b) T. Aida, E. W. Meijer and S. I. Stupp, *Science*, 2012, **335**, 813.
- A. R. A. Palmans and E. W. Meijer, *Angew. Chem., Int. Ed.*, 2007, **46**, 8948.
- (a) F. Aparicio, B. Nieto-Ortega, F. Nájera, F. J. Ramírez, J. T. López Navarrete, J. Casado and L. Sánchez, *Angew. Chem., Int. Ed.*, 2014, **53**, 1373; (b) J. Buendía, E. E. Greciano and L. Sánchez, *J. Org. Chem.*, 2015, **80**, 12444.
- P. Iavicoli, H. Xu, L. N. Feldborg, M. Linares, M. Paradinas, C. Stafström, C. Ocal, B. Nieto-Ortega, J. Casado, J. T. López Navarrete, R. Lazzaroni, S. De Feyter and D. B. Amabilino, *J. Am. Chem. Soc.*, 2010, **132**, 93502.
- (a) F. García, P. M. Viruela, E. Matesanz, E. Ortí and L. Sánchez, *Chem. - Eur. J.*, 2011, **17**, 7755; (b) F. García, P. Korevaar, A. Verlee, E. W. Meijer, A. R. A. Palmans and L. Sánchez, *Chem. Commun.*, 2013, **49**, 8674.
- P. J. M. Stals, J. C. Everts, R. de Bruijn, I. A. W. Filot, M. M. J. Smulders, R. Martín-Rapún, E. A. Pidko, T. F. A. de Greef, A. R. A. Palmans and E. W. Meijer, *Chem. - Eur. J.*, 2010, **16**, 810.
- F. Wang, M. A. J. Gillissen, P. J. M. Stals, A. R. A. Palmans and E. W. Meijer, *Chem. - Eur. J.*, 2012, **18**, 11761.
- H. M. M. ten Eikelder, A. J. Markvoort, T. F. A. de Greef and P. A. J. Hilbers, *J. Phys. Chem. B*, 2012, **116**, 5291.
- S. Cantekin, T. F. A. de Greef and A. R. A. Palmans, *Chem. Soc. Rev.*, 2012, **41**, 6125.
- B. Nieto-Ortega, F. García, G. Longhi, E. Castiglioni, J. Calbo, S. Abbate, J. T. López Navarrete, F. J. Ramírez, E. Ortí, L. Sánchez and J. Casado, *Chem. Commun.*, 2015, **51**, 9781.
- The $(\mathbf{1b})_n$ aggregates were recalculated using the more extended cc-pVTZ basis set (Table S1 and Fig. S14, ESI†) to reduce the effect of the basis set superposition error (BSSE). The energies computed for the decamer and for $n = \infty$ are -97.56 and $-104.35 \text{ kJ mol}^{-1}$, respectively, and are closer to the elongation enthalpy ($\Delta H_c = -94.4 \pm 0.8 \text{ kJ mol}^{-1}$).
- C. Kulkarni, S. Balasubramanian and S. J. George, *ChemPhysChem*, 2013, **14**, 661.



Cite this: *Chem. Commun.*, 2015, 51, 10142

Received 30th April 2015,
Accepted 12th May 2015

DOI: 10.1039/c5cc03616j

www.rsc.org/chemcomm

Blue-emitting pyrene-based aggregates†

Jorge S. Valera,^{‡a} Joaquín Calbo,^{‡b} Rafael Gómez,^a Enrique Ortí^{*b} and Luis Sánchez^{*a}

The supramolecular polymerization of pyrene imidazoles **1 and **2**, governed by H-bonding and C–H... π interactions, yields aggregates showing the characteristic bluish emission pattern of pyrene-based monomers.**

Since its discovery in 1837 by Laurent,¹ pyrene has become one of the most studied polycyclic aromatic hydrocarbons due to its attractive electronic and photophysical properties, and it has been widely tested as an active component in organic electronics.^{2,3} Pyrene is a blue-emitting material with a tendency to form excimers both in solution and in the solid state. The formation of excimers red-shifts the emission and reduces its intensity.^{2–4} To improve the emissive properties, great efforts have been devoted to the structural modification of pyrene to avoid aggregation and to suppress the quenching effect of the π - π interactions. Therefore, a challenging task in pyrene chemistry is the design of derivatives in which supramolecular order and appropriate blue-emitting features can coexist.

Herein, we describe the synthesis and the supramolecular polymerization of the pyrene imidazoles **1** and **2** endowed with peripheral achiral and chiral alkyl chains, respectively (Fig. 1).⁴ **1** and **2** have been designed with a variety of supramolecular interaction motifs that guide their self-assembly through H-bonding interactions between amide groups and imidazole moieties together with a number of C–H... π dispersion interactions. The organized supramolecular structures are able to immobilize apolar solvents like cyclohexane forming gels.⁵ Notably, the aggregates formed by **1** and **2** show the characteristic blue-emitting pattern of pyrene-based monomers.

The preparation of **1** and **2** was accomplished starting from pyrene, 4-carboxybenzaldehyde and the corresponding

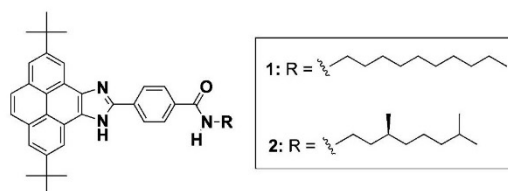


Fig. 1 Chemical structure of pyrene imidazoles **1** and **2**.

amine (Scheme S1, ESI†).⁶ Prior to the synthesis of the final derivatives, two *tert*-butyl groups were incorporated at positions 2 and 7 of the pyrene moiety to increase the solubility of the target compounds. The chemical structure of **1** and **2** was confirmed by NMR, FT-IR and HRMS analysis (see the ESI†).

To unravel the supramolecular polymerization mechanism of **1** and **2**, temperature-dependent UV-Vis spectroscopy measurements were performed in methylcyclohexane (MCH) as solvent (Fig. S1 and S2, ESI†). The bands observed at around 355 and 400 nm in the UV-Vis spectra of both **1** and **2** experience a slight bathochromic shift and a broadening upon decreasing the temperature, which is diagnostic of the aggregation process. Plotting the variation of the absorbance at 404 nm with the temperature results in cooling curves with an apparent sigmoidal shape, characteristic of an isodesmic supramolecular polymerization mechanism (Fig. S1b and S2b, ESI†).⁷

To obtain a complete set of thermodynamic parameters, the UV-Vis cooling curves derived for **1** and **2** were fitted to the model recently reported by ten Eikelder *et al.*⁸ The thermodynamic parameters obtained for **1** and **2** demonstrate that the branched nature of the peripheral alkyl chain in **2** plays a relevant role, showing significantly different values of the enthalpy of elongation (ΔH_e), the entropy of elongation (ΔS) and the nucleation penalty (ΔH_n) (Table 1). In contrast, the total free energy (ΔG) is very similar in both pyrene derivatives (~ 35 kJ mol⁻¹). Especially interesting is the calculated value of the degree of cooperativity σ . Despite the sigmoidal shape of the cooling curves, σ presents values

^a Departamento de Química Orgánica, Facultad de Ciencias Químicas, Universidad Complutense de Madrid, 28040 Madrid, Spain. E-mail: lusamar@quim.ucm.es

^b Instituto de Ciencia Molecular, Universidad de Valencia, 46980 Paterna, Spain. E-mail: enrique.orti@uv.es

† Electronic supplementary information (ESI) available: Fig. S1–S12, theoretical computational details and experimental section. See DOI: 10.1039/c5cc03616j

‡ These authors contributed equally.

Table 1 Thermodynamic parameters for **1** and **2** (MCH)

	1	2
ΔH_e [kJ mol ⁻¹]	-72 ± 1	-52 ± 1
ΔS [J Kmol ⁻¹]	-122 ± 3	-58 ± 2
ΔH_n [kJ mol ⁻¹] ^a	-7.1 ± 0.2	-11.5 ± 0.2
ΔG [kJ mol ⁻¹] ^a	-35.88	-34.73
σ [-] ^b	5.5 × 10 ⁻²	9.3 × 10 ⁻³
K_e [L mol ⁻¹] ^b	2.04 × 10 ⁶	1.5 × 10 ⁶
K_n [L mol ⁻¹] ^b	1.13 × 10 ⁵	1.21 × 10 ⁴

^a The nucleation penalty ΔH_n is negative, which implies that the enthalpy gain is smaller for nucleation compared to elongation. ^b The equilibrium constants for elongation (K_e) and dimerization (K_n), and the cooperativity factor ($\sigma = K_n/K_e$) are calculated at 298 K.

of 5.5 × 10⁻² and 9.3 × 10⁻³ for compounds **1** and **2**, respectively, which denote a certain degree of cooperativity in the supramolecular polymerization of these pyrene derivatives (Table 1). Interestingly, the self-assembling properties of compounds **1** and **2** are similar and both readily form gels in cyclohexane at a concentration of ca. 1 wt%. The organogels exhibit blue emission upon irradiation at 364 nm (Fig. 2).

The emission properties of **1** and **2** were investigated in CHCl₃ and MCH. The emission spectra in MCH at 1 × 10⁻⁵ M, conditions under which **1** and **2** are aggregated, show the typical pattern of monomeric pyrene with maxima at 400, 423 and 447 nm (Fig. 2 and Fig. S3, ESI[†]). In contrast, the emission spectra in CHCl₃, a good solvent that facilitates the solvation of isolated molecules, at 1 × 10⁻⁵ M feature broad and structureless bands centred at 448 nm, evidencing the formation of pyrene excimers (Fig. 2 and Fig. S3, ESI[†]).^{9,10} Compounds **1** and **2** show a remarkable fluorescence quantum yield (ϕ_f) in the aggregated state (MCH, 1 × 10⁻⁵ M) of 0.43. A lower ϕ_f value is measured for the excimer formed in CHCl₃ (0.38 and 0.22 for **1** and **2**, respectively). To the best of our knowledge, this unusual emissive behaviour has only been described for a pyrene derivative endowed with a chiral oligo(glutamic acid) side chain,¹¹ and it was ascribed to a helical supramolecular organization.

The presence of the stereogenic center on **2** was utilized to put in evidence the possible helical organization of the aggregates

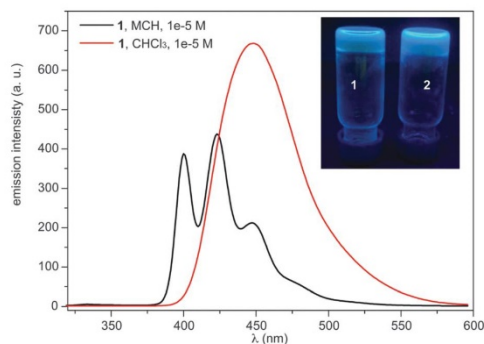


Fig. 2 Emission spectra of **1** in MCH and CHCl₃ (298 K, 1 × 10⁻⁵ M, λ_{exc} = 334 nm). The inset shows a picture of the cyclohexane gels obtained from compounds **1** and **2** with illumination at 364 nm.

formed by **1** and **2** in an attempt to justify the observed emission properties. Compound **2** shows a weak dichroic response with a poorly defined bisignated Cotton effect centered at around 250 nm (Fig. S5a, ESI[†]). In addition, sergeants-and-soldiers (SaS) experiments were performed by mixing achiral **1** and chiral **2** to investigate the amplification of chirality.¹² The SaS experiment shows a linear increase of the dichroic response upon increasing the amount of chiral sergeant **2** (Fig. S5b, ESI[†]). The dichroic data reveal that compounds **1** and **2** do not self-assemble forming helical structures and, therefore, this supramolecular organization cannot be invoked to justify the observed emission features.

The experimental data arise two questions: (1) which are the non-covalent forces participating in the self-assembly of **1** and **2**? and (2) what kind of supramolecular aggregate is formed upon their self-assembly capable of exhibiting the above-mentioned emissive features? To give an appropriate answer to these questions, experimental and theoretical studies were performed. In the FTIR spectra of **1** and **2**, the amide I and amide II bands at around 1635 and 1560 cm⁻¹, diagnostic of the formation of H-bonds between the amides, are visible (Fig. S6, ESI[†]).¹³ In the concentration-dependent ¹H NMR experiments, the triplet at $\delta \sim 6.3$, corresponding to the amide groups, and the resonance corresponding to the imidazole N-H group ($\delta \sim 13$) show a downfield shift with increasing concentrations that is indicative of the formation of an array of H-bonds (Fig. S7, ESI[†]). On the other hand, the aromatic resonances, used to envisage the intermolecular interactions between the aromatic fragments, show an opposite shifting of the δ values upon increasing the concentration. Thus, whilst the resonance of pyrene at $\delta \sim 9$ experiences a shielding effect, one of the anisochronous protons at the *para* position of the benzamide moiety ($\delta \sim 8.2$) shifts to lower δ values. A rotating-frame Overhauser effect spectroscopy (ROESY) NMR experiment in a concentrated solution of **1** (45 mM, CDCl₃, 298 K) was therefore conducted to extract more information about the supramolecular organization of this pyrene derivative.¹⁴

The ROESY experiment shows a number of intramolecular through-space coupling signals between the protons spatially close within the molecule (dotted blue circles in Fig. 3). In addition, ROESY signals corresponding to intermolecular contacts are also observed (dotted green lines in Fig. 3). Especially interesting are the contacts observed between the methylene units of the alkyl side chain and most of the aromatic protons of the pyrene unit. These contacts suggest an alternated distribution of the pyrene units in the aggregated state that could justify the observed monomeric emission properties.

Theoretical calculations were performed on compound **1** within the density functional theory (DFT) framework to shed light on the structural and energetic aspects of the pyrene imidazole system upon aggregation (see the ESI[†] for computational details). The isolated molecule shows a planar minimum-energy structure with an out-of-plane disposition of the amide group (Fig. S8, ESI[†]) that facilitates H-bonding interactions between neighbouring molecules. To unravel the possible contribution of the different parts of the molecule in the operation of non-covalent forces, the molecular electrostatic potential (MEP) calculated for **1** (Fig. S9, ESI[†]) was analysed. The MEP surface shows that the

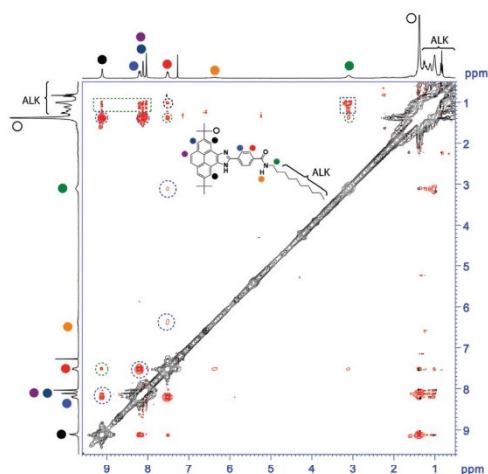


Fig. 3 ROESY NMR spectrum (CDCl_3 , 300 MHz, 45×10^{-3} M, 293 K) of **1**. The dotted blue, green and black lines highlight intra-, intermolecular or both through-space coupling signals, respectively. The inset shows the chemical structure of **1** depicting the anisochronous protons by coloured circles.

largest potential energy points are concentrated in the amide and the imidazole groups. Negative potential energies of -55.7 and -54.6 kcal mol $^{-1}$ are calculated in the oxygen and nitrogen vicinity, respectively, whereas positive potentials of $+101.2$ and $+121.0$ kcal mol $^{-1}$ are located in the N-H region of the amide and imidazole, respectively. Strong electrostatic interactions are then expected between monomers by means of H-bonding interactions involving the amide and imidazole units, as well as weak π - π and/or C-H \cdots π dispersion interactions between the aromatic units and the aliphatic chains.

A number of dimers, as minimal supramolecular units, can be modelled for **1** owing to the variety of supramolecular interaction motifs present in the monomer: (i) the aromatic structure, (ii) the polar amide and imidazole groups and (iii) the nonpolar long aliphatic chain. In a first approach, two monomers may accommodate either in a parallel or antiparallel disposition by the π -stacking of the pyrene imidazole cores with themselves or with the benzamide group, respectively (dimers A and B in Fig. 4). In dimer A, an amide-amide H bond is formed due to the rotation of $\sim 30^\circ$ of the upper monomer around the perpendicular axis. This structure would grow up in a helical column, but this possibility has been discarded by CD measurements. Similar to A, dimer C is arranged in a parallel mode but with the amide groups pointing in opposite directions and forming a non-linear H-bond (Fig. 4). A weak H-bonding N-H \cdots N interaction between the imidazole rings is also present in antiparallel dimer B.

Besides the π - π recognition motif that gives rise to structures A-C, the polar imidazole and amide groups constitute high potential energy regions for the supramolecular stabilization of the dimers. Thereby, dimers D-F, in which the formation of strong H-bonds is the recognition driving force, have been modelled (Fig. 4). Whereas dimers D and E are only stabilized

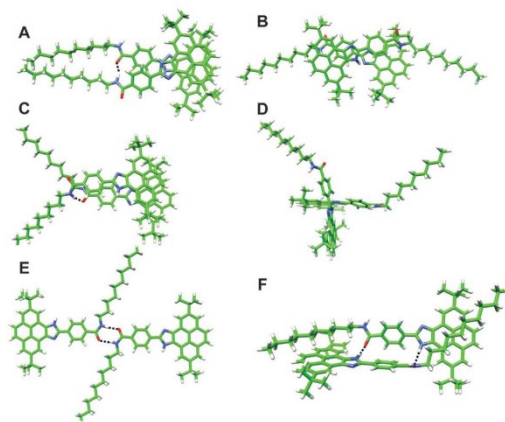


Fig. 4 Minimum-energy geometries calculated for the different dimers postulated for **1** at the B97D3/6-31G** level of theory.

Table 2 Interaction energy (E_{int}), number of H-bond contacts (n_{HB}), distance of the closest H-bond contact (d_{HB}) and dominant dispersion interactions (π - π , CH \cdots π and CH \cdots CH) that characterize dimers A-F

	E_{int} (kcal mol $^{-1}$)	n_{HB}	d_{HB} (Å)	π - π	CH \cdots π	CH \cdots CH
A	-54.6	1	1.918	✓	—	✓
B	-51.0	1	2.064	✓	—	—
C	-53.7	1	2.051	✓	—	—
D	-32.0	1	1.826	—	✓	—
E	-7.7	2	1.822	—	—	—
F	-61.7	2	1.839	—	✓	—

by the H-bond interaction between the imidazole and the amide groups, respectively, dimer F forms two H-bonds between the amide and the imidazole groups together with an extended CH \cdots π stabilization due to the interaction between the aliphatic chains and the pyrene imidazole cores.

Table 2 summarizes the interaction energy (E_{int}) and the main intermolecular forces governing the self-assembly of dimers A-F calculated at the B97D3/6-31G** level. A topological analysis of the electron density was also carried out by means of the NCIPLOT software to obtain the non-covalent interaction (NCI) surfaces, which provide additional information on the origin of the supramolecular aggregation (Fig. S10 and S11, ESI †).

Dimers A, B and C are computed very close in energy owing to the similar number and nature of the interactions stabilizing the aggregate. Dimers B and C display the typical green surface indicative of dispersion interactions along the π - π skeleton between monomers (Fig. S10, ESI †). Stabilizing CH \cdots CH interactions between the aliphatic chains are additionally found for A, which is calculated to be slightly more stable than B and C. In these three dimers, weak H-bonds are formed as indicated by the closest NH \cdots N/O contacts in the range of 1.92–2.06 Å (Table 2).

The situation is different for dimers D, E and F. Dimer E is stabilized by two H-bonding interactions between the two amides in a *cis* disposition. The occurrence of dimer E is however very unlikely because of: (i) the high barrier (15 kcal mol $^{-1}$) that

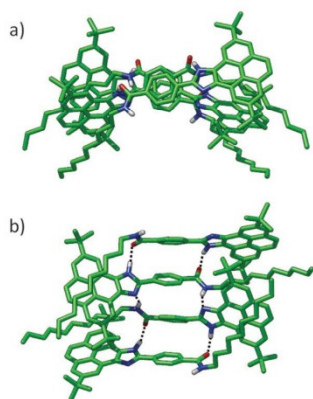


Fig. 5 Top (a) and side (b) views of the B97D3/6-31G**-optimized geometry calculated for the tetramer of **1**. Dotted lines emphasise the H-bonding array established between the imidazole and amide units. Only hydrogen atoms involved in H-bonding interactions are shown.

has to be overcome to convert a *trans* amide into a *cis* amide (Fig. S12, ESI†) and (ii) the small interaction energy (-7.7 kcal mol $^{-1}$) resulting from the lower stability of the *cis* conformation. The cross shape of dimer D enables a strong H-bond interaction between the imidazole groups (N \cdots H-N distance of 1.83 Å) and incorporates C-H \cdots π interactions between the *tert*-butyl groups of one monomer and the aromatic pyrene core of the other (Fig. S10, ESI†). Nonetheless, the E_{int} computed for this dimer (-32.0 kcal mol $^{-1}$) cannot compete with the stabilization obtained for the π - π patterned dimers A-C. Finally, dimer F combines H-bonding interactions between the imidazole and amide groups and C-H \cdots π stabilizing interactions between the alkyl chains and the pyrene cores (Fig. 4 and Fig. S10, ESI†). The additive effect of these interactions leads to the highest stability ($E_{\text{int}} = -61.7$ kcal mol $^{-1}$) among all the computed dimers. The structure of dimer F allows us to identify all the ROESY signals observed experimentally and, in particular, the short contacts between the alkyl chains and the pyrene cores (Fig. S13, ESI†). In addition, the absence of π - π interactions between the pyrene cores in dimer F explains the emission properties similar to the monomer. Dimer F is therefore proposed as the most plausible associate for compounds **1** and **2**.

To rationalize how dimer F can grow up from such non-planar, distorted disposition of the monomers, the tetramer shown in Fig. 5 was built up through an imidazole-amide-imidazole H-bond sequence. The minimum-energy geometry computed for the tetramer reveals that the H-bonding motifs are preserved along the monomeric pairs. The average NH(amide)-N(imidazole) contact is computed to be 2.18 Å, whereas the CO(amide)-HN(imidazole) interaction is calculated to be 1.82 Å. The total interaction energy in the tetramer reaches -182.1 kcal mol $^{-1}$,

which corresponds with an $E_{\text{int}} = -60.7$ kcal mol $^{-1}$ per monomer pair. This value is very close to the E_{int} computed for dimer F (-61.7 kcal mol $^{-1}$), suggesting that: (i) the oligomer can easily grow keeping the strong H-bond pattern and the stabilizing C-H \cdots π forces and (ii) the degree of cooperativity in the supramolecular polymerization should be very small.

In summary, we have synthesised pyrene imidazoles **1** and **2** that prevent the formation of excimers upon aggregation. The number and type of non-covalent interactions operating in the aggregation of these pyrene derivatives result in an amazing scenario of possibilities for **1** and **2** to self-assemble. Both experimental and theoretical studies demonstrate that the formation of the aggregates is mainly governed by the H-bonding interaction between the amide functionality and the imidazole moiety, together with a number of C-H \cdots π interactions. The absence of π - π interactions between the pyrene cores determines that the aggregate preserves the blue-emitting properties of the monomer. The results presented herein demonstrate the complex pathway followed by **1** and **2** to finally yield blue-emitting supramolecular aggregates.

Financial support from the MINECO of Spain (CTQ2011-22581 and CTQ2012-31914), European Feder funds (CTQ2012-31914), UCM (UCM-SCH-PR34/07-15826), Generalitat Valenciana (PRO-METEO/2012/053) and Comunidad de Madrid (NanoBIOSOMA, S2013/MIT-2807) is acknowledged. JC thanks the MECED for a doctoral FPU grant.

Notes and references

- 1 A. Laurent, *Ann. Chim. Phys.*, 1837, **66**, 136.
- 2 C. Wang, H. Dong, W. Hu, Y. Liu and D. Zhu, *Chem. Rev.*, 2012, **112**, 2208.
- 3 T. M. Figueira-Duarte and K. Müllen, *Chem. Rev.*, 2011, **111**, 7260.
- 4 (a) N. Tchebotareva, X. M. Yin, M. D. Watson, P. Samori, J. P. Rabe and K. Müllen, *J. Am. Chem. Soc.*, 2003, **125**, 9734; (b) D. Venkataraman, S. Lee, J. S. Zhang and J. S. Moore, *Nature*, 1994, **371**, 591.
- 5 (a) A. Ajayaghosh, V. K. Praveen and C. Vijayakumar, *Chem. Soc. Rev.*, 2008, **37**, 109; (b) J. W. Steed, *Chem. Soc. Rev.*, 2010, **46**, 3686.
- 6 D. Kumar, K. R. J. Thomas, C.-C. Lin and J.-H. Jou, *Chem. - Asian J.*, 2013, **8**, 2111.
- 7 T. F. A. De Greef, M. M. J. Smulders, M. Wolfs, A. P. H. J. Schenning, R. P. Sijbesma and E. W. Meijer, *Chem. Rev.*, 2009, **109**, 5687.
- 8 H. M. M. ten Eikelder, A. J. Markvoort, T. F. A. de Greef and P. A. J. Hilbers, *J. Phys. Chem. B*, 2012, **116**, 5291.
- 9 F. M. Winnik, *Chem. Rev.*, 1993, **93**, 587.
- 10 The emission corresponding to the pyrene monomer is only reached in CHCl₃ by using highly diluted (7×10^{-9} M), deoxygenated solutions (Fig. S4, ESI†).
- 11 Y. Kamikawa and T. Kato, *Langmuir*, 2007, **23**, 274.
- 12 (a) M. M. J. Smulders, A. P. H. J. Schenning and E. W. Meijer, *J. Am. Chem. Soc.*, 2008, **130**, 606; (b) F. Garcia, P. A. Korevaar, A. Verlee, E. W. Meijer, A. R. A. Palmans and L. Sánchez, *Chem. Commun.*, 2013, **49**, 8674.
- 13 (a) Y. Matsunaga, N. Miyajima, Y. Nakayasu, S. Sakai and M. Yonemura, *Bull. Chem. Soc. Jpn.*, 1988, **61**, 207; (b) F. Garcia, P. M. Viruela, E. Matesanz, E. Ortí and L. Sánchez, *Chem. - Eur. J.*, 2011, **17**, 7755.
- 14 Prior to this ROESY experiment, the aggregation of **1** was assessed by diffusion-ordered spectroscopy (DOSY) NMR, which reveals a larger value of the diffusion coefficient when compared to a more diluted solution (Fig. S6b, ESI†). A. Wong, R. Ida, L. Spindler and G. Wu, *J. Am. Chem. Soc.*, 2005, **127**, 6990.

*“ To succeed, jump as quickly at opportunities
as you do at conclusions.”*

Benjamin Franklin

Chapter 7. Conclusions

In the present Thesis, a thorough theoretical study has been performed on a wide variety of electroactive molecular systems with appealing optical, electronic and self-assembling properties to be exploited in organic electronics and materials science. The following conclusions are summarised according to the three Chapters in which the results of the Thesis have been divided:

Covalent donor-acceptor architectures

The electronic and optical properties of donor-acceptor chromophores absorbing in the whole visible spectrum have been theoretically characterised. In particular, DFT calculations provide information on the most interesting regioisomers of exTTF-DCF to be synthesized for maximum benefit in dye-sensitized solar cells (DSCs). The three possible regioisomers show equivalent absorption features in comparison with the parent exTTF-TCF, with intense low-lying charge-transfer bands calculated in the visible range. However, the exTTF-DCF-A derivative is found as the most promising dye owing to its more stable anchorage and perpendicular disposition upon linkage to the semiconductor.

Di-branched chromophores based on an analogous donor hemiexTTF moiety have also been investigated, showing low-lying charge-transfer bands and a red-shift of the absorption upon inclusion of the EDOT π -conjugated bridge between donor and acceptor units. First-principles calculations demonstrate that the most plausible adsorption mode of the carboxylic-substituted di-branched dyes onto titania is a monodentate

coordination of the cyanoacrylic acid group in both anchoring branches. This coordination displays the most stable anchorage of the target dye to the semiconductor surface, as well as two broad and intense LUMO bands that would enhance the electron injection into the semiconductor.

Supramolecular donor–acceptor complexes

Supramolecular donor–acceptor complexes have been studied under the DFT framework including dispersion corrections to help rationalize the origin of the forces guiding the self-assembly of carbon-based nanoforms by electroactive hosts. Theoretical calculations show that the convex–planar mismatch between porphyrin hosts and a C₆₀ fullerene derivative is overcome by strong noncovalent interactions, which show predominant electrostatic nature upon metal substitution in the porphyrin. Quantum chemistry calculations on ditopic porphyrin receptors of C₆₀ fullerene confirm a reduction of the electron density of the host upon inclusion of the first fullerene guest, in good accord with the negative cooperativity found experimentally for these systems. Interestingly, the ditopic porphyrin tape may accommodate the second C₆₀ ball in a *syn* or an *anti* disposition. First-principles calculations demonstrate that the *syn* arrangement is ~ 5 kcal mol⁻¹ more stable, a fact that arises from a stabilizing π – π interaction between the two fullerene balls and partially compensates the negative cooperativity.

On the other hand, unexpected concave–concave supramolecular assemblies are calculated as the most stable arrangements in donor–acceptor truxTTF•buckybowl complexes. In these conformations, not only π – π but especially CH \cdots π interactions are prominent. Free-energy estimations for the donor–acceptor association indicate that only the staggered (concave–concave) assemblies are formed in solution, in nice

agreement with the relevant NMR information. Theoretical calculations confirm the existence of low-lying weak charge-transfer bands described by the one-electron promotion from the electron-donor truxTTF to the bucky bowl, which acts as an acceptor. The existence of the corresponding charge-separated species upon photoexcitation is confirmed by spectroscopic techniques in a fruitful collaboration with experimentalist research groups.

Supramolecular polymers

Discotic-like electroactive building blocks have been used to theoretically analyse the self-assembling properties of supramolecular polymers governed by noncovalent interactions. In particular, N-centred trisamides are calculated to aggregate in supramolecular helices guided by π - π interactions between the aromatic cores and, especially, by a triple array of H-bonds between amides. This H-bond pattern is calculated as the responsible of the cooperativity of the polymerization process, which leads to an increasing binding energy and dipole moment per monomeric unit upon growth. The multi-level theoretical approach employed unambiguously allows identification of the helical sense as a function of the stereogenic aliphatic chain, and indicates a negligible role of the connectivity of the amide groups in the resulting helical orientation.

On the other hand, pyreneimidazole derivatives are shown to promote the self-assembly of organogels with an unexpected blue-emission. Theoretical calculations demonstrate, in synergy with the experimental evidences, that the self-assembly process is governed by the H-bond interactions between imidazole and amide groups together with a large number of $\text{CH}\cdots\pi$ interactions between the aliphatic chain and the pyrene

aromatic core. The absence of π - π interactions between the pyreneimidazole cores allows explaining the preservation of the blue-emitting features exhibited by our derivatives upon polymerization.

Capítulo 8. Resumen

8.1. Introducción

En los últimos años, la ciencia asociada a los nuevos materiales moleculares ha avanzado extraordinariamente, surgiendo un área interdisciplinar que requiere principalmente de la química para el diseño y caracterización, de la física para el estudio de las propiedades, y de la ingeniería para sus aplicaciones industriales. Una gran mayoría de los compuestos químicos con propiedades ópticas y electrónicas útiles para su implementación en dispositivos optoelectrónicos pertenecen a arquitecturas electroactivas basadas en la unión de una entidad rica en densidad electrónica (dador o D) y otra con deficiencia electrónica (aceptor o A). Dicha unión puede construirse tanto a través de la química covalente, por ejemplo mediante espaciadores π -conjugados, como haciendo uso de la química supramolecular, en la que participan interacciones no-covalentes como los enlaces de hidrógeno o las fuerzas de dispersión.

Las arquitecturas covalentes dador-aceptor (o *push-pull*) han sido utilizadas como cromóforos en muy distintas aplicaciones, tales como óptica no-lineal, materiales piezoeléctricos y electro-ópticos, sondas fotocromáticas y solvocrómicas, etc., entre las que destaca su utilización en celdas fotovoltaicas. Los colorantes *push-pull* son empleados en las denominadas celdas solares de tipo Grätzel, o celdas solares sensibilizadas por colorante (DSCs), para transferir la energía que absorben de la luz solar a un semiconductor mediante la transferencia de los electrones fotoexcitados. El bajo coste, la versatilidad química y el bajo

impacto medioambiental constituyen las mayores ventajas de los colorantes puramente orgánicos frente a los análogos metálicos. Sin embargo, sólo unos pocos de estos cromóforos orgánicos son capaces de competir con las elevadas eficiencias obtenidas con los complejos de rutenio(II).

La clave para conseguir DSCs con eficiencias crecientes no sólo depende de la naturaleza del cromóforo, sino también de las características del par electrolítico, así como del disolvente y de la topología del semiconductor. Recientes estudios han demostrado que la alta eficiencia obtenida con los colorantes de rutenio tiene en parte su origen en el número de grupos carboxílicos que pueden anclarse al semiconductor. Una mejor comprensión del efecto multi-anclaje es, por tanto, de gran interés para el diseño de nuevos cromóforos puramente orgánicos que mejoren las eficiencias obtenidas en DSCs.

Mientras el proceso de transferencia de carga en un sistema covalente dador-aceptor tiene lugar intramolecularmente, el proceso análogo ocurre de forma intermolecular en los sistemas conocidos como complejos supramoleculares dador-aceptor. La combinación de la versatilidad química para sintetizar sistemas dadores y aceptores con la infinidad de posibilidades que brinda la química supramolecular, ha permitido la construcción de complejos dador-aceptor "*host-guest*" utilizados en el reconocimiento de nanoformas de carbono (fullerenos, nanotubos o fragmentos de fullereno) y otras entidades químicas de interés. El diseño de complejos supramoleculares ayuda en última instancia a entender el origen físico de las fuerzas que participan en el proceso de autoensamblaje, así como los mecanismos por los que transcurren los fenómenos de transferencia de carga.

El ensamblaje de sistemas químicos electroactivos mediante química supramolecular para la generación de agregados poliméricos sienta las bases de la química de polimerización supramolecular. Al contrario que la polimerización covalente, en la cual las unidades químicas se unen mediante enlaces covalentes, la polimerización supramolecular se basa en el crecimiento direccional de entidades moleculares discretas unidas a través de interacciones no-covalentes. Debido a sus propiedades de emisión de luz, transferencia de energía y carga, y conductividad eléctrica, el uso de los polímeros supramoleculares como materiales reciclables, degradables, sensibles a estímulos externos y autorreparables está cada vez más extendido.

La química supramolecular de materiales poliméricos, a su vez, abre las puertas al estudio de una característica fundamental de la materia viva y la naturaleza: la quiralidad. El fenómeno de la quiralidad es muy habitual, encontrándose en sistemas de dimensiones tan distintas como las moléculas, los virus, los caracoles, las enredaderas o incluso nuestra propia galaxia. Sin embargo, los fenómenos físicos que originan y promocionan una entidad quiral frente a su imagen especular siguen siendo un misterio. Dentro de la química supramolecular, el autoensamblaje tiene lugar a través de la organización autónoma de los componentes moleculares. A pesar de que la quiralidad supramolecular está fuertemente relacionada con la presencia de componentes quirales en las moléculas, entidades aquirales también pueden producir superestructuras quirales a través del autoensamblaje. El diseño y estudio de nuevos polímeros supramoleculares es, por tanto, esencial para comprender y profundizar en el fenómeno de la autoagregación y el origen de la quiralidad.

8.2. Objetivos

La presente Tesis se ha dividido en tres partes de acuerdo con los Capítulos en los que se ha desarrollado la exposición de los resultados. Los objetivos dentro de cada Capítulo se resumen de la forma que sigue (las estructuras de los distintos compuestos se muestran en las figuras correspondientes en cada sección).

Arquitecturas dador-aceptor covalentes:

- Caracterización de las propiedades ópticas, electrónicas y de anclaje al semiconductor del regioisómero de exTTF-DCF que permita una mayor eficiencia en celdas solares de tipo Grätzel.
- Determinación de las características de absorción en derivados dador-aceptor di-ramificados de hemioxTTF. Cálculo del efecto de la naturaleza del espaciador- π (benceno o EDOT) en las propiedades ópticas del cromóforo.
- Inspección teórica de los aspectos energéticos y geométricos de los distintos tipos de anclaje de un colorante di-ramificado de hemioxTTF en una superficie de TiO_2 . Determinación del modo preferencial de anclaje (simple vs. doble, monodentado vs. bidentado) y los efectos de dicho modo en la eficiencia final del dispositivo fotovoltaico.

Complejos dador-aceptor supramoleculares:

- Descripción químico-cuántica de las fuerzas no-covalentes que gobiernan el reconocimiento supramolecular de un huésped de fullereno por anfitriones de metaloporfirina: efecto del metal.
- Cuantificación de las fuerzas no-covalentes y del efecto de cooperatividad que dan lugar al reconocimiento supramolecular

entre anfitriones de porfirina ditópicos y un derivado de fullereno en complejos de estequiometría 1:2.

- Caracterización teórica de las distintas estructuras posibles para agregados dador–aceptor de truxTTF con una serie de fragmentos de fullereno de distinto tamaño.
- Determinación de las propiedades ópticas y electrónicas de los complejos de truxTTF•buckybowl que permitan explicar el proceso de transferencia electrónica supramolecular tras la fotoexcitación.

Polímeros supramoleculares:

- Caracterización teórica de las fuerzas que originan el autoensamblaje cooperativo en derivados trisamida discóticos.
- Asignación de la orientación helicoidal del polímero supramolecular en función de la cadena alifática quiral y la conectividad de los grupos amida al esqueleto bencénico.
- Determinación de la naturaleza de las interacciones no-covalentes que gobiernan el autoensamblaje en derivados de pirenoimidazol: predicción de la estructura de los agregados y justificación de las propiedades ópticas.

8.3. Metodología

Para lograr los objetivos de la presente Tesis, se ha hecho uso extensivo de cálculos químico–cuánticos y de mecánica molecular, además de la serie de técnicas computacionales y herramientas de modelización que se resumen a continuación.

La teoría del funcional de la densidad (DFT) ha sido el marco general en el que se ha desarrollado la investigación teórica expuesta en la presente Tesis. Tanto las optimizaciones de geometría como los cálculos puntuales de energía se han realizado utilizando los funcionales de la densidad detallados en cada caso. En función del tamaño del sistema a tratar, así como de la exactitud en (y la complejidad de) la propiedad a calcular, se ha hecho una elección razonada del funcional atendiendo a su rango de acuerdo con la famosa escala de Jacob propuesta por Perdew en el 2000. Asimismo, los cálculos de propiedades ópticas se han llevado a cabo mediante la teoría DFT dependiente del tiempo (TDDFT).

En particular, el funcional híbrido B3LYP se ha utilizado para la optimización de sistemas covalentemente unidos, como los descritos en el Capítulo 4. El funcional B3LYP también se ha usado para realizar los cálculos de frecuencias y la predicción de las propiedades ópticas, tanto en los compuestos dador-aceptor covalentes (Capítulo 4) como en los complejos supramoleculares (Capítulo 5 y 6). Para la optimización de los sistemas supramoleculares descritos mediante interacciones no-covalentes, se ha usado la aproximación de Grimme (-D, o su última versión -D3) acoplada a funcionales puros GGA como el B97 o híbridos como el revPBE0. Finalmente, el funcional híbrido meta-GGA MPWB1K se ha empleado en la determinación cuantitativa de la energía de asociación y momento dipolar en los agregados helicoidales de trisamida (Sección 6.2.1).

El conjunto de funciones de base necesario en cualquier cálculo DFT ha sido elegido para conseguir una relación precisión-coste computacional lo más alta posible. En líneas generales, se han utilizado conjuntos de funciones de base doble o triple- ζ de valencia para optimizaciones de

geometría y cálculos puntuales de energía. Además, se han utilizado pseudopotenciales para la descripción de la parte electrónica interna en elementos con un elevado número atómico, como son los metales de transición en el modelizado del semiconductor de TiO₂ (Capítulo 4) y de metaloporfirinas (Capítulo 5).

En los casos donde el tamaño del sistema ha hecho inaccesible el uso de la metodología DFT para la exploración inicial de las estructuras geométricas, por ejemplo en los agregados supramoleculares basados en porfirina con fullereno (Capítulo 5), el uso de métodos semiempíricos (PM7) ha permitido el cálculo computacional a un coste asumible. En el Capítulo 6, se ha utilizado la mecánica molecular y el campo de fuerzas general MM3 para el cálculo de los polímeros supramoleculares (más de 1000 átomos). Este campo de fuerzas también se ha usado para entender la evolución de los polímeros supramoleculares helicoidales en función del tiempo (Capítulo 6) mediante cálculos de dinámica molecular. En una simulación de dinámica molecular, la resolución numérica de las ecuaciones de movimiento de Newton permite determinar las trayectorias de los átomos y moléculas en función del tiempo. Para el cálculo de las dinámicas moleculares se ha empleado el algoritmo de Verlet.

Por otro lado, la dinámica molecular clásica no permite dar una solución para la modelización de sistemas que implican la ruptura y formación de enlaces químicos (Capítulo 4). Para ello, se ha empleado una dinámica molecular *ab initio* con el algoritmo de Car-Parrinello, el cual considera el comportamiento electrónico a través de la simulación mediante métodos químico-cuánticos. En concreto, el método Car-Parrinello introduce explícitamente los grados de libertad electrónicos como

variables dinámicas (ficticias), donde los grados de libertad nucleares se propagan mediante fuerzas iónicas tras la resolución del problema electrónico en cada iteración.

Las condiciones de entorno de disolvente en los cálculos químico-cuántico se han introducido utilizando modelos de continuo. Un modelo de disolvente continuo consiste en la descripción del disolvente como un dieléctrico homogéneo alrededor del soluto. En estos modelos, la interacción soluto-disolvente se calcula a través del denominado campo de reacción, el cual se introduce como un potencial de reacción a modo de perturbación dentro del Hamiltoniano. De entre los métodos de campo de reacción más utilizados, se ha hecho uso del modelo continuo polarizable (PCM) y del modelo basado en la densidad electrónica del soluto (SMD).

Con el fin de simular las condiciones periódicas necesarias para un semiconductor sólido (Capítulo 4) o un polímero supramolecular unidimensional (Capítulo 6), se han utilizado condiciones de contorno periódicas (PBC). Esta herramienta computacional permite modelizar un sistema continuo mediante la replicación de una pequeña parte llamada celda unidad. Las condiciones de contorno periódicas se usan ampliamente en dinámica molecular para evitar problemas de efectos de frontera provocados por la naturaleza finita del sistema modelizado mediante la creación de una representación similar al infinito.

Por último, se han utilizado herramientas computacionales específicas para una mejor comprensión de las interacciones no-covalentes que rigen el autoensamblaje supramolecular. Por ejemplo, la teoría de perturbaciones de simetría adaptada (SAPT) ha permitido la partición de la energía intermolecular entre dos entidades moleculares en un

agregado supramolecular (Capítulo 5). Asimismo, el índice no-covalente (NCI) desarrollado por Contreras y colaboradores se ha empleado en la descripción y racionalización de las interacciones involucradas en la polimerización supramolecular de derivados de pirenoimidazol (Capítulo 6).

8.4. Arquitecturas dador–aceptor covalentes

En este Capítulo, se ha llevado a cabo la caracterización teórica de sistemas dador–aceptor basados en las unidades dadoras de exTTF y hemiexTTF para su uso como colorantes en celdas solares tipo DSC. En concreto, se han analizado las propiedades ópticas y electrónicas de derivados de exTTF-TCF en los que se sustituye un grupo ciano por un grupo de anclaje eficiente carboxílico. Asimismo, se han estudiado análogos di-ramificados derivados del hemiexTTF donde se ha analizado la naturaleza del espaciador π (benceno o EDOT) y su efecto en las propiedades ópticas del cromóforo. Por último, se han determinado las implicaciones de los posibles modos de anclaje (mono vs. di-dentado; simple vs. doble) en colorantes di-ramificados, y sus consecuencias en la eficiencia final del dispositivo fotovoltaico.

8.4.1. Cromóforos de exTTF mono-ramificados

En esta Sección, se ha realizado el estudio teórico sobre cromóforos dador- π -aceptor basados en la unidad dadora de electrones de exTTF y la unidad aceptora de tricianofurano (TCF) sustituida con un grupo cianoacrílico (derivados exTTF-DCF) para investigar su potencial como colorantes en DSCs (Figura 1). Los resultados teóricos indican que el grupo carboxílico no sólo es más apropiado para el anclaje del colorante

al semiconductor, sino que también favorece la inyección de carga hacia el dispositivo dada su mayor capacidad para acumular densidad electrónica. Los tres posibles regioisómeros del exTTF-DCF absorben intensamente la radiación en todo el espectro visible, independientemente de la posición en la que se introduzca el grupo de anclaje carboxílico. La absorción en todo el visible es debida a las transiciones de transferencia de carga de baja energía que tienen lugar entre la unidad dadora de exTTF y la unidad aceptora π -conjugada, a semejanza de su análogo de exTTF-TCF.

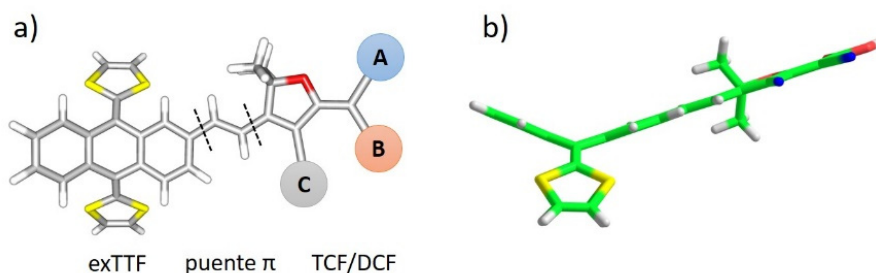


Figura 1. a) Representación esquemática de los tres regioisómeros posibles estudiados por sustitución de un grupo ciano en la unidad de TCF del exTTF-TCF por un ácido carboxílico (A, B o C). b) Vista lateral de la estructura de mínima energía para el regioisómero exTTF-DCF-A.

El proceso de adsorción del exTTF-DCF sobre la superficie del semiconductor se ha estudiado mediante cálculos de estado sólido periódicos utilizando el algoritmo de Car-Parrinello. Los cálculos teóricos demuestran que hay diferencias importantes en la distancia que separa la unidad dadora de exTTF y la superficie de TiO_2 en función de la posición en que se introduzca el grupo carboxílico, sugiriendo uno sólo de los derivados de exTTF-DCF (el exTTF-DCF-A, Figura 1) como el óptimo para su uso como colorante en DSCs. Dicho derivado, debido a su

disposición cuasi-perpendicular con respecto a la superficie de TiO_2 , permitiría reducir los procesos de recombinación de carga y provocaría un aumento del voltaje de circuito abierto en el dispositivo. Asimismo, el fenómeno indeseado de la autoagregación quedaría prevenido por la particular forma de mariposa que posee la unidad dadora de exTTF. El exTTF-DCF-A muestra, por tanto, unas propiedades ópticas y de adsorción idóneas para su utilización como colorante en celdas solares tipo DSC.

8.4.2. Cromóforos de hemiexTTF di-ramificados

Inspirados por las recientes evidencias sobre la importancia del número de grupos de anclaje del colorante en el rendimiento de un dispositivo DSC, hemos diseñado, en colaboración con el grupo experimental del Prof. Nazario Martín, una serie de díadas dador-aceptor basadas en la molécula dadora de exTTF poseyendo dos ramas de anclaje electron-aceptoras. En primer lugar, exploramos las propiedades electrónicas y ópticas de cromóforos en los que el fragmento dador de 10-(1,3-ditioil-2-iliden)-antraceno (hemiexTTF) se ha combinado con unidades aceptoras de dicianovinileno (DCV) a través de puentes conjugados de benceno (Ph) o 3,4-etilendioxitiofeno (EDOT) —Figura 2—.

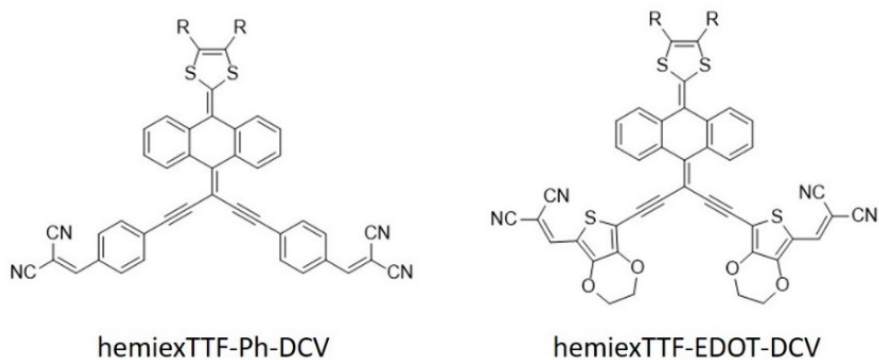


Figura 2. Estructura química de los cromóforos *push-pull* basados en la unidad de hemiexTTF incorporando dos tipos de espaciadores π : un fenilo (hemiexTTF-Ph-DCV, izquierda) y un grupo EDOT (hemiexTTF-EDOT-DCV, derecha).

Los cálculos teóricos predicen estructuras muy distorsionadas tipo silla de montar, en las cuales el antraceno central se dispone en una conformación de bote y las unidades laterales se pliegan en dirección contraria, de forma similar a las estructuras obtenidas para los derivados de exTTF. Los derivados de hemiexTTF-Ph-DCV y hemiexTTF-EDOT-DCV presentan una elevada absorción en todo el espectro visible debido a las transiciones electrónicas de transferencia de carga de baja energía que tienen lugar entre la unidad dadora y aceptora. Estas transiciones son muy intensas debido al solapamiento efectivo existente entre los niveles HOMO y HOMO-1, localizados en la unidad dadora de hemiexTTF, y los niveles LUMO y LUMO+1, localizados en las ramas aceptoras, implicados en dichas transiciones.

8.4.3. Modos de adsorción de anclaje simple vs. doble

Dadas las excelentes propiedades de absorción mostradas por los colorantes di-ramificados basados en el hemiexTTF, en una segunda etapa se sustituyeron las unidades aceptoras de dicianovinileno por

unidades aceptoras de anclaje cianoacrílicas. Los cálculos teóricos indican que estos sistemas poseen bandas de transferencia de carga intramolecular a bajas energías, que determinan una intensa y amplia absorción en todo el espectro visible, en analogía con los cromóforos de hemixTTF- π -DCV. Si bien los experimentos de infrarrojo indicaban que estos nuevos cromóforos se anclan a la superficie del semiconductor de TiO₂ mediante un modo de adsorción doble, el modo de coordinación de cada grupo carboxílico al semiconductor no se pudo elucidar de forma inequívoca. Con el fin de determinar dicho modo de coordinación y las implicaciones que el modo de adsorción di-anclaje tiene en el rendimiento de la DSC (Figura 3), se ha llevado a cabo una exhaustiva investigación teórica sobre cromóforos di-anclaje modelo combinando cálculos de primeros principios DFT y dinámica molecular *ab initio*.

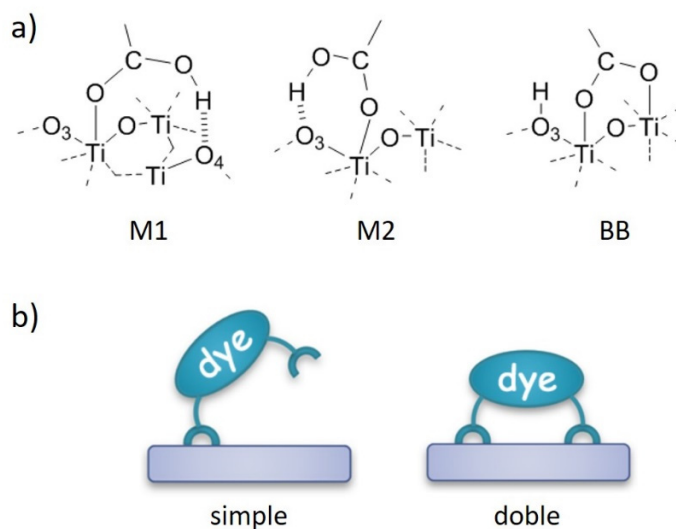


Figura 3. Representación gráfica de: a) los tres modos de coordinación principales del grupo carboxílico/carboxilato (monodentados M1 y M2, y bidentado BB), y b) los dos modos de adsorción posibles para un cromóforo di-ramificado en DSCs.

En primer lugar, el análisis de las frecuencias calculadas teóricamente ha permitido la asignación inequívoca de los modos característicos del grupo CO en los espectros experimentales publicados por Bouit y colaboradores. Así, los cálculos teóricos indican inequívocamente que los cromóforos de hemixTTF con grupos carboxílicos se anclan sobre el conductor mediante una unión monodentada.

Con el fin de esclarecer el orden energético de las diferentes estructuras posibles para el sistema colorante•TiO₂, se ha modelizado un sistema diramificado unido a una superficie de anatasa (101) usando condiciones de contorno periódicas. De entre todas las estructuras calculadas, la conformación monodentada de anclaje doble (M1-M1) es la más estable. Además, dinámicas moleculares Car-Parrinello indican que, a temperatura ambiente, los enlaces de hidrógeno entre el grupo carboxílico y el semiconductor se pueden romper y formar con facilidad. La consecución de la dinámica permitió confirmar que la conformación de di-anclaje monodentada M1-M1 es la más estable, y que supera en más de 13 kcal mol⁻¹ en estabilidad al resto de conformaciones posibles, en buen acuerdo con las evidencias experimentales.

Por último, el análisis de la densidad de estados proyectada nos permite concluir que los modos de adsorción de anclaje doble desplazan la banda de conducción del TiO₂ a energías ligeramente más altas que los modos de anclaje simple. Este desplazamiento provoca un incremento del voltaje de circuito abierto, dando lugar a mayores eficiencias de conversión en DSCs. Por otro lado, la existencia de dos bandas LUMO cuasi-degeneradas, correspondientes a las dos ramas de anclaje idénticas del colorante, da lugar a una mayor interacción con el semiconductor en el modo di-

anclaje, lo cual permitiría una inyección electrónica más eficiente y una mejora en el rendimiento del dispositivo.

8.5. Complejos dador–aceptor supramoleculares

En este Capítulo, se han investigado una serie de compuestos monotópicos y ditópicos de porfirina utilizados como receptores en el reconocimiento supramolecular de derivados del fullereno C_{60} . Asimismo, se ha estudiado la formación de agregados supramoleculares dador–aceptor entre el dador de electrones *truxTTF* y fragmentos de fullereno de distinto tamaño. Estos sistemas presentan propiedades interesantes de transferencia electrónica fotoinducida. Mediante cálculos de primeros principios, se ha caracterizado la naturaleza e intensidad de las fuerzas que gobiernan el proceso de asociación, y el origen de la transferencia de carga supramolecular que ocurre tras la fotoexcitación.

8.5.1. Efecto del átomo metálico: ensamblajes monotópicos de porfirina• C_{60}

Se ha llevado a cabo la investigación teórica de una serie de nuevos complejos *cup-and-ball* metaloporfirina•fullereno en colaboración con los grupos liderados por los Profs. Nazario Martín y Jean-François Nierengarten, con el fin de arrojar luz sobre la naturaleza y fuerza de las interacciones no-covalentes que gobiernan el autoensamblaje supramolecular de derivados de fullereno con porfirinas metalosustituidas. Los complejos estudiados se generan a partir de la unión supramolecular de un derivado del metano[60]fullereno con sistemas conjugados de porfirina–éter corona incorporando como átomos centrales 2H, Co, Ni, Cu y Zn (Figura 4).

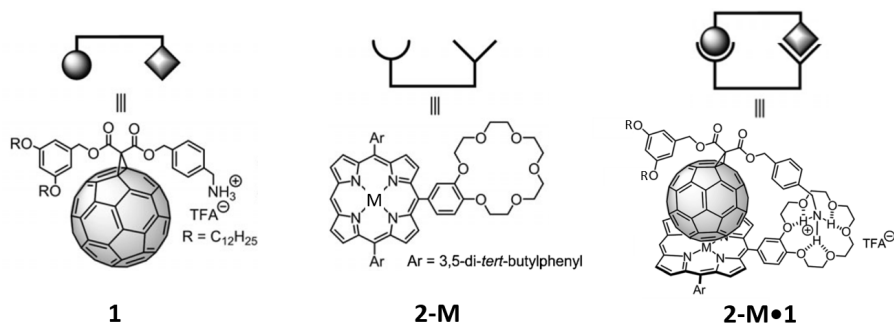


Figura 4. Estructura química del huésped de metano[60]fullereno **1** (izquierda), el receptor de metaloporfirina **2-M** (centro), y el complejo supramolecular *host-guest* **2-M•1** (derecha). **M** puede ser: 2H, Co, Ni, Cu, Zn.

Los cálculos teóricos en los complejos de porfirina•fullereno indican que la asociación supramolecular se origina por dos interacciones clave: la interacción metal- C_{60} y los enlaces $NH\cdots O$ entre el grupo amonio y el éter corona. Asimismo, los cálculos teóricos muestran que las interacciones de tipo dispersión $CH\cdots\pi$ entre los *tert*-butilos de los anillos bencénicos de la porfirina y la nube π del fullereno también contribuyen, aunque en menor medida, a la complejación supramolecular. La energía de asociación calculada para los distintos asociados indica que la complejación es más eficiente a medida que el metal posee mayor densidad electrónica, siendo sin embargo el complejo con Co el más estable.

Teniendo en cuenta que el C_{60} interactúa con la porfirina fundamentalmente a través de uno de los dobles enlaces [6,6] ricos en electrones, decidimos modelizar un sistema supramolecular simplificado de porfirina interactuando con una molécula de etileno. Los cálculos de alta precisión sobre este modelo han permitido establecer una relación inversa entre la distancia metal-etileno y la energía de asociación de

acuerdo con el siguiente orden (de mayor a menor distancia) para la sustitución metálica: $Ni > Cu > Zn > Co$.

Cálculos químico-cuánticos usando la teoría de perturbaciones de simetría adaptada (SAPT) muestran que el complejo con porfirina no-metalada se estabiliza en mayor medida gracias a fuerzas de dispersión. Para los complejos de porfirina con sustitución metálica, la contribución electrostática a la estabilización del complejo aumenta y se hace predominante, especialmente para el ensamblaje con porfirina de Zn.

8.5.2. Cooperatividad en complejos ditópicos de porfirina•C₆₀

Tomando como referencia el conocimiento adquirido en el estudio de los sistemas descritos sobre derivados monotópicos de metaloporfirina con fullereno, decimos llevar a cabo una investigación sobre dos nuevos análogos ditópicos de porfirina para su complejación con fullereno. Este trabajo se realizó en colaboración con los grupos experimentales dirigidos por los Profs. Nazario Martín y Jean-François Nierengarten.

En primer lugar, las estructuras de mínima energía indican que el ensamblaje supramolecular entre las entidades ditópicas de porfirina con el derivado de metano[60]fullereno se origina a través de interacciones metaloporfirina-C₆₀ y NH...O (Figura 5 y Figura 6), en analogía con los resultados obtenidos con los homólogos monotópicos descritos en el apartado anterior. Tras la incorporación del primer huésped de fullereno, la mitad porfirínica más alejada se acomoda espacialmente para intentar interactuar con el fullereno, bien mediante interacciones CH...π en el derivado *meso-meso* o a través de contactos π-π en el *tape*. La introducción del huésped de fullereno produce, a su vez, una disminución en la densidad electrónica de la porfirina no-interaccionante, permitiendo explicar la cooperatividad negativa obtenida

experimentalmente para estos complejos tras la inclusión de la segunda unidad fullerénica.

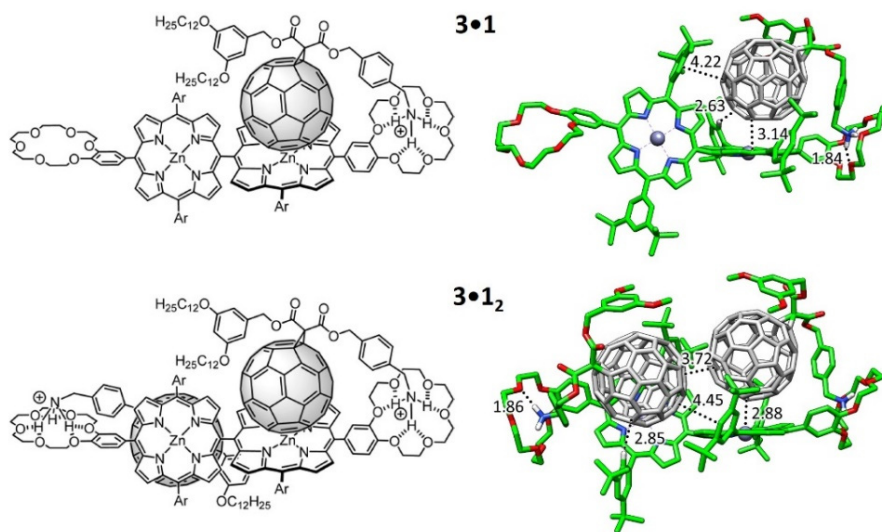


Figura 5. Estructura química (izquierda) y geometría de mínima energía calculada a nivel B97-D3/(6-31G**+LANL2DZ) (derecha) para el ensamblaje supramolecular del receptor ditópico de porfirina *meso-meso* **3** con una y dos moléculas de huésped de fullereno **1**.

Las estructuras de mínima energía calculadas para el agregado de estequiometría 1:2 muestran distancias entre los dos fullerenos de 3.7 Å en la porfirina *meso-meso*, a expensas de distorsiones entre las dos mitades porfirínicas fuera de la perpendicularidad (Figura 5). En el agregado de porfirina *tape*, la introducción del segundo huésped de fullereno puede dar lugar a: una conformación en la que las dos bolas de fullereno se sitúan en el mismo lado (disposición *syn*), u otra en la que las dos bolas se sitúan en lados opuestos del plano generado por la cinta porfirínica (disposición *anti*) —Figura 6—. El análisis teórico de ambas conformaciones indica que la presencia de una interacción π - π

estabilizante entre los dos fullerenos es la causa fundamental de la mayor estabilidad encontrada para el complejo *syn*. Dicha interacción reduciría la cooperatividad negativa en la introducción de la segunda unidad de fullereno en la porfirina *tape*, tal y como sugieren las evidencias experimentales.

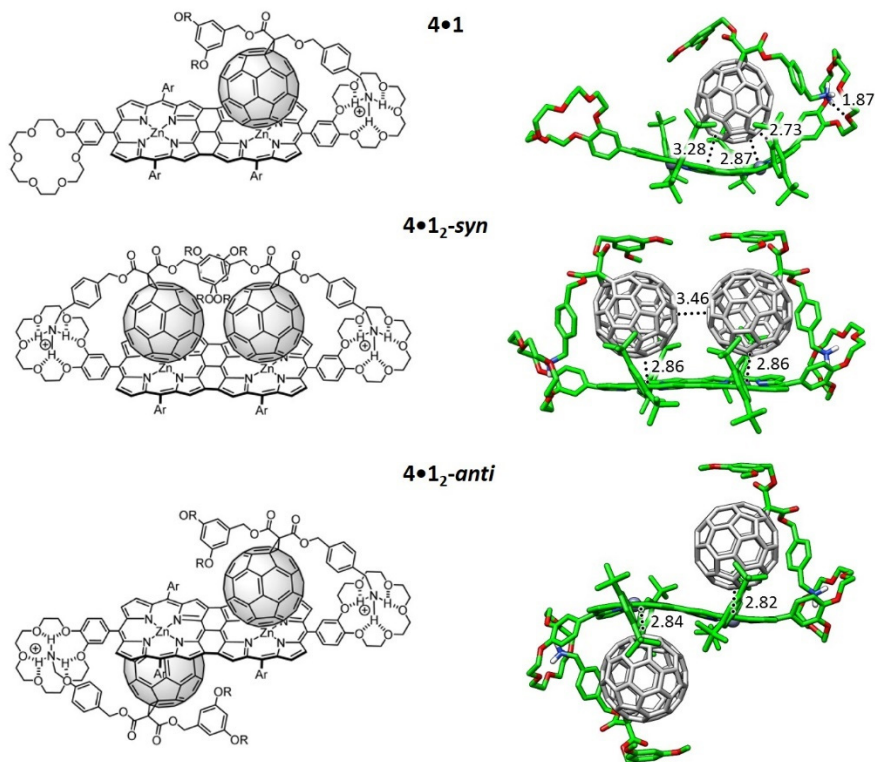


Figura 6. Estructura química (izquierda) y geometría de mínima energía calculada a nivel B97-D3/(6-31G**+LANL2DZ) (derecha) para el ensamblaje supramolecular del receptor ditópico de porfirina *tape* **4** con una y dos moléculas de huésped de fullereno **1**.

La energía de asociación (E_{bind}) calculada teóricamente para los agregados supramoleculares demuestra que la incorporación del primer huésped de fullereno en la porfirina *meso-meso* da lugar a una elevada

estabilización originada en gran medida por los contactos NH...O y la interacción porfirina–fullereno. Tras la inclusión de la segunda molécula huésped, la E_{bind} aproximadamente se duplica. El estudio teórico comparativo de las energías de asociación entre los complejos ditópicos de porfirina *meso-meso* y *tape* permiten concluir que la incorporación de la primera molécula de fullereno está más favorecida en la porfirina *meso-meso*, mientras que la inclusión del segundo huésped es más favorable en la porfirina *tape*. Dichos resultados están en perfecto acuerdo con las constantes de asociación medidas experimentalmente para los agregados supramoleculares descritos.

8.5.3. El complejo supramolecular truxTTF•hemifullereno

La molécula de truxTTF ha demostrado una especial habilidad para formar complejos supramoleculares dador–aceptor con el fullereno, la cual está favorecida por la complementariedad cóncavo–convexo de sus superficies moleculares. Teniendo en cuenta dicha habilidad, pensamos que el truxTTF también debería ser capaz de unirse a fragmentos de fullereno, como por ejemplo el hemifullereno o $C_{30}H_{12}$ (Figura 7a), formando complejos *bowl-to-bowl* dador–aceptor heteromoleculares. Con el fin de explorar esta posibilidad, se han llevado a cabo cálculos DFT para cuatro estructuras distintas del complejo de truxTTF• $C_{30}H_{12}$ (Figura 7b) en base a la información cristalográfica existente para ambos fragmentos. Las dos primeras estructuras corresponden a disposiciones *bowl-in-bowl* donde se maximizan las interacciones π – π , en las que la superficie convexa del $C_{30}H_{12}$ encaja perfectamente con una de las dos superficies cóncavas del truxTTF —bien con la superficie formada por el esqueleto carbonado o a través de la parte de los ditioles—. Por otro lado, las cavidades cóncavas del truxTTF y $C_{30}H_{12}$ pueden interaccionar de tal forma que se generan heterodímeros en los que, bien un benceno o un

anillo de ditiol del truxTTF se posiciona dentro de la cavidad del hemifullereno (estructuras alternadas o escalonadas). Estas estructuras estarían estabilizadas no sólo por interacciones de tipo π - π sino también, y especialmente, por contactos $\text{CH}\cdots\pi$.

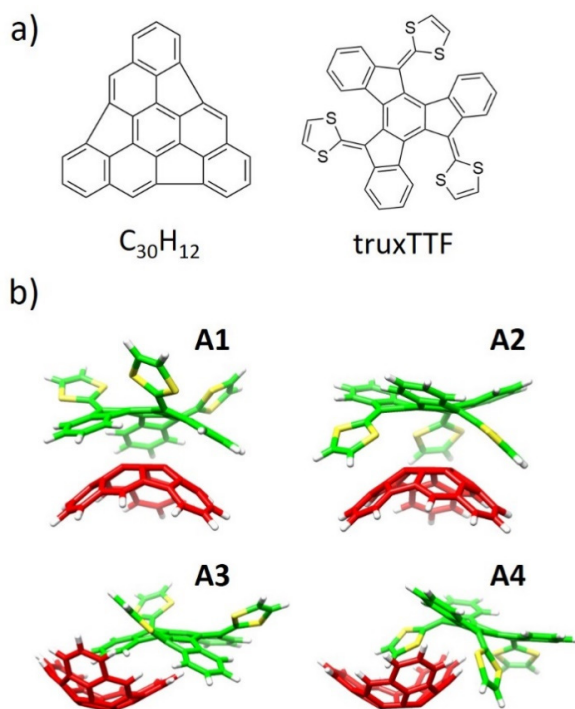


Figura 7. a) Estructuras químicas del hemifullereno $\text{C}_{30}\text{H}_{12}$ y truxTTF. b) Estructuras de mínima energía calculadas para el heterodímero de $\text{truxTTF}\cdot\text{C}_{30}\text{H}_{12}$ a nivel revPBE0-D3/cc-pVTZ: disposiciones cóncavo-convexo o *bowl-in-bowl* (A1 y A2), y cóncavo-cóncavo o escalonadas (A3 y A4).

Las energías de asociación (E_{bind}) calculadas teóricamente indican que los cuatro heterodímeros posibles poseen una interacción elevada, entre -20 y -30 kcal mol^{-1} , siendo una de las estructuras escalonadas (A4) con disposición cóncavo-cóncavo la más estable, con una E_{bind} de -28.5 kcal mol^{-1} . Recientemente, cálculos *ab initio* de alta precisión llevados a cabo

en nuestro grupo de investigación han permitido confirmar el orden energético descrito por DFT.

Por otro lado, los resultados TDDFT apoyan la aparición de la banda de transferencia de carga en la región de 500–550 nm para el agregado supramolecular de $\text{truxTTF}\cdot\text{C}_{30}\text{H}_{12}$, tal y como se observó experimentalmente. La formación del estado de separación de cargas $\text{truxTTF}^+\cdot\text{C}_{30}\text{H}_{12}^-$ tras la fotoexcitación se ha confirmado por experimentos de absorción transitoria (*pump-probe*) de femtosegundo llevados a cabo por el grupo del Prof. Dirk M. Guldi. Las constantes de velocidad para los procesos de separación y recombinación de carga tienen valores de 6.6×10^{11} y $1.0 \times 10^{10} \text{ s}^{-1}$, respectivamente. Este estudio constituye la primera evidencia de la formación de agregados supramoleculares dador–aceptor basados en un fragmento de fullereno, el cual presenta en el agregado propiedades de transferencia de carga fotoinducida similares al fullereno C_{60} .

8.5.4. Fragmentos de fullereno para ensamblajes dador–aceptor

Para explorar de forma más profunda las propiedades de los fragmentos de fullereno, evidenciadas para el caso del heterodímero de $\text{truxTTF}\cdot\text{C}_{30}\text{H}_{12}$ en el apartado anterior, se ha llevado a cabo una investigación combinada teórico–experimental de la complejación de nuevos fragmentos de carbono de tamaño creciente con el compuesto dador de electrones de truxTTF . En concreto, se han modelizado los fragmentos de $\text{C}_{32}\text{H}_{12}$ y $\text{C}_{38}\text{H}_{14}$ que, al contrario que el hemifullereno, son fragmentos de las estructuras de fullereno[60] y [70], respectivamente, basados en el coranuleno (Figura 8). Dicha diferencia en la estructura aromática central podría venir acompañada de diferencias en términos de propiedades electrónicas y complejación supramolecular.

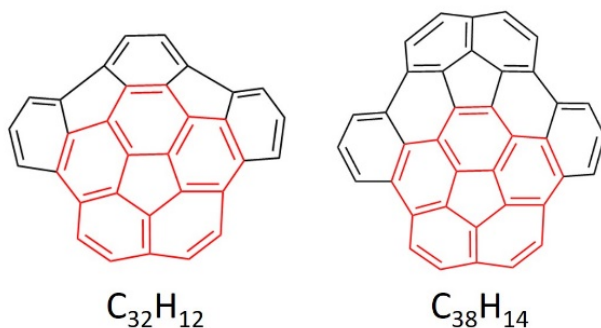


Figura 8. Estructura química de los fragmentos de fullereno de $C_{32}H_{12}$ y $C_{38}H_{14}$ basados en el coranuleno. El esqueleto de coranuleno está resaltado en rojo.

En analogía con los resultados obtenidos para el $C_{30}H_{12}$, los fragmentos de $C_{32}H_{12}$ y $C_{38}H_{14}$ pueden interactuar con el truxTTF a través de agrupamientos *bowl-in-bowl* (cóncavo-convexo), en los que se maximizan las interacciones π - π , o a través de disposiciones alternadas (cóncavo-cóncavo), implicando una mezcla de interacciones π - π y $CH\cdots\pi$. La energía de asociación calculada para los heterodímeros de $C_{32}H_{12}$ se encuentra en un rango de -20 a -30 kcal mol $^{-1}$, mientras que para los complejos de $C_{38}H_{14}$ la estabilización es de -21 a -35 kcal mol $^{-1}$. En ambos casos, los complejos con una estructura escalonada son los más estables. Por tanto, el estudio teórico de las energías de asociación sugiere que la interacción supramolecular con el truxTTF se ve fortalecida al incrementar el tamaño del fragmento de fullereno, debido a un aumento del número de interacciones no-covalentes.

Con el fin de dar una descripción más realista de la fuerza de complejación a temperatura ambiente y en disolución, se han estimado teóricamente las energías libres para el proceso de dimerización (ΔG_{theor}) teniendo en cuenta todos los conformeros posibles de truxTTF• $C_{32}H_{12}$ y truxTTF• $C_{38}H_{14}$, así como los de truxTTF• $C_{30}H_{12}$. El cálculo teórico de los

valores de ΔG_{theor} nos permite concluir que las estructuras *bowl-in-bowl* no se llegarían a formar en disolución, mientras que los complejos con estructura escalonada energéticamente más favorables sí que se formarían ($\Delta G_{\text{theor}} = -5.00$, -4.29 y -4.93 kcal mol⁻¹ para truxTTF•C₃₀H₁₂, truxTTF•C₃₂H₁₂ y truxTTF•C₃₈H₁₄, respectivamente). Posteriores experimentos de ¹H-RMN han permitido confirmar las predicciones teóricas en la formación exclusiva de estructuras alternadas para nuestros agregados supramoleculares dador–aceptor en disolución.

Finalmente, cálculos TDDFT para los heterodímeros indican la existencia de bandas de transferencia de carga a bajas energías, en similitud a lo obtenido para el truxTTF•C₃₀H₁₂, que darían lugar a especies de separación de carga tras la fotoexcitación. Experimentos *pump-probe* de femtosegundo han confirmado esta hipótesis para el caso de truxTTF•C₃₈H₁₄, cuya especie transitoria de truxTTF⁺•C₃₈H₁₄⁻ se ha detectado con un tiempo de vida de 160 ps. No se pudo confirmar sin embargo la detección de la especie de separación de cargas para el complejo dador–aceptor de C₃₂H₁₂ pero, en base a los resultados obtenidos para los fragmentos de fullereno análogos, es muy probable que también ocurra para este agregado supramolecular.

8.6. Polímeros supramoleculares

En este capítulo, se ha llevado a cabo la caracterización teórica de la agregación supramolecular en derivados discóticos de trisamida para obtener información sobre las fuerzas que originan el autoensamblaje cooperativo. Se ha analizado la preferencia energética de una orientación en sentido horario o antihorario para la agregación helicoidal en función

de: (i) la presencia de cadenas alifáticas quirales, y (ii) la conectividad de los grupos amida al esqueleto aromático. Por otro lado, se ha modelizado la agregación de derivados de pirenoimidazol que presentan una amplia gama de motivos estructurales para el autoensamblaje supramolecular. El análisis teórico de primeros principios realizado ha permitido racionalizar la agregación supramolecular que permite preservar las propiedades emisoras de luz tras la formación del material fibrilar.

8.6.1. Cooperatividad en tricarboxamidas

Tomando como inspiración el motivo estructural de los compuestos de benceno-1,3,5-tricarboxamida, en esta Sección estudiamos la polimerización supramolecular de una serie de retroamidas N-centradas basadas en una unidad central de oligo(fenilenoetinileno) (OPE) en forma de estrella (Figura 9). El estudio se ha realizado en colaboración con el grupo experimental dirigido por el Prof. Luis Sánchez. Las características de polimerización supramolecular se han comparado extensivamente con las estructuras análogas derivadas de las carboxamidas CO-centradas.

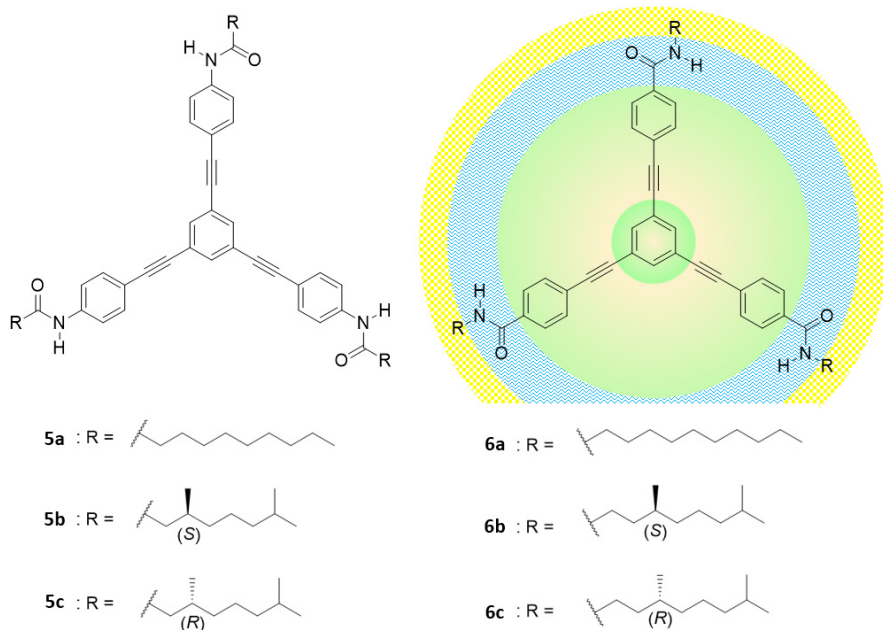


Figura 9. Estructuras químicas de las trisamidas discóticas N-centradas **5** y CO-centradas **6**.

Las primeras evidencias experimentales sobre la agregación supramolecular de estos sistemas sugieren que el ensamblaje de las unidades OPE tiene lugar mediante un mecanismo cooperativo a través de la formación de una red triple de enlaces de hidrógeno, resultando en un polímero supramolecular helicoidal. El cálculo teórico del espectro de dicroísmo circular para las trisamidas N- y CO-centradas ha permitido la asignación inequívoca de la orientación helicoidal en función del grupo estereogénico (*R* o *S*) introducido en las cadenas alifáticas periféricas. Las moléculas con grupos *S* dan lugar a hélices tipo *P* que giran en el sentido de las agujas del reloj, mientras que las moléculas con grupos *R* dan lugar a hélices de tipo *M* que giran en sentido contrario. Además, la helicidad asignada para los compuestos N- y CO-centrados es la misma,

demostrando que la conectividad de la amida no es un factor determinante en la orientación de la hélice supramolecular.

La organización helicoidal de los agregados formados por las trisamidas N- y CO-centradas se ha estudiado mediante simulaciones teóricas de mecánica molecular/dinámica molecular (MM/MD) utilizando condiciones de contorno periódicas. Los resultados teóricos muestran que la diferencia de energía entre las configuraciones helicoidales *M* y *P* aumenta de forma notable al aumentar la longitud de las cadenas alifáticas periféricas, confirmando el sentido preferido de la hélice en función del grupo estereogénico *S* (hélice *P*) o *R* (hélice *M*) presente en las cadenas laterales. En el apilamiento, los centros de OPE permanecen prácticamente planos para maximizar las interacciones π - π , mientras que los grupos amida giran fuera del plano aromático para formar enlaces de hidrógeno eficientes con los monómeros vecinos (Figura 10a,b). Ambos tipos de interacciones son las fuerzas motrices que dirigen el autoensamblaje en la formación de las hélices supramoleculares columnares.

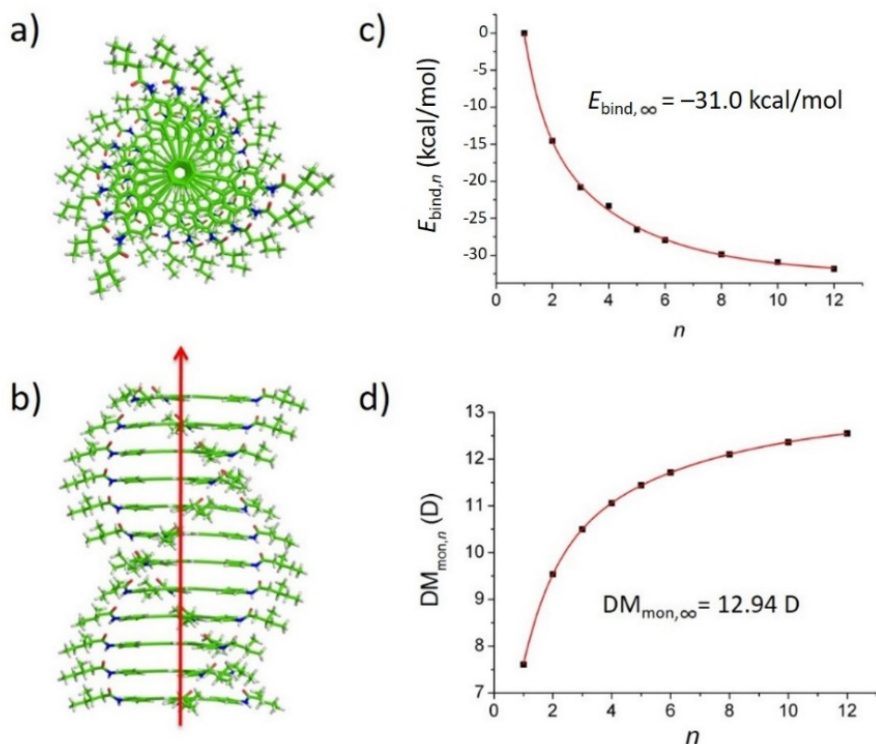


Figura 10. Vista superior (a) y lateral (b) del ensamblaje helicoidal en sentido horario de un agregado de $(5b)_{12}$ que incluye cadenas alifáticas cortas con centro estereogénico *S*. La dirección del momento dipolar en el apilamiento se muestra en rojo. Comportamiento asintótico de la energía de asociación (c) y del momento dipolar (d) por unidad monomérica ($E_{bind,n}$ y $DM_{mon,n}$ respectivamente) al incrementar el número de monómeros en el agregado $(5b)_n$; los valores se han ajustado a una función biexponencial (líneas rojas).

Los cálculos de mecánica molecular se han complementado con cálculos más precisos a nivel DFT para agregados helicoidales de amidas N- y CO-centradas de tamaño creciente. A medida que el agregado crece, el valor absoluto de la energía de asociación por unidad monomérica ($E_{bind,n}$) aumenta, tendiendo a un valor asintótico para unas 12–14 unidades monoméricas (Figura 10c). Este comportamiento evidencia el carácter

cooperativo del proceso de agregación y es característico de un mecanismo de polimerización de tipo nucleación–elongación. El carácter cooperativo es debido a la mayor polarización del apilamiento a medida que se añaden unidades monoméricas, lo cual fortalece la red de enlaces de hidrógeno y hace el agregado cada vez más estable. Dicha polarización queda evidenciada por el crecimiento del momento dipolar por monómero ($DM_{\text{mon},n}$) que tiene lugar al aumentar el número de unidades en el polímero supramolecular (Figura 10d). El valor teórico de $E_{\text{mon},n}$ y $DM_{\text{mon},n}$ cuando n tiene a infinito es mayor para las amidas N-centradas con respecto a las CO-centradas, en buen acuerdo con la mayor cooperatividad encontrada experimentalmente para las retroamidas.

8.6.2. Oligómeros basados en el pirenoimidazol

Si bien la organización supramolecular en polímeros gobernados por interacciones no-covalentes, especialmente enlaces de hidrógeno, es previsible en muchos casos (por ejemplo, las trisamidas del apartado anterior), el autoensamblaje de las unidades electroactivas no es, en general, evidente.

Desde el descubrimiento del pireno, se ha hecho un gran esfuerzo en su modificación estructural con el fin de conseguir agregados supramoleculares que eviten el efecto de desactivación de las propiedades emisoras derivado de la interacción entre unidades de pireno. En este Capítulo se han estudiado a fondo las propiedades de autoensamblaje de derivados del pirenoimidazol que incorporan grupos amida para facilitar la polimerización supramolecular mediante enlaces de hidrógeno. El estudio se ha realizado en colaboración con el grupo del Prof. Luis Sánchez y constituye un claro ejemplo de la utilidad de la

retroalimentación teórico-experimental en el desarrollo de un proyecto de investigación.

Los primeros resultados experimentales evidencian que los derivados de pirenoimidazol forman geles con una inesperada emisión azul y con una baja cooperatividad para la agregación. Por otro lado, los estudios de dicroísmo circular indican que el agregado supramolecular no posee helicidad, incluso cuando la cadena alifática periférica es quiral.

El estudio teórico DFT llevado a cabo ha permitido esclarecer los aspectos estructurales y energéticos de la agregación supramolecular. En primer lugar, se han diseñado una serie de dímeros, como unidades supramoleculares mínimas, de acuerdo con los distintos motivos para la interacción supramolecular presentes en el monómero: (i) el esqueleto aromático del pireno, (ii) los grupos polares de amida e imidazol, (iii) las cadenas largas alifáticas no polares, y (iv) los grupos voluminosos de *tert*-butilo (Figura 11).

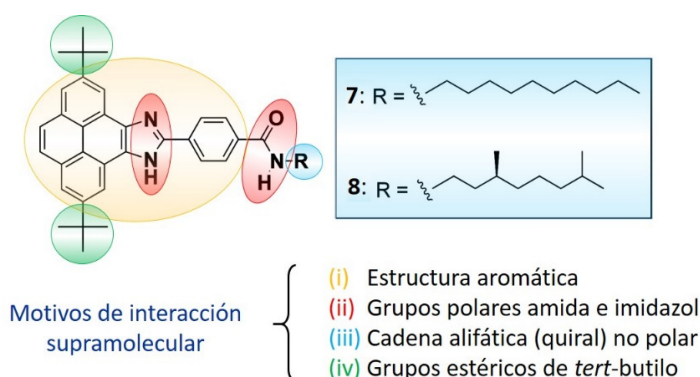


Figura 11. Estructura química de los derivados de pirenoimidazol, y representación esquemática de los distintos motivos para la interacción supramolecular.

De entre todos los dímeros modelizados, el agregado más estable corresponde a un dímero que combina enlaces de H entre los grupos imidazol y amida junto con interacciones estabilizantes $\text{CH}\cdots\pi$ entre las cadenas alquílicas y el esqueleto pirénico. El análisis topológico de la densidad electrónica llevado a cabo mediante el índice no-covalente (NCI) permite explicar la estabilidad del agregado mediante la visualización de las superficies de interacción no-covalente correspondientes (Figura 12a). La estructura de este dímero se ha utilizado en el modelizado teórico de un tetrámero (Figura 12b) que nos ha permitido concluir: (i) el oligómero puede crecer fácilmente a través de la red de enlaces de hidrógeno imidazol-amida y las fuerzas $\text{CH}\cdots\pi$ estabilizantes, (ii) el grado de cooperatividad de la polimerización supramolecular de acuerdo con este patrón de enlaces de hidrógeno es pequeño, en buen acuerdo con las evidencias experimentales, y (iii) la ausencia de interacciones π - π entre las unidades pirénicas justifica la preservación de las propiedades emisoras en el azul propias del pireno.

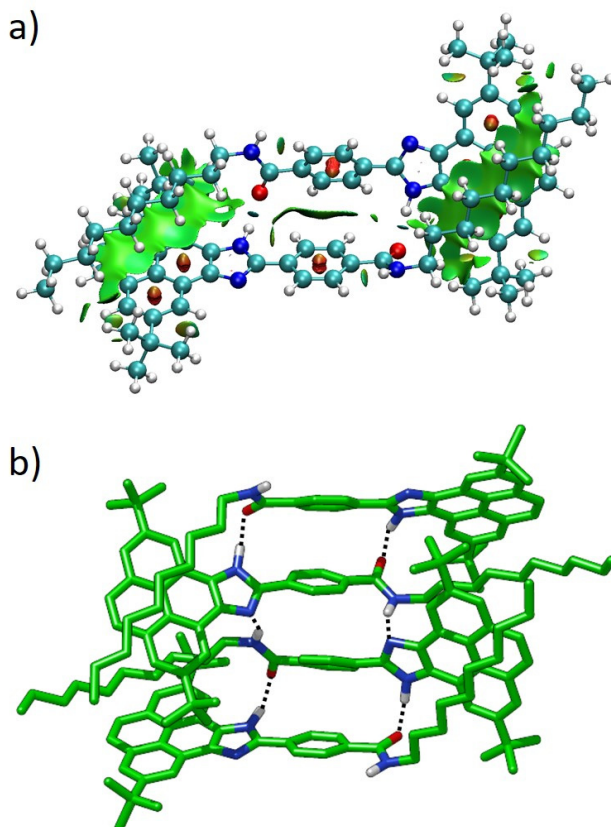


Figura 12. Superficies NCI representando las interacciones de enlace de hidrógeno (azul) y fuerzas de dispersión (verde) para el dímero más estable del derivado de pteroinimidazol **7**. b) Estructura de mínima energía calculada para el tetrámero indicando la red de enlaces de hidrógeno entre las unidades de imidazol y amida.

8.7. Conclusiones

En conclusión, a lo largo de esta Tesis se han llevado a cabo estudios teóricos combinados con colaboraciones experimentales muy fructíferas con el fin de abordar una gran variedad de sistemas electroactivos para

su posterior uso en electrónica molecular y ciencia de nuevos materiales. Asimismo, algunos de los sistemas estudiados han permitido ayudar a dar respuesta a preguntas fundamentales en fenómenos de transferencia de carga, autoensamblaje supramolecular y origen de la quiralidad. En concreto, se pueden extraer las siguientes conclusiones focalizadas en los tres Capítulos en los que se divide la presentación de los resultados obtenidos en la Tesis:

Arquitecturas dador-aceptor covalentes

Se ha realizado una investigación químico-cuántica sobre cromóforos dador- π -aceptor tanto de anclaje simple como doble basados en las unidades dadoras de electrones de exTTF y hemiexTTF, para su posterior aplicación en celdas solares sensibilizadas por colorante (DSC). Los cálculos teóricos indican que el regioisómero de exTTF-DCF de mayor interés es el exTTF-DCF-A, con absorción en todo el rango visible y anclaje óptimo para la generación de DSCs eficientes. Además, se han caracterizado colorantes di-ramificados basados en la unidad dadora de hemiexTTF y la unidad aceptora de DCV, capaces de absorber luz en todo el espectro visible gracias a la presencia de bandas de transferencia de carga de baja energía. Cálculos de primeros principios nos han permitido comprender las implicaciones del modo de anclaje doble en estos cromóforos para DSCs cuando se sustituye un grupo ciano por un ácido carboxílico. Se ha demostrado que el modo di-anclado con coordinación monodentada del grupo cianoacrílico es el modo de adsorción más plausible para estos cromóforos di-ramificados. Esta coordinación, además de ser el anclaje a la superficie del semiconductor más estable, ofrece dos bandas LUMO anchas prácticamente degeneradas que permiten una mejora en la inyección de carga al semiconductor.

Complejos dador–aceptor supramoleculares

Las formaciones supramoleculares investigadas en este Capítulo constituyen ejemplos únicos que han permitido entender en profundidad el reconocimiento supramolecular de huéspedes de fullereno con receptores de porfirina. Los estudios presentados demuestran un autoensamblaje gobernado por interacciones $\text{NH}\cdots\text{O}$ y porfirina–fullereno, siendo estas últimas de naturaleza dispersiva y electrostática. El estudio teórico de los complejos formados por receptores ditópicos de porfirina con el huésped de fullereno en agregados de estequiometría 1:2 demuestra una cooperatividad negativa originada por la extracción de carga del receptor por parte del fullereno tras la inclusión del primer huésped. Dicha cooperatividad negativa queda parcialmente contrarrestada en el receptor de tipo *tape* debido a la interacción estabilizante entre las dos esferas de fullereno al formarse el complejo 1:2 en disposición *syn*.

Por otro lado, el estudio supramolecular llevado a cabo para una serie de fragmentos de fullereno — $\text{C}_{30}\text{H}_{12}$, $\text{C}_{32}\text{H}_{12}$ and $\text{C}_{38}\text{H}_{14}$ — con el compuesto de truxTTF, el cual es un dador electrónico y presenta una estructura molecular curvada, ha revelado que la configuración cóncavo–cóncavo en la que un anillo de ditiol del truxTTF se sitúa en la cavidad del fragmento de fullereno es la más estable. Las fuerzas no-covalentes que gobiernan el ensamblaje de dicho agregado, cuya estructura resulta contradictoria con la interacción cóncavo–convexo esperada, no quedan solamente determinadas por interacciones de tipo π – π , sino por los contactos $\text{CH}\cdots\pi$ y $\text{S}\cdots\text{C}$ que juegan un papel decisivo. Los cálculos TDDFT han proporcionado evidencias de la existencia de bandas de transferencia de carga a bajas energías correspondientes a transiciones electrónicas desde

el fragmento dador de electrones de truxTTF al fragmento de fullereno aceptor de electrones, confirmándose la formación de la especie de separación de cargas para el $C_{30}H_{12}$ y $C_{38}H_{14}$ mediante técnicas espectroscópicas de femtosegundo.

Polímeros supramoleculares

En este Capítulo, se ha investigado la polimerización supramolecular cooperativa de trisamidas N-centradas basadas en la unidad central de OPE. Los compuestos estudiados presentan una estructura molecular discótica y dan lugar a agregados helicoidales columnares, cuyo sentido de giro (*M* o *P*) no depende de la conectividad de los grupos amida sino de la configuración (*R* o *S*) del grupo estereogénico presente en las cadenas alifáticas periféricas. La sinergia de las interacciones π - π , la red triple de enlaces de hidrógeno entre las amidas y las fuerzas de dispersión débiles entre las cadenas alifáticas periféricas han permitido explicar el autoensamblaje supramolecular de las superestructuras helicoidales. El carácter cooperativo del mecanismo de polimerización, de mayor magnitud en las amidas N-centradas que en las CO-centradas, se ha podido explicar en términos de energía de asociación y momento dipolar por unidad monomérica. Ambas magnitudes crecen asintóticamente debido al incremento de la polarización de la red de enlaces de hidrógeno durante el proceso de nucleación.

Por último, se han estudiado derivados de pirenoimidazol que incorporan una gran variedad de motivos de interacción supramolecular, con el fin de guiar el autoensamblaje manteniendo las propiedades de emisión en el azul del monómero pirénico. Los cálculos teóricos han demostrado, en sinergia con estudios experimentales, que la formación de los agregados queda gobernada por enlaces de hidrógeno entre los grupos amida e

imidazol junto con un número importante de interacciones CH \cdots π entre la cadena alifática y el esqueleto aromático del pirenoimidazol. La ausencia de interacciones π - π entre los centros pirénicos permite explicar la preservación de las propiedades de emisión azul tras la formación del material polimérico supramolecular.

Bibliography

- [1] *IUPAC. Compendium of Chemical Terminology, 2nd ed. (the "Gold Book")*. Compiled by A. D. McNaught and A. Wilkinson. Blackwell Scientific Publications, Oxford (1997). XML on-line corrected version: <http://goldbook.iupac.org> (2006-) created by M. Nic, J. Jirat, B. Kosata; updates compiled by A. Jenkins. ISBN 0-9678550-9-8. doi:10.1351/goldbook.
- [2] W. B. Jensen, *The Lewis acid-base concepts : an overview.*, New York: Wiley, **1980**, p. 364.
- [3] M. C. Petty, *Electroactive Organic Compounds*, John Wiley & Sons, Ltd, **2007**, pp. 169-211.
- [4] S. R. Forrest and M. E. Thompson, *Chem. Rev.* **2007**, *107*, 923-925.
- [5] P. Batail, *Chem. Rev.* **2004**, *104*, 4887-4890.
- [6] J.-L. Bredas and J. R. Durrant, *Acc. Chem. Res.* **2009**, *42*, 1689-1690.
- [7] A. J. Nozik and J. Miller, *Chem. Rev.* **2010**, *110*, 6443-6445.
- [8] R. A. Marcus and N. Sutin, *Biochim. Biophys. Acta* **1985**, *811*, 265-322.
- [9] G. Booth, *Nitro Compounds, Aromatic*, Wiley-VCH: Weinheim, **2005**, p. 29456.
- [10] D. Burland, *Chem. Rev.* **1994**, *94*, 1-2.
- [11] P. A. Sullivan and L. R. Dalton, *Acc. Chem. Res.* **2010**, *43*, 10-18.
- [12] F. Chen, J. Zhang and X. Wan, *Chem. Eur. J.* **2012**, *18*, 4558-4567.
- [13] I. Asselberghs, K. Clays, A. Persoons, M. D. Ward and J. McCleverty, *J. Mater. Chem.* **2004**, *14*, 2831-2839.
- [14] F. M. Raymo and M. Tomasulo, *Chem. Eur. J.* **2006**, *12*, 3186-3193.
- [15] C. Reichardt and T. Welton, *Solvents and Solvent Effects in Organic Chemistry*, Wiley-VCH Verlag GmbH & Co. KGaA, **2010**, p. 718.
- [16] a) Y. Wu and W. Zhu, *Chem. Soc. Rev.* **2013**, *42*, 2039-2058; b) C. Duan, K. Zhang, C. Zhong, F. Huang and Y. Cao, *Chem. Soc. Rev.* **2013**, *42*, 9071-9104.

- [17] a) A. Gupta, V. Armel, W. Xiang, G. Fanchini, S. E. Watkins, D. R. MacFarlane, U. Bach and R. A. Evans, *Tetrahedron* **2013**, *69*, 3584-3592; b) P. Gautam, R. Misra, S. Biswas and G. D. Sharma, *Phys. Chem. Chem. Phys.* **2016**, *18*, 13918-13926; c) P. Gautam, R. Misra, E. N. Koukaras, A. Sharma and G. D. Sharma, *Org. Electron.* **2015**, *27*, 72-83.
- [18] a) J. N. Clifford, E. Martínez-Ferrero, A. Viterisi and E. Palomares, *Chem. Soc. Rev.* **2011**, *40*, 1635-1646; b) M. Liang and J. Chen, *Chem. Soc. Rev.* **2013**, *42*, 3453-3488.
- [19] a) M. Grätzel, *J. Photochem. Photobiol. C: Photochem. Rev.* **2003**, *4*, 145-153; b) A. Hagfeldt, G. Boschloo, L. Sun, L. Kloo and H. Pettersson, *Chem. Rev.* **2010**, *110*, 6595-6663.
- [20] a) Workspace.imperial.ac.uk, *EarlyHistory: The "invention" of the DSSC*, **1988**; b) B. O'Regan and M. Gratzel, *Nature* **1991**, *353*, 737-740.
- [21] M. Jacoby, *The future of low-cost solar cells*, *94*, **2016**, pp. 30-35.
- [22] a) M. K. Nazeeruddin, A. Kay, I. Rodicio, R. Humphry-Baker, E. Mueller, P. Liska, N. Vlachopoulos and M. Graetzel, *J. Am. Chem. Soc.* **1993**, *115*, 6382-6390; b) M. K. Nazeeruddin, F. De Angelis, S. Fantacci, A. Selloni, G. Viscardi, P. Liska, S. Ito, B. Takeru and M. Grätzel, *J. Am. Chem. Soc.* **2005**, *127*, 16835-16847.
- [23] a) S. M. Feldt, E. A. Gibson, E. Gabrielsson, L. Sun, G. Boschloo and A. Hagfeldt, *J. Am. Chem. Soc.* **2010**, *132*, 16714-16724; b) T. Daeneke, T.-H. Kwon, A. B. Holmes, N. W. Duffy, U. Bach and L. Spiccia, *Nat. Chem.* **2011**, *3*, 211-215; c) Y. Bai, J. Zhang, D. Zhou, Y. Wang, M. Zhang and P. Wang, *J. Am. Chem. Soc.* **2011**, *133*, 11442-11445.
- [24] V. Strauss, A. Roth, M. Sekita and Dirk M. Guldi, *Chem* **2016**, *1*, 531-556.
- [25] a) D. S. Acker and W. R. Hertler, *J. Am. Chem. Soc.* **1962**, *84*, 3370-3374; b) W. Kaim and M. Moscherosch, *Coord. Chem. Rev.* **1994**, *129*, 157-193.
- [26] J. L. Segura and N. Martín, *Angew. Chem. Int. Ed.* **2001**, *40*, 1372-1409.
- [27] a) J. Ferraris, D. O. Cowan, V. Walatka and J. H. Perlstein, *J. Am. Chem. Soc.* **1973**, *95*, 948-949; b) M. Bendikov, F. Wudl and D. F. Perepichka, *Chem. Rev.* **2004**, *104*, 4891-4946.

- [28] I. Avilov, V. Geskin and J. Cornil, *Adv. Funct. Mater.* **2009**, *19*, 624-633.
- [29] J. L. Atwood and J. W. Steed, *Encyclopedia of Supramolecular Chemistry*, CRC Press, **2004**, p. 1744.
- [30] N. Martín and J.-F. Nierengarten, *Supramolecular Chemistry of Fullerenes and Carbon Nanotubes*, Wiley-VCH, Weinheim, **2012**, p. 418.
- [31] P. Ceroni and V. Balzani, *Photoinduced Energy and Electron Transfer Processes*, (Ed. P. Ceroni), Springer Netherlands, Dordrecht, **2012**, pp. 21-38.
- [32] a) A. S. Mahadevi and G. N. Sastry, *Chem. Rev.* **2016**, *116*, 2775-2825; b) J.-M. Lehn, *Supramolecular Chemistry: Concepts and Perspectives*, Wiley-VCH Verlag GmbH & Co. KGaA, **1995**, p; c) M. R. Wasielewski, *Chem. Rev.* **1992**, *92*, 435-461.
- [33] E. Mattia and S. Otto, *Nat. Nanotechnol.* **2015**, *10*, 111-119.
- [34] A. Harada, *Supramolecular Polymer Chemistry*, Wiley-VCH Verlag GmbH & Co. KGaA, **2012**, p.
- [35] a) J. M. Pollino and M. Weck, *Chem. Soc. Rev.* **2005**, *34*, 193-207; b) T. Aida, E. W. Meijer and S. I. Stupp, *Science* **2012**, *335*, 813-817.
- [36] a) X. Yan, F. Wang, B. Zheng and F. Huang, *Chem. Soc. Rev.* **2012**, *41*, 6042-6065; b) E. A. Appel, J. del Barrio, X. J. Loh and O. A. Scherman, *Chem. Soc. Rev.* **2012**, *41*, 6195-6214.
- [37] a) S. Ghosh, V. K. Praveen and A. Ajayaghosh, *Annual Review of Materials Research* **2016**, *46*, 235-262; b) L. Yang, X. Tan, Z. Wang and X. Zhang, *Chem. Rev.* **2015**, *115*, 7196-7239; c) E. Moulin, E. Busseron and N. Giuseppone, *CHAPTER 1 Self-assembled Supramolecular Materials in Organic Electronics*, The Royal Society of Chemistry, **2015**, pp. 1-52.
- [38] a) M. Liu, L. Zhang and T. Wang, *Chem. Rev.* **2015**, *115*, 7304-7397; b) E. Busseron, Y. Ruff, E. Moulin and N. Giuseppone, *Nanoscale* **2013**, *5*, 7098-7140; c) I. Danila, F. Riobé, F. Piron, J. Puigmartí-Luis, J. D. Wallis, M. Linares, H. Ågren, D. Beljonne, D. B. Amabilino and N. Avarvari, *J. Am. Chem. Soc.* **2011**, *133*, 8344-8353.
- [39] G. A. Hembury, V. V. Borovkov and Y. Inoue, *Chem. Rev.* **2008**, *108*, 1-73.
- [40] G. M. Whitesides and M. Boncheva, *Proc. Natl. Acad. Sci. U. S. A.* **2002**, *99*, 4769-4774.

- [41] B. Alberts, D. Bray, J. Lewis, M. Raff, K. Roberts and J. D. Watson, *Molecular Biology of the Cell*, Garland Press: New York, **1994**, p. 1392.
- [42] C. J. Cramer, *Essentials of Computational Chemistry: Theories and Models (2nd Edition)*, John Wiley & Sons, **2004**, p. 618.
- [43] K. T. Butler, J. M. Frost, J. M. Skelton, K. L. Svane and A. Walsh, *Chem. Soc. Rev.* **2016**, *45*, 6138-6146.
- [44] Y. Zhao and D. G. Truhlar, *Acc. Chem. Res.* **2008**, *41*, 157-167.
- [45] M. J. Frisch, G. W. Trucks, H. B. Schlegel, G. E. Scuseria, M. A. Robb, J. R. Cheeseman, G. Scalmani, V. Barone, B. Mennucci, G. A. Petersson, H. Nakatsuji, M. Caricato, X. Li, H. P. Hratchian, A. F. Izmaylov, J. Bloino, G. Zheng, J. L. Sonnenberg, M. Hada, M. Ehara, K. Toyota, R. Fukuda, J. Hasegawa, M. Ishida, T. Nakajima, Y. Honda, O. Kitao, H. Nakai, T. Vreven, J. A. Montgomery, J. E. Peralta, F. Ogliaro, M. Bearpark, J. J. Heyd, E. Brothers, K. N. Kudin, V. N. Staroverov, R. Kobayashi, J. Normand, K. Raghavachari, A. Rendell, J. C. Burant, S. S. Iyengar, J. Tomasi, M. Cossi, N. Rega, J. M. Millam, M. Klene, J. E. Knox, J. B. Cross, V. Bakken, C. Adamo, J. Jaramillo, R. Gomperts, R. E. Stratmann, O. Yazyev, A. J. Austin, R. Cammi, C. Pomelli, J. W. Ochterski, R. L. Martin, K. Morokuma, V. G. Zakrzewski, G. A. Voth, P. Salvador, J. J. Dannenberg, S. Dapprich, A. D. Daniels, Farkas, J. B. Foresman, J. V. Ortiz, J. Cioslowski and D. J. Fox, *Gaussian 09, Revision D.01*, Wallingford CT, **2009**.
- [46] F. Neese, *WIREs Comput. Mol. Sci.* **2012**, *2*, 73-78.
- [47] P. Giannozzi, S. Baroni, N. Bonini, M. Calandra, R. Car, C. Cavazzoni, D. Ceresoli, G. L. Chiarotti, M. Cococcioni, I. Dabo, A. D. Corso, S. d. Gironcoli, S. Fabris, G. Fratesi, R. Gebauer, U. Gerstmann, C. Gougoussis, A. Kokalj, M. Lazzeri, L. Martin-Samos, N. Marzari, F. Mauri, R. Mazzarello, S. Paolini, A. Pasquarello, L. Paulatto, C. Sbraccia, S. Scandolo, G. Sclauzero, A. P. Seitsonen, A. Smogunov, P. Umari and R. M. Wentzcovitch, *J. Phys.: Condens. Matter* **2009**, *21*, 395502.
- [48] *MOPAC2012*, James J. P. Stewart, *Stewart Computational Chemistry, Colorado Springs, CO, USA*, <http://OpenMOPAC.net> (2012).
- [49] J. W. Ponder, *TINKER Version 7.1*, **2015**.
- [50] J. M. Turney, A. C. Simmonett, R. M. Parrish, E. G. Hohenstein, F. A. Evangelista, J. T. Fermann, B. J. Mintz, L. A. Burns, J. J. Wilke, M. L.

- Abrams, N. J. Russ, M. L. Leininger, C. L. Janssen, E. T. Seidl, W. D. Allen, H. F. Schaefer, R. A. King, E. F. Valeev, C. D. Sherrill and T. D. Crawford, *WIREs Comput. Mol. Sci.* **2012**, *2*, 556-565.
- [51] a) E. R. Johnson, S. Keinan, P. Mori-Sánchez, J. Contreras-García, A. J. Cohen and W. Yang, *J. Am. Chem. Soc.* **2010**, *132*, 6498-6506; b) J. Contreras-García, E. R. Johnson, S. Keinan, R. Chaudret, J.-P. Piquemal, D. N. Beratan and W. Yang, *J. Chem. Theory Comput.* **2011**, *7*, 625-632.
- [52] P. Hohenberg and W. Kohn, *Phys. Rev.* **1964**, *136*, B864-B871.
- [53] a) T. Ziegler, *Chem. Rev.* **1991**, *91*, 651-667; b) E. J. Baerends and O. V. Gritsenko, *J. Phys. Chem. A* **1997**, *101*, 5383-5403; c) R. G. Parr, *Density Functional Theory of Atoms and Molecules*, Eds.: K. Fukui and B. Pullman), Springer Netherlands, Dordrecht, **1980**, pp. 5-15.
- [54] M. Born and R. Oppenheimer, *Annalen der Physik* **1927**, *389*, 457-484.
- [55] W. Kohn and L. J. Sham, *Phys. Rev.* **1965**, *140*, A1133-A1138.
- [56] R. G. Parr and W. Yang, *Density-Functional Theory of Atoms and Molecules*, New York: Oxford University Press, **1989**, p. 352.
- [57] J. P. Perdew, K. Burke and M. Ernzerhof, *Phys. Rev. Lett.* **1996**, *77*, 3865-3868.
- [58] J. Tao, J. P. Perdew, V. N. Staroverov and G. E. Scuseria, *Phys. Rev. Lett.* **2003**, *91*, 146401.
- [59] A. D. Becke, *J. Chem. Phys.* **1993**, *98*, 1372-1377.
- [60] A. D. Becke, *Phys. Rev. A* **1988**, *38*, 3098-3100.
- [61] C. Lee, W. Yang and R. G. Parr, *Phys. Rev. B* **1988**, *37*, 785-789.
- [62] S. H. Vosko, L. Wilk and M. Nusair, *Can. J. Phys.* **1980**, *58*, 1200-1211.
- [63] C. Adamo and V. Barone, *J. Chem. Phys.* **1999**, *110*, 6158-6170.
- [64] Y. Zhao and D. G. Truhlar, *J. Chem. Phys.* **2006**, *125*, 194101.
- [65] Y. Zhao and D. Truhlar, *Theor. Chem. Acc.* **2008**, *120*, 215-241.
- [66] Y. Zhao and D. G. Truhlar, *J. Phys. Chem. A* **2006**, *110*, 5121-5129.
- [67] Y. Zhao and D. G. Truhlar, *J. Phys. Chem. A* **2004**, *108*, 6908-6918.
- [68] T. Yanai, D. P. Tew and N. C. Handy, *Chem. Phys. Lett.* **2004**, *393*, 51-57.
- [69] J.-D. Chai and M. Head-Gordon, *J. Chem. Phys.* **2008**, *128*, 084106.

- [70] E. Brémond, I. Ciofini, J. C. Sancho-García and C. Adamo, *Acc. Chem. Res.* **2016**, *49*, 1503-1513.
- [71] S. Grimme, *J. Chem. Phys.* **2006**, *124*, 034108.
- [72] J. P. Perdew and K. Schmidt, *AIP Conf. Proc.* **2001**, *577*, 1-20.
- [73] a) S. Grimme, *J. Comput. Chem.* **2006**, *27*, 1787-1799; b) J. Antony and S. Grimme, *Phys. Chem. Chem. Phys.* **2006**, *8*, 5287-5293; c) S. Grimme, J. Antony, S. Ehrlich and H. Krieg, *J. Chem. Phys.* **2010**, *132*, 154104.
- [74] S. Grimme, S. Ehrlich and L. Goerigk, *J. Comput. Chem.* **2011**, *32*, 1456-1465.
- [75] S. Grimme, *Chem. Eur. J.* **2012**, *18*, 9955-9964.
- [76] M. Dion, H. Rydberg, E. Schröder, D. C. Langreth and B. I. Lundqvist, *Phys. Rev. Lett.* **2004**, *92*, 246401.
- [77] O. A. Vydrov and T. Van Voorhis, *J. Chem. Phys.* **2010**, *133*, 244103.
- [78] B. Jeziorski, R. Moszynski and K. Szalewicz, *Chem. Rev.* **1994**, *94*, 1887-1930.
- [79] A. Tkatchenko and M. Scheffler, *Phys. Rev. Lett.* **2009**, *102*, 073005.
- [80] S. N. Steinmann and C. Corminboeuf, *J. Chem. Theory Comput.* **2011**, *7*, 3567-3577.
- [81] a) A. D. Becke and E. R. Johnson, *J. Chem. Phys.* **2007**, *127*, 154108; b) A. D. Becke and E. R. Johnson, *J. Chem. Phys.* **2007**, *127*, 124108.
- [82] E. Runge and E. K. U. Gross, *Phys. Rev. Lett.* **1984**, *52*, 997-1000.
- [83] M. A. L. Marques, C. Ullrich, F. Nogueira, A. Rubio, K. Burke and E. K. U. Gross, *Time-Dependent Density Functional Theory*, Springer-Verlag Berlin Heidelberg, **2006**, p. 555.
- [84] a) M. E. Casida and M. Huix-Rotllant, *Annu. Rev. Phys. Chem.* **2012**, *63*, 287-323; b) M. A. L. Marques and E. K. U. Gross, *Annu. Rev. Phys. Chem.* **2004**, *55*, 427-455.
- [85] M. Petersilka, U. J. Gossmann and E. K. U. Gross, *Phys. Rev. Lett.* **1996**, *76*, 1212-1215.
- [86] D. P. Chong, *Recent advances in density functional methods*, World Scientific, **2011**, p. 340.
- [87] R. Ditchfield, W. J. Hehre and J. A. Pople, *J. Chem. Phys.* **1971**, *54*, 724-728.

- [88] T. H. Dunning, *J. Chem. Phys.* **1989**, *90*, 1007-1023.
- [89] F. Weigend and R. Ahlrichs, *Phys. Chem. Chem. Phys.* **2005**, *7*, 3297-3305.
- [90] M. J. S. Dewar and W. Thiel, *J. Am. Chem. Soc.* **1977**, *99*, 4899-4907.
- [91] M. J. S. Dewar, E. G. Zoebisch, E. F. Healy and J. J. P. Stewart, *J. Am. Chem. Soc.* **1985**, *107*, 3902-3909.
- [92] J. J. P. Stewart, *J. Comput. Chem.* **1989**, *10*, 209-220.
- [93] J. Pople and D. Beveridge, *Approximate Molecular Orbital Theory*, McGraw-Hill, **1970**, p. 224.
- [94] J. P. Stewart, *J. Mol. Model.* **2013**, *19*, 1-32.
- [95] J. J. P. Stewart, *J. Mol. Model.* **2007**, *13*, 1173-1213.
- [96] N. L. Allinger and U. Burkert, *Molecular Mechanics*, An American Chemical Society Publication, **1982**, p. 339.
- [97] J. E. Lennard-Jones, *Proc. Phys. Soc.* **1931**, *43*, 461.
- [98] M. P. Allen and D. J. Tildesley, *Computer simulation of liquids*, Oxford university press: New York, **1987**, p. 408.
- [99] L. Verlet, *Phys. Rev.* **1967**, *159*, 98-103.
- [100] J. Grotendorst, *Ab initio molecular dynamics: Theory and Implementation, 1* (Ed. J. Grotendorst), John von Neumann Institute for Computing, **2000**, pp. 301-449.
- [101] R. Car and M. Parrinello, *Phys. Rev. Lett.* **1985**, *55*, 2471-2474.
- [102] F. Jensen, *Introduction to Computational Chemistry, 2nd Edition*, John Wiley and Sons, **2006**, p. 624.
- [103] J. Tomasi, B. Mennucci and R. Cammi, *Chem. Rev.* **2005**, *105*, 2999-3094.
- [104] B. Mennucci and R. Cammi, *Continuum Solvation Models in Chemical Physics: From Theory to Applications*, John Wiley & Sons, **2007**, p. 636.
- [105] A. V. Marenich, C. J. Cramer and D. G. Truhlar, *J. Phys. Chem. B* **2009**, *113*, 6378-6396.
- [106] E. G. Hohenstein and C. D. Sherrill, *J. Chem. Phys.* **2010**, *132*, 184111.
- [107] J.-i. Yamada and T. Sugimoto, *TTF chemistry: fundamentals and applications of tetrathiafulvalene*, Kodansha Springer, **2004**, p. 445.

- [108] a) J. J. Bergkamp, S. Decurtins and S.-X. Liu, *Chem. Soc. Rev.* **2015**, *44*, 863-874; b) M. B. Nielsen, C. Lomholt and J. Becher, *Chem. Soc. Rev.* **2000**, *29*, 153-164.
- [109] D. Canevet, M. Salle, G. Zhang, D. Zhang and D. Zhu, *Chem. Commun.* **2009**, 2245-2269.
- [110] Y. Yamashita, Y. Kobayashi and T. Miyashi, *Angew. Chem. Int. Ed.* **1989**, *28*, 1052-1053.
- [111] a) N. Martín, L. Sánchez, C. Seoane, E. Ortí, P. M. Viruela and R. Viruela, *J. Org. Chem.* **1998**, *63*, 1268-1279; b) M. C. Díaz, B. M. Illescas, N. Martín, R. Viruela, P. M. Viruela, E. Ortí, O. Brede, I. Zilbermann and D. M. Guldi, *Chem. Eur. J.* **2004**, *10*, 2067-2077; c) C. A. Christensen, A. S. Batsanov and M. R. Bryce, *J. Am. Chem. Soc.* **2006**, *128*, 10484-10490.
- [112] F. G. Brunetti, J. L. Lopez, C. Atienza and N. Martín, *J. Mater. Chem.* **2012**, *22*, 4188-4205.
- [113] F. Giacalone, J. L. Segura, N. Martín and D. M. Guldi, *J. Am. Chem. Soc.* **2004**, *126*, 5340-5341.
- [114] Y. Takano, M. Á. Herranz, N. Martín, G. de Miguel Rojas, D. M. Guldi, I. E. Kareev, S. H. Strauss, O. V. Boltalina, T. Tsuchiya and T. Akasaka, *Chem. Eur. J.* **2010**, *16*, 5343-5353.
- [115] Y. Takano, M. Á. Herranz, N. Martín, S. G. Radhakrishnan, D. M. Guldi, T. Tsuchiya, S. Nagase and T. Akasaka, *J. Am. Chem. Soc.* **2010**, *132*, 8048-8055.
- [116] S. S. Gayathri, M. Wielopolski, E. M. Pérez, G. Fernández, L. Sánchez, R. Viruela, E. Ortí, D. M. Guldi and N. Martín, *Angew. Chem. Int. Ed.* **2009**, *48*, 815-819.
- [117] P.-A. Bouit, C. Villegas, J. L. Delgado, P. M. Viruela, R. Pou-Amérigo, E. Ortí and N. Martín, *Org. Lett.* **2011**, *13*, 604-607.
- [118] M. Pastore and F. D. Angelis, *ACS Nano* **2009**, *4*, 556-562.
- [119] F. Ambrosio, N. Martsinovich and A. Troisi, *J. Phys. Chem. Lett.* **2012**, *3*, 1531-1535.
- [120] a) F. De Angelis, S. Fantacci, A. Selloni, M. K. Nazeeruddin and M. Grätzel, *J. Phys. Chem. C* **2010**, *114*, 6054-6061; b) F. De Angelis, S. Fantacci, A. Selloni, M. Grätzel and M. K. Nazeeruddin, *Nano Lett.* **2007**, *7*, 3189-3195.

- [121] P.-A. Bouit, M. Marszalek, R. Humphry-Baker, R. Viruela, E. Ortí, S. M. Zakeeruddin, M. Grätzel, J. L. Delgado and N. Martín, *Chem. Eur. J.* **2012**, *18*, 11621-11629.
- [122] R. García, M. Á. Herranz, M. R. Torres, P.-A. Bouit, J. L. Delgado, J. Calbo, P. M. Viruela, E. Ortí and N. Martín, *J. Org. Chem.* **2012**, *77*, 10707-10717.
- [123] a) S. Tatay, S. A. Haque, B. O'Regan, J. R. Durrant, W. J. H. Verhees, J. M. Kroon, A. Vidal-Ferran, P. Gavina and E. Palomares, *J. Mater. Chem.* **2007**, *17*, 3037-3044; b) A. Ehret, L. Stuhl and M. T. Spitler, *J. Phys. Chem. B* **2001**, *105*, 9960-9965; c) Z.-S. Wang, Y. Cui, Y. Danoh, C. Kasada, A. Shinpo and K. Hara, *J. Phys. Chem. C* **2007**, *111*, 7224-7230.
- [124] a) A. Vittadini, A. Selloni, F. P. Rotzinger and M. Grätzel, *J. Phys. Chem. B* **2000**, *104*, 1300-1306; b) F. Nunzi and F. De Angelis, *J. Phys. Chem. C* **2010**, *115*, 2179-2186.
- [125] J. N. Clifford, E. Palomares, M. K. Nazeeruddin, M. Grätzel, J. Nelson, X. Li, N. J. Long and J. R. Durrant, *J. Am. Chem. Soc.* **2004**, *126*, 5225-5233.
- [126] a) P. Chen, J. H. Yum, F. D. Angelis, E. Mosconi, S. Fantacci, S.-J. Moon, R. H. Baker, J. Ko, M. K. Nazeeruddin and M. Grätzel, *Nano Lett.* **2009**, *9*, 2487-2492; b) S. Rühle, M. Greenshtein, S. G. Chen, A. Merson, H. Pizem, C. S. Sukenik, D. Cahen and A. Zaban, *J. Phys. Chem. B* **2005**, *109*, 18907-18913.
- [127] E. Ronca, M. Pastore, L. Belpassi, F. Tarantelli and F. De Angelis, *Energy Environ. Sci.* **2013**, *6*, 183-193.
- [128] a) S. Wenger, P.-A. Bouit, Q. Chen, J. Teuscher, D. D. Censo, R. Humphry-Baker, J.-E. Moser, J. L. Delgado, N. Martín, S. M. Zakeeruddin and M. Grätzel, *J. Am. Chem. Soc.* **2010**, *132*, 5164-5169; b) G. Zhang, H. Bala, Y. Cheng, D. Shi, X. Lv, Q. Yu and P. Wang, *Chem. Commun.* **2009**, 2198-2200; c) M. Xu, S. Wenger, H. Bala, D. Shi, R. Li, Y. Zhou, S. M. Zakeeruddin, M. Grätzel and P. Wang, *J. Phys. Chem. C* **2009**, *113*, 2966-2973.
- [129] C. Anselmi, E. Mosconi, M. Pastore, E. Ronca and F. De Angelis, *Phys. Chem. Chem. Phys.* **2012**, *14*, 15963-15974.
- [130] E. Mosconi, A. Selloni and F. De Angelis, *J. Phys. Chem. C* **2012**, *116*, 5932-5940.

- [131] B. Pelado, F. Abou-Chahine, J. Calbo, R. Caballero, P. de la Cruz, J. M. Junquera-Hernández, E. Ortí, N. V. Tkachenko and F. Langa, *Chem. Eur. J.* **2015**, *21*, 5814-5825.
- [132] M. Wielopolski, M. Marszalek, F. G. Brunetti, D. Joly, J. Calbo, J. Aragón, J.-E. Moser, R. Humphry-Baker, S. M. Zakeeruddin, J. L. Delgado, M. Gratzel, E. Ortí and N. Martín, *J. Mater. Chem. C* **2016**, *4*, 3798-3808.
- [133] a) J. Calbo, J. Aragón and E. Ortí, *Theor. Chem. Acc.* **2013**, *132*, 1-10; b) J. Calbo, J. Aragón, F. Otón, V. Lloveras, M. Mas-Torrent, J. Vidal-Gancedo, J. Veciana, C. Rovira and E. Ortí, *Chem. Eur. J.* **2013**, *19*, 16656-16664.
- [134] J. Calbo, R. Viruela, E. Ortí and J. Aragón, *ChemPhysChem* **2016**, *17*, 3881-3890.
- [135] J. Calbo, C. E. Weston, A. J. P. White, H. S. Rzepa, J. Contreras-García and M. J. Fuchter, *submitted*.
- [136] V. Balzani, M. Venturi and A. Credi, *Molecular Devices and Machines: A Journey into the Nanoworld*, Wiley-VCH Verlag GmbH & Co. KGaA, **2006**, p. 511.
- [137] a) S. Berardi, S. Drouet, L. Francas, C. Gimbert-Surinach, M. Guttentag, C. Richmond, T. Stoll and A. Llobet, *Chem. Soc. Rev.* **2014**, *43*, 7501-7519; b) M. D. Kärkäs, E. V. Johnston, O. Verho and B. Åkermark, *Acc. Chem. Res.* **2014**, *47*, 100-111.
- [138] S. Fukuzumi, *Functional Organic Materials: Syntheses, Strategies and Applications*, Wiley-VCH Verlag GmbH & Co. KGaA, **2007**, p. 612.
- [139] E. M. Pérez and N. Martín, *Chem. Soc. Rev.* **2008**, *37*, 1512-1519.
- [140] a) L.-L. Li and E. W.-G. Diau, *Chem. Soc. Rev.* **2013**, *42*, 291-304; b) M. Urbani, M. Grätzel, M. K. Nazeeruddin and T. Torres, *Chem. Rev.* **2014**, *114*, 12330-12396.
- [141] S. Mathew, A. Yella, P. Gao, R. Humphry-Baker, F. E. Curchod Basile, N. Ashari-Astani, I. Tavernelli, U. Rothlisberger, M. K. Nazeeruddin and M. Grätzel, *Nat. Chem.* **2014**, *6*, 242-247.
- [142] P. A. Liddell, J. P. Sumida, A. N. Macpherson, L. Noss, G. R. Seely, K. N. Clark, A. L. Moore, T. A. Moore and D. Gust, *Photochem. Photobiol.* **1994**, *60*, 537-541.
- [143] G. Bottari, O. Trukhina, M. Ince and T. Torres, *Coord. Chem. Rev.* **2012**, *256*, 2453-2477.

- [144] a) M. Kimura, Y. Saito, K. Ohta, K. Hanabusa, H. Shirai and N. Kobayashi, *J. Am. Chem. Soc.* **2002**, *124*, 5274-5275; b) K. Yoosaf, J. Iehl, I. Nierengarten, M. Hmadeh, A.-M. Albrecht-Gary, J.-F. Nierengarten and N. Armaroli, *Chem. Eur. J.* **2014**, *20*, 223-231; c) F. D'Souza and O. Ito, *Chem. Commun.* **2009**, 4913-4928; d) P. D. W. Boyd and C. A. Reed, *Acc. Chem. Res.* **2005**, *38*, 235-242.
- [145] J.-Y. Zheng, K. Tashiro, Y. Hirabayashi, K. Kinbara, K. Saigo, T. Aida, S. Sakamoto and K. Yamaguchi, *Angew. Chem. Int. Ed.* **2001**, *40*, 1857-1861.
- [146] a) L. T. Scott, *Angew. Chem. Int. Ed.* **2004**, *43*, 4994-5007; b) M. A. Petrukhina and L. T. Scott, *Fragments of Fullerenes and Carbon Nanotubes: Designed Synthesis, Unusual Reactions, and Coordination Chemistry*, John Wiley & Sons, Hoboken, **2011**, p. 440.
- [147] A. Sygula, F. R. Fronczek, R. Sygula, P. W. Rabideau and M. M. Olmstead, *J. Am. Chem. Soc.* **2007**, *129*, 3842-3843.
- [148] D. Bonifazi, G. Accorsi, N. Armaroli, F. Song, A. Palkar, L. Echegoyen, M. Scholl, P. Seiler, B. Jaun and F. Diederich, *Helv. Chim. Acta* **2005**, *88*, 1839-1884.
- [149] a) Y.-B. Wang and Z. Lin, *J. Am. Chem. Soc.* **2003**, *125*, 6072-6073; b) M. Nishio, M. Hirota and Y. Umezawa, *The CH/ π Interaction: Evidence, Nature, and Consequences*, John Wiley & Sons, **1998**, p. 232.
- [150] P. D. W. Boyd and C. A. Reed, *Acc. Chem. Res.* **2004**, *38*, 235-242.
- [151] a) A. Hosseini, S. Taylor, G. Accorsi, N. Armaroli, C. A. Reed and P. D. W. Boyd, *J. Am. Chem. Soc.* **2006**, *128*, 15903-15913; b) C. García-Simón, M. Costas and X. Ribas, *Chem. Soc. Rev.* **2016**, *45*, 40-62.
- [152] a) C. Stangel, C. Schubert, S. Kuhri, G. Rotas, J. T. Margraf, E. Regulska, T. Clark, T. Torres, N. Tagmatarchis, A. G. Coutsolelos and D. M. Guldi, *Nanoscale* **2015**, *7*, 2597-2608; b) F. D'Souza, P. M. Smith, M. E. Zandler, A. L. McCarty, M. Itou, Y. Araki and O. Ito, *J. Am. Chem. Soc.* **2004**, *126*, 7898-7907.
- [153] a) L. Sánchez, M. Sierra, N. Martín, A. J. Myles, T. J. Dale, J. Rebek, W. Seitz and D. M. Guldi, *Angew. Chem. Int. Ed.* **2006**, *45*, 4637-4641; b) F. Wessendorf, J.-F. Gnichwitz, G. H. Sarova, K. Hager, U. Hartnagel, D. M. Guldi and A. Hirsch, *J. Am. Chem. Soc.* **2007**, *129*, 16057-16071; c) F. D'Souza, E. Maligaspe, K. Ohkubo, M. E. Zandler, N. K. Subbaiyan and S. Fukuzumi, *J. Am. Chem. Soc.* **2009**, *131*, 8787-8797.

- [154] B. Grimm, E. Karnas, M. Brettreich, K. Ohta, A. Hirsch, D. M. Guldi, T. Torres and J. L. Sessler, *J. Phys. Chem. B* **2010**, *114*, 14134-14139.
- [155] a) J. D. Megiatto, D. I. Schuster, S. Abwandner, G. de Miguel and D. M. Guldi, *J. Am. Chem. Soc.* **2010**, *132*, 3847-3861; b) K. Li, D. I. Schuster, D. M. Guldi, M. Á. Herranz and L. Echegoyen, *J. Am. Chem. Soc.* **2004**, *126*, 3388-3389.
- [156] a) R. M. K. Calderon, J. Valero, B. Grimm, J. de Mendoza and D. M. Guldi, *J. Am. Chem. Soc.* **2014**, *136*, 11436-11443; b) Z.-Q. Wu, X.-B. Shao, C. Li, J.-L. Hou, K. Wang, X.-K. Jiang and Z.-T. Li, *J. Am. Chem. Soc.* **2005**, *127*, 17460-17468.
- [157] L. Moreira, J. Calbo, R. M. Krick Calderon, J. Santos, B. M. Illescas, J. Aragón, J.-F. Nierengarten, D. M. Guldi, E. Ortí and N. Martín, *Chem. Sci.* **2015**, *6*, 4426-4432.
- [158] J. Calbo, A. de Juan, A. López-Moreno, E. Ortí and E. M. Pérez, *writing*.
- [159] H. Isla, M. Gallego, E. M. Pérez, R. Viruela, E. Ortí and N. Martín, *J. Am. Chem. Soc.* **2010**, *132*, 1772-1773.
- [160] a) A. de Juan, A. López-Moreno, J. Calbo, E. Ortí and E. M. Pérez, *Chem. Sci.* **2015**, *6*, 7008-7014; b) J. Calbo, A. de Juan, A. López-Moreno, J. Comer, E. Ortí and E. M. Pérez, *writing*.
- [161] M. A. Petrukhina, L. T. Scott and H. W. Kroto, *Fragments of Fullerenes and Carbon Nanotubes: Designed Synthesis, Unusual Reactions, and Coordination Chemistry*, Wiley, **2011**, p. 440.
- [162] F. Goubard and F. Dumur, *RSC Advances* **2015**, *5*, 3521-3551.
- [163] Y. Tao, C. Yang and J. Qin, *Chem. Soc. Rev.* **2011**, *40*, 2943-2970.
- [164] E. M. Pérez, M. Sierra, L. Sánchez, M. R. Torres, R. Viruela, P. M. Viruela, E. Ortí and N. Martín, *Angew. Chem. Int. Ed.* **2007**, *46*, 1847-1851.
- [165] H. Isla, B. Grimm, E. M. Pérez, M. R. Torres, M. Á. Herranz, R. Viruela, J. Aragón, E. Ortí, D. M. Guldi and N. Martín, *Chem. Sci.* **2012**, *3*, 498-508.
- [166] M. A. Petrukhina, K. W. Andreini, L. Peng and L. T. Scott, *Angew. Chem. Int. Ed.* **2004**, *116*, 5593-5597.
- [167] J. Calbo, J. Aragón, J. C. Sancho-García and E. Ortí, *submitted*.
- [168] a) M.-K. Chen, H.-J. Hsin, T.-C. Wu, B.-Y. Kang, Y.-W. Lee, M.-Y. Kuo and Y.-T. Wu, *Chem. Eur. J.* **2014**, *20*, 598-608; b) T.-C. Wu, M.-K.

- Chen, Y.-W. Lee, M.-Y. Kuo and Y.-T. Wu, *Angew. Chem. Int. Ed.* **2013**, *52*, 1289-1293.
- [169] M. Gallego, J. Calbo, J. Aragón, R. M. Krick Calderon, F. H. Liquido, T. Iwamoto, A. K. Greene, E. A. Jackson, E. M. Pérez, E. Ortí, D. M. Guldi, L. T. Scott and N. Martín, *Angew. Chem. Int. Ed.* **2014**, *53*, 2170-2175.
- [170] A. Harada, *Supramolecular Polymer Chemistry*, Wiley-VCH Verlag GmbH & Co. KGaA, **2011**, p. 390.
- [171] a) J.-M. Lehn, *Polym. Int.* **2002**, *51*, 825-839; b) A. Ciferri, *Supramolecular Polymers, Second Edition*, CRC Press, **2005**, p. 776.
- [172] C. Fouquey, J.-M. Lehn and A.-M. Levelut, *Adv. Mater.* **1990**, *2*, 254-257.
- [173] a) R. P. Sijbesma, F. H. Beijer, L. Brunsveld, B. J. B. Folmer, J. H. K. K. Hirschberg, R. F. M. Lange, J. K. L. Lowe and E. W. Meijer, *Science* **1997**, *278*, 1601-1604; b) B. J. B. Folmer, R. P. Sijbesma and E. W. Meijer, *J. Am. Chem. Soc.* **2001**, *123*, 2093-2094; c) V. Berl, M. Schmutz, M. J. Krische, R. G. Khoury and J.-M. Lehn, *Chem. Eur. J.* **2002**, *8*, 1227-1244.
- [174] M. Rehahn, *Acta Polym.* **1998**, *49*, 201-224.
- [175] F. Huang and L. Isaacs, *Acc. Chem. Res.* **2014**, *47*, 1923-1924.
- [176] a) C. C. Lee, C. Grenier, E. W. Meijer and A. P. H. J. Schenning, *Chem. Soc. Rev.* **2009**, *38*, 671-683; b) F. J. M. Hoeben, P. Jonkheijm, E. W. Meijer and A. P. H. J. Schenning, *Chem. Rev.* **2005**, *105*, 1491-1546.
- [177] a) S.-L. Li, T. Xiao, C. Lin and L. Wang, *Chem. Soc. Rev.* **2012**, *41*, 5950-5968; b) B. J. Cafferty, I. Gállego, M. C. Chen, K. I. Farley, R. Eritja and N. V. Hud, *J. Am. Chem. Soc.* **2013**, *135*, 2447-2450.
- [178] T. Qin, S. L. Skraba-Joiner, Z. G. Khalil, R. P. Johnson, R. J. Capon and J. A. Porco Jr, *Nat. Chem.* **2015**, *7*, 234-240.
- [179] F. Vera, J. Barberá, P. Romero, J. L. Serrano, M. B. Ros and T. Sierra, *Angew. Chem. Int. Ed.* **2010**, *49*, 4910-4914.
- [180] P. Iavicoli, H. Xu, L. N. Feldborg, M. Linares, M. Paradinas, S. Stafström, C. Ocal, B. Nieto-Ortega, J. Casado, J. T. López Navarrete, R. Lazzaroni, S. D. Feyter and D. B. Amabilino, *J. Am. Chem. Soc.* **2010**, *132*, 9350-9362.
- [181] J. Labuta, J. P. Hill, S. Ishihara, L. Hanyková and K. Ariga, *Acc. Chem. Res.* **2015**, *48*, 521-529.

- [182] a) S. Sergeev, W. Pisula and Y. H. Geerts, *Chem. Soc. Rev.* **2007**, *36*, 1902-1929; b) T. Wöhrle, I. Wurzbach, J. Kirres, A. Kostidou, N. Kapernaum, J. Litterscheidt, J. C. Haenle, P. Staffeld, A. Baro, F. Giesselmann and S. Laschat, *Chem. Rev.* **2016**, *116*, 1139-1241.
- [183] S. Cantekin, T. F. A. de Greef and A. R. A. Palmans, *Chem. Soc. Rev.* **2012**, *41*, 6125-6137.
- [184] a) J. Roosma, T. Mes, P. Leclère, A. R. A. Palmans and E. W. Meijer, *J. Am. Chem. Soc.* **2008**, *130*, 1120-1121; b) S. Cantekin, D. W. R. Balkenende, M. M. J. Smulders, A. R. A. Palmans and E. W. Meijer, *Nat. Chem.* **2011**, *3*, 42-46; c) P. J. M. Stals, J. C. Everts, R. de Bruijn, I. A. W. Filot, M. M. J. Smulders, R. Martín-Rapún, E. A. Pidko, T. F. A. de Greef, A. R. A. Palmans and E. W. Meijer, *Chem. Eur. J.* **2010**, *16*, 810-821; d) A. R. A. Palmans and E. W. Meijer, *Angew. Chem. Int. Ed.* **2007**, *46*, 8948-8968; e) F. Wang, M. A. J. Gillissen, P. J. M. Stals, A. R. A. Palmans and E. W. Meijer, *Chem. Eur. J.* **2012**, *18*, 11761-11770; f) F. García and L. Sánchez, *J. Am. Chem. Soc.* **2012**, *134*, 734-742.
- [185] F. García, P. M. Viruela, E. Matesanz, E. Ortí and L. Sánchez, *Chem. Eur. J.* **2011**, *17*, 7755-7759.
- [186] B. Nieto-Ortega, F. García, G. Longhi, E. Castiglioni, J. Calbo, S. Abbate, J. T. López Navarrete, F. J. Ramírez, E. Ortí, L. Sánchez and J. Casado, *Chem. Commun.* **2015**, *51*, 9781-9784.
- [187] J. Guilleme, M. J. Mayoral, J. Calbo, J. Aragón, P. M. Viruela, E. Ortí, T. Torres and D. González-Rodríguez, *Angew. Chem. Int. Ed.* **2015**, *54*, 2543-2547.
- [188] J. Guilleme, J. Calbo, J. Aragón, P. A. Korevaar, E. W. Meijer, E. Ortí, T. Torres and D. González-Rodríguez, *writing*.
- [189] A. Laurent, *Ann. Chim. Phys.* **1837**, *66*, 136.
- [190] a) C. Wang, H. Dong, W. Hu, Y. Liu and D. Zhu, *Chem. Rev.* **2012**, *112*, 2208-2267; b) T. M. Figueira-Duarte and K. Müllen, *Chem. Rev.* **2011**, *111*, 7260-7314.
- [191] J. Duhamel, *Langmuir* **2012**, *28*, 6527-6538.
- [192] J. Buendía, J. Calbo, E. Ortí and L. Sánchez, *submitted*.

List of publications

Colour coding:

■ Published ■ Accepted ■ Submitted

Articles in the Thesis

The author of the present thesis has carried out all the calculations and theoretical analyses presented in the articles discussed herein. Moreover, the author has played a primary role in the writing process of the articles. The PhD student has signed in all the works as the first author of his group. Nevertheless, due to the collaborative nature of the research developed, the author is not always placed at the first position in some of the research articles discussed in this Thesis. A mark (†) has recently been introduced accounting for the equal contribution as the first author of the article (see contributions 7, 8 and 9).

* Corresponding author

Covalent Donor–Acceptor Architectures

1 P.-A. Bouit, L. Infantes, J. Calbo, R. Viruela, E. Ortí, J. L. Delgado and N. Martín, “Efficient Light Harvesters Based on the 10-(1,3-Dithiol-2-ylidene)anthracene Core”, *Org. Lett.* **2013**, *15*, 4166-4169.

2 J. Calbo, P. M. Viruela and E. Ortí, “Theoretical insight on novel donor-acceptor exTTF-based dyes for dye-sensitized solar cells”, *J. Mol. Model.* **2014**, *20*, 1-10.

3 J. Calbo, M. Pastore, E. Mosconi, E. Ortí and F. De Angelis, “Computational modelling of single- versus double-anchoring modes in di-branched organic sensitizers on TiO₂ surfaces: structural and electronic properties”, *Phys. Chem. Chem. Phys.* **2014**, *16*, 4709-4719.

Supramolecular Donor–Acceptor Complexes

4 L. Moreira, J. Calbo, B. M. Illescas, J. Aragón, I. Nierengarten, B. Delavaux-Nicot, E. Ortí, N. Martín and J.-F. Nierengarten, “Metal-Atom Impact on the Self-Assembly of Cup-and-Ball Metalloporphyrin–Fullerene Conjugates”, *Angew. Chem. Int. Ed.* **2015**, *54*, 1255-1260.

5 L. Moreira, J. Calbo, J. Aragón, B. M. Illescas, I. Nierengarten, B. Delavaux-Nicot, E. Ortí, N. Martín and J.-F. Nierengarten. “Conjugated Porphyrin Dimers: Cooperative Effects and Electronic Communication in Supramolecular Ensembles with C₆₀”, *J. Am. Chem. Soc.* **2016**, *138*, 15359-15367.

6 M. Gallego, J. Calbo, J. Aragón, R. M. Krick Calderon, F. H. Liquido, T. Iwamoto, A. K. Greene, E. A. Jackson, E. M. Pérez, E. Ortí, D. M. Guldi, L. T. Scott and N. Martín, “Electron Transfer in a Supramolecular Associate of a Fullerene Fragment”, *Angew. Chem. Int. Ed.* **2014**, *53*, 2170-2175.

7 M. Gallego, J. Calbo,† R. M. Krick Calderon, P. Pla, Y.-C. Hsieh, E. M. Pérez, Y.-T. Wu, E. Ortí, D. M. Guldi and N. Martín, “Complexation and Electronic Communication between Corannulene-Based Buckybowls and a Curved Truxene-TTF Donor” (accepted, DOI: 10.1002/chem.201604921).

Supramolecular Polymers

8 J. Buendía, J. Calbo,† F. García, J. Aragón, P. M. Viruela, E. Ortí and L. Sánchez, "Helical supramolecular polymerization of C₃-symmetric amides and retroamides: on the origin of cooperativity and handedness", *Chem. Commun.* **2016**, *52*, 6907-6910.

9 J. S. Valera, J. Calbo,† R. Gómez, E. Ortí and L. Sánchez, "Blue-emitting pyrene-based aggregates", *Chem. Commun.* **2015**, *51*, 10142-10145.

Contributions related with the Thesis

Covalent Donor–Acceptor Architectures

10 R. García, M. Á. Herranz, M. R. Torres, P.-A. Bouit, J. L. Delgado, J. Calbo, P. M. Viruela, E. Ortí and N. Martín, "Tuning the Electronic Properties of Nonplanar exTTF-Based Push–Pull Chromophores by Aryl Substitution", *J. Org. Chem.* **2012**, *77*, 10707-10717.

11 J. Calbo, J. Aragón and E. Ortí, "Theoretical study of the benzoquinone–tetrathiafulvalene–benzoquinone triad in neutral and oxidized/reduced states", *Theor. Chem. Acc.* **2013**, *132*, 1-10.

12 J. Calbo, J. Aragón, F. Otón, V. Lloveras, M. Mas-Torrent, J. Vidal-Gancedo, J. Veciana, C. Rovira and E. Ortí, "Tetrathiafulvalene-Based Mixed-Valence Acceptor–Donor–Acceptor Triads: A Joint Theoretical and Experimental Approach", *Chem. Eur. J.* **2013**, *19*, 16656-16664.

13 A. López-Moreno, D. Clemente-Tejeda, J. Calbo, A. Naeimi, F. A. Bermejo, E. Ortí and E. M. Pérez, "Biomimetic oxidation of pyrene and related aromatic hydrocarbons. Unexpected electron accepting abilities of pyrenequinones", *Chem. Commun.* **2014**, *50*, 9372-9375.

14 B. Pelado, F. Abou-Chahine, J. Calbo, R. Caballero, P. de la Cruz, J. M. Junquera-Hernández, E. Ortí, N. V. Tkachenko and F. Langa, "Role of the Bridge in Photoinduced Electron Transfer in Porphyrin–Fullerene Dyads", *Chem. Eur. J.* **2015**, *21*, 5814-5825.

15 M. Wielopolski, M. Marszalek, F. G. Brunetti, D. Joly, J. Calbo, J. Aragón, J.-E. Moser, R. Humphry-Baker, S. M. Zakeeruddin, J. L. Delgado, M. Grätzel, E. Ortí and N. Martín, "Synthesis and optoelectronic properties of chemically modified bi-fluorenylidenes", *J. Mater. Chem. C* **2016**, *4*, 3798-3808.

16 R. Sandoval-Torrientes, J. Calbo, J. Santos, E. Ortí and N. Martín, "Rhodanine-Based Light Harvesters Absorbing in the Entire Visible Spectrum" (submitted).

Supramolecular Donor–Acceptor Complexes

17 L. Moreira, J. Calbo, R. M. Krick Calderon, J. Santos, B. M. Illescas, J. Aragón, J.-F. Nierengarten, D. M. Guldi, E. Ortí and N. Martín, "Unveiling the nature of supramolecular crown ether-C₆₀ interactions", *Chem. Sci.* **2015**, *6*, 4426-4432.

18 A. de Juan, A. López-Moreno, J. Calbo, E. Ortí and E. M. Pérez, "Determination of association constants towards carbon nanotubes", *Chem. Sci.* **2015**, *6*, 7008-7014.

19 J. Calbo, J. Aragón, J. C. Sancho-García and E. Ortí, "DLPNO-CCSD(T) Scaled Methods for the Accurate Treatment of Large Supramolecular Complexes: Unveiling the Role of CH– π versus π – π Interactions in the Donor–Acceptor Truxene-tetrathiafulvalene–Hemifullerene Complex" (submitted).

Supramolecular Polymers

20 J. Guilleme, M. J. Mayoral, J. Calbo, J. Aragón, P. M. Viruela, E. Ortí, T. Torres and D. González-Rodríguez, “Non-Centrosymmetric Homochiral Supramolecular Polymers of Tetrahedral Subphthalocyanine Molecules”, *Angew. Chem. Int. Ed.* **2015**, *54*, 2543-2547.

21 B. Nieto-Ortega, F. García, G. Longhi, E. Castiglioni, J. Calbo, S. Abbate, J. T. López Navarrete, F. J. Ramírez, E. Ortí, L. Sánchez and J. Casado, “On the handedness of helical aggregates of C₃ tricarboxamides: a multichiroptical characterization”, *Chem. Commun.* **2015**, *51*, 9781-9784.

22 J. Buendía, J. Calbo, E. Ortí and L. Sánchez, “Disregarding Molecular Chirality. Consequences on nanoscopic and macroscopic helicity” (submitted).

Other contributions

23 J. Calbo,* R. Viruela, E. Ortí and J. Aragón, “Relationship between Electron Affinity and Half-Wave Reduction Potential: A Theoretical Study on Cyclic Electron-Acceptor Compounds”, *ChemPhysChem* **2016**, *17*, 3881-3890.

24 J. Calbo, E. Ortí, J. C. Sancho-García and J. Aragón, “Accurate Treatment of Large Supramolecular Complexes by Double-Hybrid Density Functionals Coupled with Nonlocal van der Waals Corrections”, *J. Chem. Theory Comput.* **2015**, *11*, 932-939.

25 J. Calbo, C. E. Weston, A. J. P. White, H. S. Rzepa, J. Contreras-García and M. J. Fuchter, “Tuning Azoheteroarene Photoswitch Performance through Heteroaryl Design.”, *J. Am. Chem. Soc.* (accepted, DOI: 10.1021/jacs.6b11626)

Book chapters

26 J. Calbo,* E. Ortí, J. C. Sancho-García and J. Aragó, “The nonlocal correlation density functional VV10: A successful attempt to accurately capture noncovalent interactions” *Annual Reports in Computational Chemistry*, Volume 11 (Ed.: A. D. David), Elsevier, **2015**, pp. 37-102.

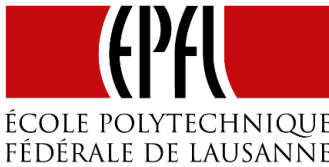
Collaborations



instituto
imdea
nanociencia



UPMC
SORBONNE UNIVERSITÉS



TAMPERE
UNIVERSITY OF
TECHNOLOGY

